N° d'ordre : 42047

THESE

Présentée à l'Université de Lille 1
École Doctorale Sciences pour l'Ingénieur

Institut d'Electronique, de Microélectronique et de Nanotechnologie

Pour obtenir le grade de :

DOCTEUR DE L'UNIVERSITE

Spécialité : MICRO ET NANOTECHNOLOGIES, ACOUSTIQUE ET TELECOMMUNICATIONS

Par

Valeria LACATENA

FABRICATION AND THERMAL CONDUCTIVITY CHARACTERIZATION OF PHONONIC ENGINEERED SILICON MEMBRANES FOR THERMOELECTRIC APPLICATIONS

Soutenue le 1er Juin 2016 devant le jury compose de :

Mme. Sylvie HEBERT, *Directeur de recherche CNRS,CRISMAT, Caen*	Rapporteur
M. Sebastian VOLZ, *Directeur de recherche CNRS, SUPELEC Châtenay Malabry*	Rapporteur
M. Lionel BUCHAILLOT, *Directeur de recherche CNRS, IEMN, Villeneuve d'Ascq*	Examinateur
M. Pierre-Olivier CHAPUIS, *Chargé de recherche au CNRS, CETHIL, Lyon*	Examinateur
M. Stéphane MONFRAY, *Ingénieur R&D, STMicroelecronics, Crolles*	Co-encadrant de thèse
M. Jean-François ROBILLARD, *Enseignant Chercheur, IEMN, Villeneuve d'Ascq*	Co-encadrant de thèse
M. Thomas SKOTNICKI, *Directeur R&D, STMicroelecronics, Crolles*	Co-directeur de thèse
M. Emmanuel DUBOIS, *Directeur de recherche CNRS, IEMN, Villeneuve d'Ascq*	Directeur de thèse

*“Go confidently in the direction of your dreams.
Live the life you've imagined.”*
(Henry David Thoreau)

Acknowledgments

Undertaking this Ph.D. has been an incredible journey, a truly life-changing experience for me and it would not have been possible without the support and guidance that I received from many people. Actually, I am a pretty lucky human being having so many friends, in many countries, who so generously supported and contributed to the work presented in this thesis. Thus, I am in need of thanking each one from the beginning of this experience.

This Ph.D. work has been carried out at the *Institut d'électronique de microélectronique et de nanotechnologie* (IEMN) in Lille in the Silicon Microelectronics group and supported, in the frame of a CIFRE contract, by ***STMicroelectronics*** and by founding received from the ***European Research Council (ERC)*** under the European Community's Seventh Framework Programme (FP7/2007-2013) ERC Grant Agreement no. 338179.

First and foremost I wish to thank my Ph.D. advisor ***Emmanuel Dubois*** for the continuous sustain of my study and research, for his advices, motivation, enthusiasm and immense knowledge. His guidance helped me in all the time of research, teaching me how good and rigorous experimental microelectronics is done. I could not have imagined having a better advisor for my Ph.D. study.

I am deeply grateful to ***Thomas Skotnicki***, my industrial Ph.D. advisor, who, thank to his enormous experience, knowledge and support, made this research work possible and allowed me to participate in this incredible academic and industrial project.

Special, very special, acknowledgments are addressed to my mentor and co-advisor (*Encadrant*) ***Jean-François Robillard***. It has been an honor to be followed by him constantly. He has taught me everything I know about the topic from the very beginning, always welcoming fruitful discussions and theoretical explanations. I appreciate all his contributions of time, ideas and hints to make my Ph.D. experience productive and stimulating. His patience, flexibility, genuine caring and concern, and faith in me during these years enabled me to attend life while also earning my Ph.D. He has been incredibly encouraging and enlightening. *Merci JF!*

Profound gratitude goes to ***Stéphane Monfray***, my co-advisor in STMicroelectronics, who has been a truly dedicated mentor. I am particularly indebted to Stéphane for his constant faith in my lab work, the fruitful calls and meetings, the constant support, despite the distance Grenoble – Lille.

I would like to thank ***Sylvie Hebert*** (CRISMAT, Caen) and ***Sebastian Volz*** (SUPELEC Châtenay Malabry) for accepting the review of this manuscript and being the referees of this Ph.D. defence. I thank you for the time dedicated to read and evaluate this dissertation.

I also thank the other members of this Ph.D. committee: ***Pierre-Olivier Chapuis*** (INSA, Lyon) for the willingness to participate this defence and the interesting suggestions and explanations during the year we collaborated.
I feel grateful to ***Lionel Buchaillot*** (IEMN, Villeneuve d'Ascq) for accepting to be the president of this Ph.D. jury.

The members of the Silicon Microelectronics group have contributed immensely to my personal and professional time at the IEMN. The group has been a source of friendships as well as good advice and collaboration.
I am especially grateful to ***Maciej Haras*** for the incredible patience and availability in standing at all my questions, curiosity, help requests and my "*I was thinking… "*. I convey him my special thanks for being an example of Ph.D student with great strategy and work organization during those three years and half. *Dziękuję Maciej!*
A group can't be a group without co-operation, suggestions, hints and (language (French)) support. Thus, many thanks are addressed to ***Valentina Giorgis***, ***Justine Philippe***, ***François Morini***, ***Matthieu Berthomé***, ***Pascale Diener***, ***Quentin Hivin***, ***Hossein Ftouni***, ***Thierno Bah*** and ***Stanislav Didenko***.
The technological work realized during these years was possible thanks to the help, knowledge and trainings of the IEMN staff, in particularly: ***Marc Derwitte***, ***Christiane Legrand***, ***Sylvie Lepilliet***, ***Yves Deblock***, ***Pascal Tilmant***, ***François Vaurette***, ***Dimitri Yareka***, ***Christophe Boyaval***, ***Isabelle Roche-Jeune***, etc. They made the fabrication and characterization work possible and easier.

Sono arrivata a Lille nel Novembre 2012, non conoscevo nessuno qui, e mai avrei potuto immaginare di trovare una *famiglia italiana* tanto speciale di cui non potrò più fare a meno.
Un immenso grazie va a ***Gabriele***, talmente simile a me che non ho bisogno di spiegargli il perchè. Colui che mi sostiene e rallegra, colui che mi ospita quando ho voglia di parlare di tutto o di nulla, colui che mi accompagna sempre ovunque, colui che si è rivelato un grande amico, ma soprattutto una gran bella persona. Poter contare su di te è una delle certezze più rincuoranti di questi ultimi anni!
Ringrazio ***Michela***, la mia torinese-lilloise che ha condiviso con me stupende giornate, serate e confidenze. La coabitazione a Lille è stata breve ed alternata, ma sempre intensa ed insostituibile, e comunque... *Insieme stravinciamo!*
Un grazie speciale a ***Riccardo***, ***Fabio***, ***Alice*** e ***Matteo*** per le serate insieme, le cene, le canzoni, le domeniche *al cavallo* e per avermi sempre fatto sentire un po' in Italia, *a casa*, anche qui!
Me alegro de tener en Lille una *familia Española* tan simpática y amable: en serio, sois la hostia! Estos años sin vosotros, sin los picnics en el parque rojo, sin las cervecitas de las 19 y sin la Latina… habrían estado mucho más aburridos y tristes ! Os quiero chicos domingueros : ***Alba***, ***Pablo C.***, ***Ana***, ***Marta***, ***Bassim***, ***Asis***, ***Pablo P.***, ***Juliette***, ***Nacho***, ***Clara, Maria***. Gracias de corazón!
Muchas gracias también à ***Gabriel*** para su amistad, los días de escalada juntos, al mercado y las risas de esto último año!

Merci ***Lucie*** pour tes incroyables découvertes quotidiennes, qu'ont apporté idées sympas de réflexion et de débat dans notre coloc. Merci aussi à ***Adrien***, ***Baptiste*** et ***Claire*** pour les années ensemble et pour supporter moi comme colocataire!

Ci sono poche persone che nonostante i (molti) kilometri di distanza, le assenze ed i silenzi sono sempre lì, al tuo fianco, a sostenerti e gioire con te e per te. Che sia in una conversazione Skype, whatsapp o in un breve incontro in qualche posto random nel mondo, voi: ***Angela***, ***Enrica***, ***Federico***, ci siete sempre! Non ci sono parole per definire questa amicizia straordinaria e forte, d'altronde noi, di parole, non ne abbiamo mai avuto bisogno. Il bello è proprio questo: poter essere me stessa, senza alcun ritegno, insieme a voi. Sappiate che siete e sarete sempre la mia fonte di ispirazione, il mio esempio e sostegno.

Il bello di vivere lontano e *rientrare* dopo mesi è anche quello di sapere che tutto resta intatto nel tempo, nonostanze le vite continuino separate. Casa, Monopoli, non sarebbe così accogliente senza la certezza di rincontrare i propri amici di sempre, quelli con cui le avventure, le chiacchierate e le serate sono immemorabili ed innumerevoli. Un grandissimo grazie a ***Paola***, la mia compagna di banco, di canoa, di scampagnate, spiaggiate e serate. Quella persona che non smette mai di farmi parlare (e quanto parliamo noi!), ridere e commuovere (sì, ho trovato la tua ultima lettera nascosta a Lille!). ***Viviana***, un grazie particolare anche a te, per essere diventata tanto speciale in così poco tempo ed a tale distanza. Sei prima stata la mia compagna di serate ed estati felici e spensierate, ed ora sei diventata una mamma-imprenditrice esemplare. Sono orgogliosa! A ***Nicoletta*** che ha sempre saputo organizzare (da leader) la nostra amicizia e le nostre serate di gruppo, ai suoi saggi, diretti ed utili consigli, ai suoi panzerotti: Grazie *Colino!*
Grazie agli amici di sempre, a quelli che quanto *scendo* sono pronti a riabbracciarmi e scambiare lunghe chiacchierate insieme, ai migliori: ***Francesca***, ***Andrea***, ***Massimo Grim***, ***Massimo Scial.***, ***Benny***, ***Rosanna***, ***Roberto***, ***Gianpaolo***. Uno speciale grazie a ***Leo***, per gli incoraggiamenti e la fiducia all'inizio di questa avventura.

Un grazie speciale ai ***Girolamini***, che hanno riempito di gioia tanti week-end in questi ultimi anni con il loro spirito festaiolo ed allegro. Una fortuna incontrarvi (ovunque nel mondo voi siate!).
Merci à ***Anne-Charlotte*** pour les incroyables moments vécu ensemble dans nôtres voyages partout dans le monde, pour ta compagnie, organisation et patience! *À le prochain voyage!*
A big thank to my brother-panda ***Raghu***, who became a real confidant, travel buddy and support in the last years. I am confident our friendship will last, we have the same spirit! A ***Sara***, ai suoi saggi consigli, discorsi, al suo adorabile animo: Grazie! Sei sempre stata di aiuto negli ultimi tre anni, sono davvero felice di aver incontrato una bella persona come te, e continuerò a seguire i *quattro accordi*!
Obrigada ***Alex***, eu não preciso me explicar, tu já sabes!
Thanks to ***Leni***, for the fun trips we had and the ones to come, for the big news and sharing it with me.
Grazie a tutti gli amici ed amiche sparse per il mondo che ho avuto il piacere di incontrare in questi ultimi anni e mi hanno rallegrato la vita: ***Silvia***, ***Mattia***, ***Serena***, ***Sara***, ***Giulia***, ***Teresa***, i

BN e tutti coloro che hanno contribuito alla riuscita di questa impresa anche con un solo abbraccio!
I should also thank Ryanair, whose cheap fares allowed me to meet family and friends all around Europe! ;-p

Per concludere, ma solo perchè meritano maggiore enfasi ed attenzione, voglio ringraziare la mia stupenda famiglia. Mia ***mamma Mariella***, la mia vera fonte di ispirazione e forza, colei che, sebbene così piccola, infonde grande sicurezza, la migliore persona che conosco, per valori, onestà, animo ed intelligenza. Colei a cui devo di più, perchè non ha mai giudicato, indicato o forzato, ma mi ha reso una persona libera di scegliere ed indipendente. Grazie! Ringrazio il mio ***papà Luigi***, una roccia, che sempre mi sostiene con orgoglio e devozione, malgrado la mia testardaggine ed il mio spirito avventuriero. Grazie alla mia sorellina, ***Roberta***, la mia più grande e tenera fan. Colei che mi strapperebbe il sorriso in ogni occasione, i cui abbracci sono i migliori del mondo (*gugugu* inclusa!), colei per cui sono sempre *Eia* e sempre mi supporta (e sopporta)!

Grazie!
Merci!
Thank you!
Gracias!
Obrigada!

Valeria

Table of contents

ACKNOWLEDGMENTS 5

TABLE OF CONTENTS 9

INTRODUCTION 13

CHAPTER 1 PHONONIC ENGINEERING FOR THERMOELECTRICITY 15

Abstract 15

1.1 Energy 15
1.1.1 Energy in the world 15
1.1.2 Alternative energy sources 17

1.2 Industrial waste heat 18

1.3 Thermoelectricity 19
1.3.1 Thermal transport 21
1.3.2 Seebeck effect 22
1.3.3 Efficiency of thermoelectric devices 23
1.3.4 Materials 24
1.3.5 Nanostructuration 32

1.4 Heat transport 42

1.5 Phononic Engineering, state of the art 47
1.5.1 Membranes 47
1.5.2 Phononic crystals 50

1.6 Conclusions and perspectives 56

CHAPTER 2 MOLECULAR DYNAMICS SIMULATIONS 59

Abstract 59

2.1 Introduction 59

2.2 Heat transport 60

2.3 Green Kubo Molecular Dynamic (GK-MD) 61

2.4 Molecular Dynamics procedure 63
2.4.1 Heat current autocorrelation function (HCAF) 63
2.4.2 Cell Geometries 65

2.5 Molecular dynamics state of the art comparison 67

2.6 Results 69

2.7 Conclusions 73

Appendix - THE CURIE SUPERCOMPUTER 75

CHAPTER 3 DEVICE DESIGN AND FABRICATION 77

Abstract 77

3.1 Phononic Crystals (PnCs) patterning 77
3.1.1 Electron Beam Lithography methodology 78
3.1.2 Reactive Ion Etching of phononic patterns 87
3.1.3 Patterning results and conclusion 88

3.2 Integration of PnCs into suspended membranes 89

3.3 Description of the different device generations 106
3.3.1 1st generation device 106
3.3.2 2nd generation device 107
3.3.3 Device for Raman measurements 108

3.4 Conclusions 111

CHAPTER 4 THERMAL CHARACTERIZATION 113

Abstract 113

4.1 Thermal characterization: methods 113

4.2 Electro-Thermal 114
4.2.1 Methodology description 115
4.2.2 Results 119

4.3 Raman thermometry 135
4.3.1 Overview of the procedure 135
4.3.2 Detailed methodology 136
4.3.3 Results 147

4.4 Scanning Thermal Microscopy 149
4.4.1 Introduction 149
4.4.2 Technique 149
4.4.3 Measurements 151
4.4.4 Results 152

4.5 Conclusions 155

CONCLUSIONS 157

PERSPECTIVES 159

RESUME EN FRANÇAIS **163**

Introduction **163**

Chapitre 1 - Théorie et état de l'art **165**

Chapitre 2 - Simulations de Dynamique Moléculaire **173**

Chapitre 3 - Conception et fabrication du dispositif **178**

Chapitre 4 - Résultats de caractérisations du dispositif **182**
Méthode Electrothermique 182
Spectroscopie Raman 184
Microscopie à Balayage Thermique 186

Conclusions et Perspectives **189**

SCIENTIFIC PRODUCTION **191**

BIBLIOGRAPHY **193**

Introduction

In the last twenty years, the continuous seek for alternative energy sources to power micro- and nano-electronic devices has marked the rise of interest toward thermoelectricity. Any kind of energy difference can potentially be used as a power source, and in many cases, this potential power is lost as waste heat. Thermoelectric materials can leverage this, turning directly, by Seebeck effect, the temperature difference into useful electric power. The need for finding an industrial-process (C-MOS) compatible material combined with its cheapness, abundance and not-harmfulness envisage silicon as the best candidate for the scope.
It is known that, to improve thermoelectric efficiency, an important role is played by material's electronic properties and its thermal conductivity. Silicon exhibits very good electrical conductivity and Seebeck parameter, but its lattice thermal conductivity represents the bigger obstacle for thermoelectric applications, preventing its direct integration as bulk material. It has been demonstrated that nanostructuring silicon in thin films enables the reduction of thermal conductivity down to one order of magnitude. Furthermore, recent works shown that a one order of magnitude supplementary decrease of thermal conductivity is possible by periodical patterning of the silicon thin film in a photonic-like way, creating Phononic Crystals (PnCs). The patterned materials would present properties similar to photonic crystals ones, such as: phononic band gap, group velocity reduction due to the band folding effect resulting from the added periodicity and PnCs anisotropy, which could be responsible of the strong reduction of thermal conductivity.
Although few groups already demonstrate this interesting phononic effect, the physics underneath the thermal conductivity reduction is still unclear and has ignited a strong debate among the various researchers in the field.

The objective of this doctoral work is to design, fabricate and characterize a thin film phononic engineered measurement platform for thermal conductivity measurements. The device has been characterized by Electro-Thermal method and the collaboration with the CETHIL-INL of Lyon allowed Raman thermometry and Scanning Thermal Microscopy characterizations. The main interest is to investigate the phonon effect and contribution to the heat transport in nanostructured silicon. In the first place, a consistent theoretical support model is formulated with Molecular Dynamics simulations by Green-Kubo method. It aims at drawing the guidelines to improve the device's capabilities and performances and justifying and consolidating the experimental achievements.
In the first chapter of this work is presented an introductory theoretical background and stat-of-the-art contextualization of thermoelectric energy harvesting possibilities and challenges, focusing on phononic engineered silicon devices to achieve the thermal conductivity reduction needed to boost the device's efficiency.
Therefore, in Chapter 2, the discussion of phononic effect in thermal conductivity reduction is tackled, pointing out its physical and theoretical interpretation. A Molecular Dynamics simulation framework with Green-Kubo method (MD-GK) is conceived and the material

nanostructuration effect is widely analyzed and compared with state-of-the-art simulation results and experimental ones. The main goal is the realization of a complete simulation procedure and context to foresee and highlight phononic engineered materials effects and behaviors when integrated into real devices. Thus, phononic patterns fabrication details and properties can attentively be designed with results perspective.

Chapter 3 is devoted to the detailing of the fabrication process of the thin film phononic engineered platform. The realization is entirely performed in the clean room of the IEMN, making autonomous use of all the tools necessary for the device fabrication (Electron-Beam Lithography, Reactive Ion Etching, Scanning Electron Microscopy, Profilometer, Ellipsometer, Spin coaters, etc.). All the steps of the device conception and realization are illustrated, highlighting the choice of methodologies and materials, along with their properties' characterization.

Chapter 4 summarizes all the results obtained for the devices' characterization. It has been divided in three parts with respect to the different measurement methods adopted. Firstly, Electro-Thermal characterization strategy is detailed. The study demonstrates the reduction of thermal conductivity in PnC membranes and compares those results to the ones of plain membranes. This method represents the main objective of our investigation, being oriented toward the conversion of the metrology platform into a complete integrated device for combined measurements of electrical conductivity and Seebeck coefficient along with thermal ones. In second place, Raman spectroscopy has been performed on another design realized to confirm the envisaged trend. Supporting COMSOL and RCWA modeling have been realized by M. Massoud in CETHIL-INL (Lyon) to extract the results.

A third characterization method, Scanning Thermal Microscopy, performed at the CETHIL (Lyon), also investigates the lattice thermal conductivity reduction distinguishing between the different heat transport mechanisms playing a role in calculating material's thermal properties by contact method.

Chapter 1 **Phononic Engineering for Thermoelectricity**

Abstract

This first chapter reviews the theoretical and experimental background in the field of phononic engineering for thermoelectric applications. The necessity of seeking for alternative energy sources impose us to consider solutions reliable, safe and easily available. Taking into account the possible social, environmental and technological impacts at which a boost of thermoelectric energy production would lead, this chapter focuses on the different alternatives envisageable and the possible solutions. In a first part it will analyze its recent developments, prospective applications, perspectives and related challenges. Therefore, an overview of the materials for thermoelectric application is presented and the different methodologies to boost their efficiency analyzed. One answer to the problem might be the improvement of thermoelectric devices capabilities by means of phononic crystal patterning which entails a sensible reduction of thermal conductivity. Thus, the argument of the second part of this chapter will be the study of heat transport mechanisms in relation to thermoelectric devices properties improvement, focusing on phononic engineering. The coupling of the enhanced performances yielded by phononic crystals (PnCs) periodically patterned and thin film membranes could lead to a consistent increase of the thermoelectric figure of merit up to a highly competitive value. The fabrication of devices using CMOS compatible materials, for instance silicon and germanium, represents a great advantage in terms of industrial applicability.

1.1 Energy

1.1.1 Energy in the world

Nowadays energy supply represents one of the most important issues to deal with. The 'World energy outlook 2014 - Executive summary' raises the alarm over the topic announcing that *the global energy system is in danger of falling short of the hopes and expectations placed upon it* [1]. Nevertheless, in 2014 the amount of energy consumption marked an historical stagnation, the value reported by Enerdata in the Global Year Statistical Yearbook is of 13737 Mtoe (1 toe = 11.63 MW·h), a very little increase of 0.5% with respect to the value of 2013 of 13671 Mtoe [2]. The report sheds light on the trends for energy production and consumption during the last years. Table 1.1 summarizes the results for some selected regions of the world.

Table 1.1 Summary of the energy consumption and production reported by Enerdata in the Global Year Statistical Yearbook 2014 [2].

Region	**CONSUMPTION**			**PRODUCTION**		
	2014	2013-2014 (%year)	2000-2014 (%year)	2014	2013-2014 (%year)	2000-2014 (%year)
World	13737	0,5	2,2	13768	1,1	2,3
Europe	1777	-3,5	-0,3	1043	-1,0	-1,2
France	243	-4,1	-0,3	138	1,6	0,4
US	2224	1,1	-0,1	1989	6,3	1,3
Latin America	861	0,5	2,6	1040	0,0	1,5
China	3034	-0,2	7,1	2555	-0,4	6,0
Asia	5545	1,3	4,7	4152	0,4	4,6
Africa	737	0,5	3,0	1086	-2,1	1,6

The results of this study are depicted in Figure 1.1 and show the total energy consumption and production in terms of Mtoe (1 million of tons of oil equivalent (toe)). It has to be considered that the global energy demand is foreseen to grow by 37% in the scenario drafted in [1], but the development path for a parallel and constant growing of population and economy is less energy-intensive than what it used to be. Thus, as explicated in the report, the growth of global demand will slowly decrease from 2% per year over the last two decades to 1% per year after the 2025. The reason of this is explained to be a result both of price and policy effects, and a structural shift in the global economy towards services and lighter industrial sectors. Therefore, the energy use is foreseen to stay flat in much of Europe, Japan, Korea and North America, and dramatically rise in consumption in the rest of Asia (60% of the total), Africa, the Middle East and Latin America (Figure 1.2).

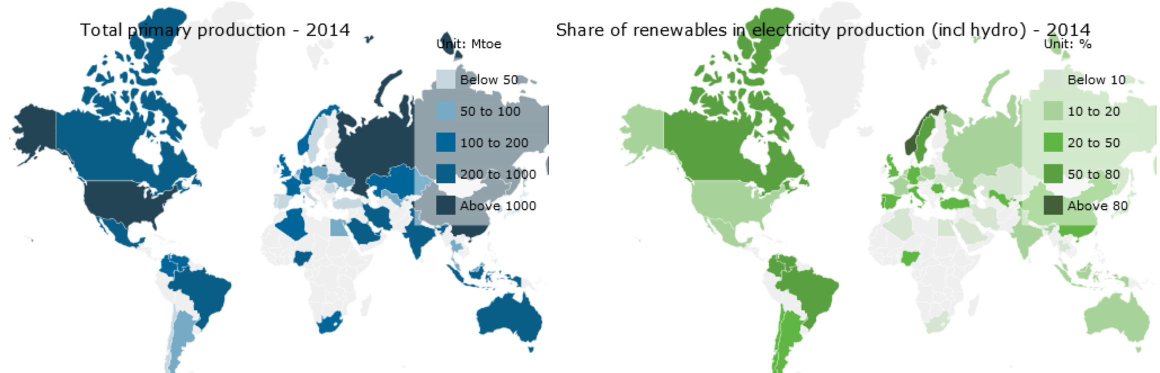

Figure 1.1 Total energy consumption (left) and production (right) worldwide in 2014. Study by Enerdata [1].

The British Pertroleum's Statistical Review of World Energy published in June 2015 [3] confirms the described scenario, underlining that *global primary energy consumption decelerated sharply in 2014, even though global economic growth was similar to 2013*.

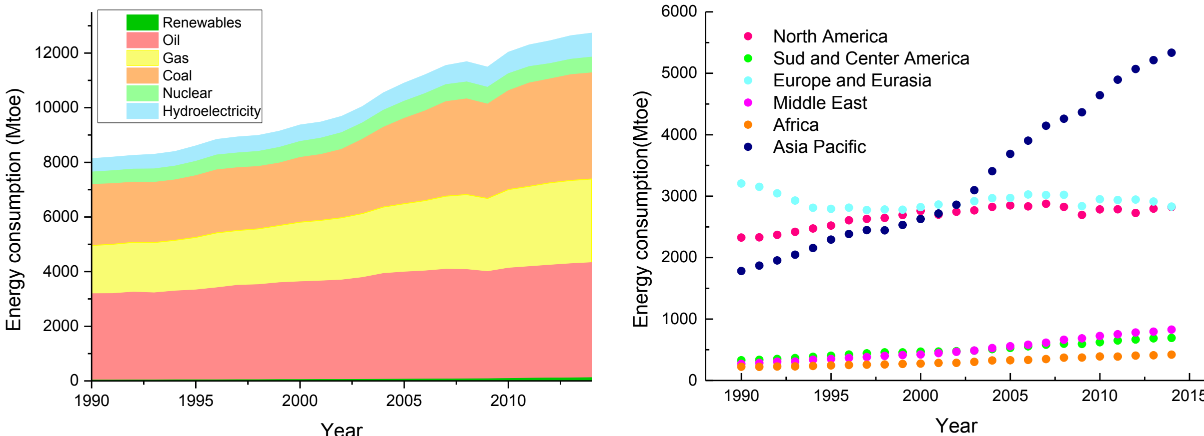

Figure 1.2 Primary energy regional consumption pattern 2014 in percentage (upper figure) for different fuels. Primary energy world consumption growth during the last 15 years (Million tonnes oil equivalent) as reported by BP Statistical Review of World Energy 2015 [3].

Figure 1.2 depicts that the Asia Pacific region accounted during the past years for the largest increment to global primary energy consumption and continues to account for the largest share (41.3% of the global total). This region represented over 71% of global coal consumption for the first time in 2014, and coal remains the region's dominant fuel. Gas is the dominant fuel in Europe, Eurasia and the Middle East, while oil is the largest source of energy in the Americas and Africa [3].
World primary energy consumption grew little in 2014, the slowest rate of growth since 1998 other than the decline in the aftermath of the financial crisis. Growth was below average in all regions except North America and Africa. It also shows that all fuels, except nuclear, grew at below-average rates. Currently, oil remains the world's dominant fuel, while hydroelectric and other renewables in power generation both reached record shares of global primary energy consumption (6.8% and 2.5%, respectively).

1.1.2 Alternative energy sources

The International Energy Agency, through its programs (i.e. '*Solar Heating and Cooling'* established in 1977), is actively working to improve the new energy technologies and strategies needed to meet future demand while limiting the dependence on the liquid fossil fuels that currently drive the planet's economies. In the report *'A fundamental look at the energy reserves for the planet'*, Perez *et al.*[4] compared the annual consumptions of the world to the known reserves of the finite fossil and nuclear resources, and to the yearly potential of the renewable alternatives. From Figure 1.3, the main facts to highlight are three folds. Firstly, the renewable sources are not equivalent: few of them are not exploited at the most of their potential (i.e. wind), at which they could provide and meet the whole planet demands. Furthermore, it is understandable that even exploiting a small fraction of earth's solar potential could satisfy the needs. Secondly, the lifetime of coal reserves is limited, despite nowadays those are still available, thus, a possible environmental impact of their intensive exploitation has to be taken into account if other clean coal technologies are not found. Finally, another point worth to be mentioned is that the nuclear energy sources

(uranium) are not limitless, being well below the solar energy potential of one year. Besides, the fuel available from them is not sufficient to take over the role of fossil fuels.

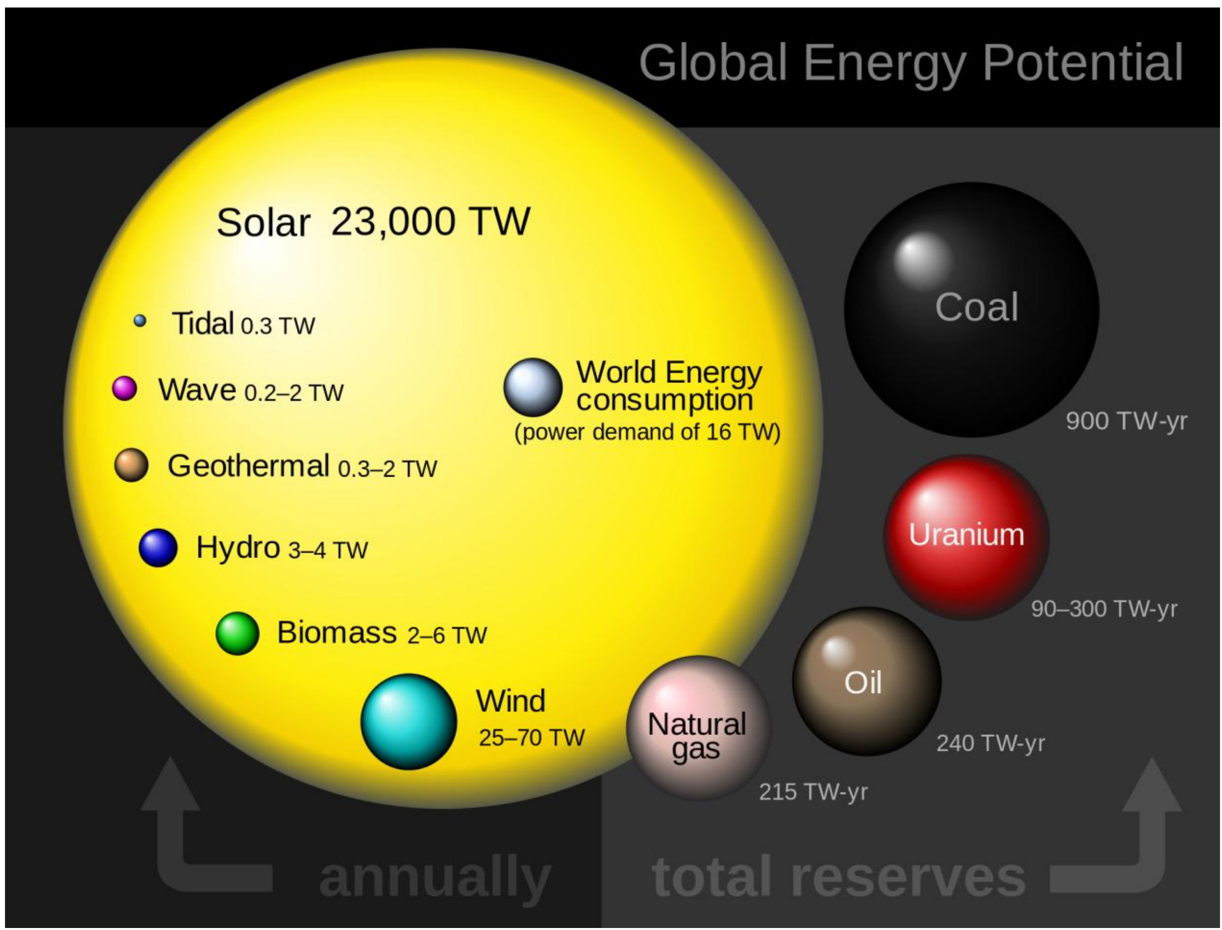

Figure 1.3 Comparison between finite and renewable planetary energy reserves (Terawatt – years). Total recoverable reserves are indicated for the finite sources and yearly potential is shown for the renewable ones [4].

1.2 Industrial waste heat

Industrial waste heat refers to energy that is generated in industrial processes without being put to practical use. The exact amount is difficult to be quantified, but various studies have estimated that as much as 20 to 50 % of industrial energy consumption is ultimately discharged as waste heat. Thus, the recovery of waste heat entails capturing and reusing it in industrial processes for heating or for generating mechanical or electrical work. In Table 1.2 typical thermal efficiencies of selected energy systems and industrial equipments are depicted.

Table 1.2 Typical thermal efficiencies of selected energy systems and industrial equipments (from [5]).

Energy Systems/ Industrial Equipments	Thermal Efficiencies
Power generation	25-44%
Steam boilers (natural gas)	80%
Steam boilers (coal and oil)	84-85%
Waste heat Boilers	60-70%
Thermal Cracking (refineries)	58-61%

Energy Systems/ Industrial Equipments	Thermal Efficiencies
EAF Steelmaking	56%
Paper Drying	48%
Kraft Pulping	60-69%
Distillation Column	25-40%
Cement Calciner	30-70%
Compressors	10-20%
Pumps and Fans	55-65%
Motors	90-95%

Heat is generally recovered from clean, high – temperature waste heat sources in large capacity systems. The main trends in heat recovery are:

- Waste heat recovery systems are implemented, but constrained by factors such as temperature limits and costs of recovery equipments;
- Most uncovered waste heat is at low temperatures;
- There are certain industrial sectors for which heat recovery is less common (due to factors such as heat source's chemical composition and the economies-of-scale required for recovery);

To promote heat recovery and process integration it is needed to: extend the economic operating range of conventional technologies and conducting RD&D in emerging and novel technologies. Thus, at this point, the barriers which might impact the economy and effectiveness of heat recovery equipments and impede their wider installation, are:

- Cost
- Temperature
- Chemical composition
- Application-specific constraints
- Inaccessibility-transportability

Heat can be reused in the same process or transferred to another one. Ways of reusing heat locally include using combustion exhaust gases to preheat combustion air or feed water in industrial boilers (to reduce the energy amount required to heat the water to its final temperature). Ways of transferring the heat to other processes are: heat exchanger used to transfer heat from combustion exhaust gases to hot air needed for a drying oven. Thus, the recovery heat can replace fossil energy that would have otherwise used in the oven.

In nanotechnologies direct electrical conversion devices are used to achieve this goal. New technologies are being developed to generate electricity directly from heat. These include thermoelectric, thermoionic and piezo-electric devices.

1.3 Thermoelectricity

The most common sources of energy available for harvesting are vibrations (or motion), light and heat. Considering the previously cited alternatives, waste-heat energy is an interesting solution. Indeed, there are contexts in which photovoltaic is not an applicable alternative (i.e. for space missions or for inaccessible military equipments). According to E. Cook [6], at least the 50% of the primary energy is released as waste heat (ex: hot exhaust gases, cooling water, and heat lost from hot equipment surfaces and heated products).

Thus, why do not exploit this universally present resource to produce energy?
Waste heat is present everywhere, released from industrial processes, engines, buildings and even human bodies. The main advantages offered by this methodology are: clean power generation, no emission of green house gases (ex: CO_2), no emission of air polluting gases (NOx, SOx), reduction of global warming effect.
Currently, the technology development of devices which are portable, wireless, battery-powered handheld wearable and implantable, pose the need for power supply efficient methodologies. Those devices require a compact, low-cost and lightweight energy source, enabling portability and energy autonomy. An answer to this request could be the integration of a thermoelectric module able to recover waste heat and convert it into electric energy. This option would represent a solution to the everlasting problem of batteries, being their size and cost an obstacle to the device autonomy.
In Table 1.3 different device are shown, with their related power consumption and energy autonomy.

Table 1.3 Selected battery-operated systems with related power consumption and energy autonomy [7].

	Device type	
	Power consumption	Energy autonomy
Smartphones	1 W	5 h
MP3 player	50 nW	15 h
Hearing aid	1 mW	5 days
Wireless sensor node	100 µW	Lifetime
Cardiac pacemaker	50 µW	7 years
Quartz watch	5 µW	5 years

Taking into account the different output power that could be obtained from the different environmental sources, detailed in Table 1.4, the proper harvester design has to be chosen, meeting the request for small-sized and rechargeable batteries (or other energy storage systems).

Table 1.4 Source and harvested power for different energy sources [7].

	Source power	Harvested power
Ambient light		
Indoor	0.1 mW cm^{-2}	10 µW cm^{-2}
Outdoor	100 mW cm^{-2}	10 mW cm^{-2}
Vibration/motion		
Human	0.5 m at 1 Hz, 1 m s^{-2} at 50 Hz	4 µW cm^{-2}
Industrial	1 m at 5 Hz, 10 m s^{-2} at 1 kHz	100 µW cm^{-2}
Thermal energy		
Human	20 mW cm^{-2}	30 µW cm^{-2}
Industrial	100 mW cm^{-2}	1 – 10 mW cm^{-2}
RF		
Cell phone	0.3 µW cm^{-2}	0.1 µW cm^{-2}

1.3.1 Thermal transport

The fundamentals of thermoelectric energy generation are quite simple and easily to be implemented. If a small temperature difference is applied at the extremities of a bar in open circuit, connecting one side to a heat source and the other to a heat sink, the experience shows that the heat ($\vec{q}$) propagates from the hot to the cold extremity. The equation which express this phenomenon is Fourier's law:

$$\vec{q} = -\kappa\vec{\nabla}T \tag{1}$$

where $\vec{\nabla}T$ is the temperature gradient and κ the material's thermal conductivity.
Different mechanisms contribute to the heat transport in solids. In metals, heat is carried by electrons, as stated by the Wiedemann-Franz law, which relates the electron thermal conductivity, κ_e, to the material's electrical resistivity ρ:

$$\kappa_e = \frac{L}{\rho}T \tag{2}$$

where T is the absolute temperature, L the Lorenz's number, equals to $2.5 \cdot 10^{-8}$ W Ω^{-1} K^{-2} for a free electrons gas. For an insulating material, the heat transport is conveyed through the vibrations of the lattice. The lattice (phononic) thermal conductivity κ_{ph} can be formulated in a first approximation, considering the Debye's relation:

$$k_{ph} = \frac{1}{3}c\Lambda v \tag{3}$$

where c is the volumetric specific heat, Λ the phonons mean free path and v the sound speed. In semiconductors the heat is carried by electrons and phonons. So, the thermal conductivity is composed by the two terms:

$$k = k_{ph} + k_e \tag{4}$$

The two parameters are strictly related to the material chosen. For this reason, the next graphs depict in details the characteristic parameters of common materials.
Firstly, the electrical conductivity at room temperature for different materials is introduced (Figure 1.4).

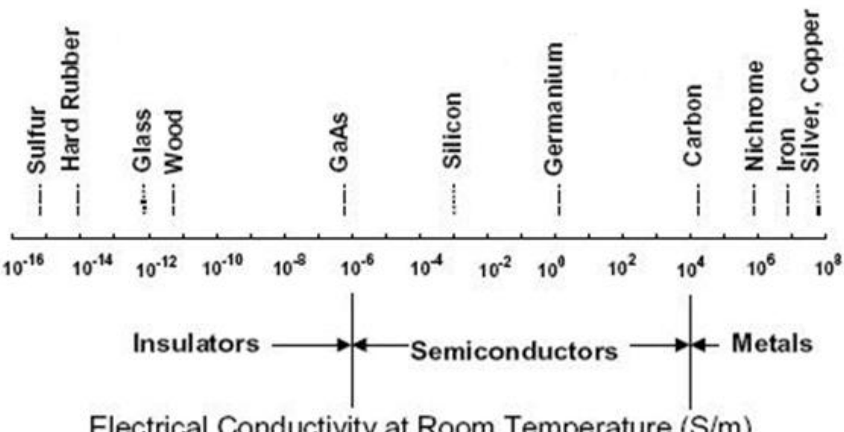

Figure 1.4 Electrical conductivity at room temperature of different materials [8] [9] [10].

Differently from the electrical resistivity that, depending on the material, spans 24 order of magnitude at room temperature, the thermal conductivity cover a range of 4 orders of magnitude (between 0.1 and 2000 W m^{-1} K^{-1}) (see Table 1.5).

Table 1.5 Thermal conductivity at 300 K of common materials [11], [12].

Material	Thermal conductivity (W K^{-1} m^{-1})
Air	0.024
Aluminum	250
Copper	401
Glass	1.05
Gold	310
PVC	0.19
Silicon	149
Silver	429
Steel	46
Titanium	22
Water	0.58
Wood	0.13
Zinc	216

Thus, the choice of a material for TE applications results strictly related to the need of a material owing a high Seebeck coefficient, guaranteeing a good electrical transport (being electrical conductivity widely variable depending on the material) and low thermal transport (adjustable in a smaller range of values and materials).

1.3.2 Seebeck effect

The effect of generating an electric field by applying a temperature gradient between the opposite extremities of a bar was discovered in 1824 by Thomas Seebeck. The relation is:

$$\vec{E} = S\vec{\nabla}T \quad (5)$$

where S is the Seebeck coefficient, or thermopower, positive or negative depending on the majority carriers.

The thermopower depends on the carriers concentration in the material. For a metal, *S* is small at room temperature. If the concentration of the carriers decreases the Seebeck coefficient increases and it could reach values of few mV K^{-1} for highly pure semiconductors.

The Seebeck coefficient is not the only parameter that determines the efficiency of a material in a thermoelectric generator or a thermoelectric cooler. Under a given temperature gradient, the ability of a material to produce electrical power efficiently is quantified by its power factor:

$$Power\ Factor = \sigma \cdot S^2 \quad (6)$$

To boost this factor, a good choice of the material for the generator has to be made. The best solution is to couple two different materials, differently doped, and to connect them electrically in series and in parallel from the thermal point of view. If a thermo-generator configuration is chosen, the voltage (electromotive force) generated by mean of the temperature gradient is summed up. In Figure 1.5 it is shown the sketch of a thermoelectric

generator module, composed by a n- and a p- doped materials, connected by two metallic layers, at different temperatures (hot and cold side).

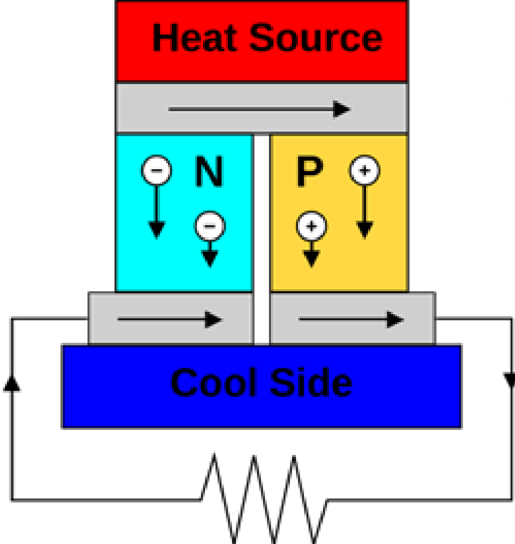

Figure 1.5 Left: Thomas Johann Seebeck (9 April 1770 – 10 December 1831); Right: A thermoelectric module composed of p- and n- doped materials (semiconductors) of different Seebeck coefficient, configured as a thermoelectric generator. If the load resistor is replaced with a voltmeter the circuit then functions as a temperature-sensing thermopile [13].

To further increase the power factor, the industrially fabricated thermoelectric devices are composed of more thermocouples, in the so called thermopile configuration.
The configuration in Figure 1.5 represents a power generator device by Seebeck effect, having a load resistance and the two sides kept at constant hot/cold temperatures. In contrast, if a voltage difference is applied at the two n- and p- sides, and no temperature gradient kept, the configuration changes, and a heating/cooling device exploiting Peltier effect is implemented.

1.3.3 Efficiency of thermoelectric devices

To evaluate the effectiveness of a thermoelectric device, a parameter is used in order to compare performances, it is named the conversion efficiency η. It is characterized by the Carnot efficiency and the figure of merit zT of the material. Assuming negligible contact resistances and optimized load conditions, the maximum conversion efficiency of thermoelectric generation, η, is:

$$\eta = \left(\frac{T_{HOT} - T_{COLD}}{T_{HOT}} \right) \left[\frac{\sqrt{1 + ZT_m} - 1}{\sqrt{1 + ZT_m} + \left(\frac{T_{COLD}}{T_{HOT}} \right)} \right] \tag{7}$$

where the Carnot efficiency is the ratio between the temperature difference between the hot and cold end and T_{HOT}, and T_m is the mean temperature. ZT is the material figure of merit, an important parameter in thermoelectricity:

$$ZT = \frac{\sigma S^2 T}{k} \tag{8}$$

where σ is the electrical conductivity, S the Seebeck coefficient, κ the thermal conductivity.
In order to boost ZT, the donor concentration needs to be maximized. Near the Fermi level, the doping increases the density of states (DOS), improving the thermopower. When the level of the donors or acceptors is close to the Fermi level the localized DOS (LDOS) is increased. This entails an augmentation in the effective mass of the carriers, although their concentration stays unchanged. This bigger effective mass leads to an improvement in thermopower [13].
The best thermoelectric material is a *"phonon glass – electron crystal"*, as formulated by Slack [15], presenting the lowest kappa and the highest σ. The materials at the state of the art have a value of zT=1~2 at the maximum of their temperature range, being strictly dependent on σ, S and κ. zT=1 is the value considered a really good achievement for an industrially competitive material.

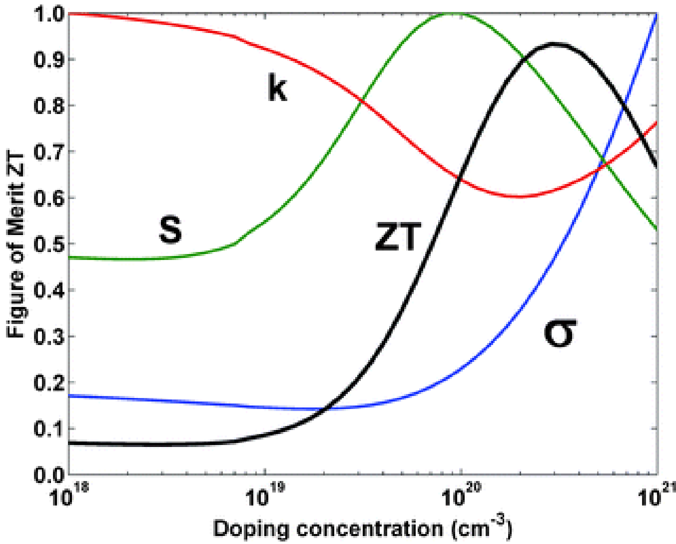

Figure 1.6 Main parameters playing a decisive role in thermoelectricity for n-type $Si_{80}Ge_{20}$. The most appropriate doping concentration can be individuated, considering the trade off between κ and σ, to boost the ZT figure of merit [16].

There are the various possible approaches to increase zT: the first one is to create a new material with a complex crystal structure (which in turns lower the κ_{ph}) [17], the second one is to nanostructure the material, modifying thermoelectric properties in different ways respect bulk materials [18], [19], [20], [21].
The discussion about complex materials synthesis and engineering is the scope of the next section, the successive one will detail the state-of-the-art of nanostructuration approaches and achievements.
To evaluate and analyze the different materials and their choice for a thermoelectric generator, few parameters and consideration need to be taken into account. The next section details the material characteristics to achieve the best TE performances.

1.3.4 Materials

Nowadays, a great interest is focused on developing high performance thermoelectric materials for the generation of power exploiting waste heat through Seebeck effect. Efforts have been done in the attempt of finding materials with high zT and able to operate at the largest temperature range possible.

Figure 1.6 indicated the best doping for a material to achieve a high zT, keeping low κ and high S and σ [16]. Those parameters could vary over several orders of magnitude, but it is clear that, because of their interdependence, zT is maximum for carriers concentrations around 10^{18}-10^{19} cm^{-3}. Further increasing the carrier concentration leads to a lower Seebeck parameter and increase the electronic part of the thermal conductivity (metallic limit). Thus, highly doped semiconductors (SC) are the target materials for such a request. It is also suggested, for industrial application, to work with *p*- and *n*-doped semiconductors with similar physical properties, to permit a similar design of the two sides of the thermocouple and minimize problems related to mechanical constraints.
Ioffe observed in 1957 [22] that heavily doped semiconductors represent the best TE materials. He posed several guidelines to select the suitable materials for such applications. Firstly, he affirms that degenerate semiconductors or semimetals with carrier concentrations of 10^{18}–10^{20} cm^{-3} are good TE materials because those ranges of doping maximize the power factor (Figure 1.6), by increasing the electrical conductivity. Secondly, SC with band gap of $\Delta \sim 10 \cdot k_B T_0 \sim 0.25\ eV$ *@ RT* (with k_B the Boltzmann constant and T_0 the operating temperature), make good TEs. Such a band gap width allows a convenient value for the carrier mobility, μ, and minimizes the negative contribution from the minority carrier to S. Normally, small band gaps lead to high carrier mobility, however, if the gap is too small, then the thermal excitation of minority carriers could negatively affect the figure of merit, by the fact that electrons and holes carry heat in the opposite direction. Another guideline is to adopt a very symmetric crystal structure and have low electronegativity mismatch between the elements constituting it. This parameter is a measure of the covalency of the bonding in a material. Large difference of it indicates ionic bonding, large charge transfer, and strong scatter of electrons by optical phonons. The strong scattering leads to a lower carriers mobility (the reason why oxides are bad TE materials). The main reason is that z is directly proportional to the effective mass of carrier, m^*, $z \propto \mu (m^*)^{3/2}$, thus, increasing it without affecting the mobility μ, will enhance the zT factor [23]. It is possible to consider the SC has several equivalent bands. Indeed, good thermoelectric materials are multivalley semiconductors and symmetric crystal structure are required to produce several equivalent bands [24]. The last point is related to the necessity of keeping κ_l as low as possible. It is achievable in materials made up of heavy elements and/or with many atoms per cell, which present low sound velocity. The majority of state-of-the-art thermoelectric materials respect these guidelines, being degenerate semiconductors or semimetals bulk materials with a crystal structure highly symmetric and one or more heavy atoms (i.e. Bi, Pb, Te, Sb) [25], [26].
Considering the materials available with such properties, zT, as a function of the temperature, is evaluated to relate them to the possible temperature range of application. The curves of the commonly investigated materials for TE application are shown in Figure 1.7.
It is known that materials with diamond or zinc blend structures, presenting a high degree of covalent bonding, frequently have high mobilities (i.e., Si, Ge, or InSb) and high thermal conductivity values. On the other hand, low lattice thermal conductivities are recorded in correspondence of low Debye temperatures and high anharmonic lattice vibrations. These conditions are met by highly covalent intermetallic compounds and alloys of the heavy elements such as (Pb, Hg, Bi, Tl, or Sb) and (S, Se, or Te). After selecting the material to use,

the elements composition can be optimized in such a way to improve *zT* through relevant doping (increasing the DOS and, consequently, the Seebeck parameter) [27].

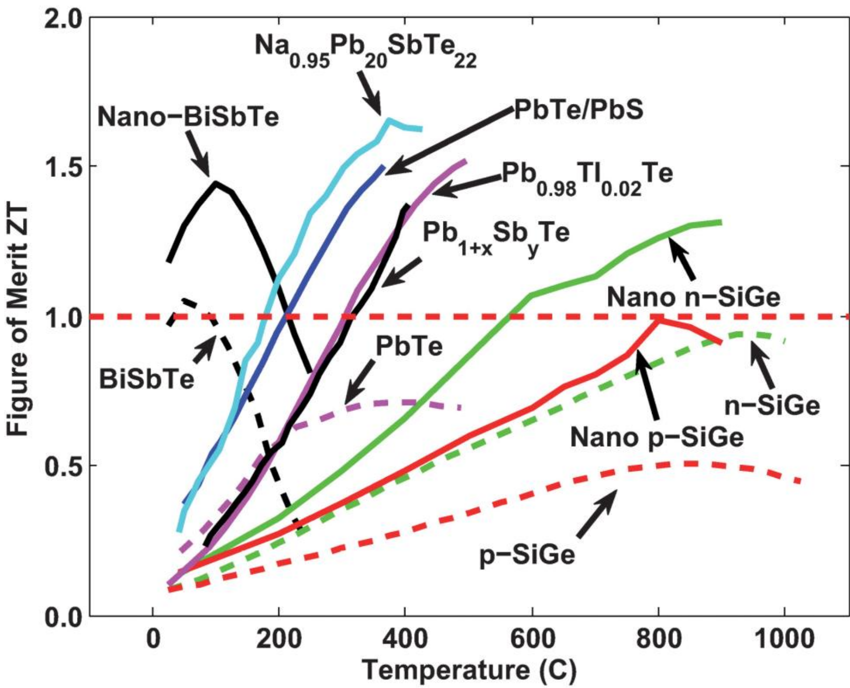

Figure 1.7 Figure of merit *zT* of commonly investigated TE materials at the state-of-the-art versus temperature. The red dashed line shows the maximum *zT* for bulk materials, the solid line indicates recent results of *zT* for nanostructured or nanocomposite materials [16].

The mostly investigated TE materials at the moment are Bi_2Te_3 alloys, presenting a rhombohedral-hexagonal symmetry with layers held by strong covalent bonds and adjacent Te layers present Van der Waals bonding. This weak binding explains the ease in cleaving along the plane perpendicularly to that bond, and the anisotropic thermal and electrical properties.

Taking into account the previous considerations [22], alloying can further reduce the lattice thermal conductivity by increasing the scattering of short-wavelength acoustic phonons. For TE cooling devices the mostly used compositions are, for n-type, $Bi_2Te_{2.7}Se_{0.3}$ and, for p-type, $Bi_{0.5}Sb_{1.5}Te_3$, achieving a zT~1 at room temperatures [27].

Poudel *et al.* have shown [19] that a peak *zT* of 1.4 at 100°C can be achieved in a p-type nanocrystalline BiSbTe bulk alloy (Figure 1.7). These materials are made by hot pressing nanopowders previously ball-milled from crystalline ingots under inert conditions. Furthermore, electrical transport measurements, coupled with microstructure studies and modelling, shows that the *zT* improvement is due to low thermal conductivity caused by the increased phonon scattering by grain boundaries and defects. It is also underlined that *zT* is about 1.2 at room temperature and 0.8 at 250°C, which makes BiSbTe bulk alloys suitable for cooling and power generation.

Poudeu *et al.* [28]report that the Ag-free system $Na_{1-x}Pb_mSb_yTe_{m+2}$, with appropriate combinations of m, y, and x, achieves record-high *zT* values for a *p*-type bulk thermoelectric material, presenting a low thermal conductivity. Those materials could be applied in devices for power generation from a wide variety of hot sources (i.e.: vehicle exhausts, coal-burning installations, electric power utilities). At room temperature $\kappa = 1.8$ W m^{-1} K^{-1}, which is about

22% lower than the typical value of $\kappa = 2.3$ W m^{-1} K^{-1}reported for *p*-type PbTe [22]. The value of $\kappa_l = 0.74$ W m^{-1} K^{-1}, calculated by subtracting the κ_{el} from the total κ, at 300 K, is one third of that of PbTe ($\kappa_l = 2.2$ W m^{-1} K^{-1})[29]. Indeed, in [28] it is shown that below 500 K, the thermal conductivity is mostly due to the electronic contribution, whereas above 500 K, the lattice contribution dominates. Nanostructuration of the bulk material leads to the large drop observed in the lattice thermal conductivity.

In [30] it is depicted how nanostructured thermoelectric materials with very low thermal conductivity and greatly enhanced figure of merit are created by solid-state transformation phenomena of spinodal decomposition and nucleation and growth. The systems $(PbTe)_{1-x}(PbS)_x$ and $(Pb_{0.95}Sn_{0.05}Te)_{1-x}(PbS)_x$ are not solid solutions but phase separate into PbTe-rich and PbS-rich regions to produce coherent nanoscale heterogeneities that reduce the thermal conductivity. Taking $x \sim 0.08$ the material presents a very low room-temperature lattice thermal conductivity κ_l ~0.4 W m^{-1} K^{-1}. This value is only 28% of the PbTe lattice thermal conductivity at room temperature. Thus, the reduction of κ is explained by nanostructure-induced acoustic impedance mismatch between the PbTe-rich and PbS-rich regions. For certain values of x, the thermoelectric properties of such material were found to be better with respect to the ones of PbTe by almost a factor of 2. Nucleation and growth has been individuated as the best methodology in suppressing the thermal conductivity, reporting a $zT \sim 1.50$ at 642 K for $x \sim 0.08$ [30].

The use of the thallium impurity levels in lead telluride (PbTe) is shown to lower κ and double zT in p-type PbTe to above 1.5 at 773 K [31], with respect to the state of the art of PbTe of 0.7 .

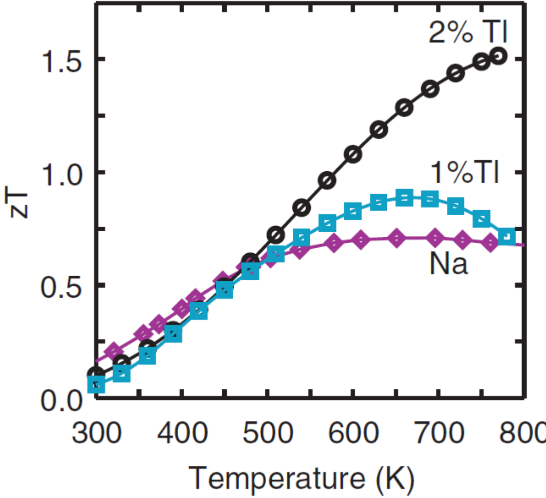

Figure 1.8 The zT values for $Tl_{0.02}Pb_{0.98}Te$ (black squares) and $Tl_{0.01}Pb_{0.99}Te$ (blue circles) compared to that of a reference sample of Na-PbTe (purple diamonds) [31].

The maximum in zT is shown to occur at the temperature where thermal excitations start creating minority carriers. This maximum is still not reached at 773 K for this material, so, higher values of zT may be expected. Considering the temperature range where $Tl_{0.02}Pb_{0.98}Te$ presents the higher zT, between 500 and 773 K, make it suitable for power power generation from waste heat sources such as automobile exhaust [31] (Figure 1.8).

Sootsman *et al.*[32] showed that when lead and antimony are present simultaneously as nanodots throughout the matrix of PbTe, for certain carrier concentrations, the power factor changes its typical temperature dependence, and instead of falling with temperature it actually rises, leading to a large enhancement at high temperatures (above 600 K). For example, in PbTe–Pb(0.5%)–Sb(2%), the κ_{latt} at 650–700 K is 0.6 W m^{-1} K^{-1}, and a *zT* of 1.4 was obtained at 650–700 K. Considering the high carrier concentrations in these samples (degenerate doping), peaking of the Seebeck coefficient is expected for higher temperatures (ca. 850–900 K). Thus, *zT* values of approximately 1.8 could be envisaged at these temperatures.
Regarding n-type silicon germanium a peak *zT* of 1.3 is registered at 900°C for a nanostructured bulk alloy [33]. It is attributed to a reduction of the thermal conductivity caused by the increased phonon scattering by nanograin boundaries. It is reported that despite the increasing of nanograins, the value of the Seebeck parameter is not affected. On the other hand, concerning p-doped SiGe nanostructured alloys the maximum value reached is of 0.95, 50% higher than the one of SiGe alloys and 90% in comparison to the common *zT* cited for spatial applications [34].
Summarizing the findings (reported in Figure 1.7): for low temperature applications (300 K and lower temperatures) it seems that the alloys of BiSb are the best solution. For temperature up to 450 K materials composed by antimony, lead and telluride looks like the target to achieve the best performances. For higher temperatures, reaching 1300 K, the mostly used materials are alloys of SiGe, *p*- or *n*-doped. In Figure 1.9 are reported the efficiency related to the discussed alloys as function of the temperature [35].

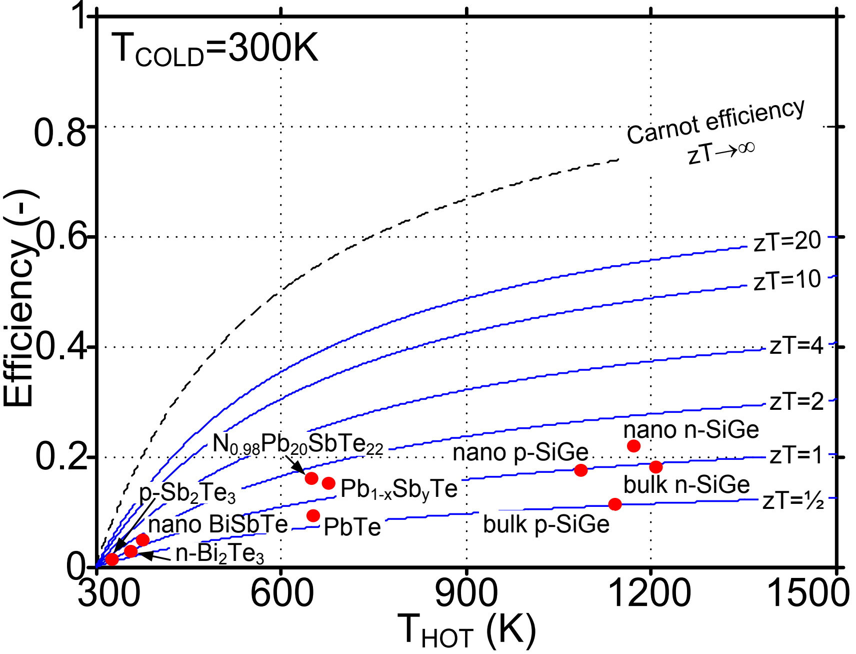

Figure 1.9 Conversion efficiency for different *zT* values. The data points refers to the highest efficiency for given material [35].

As mentioned, doping concentration is a factor to play with to act on material thermal properties. Firstly, it is worth to point out that for many thermoelectric applications a doped semiconductor is necessarily required (i.e. Seebeck generator). Thus, the impurities naturally act on the phonon transport by promoting and increasing the scattering and, in turn, reducing the thermal conductivity. Different studies have been published showing the impact on doping

on thermal conductivity for thick (3 μm) and thin films (30 nm) of silicon confirming the hypothesis that a highly doped semiconductor presents a thermal conductivity reduced respect the corresponding intrinsic one [36], [37]. Figure 1.10 shows the dependence of the Z on the doping concentration of acceptors and donors for silicon (left) and germanium (right), highlighting the importance of doping tuning to boost the TE device efficiency.

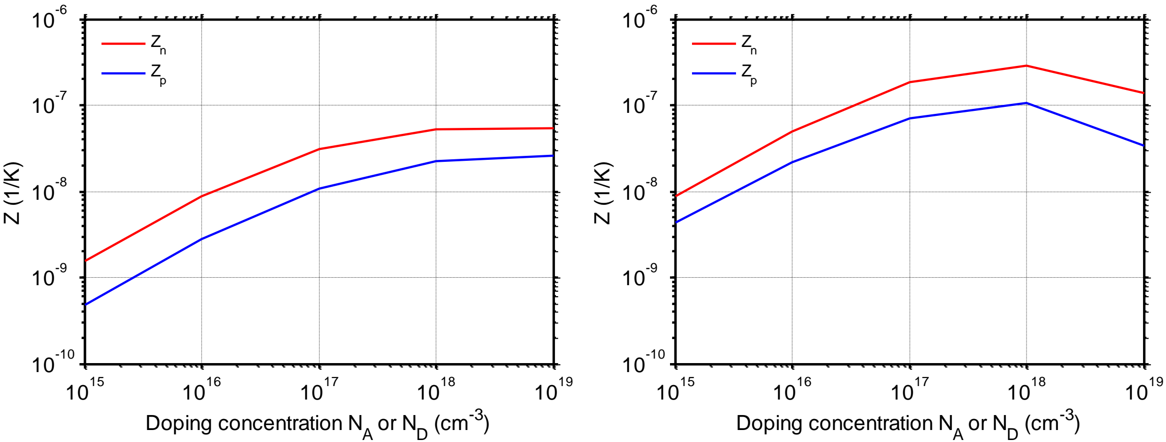

Figure 1.10 Z as function of doping concentration of acceptors and donors for silicon (left) and germanium (right).

Figure 1.11 lists the commonly used TE materials with respect to their characteristics (toxicity, rarity, eco-friendliness, abundance)(Figure 1.11 (a)) and abundance (Figure 1.11 (b)) versus the operation temperature. Indeed, many aspects have to be taken into account to choose the best material which allows to fabricate a device exploiting the existent technologies, machines and compatible with others used material, leading to a cost effective product.

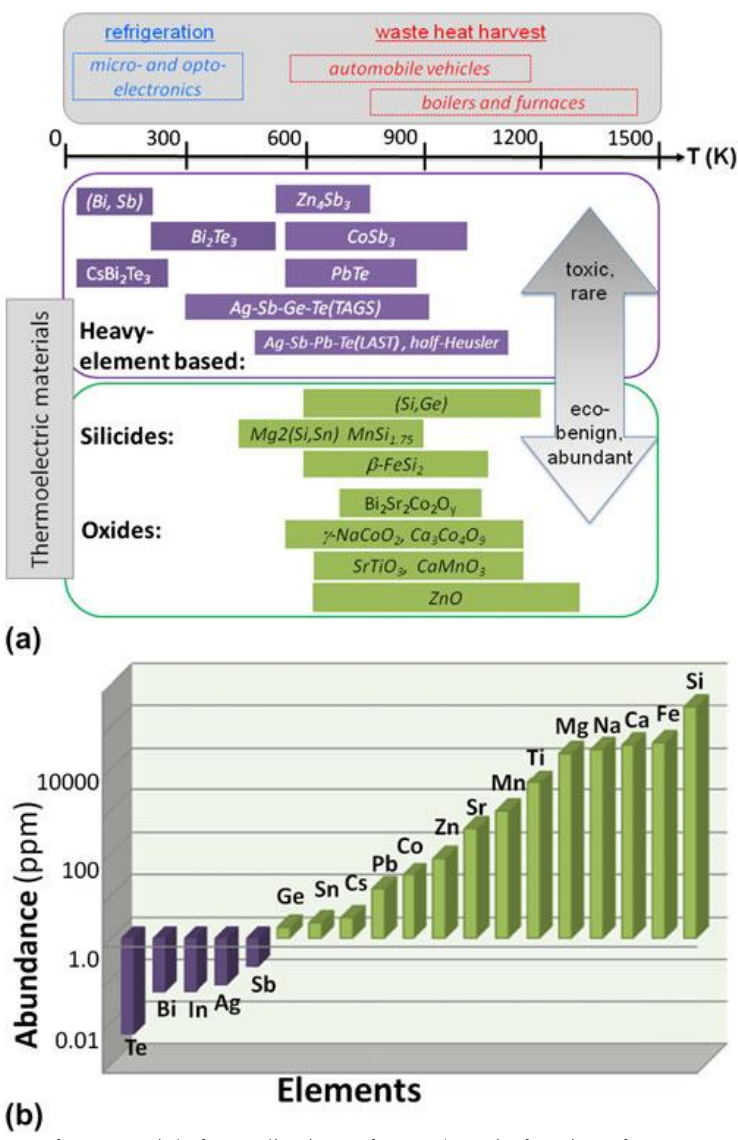

Figure 1.11 (a) Comparison of TE materials for applications of waste heat, in function of temperature range of operation and the toxicity/environmental friendliness of constituent elements. (b) The abundance of elements used in TE materials, the elements represented by dark coloured columns are < 1 ppm. From [38].

Considering the advantages of silicon: its abundance, its cheapness, its compatibility with CMOS process, which allows direct integration on chip, environment's preservation, it is individuated as a good material for thermoelectric applications. Furthermore, it presents a high Seebeck coefficient at room temperature and good electrical conductivity (carriers mobility) for the opportune doping levels [39].

In order to compare the harvesting capabilities of a silico-fabricated TE device, power densities were studied in a Seebeck-membrane based generator structure shown in Figure 1.12 and its properties are analyzed by Haras *et al.* [40]. The generator designed by our team redirects the heat from the vertical to the lateral direction, conferring the structure mechanical flexibility.

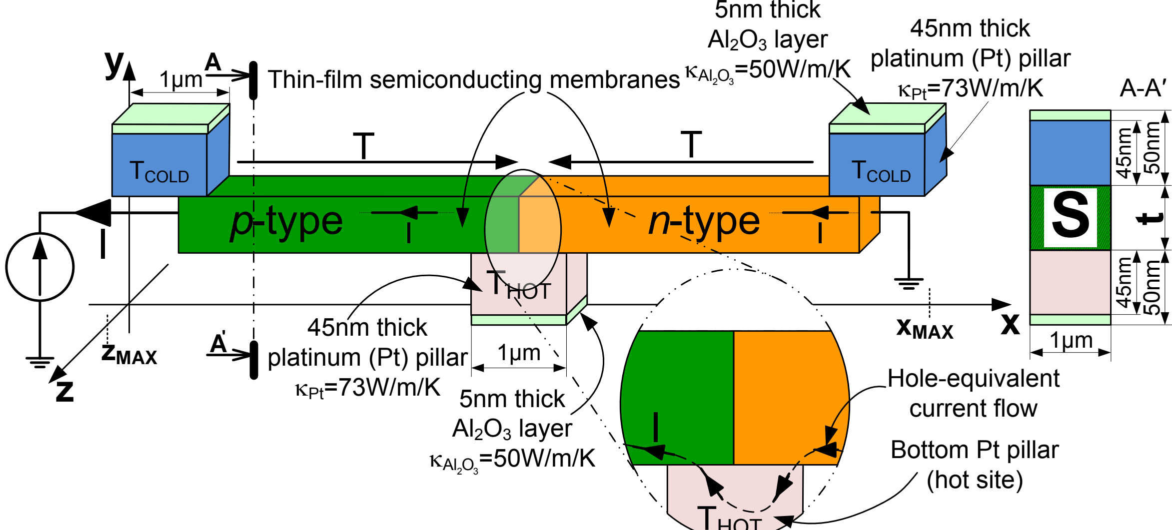

Figure 1.12 Structure of the membrane-lateral Seebeck generator designed and simulated in [40].

Figure 1.13 depicts the different electric power densities simulated for such a CMOS generator topology designed as function of the output voltage. It can be noticed that the harvested power density for Si, SiGe and Ge is slightly lower than the one for Bi_2Te_3, whose performances depend critically on the specific contact resistivity achievable. Although Si, Ge, and SiGe harvest a lower power density than Bi_2Te_3 for a same temperature gradient, it is worth emphasizing that they are compatible with conventional CMOS technology, making integration of TEGs possible. It is worth noticing that SiGe harvests less power than Si or Ge for the same ΔT. This can be readily explained by the lower electrical conductivity of SiGe compared to Si and Ge at the same doping level. However, because of a lower thermal conductivity κ, it is expected that SiGe will convert heat with higher efficiency than Si or Ge.

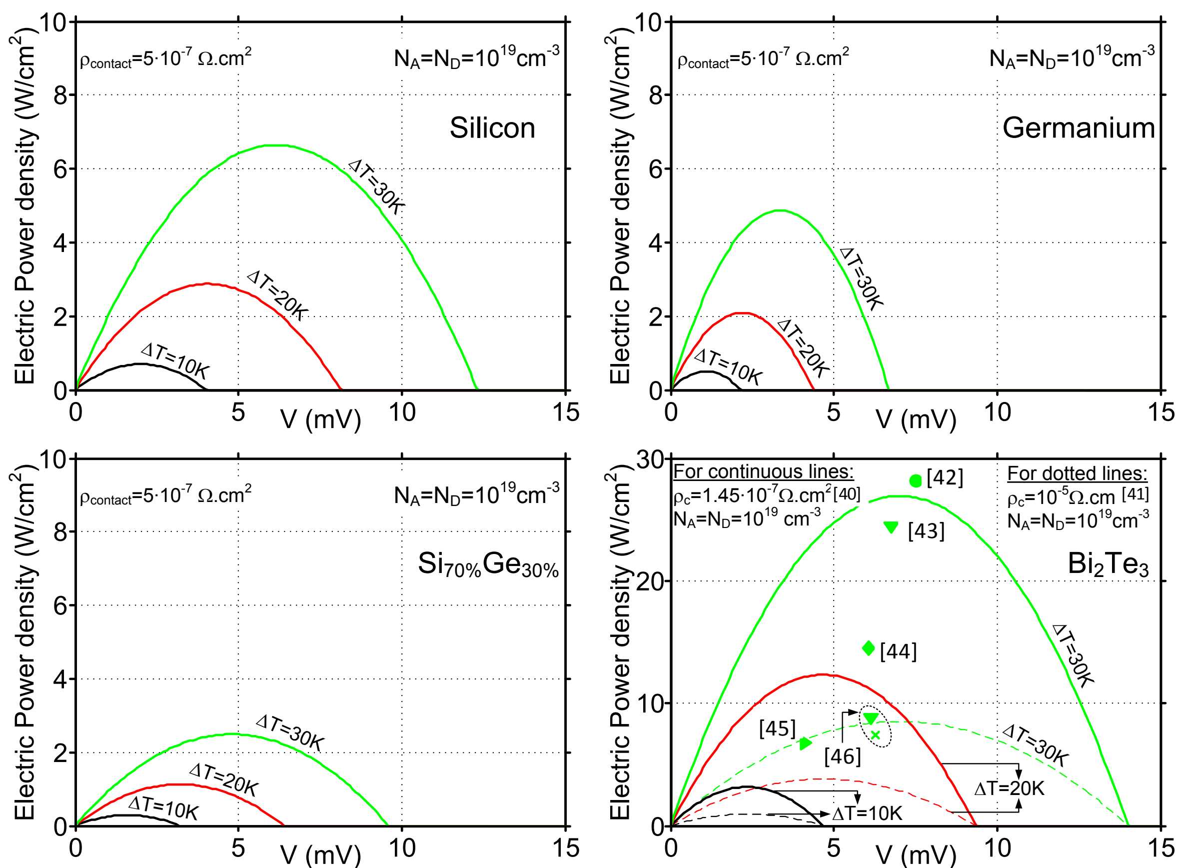

Figure 1.13 From [40]: Harvested electric power density as function of generator output voltage for different membranes Seebeck generator in silicon (a), germanium (b), Si70%Ge30% (c) and from bismuth telluride (d). In (d): references from [41], [42], [43], [44], [45], [46], [47].

The drawback of this material is related to its high lattice thermal conductivity, around 150 W m^{-1} K^{-1} at room temperature. For this purpose, methodologies to reduce this parameter are intensely investigated. In the next paragraph results related to materials nanostructuration are detailed, showing the possible approach to efficiently employ silicon in fabrication of thermoelectric energy generator and converter, achieving high efficiency.

1.3.5 Nanostructuration

The interest in nanostructured materials is mainly driven by two reasons: first, the high density of interfaces leads to a reduction of the heat flow carried by the lattice vibration (phonons), the length scale being comparable to the phonons mean free path, as detailed also in paragraph 1.4. Second, the reduced dimensionality of the electronic system which could be obtained by band engineering or nanostructuring at the scale of electron mean free path, could be exploited to improve material's electronic properties. As said, the material's efficiency is evaluated with its figure of merit $zT = T\frac{S\sigma^2}{\kappa}$, which can be enhanced by two means. The first is to act on the Seebeck coefficient and electrical conductivity, trying to maximize their value. The second deals with crystal structure, heat transport aiming at minimizing the lattice thermal conductivity.

Regarding the first, the Seebeck coefficient *S* (or thermopower) can be increased with sharp features of the electron density of states (DOS), and can consequently boost the power factor $S \cdot \sigma^2$ [31], [48], [18], [49]. As demonstrated by Mahan and Sofo [24] a narrow shape of the energy distribution of the electrons participating in the transport process is needed to achieve maximum thermoelectric efficiency. They tried to reply to the question: *What electronic structure provides the largest figure of merit for thermoelectric materials?*. Thus, if it is given the freedom to choose the distribution of energy levels and scattering of the carriers, what would be the choice for a given lattice thermal conductivity? The answer has been found writing the electrical conductivity, thermopower, and thermal conductivity as integrals of a single function, the transport distribution. Then, a mathematical function has been derived for it, which gives the maximum figure of merit. A Dirac transport distribution is found to maximize the thermoelectric properties.
This condition can occur when conduction or valence band of the host semiconductor resonates with one energy level of a localized atom in a semiconductor matrix. Mott's expression defines the effect of this local increase in DOS. The Seebeck parameter depends on the energy derivative of the energy-dependent electrical conductivity $\sigma(E) = n(E) \cdot q \cdot \mu(E)$, *S(E)* taken at the Fermi energy E_F, with $n(E) = g(E) \cdot f(E)$, the carrier density at the energy level *E* considered, where *f(E)* the Fermi function, *q* the carrier charge, and $\mu(E)$ the mobility:

$$S = \frac{\pi^2}{3}\frac{k_B}{q}k_B T\left\{\frac{d[\ln(\sigma(E))]}{dE}\right\}\Bigg|_{E=E_F} = \frac{\pi^2}{3}\frac{k_B}{q}k_B T\left\{\frac{1}{n}\frac{dn(E)}{dE} + \frac{1}{\mu}\frac{d\mu(E)}{dE}\right\}\Bigg|_{E=E_F} \quad (9)$$

The equation (9) shows that there are two mechanisms that can lead to an increase of *S*: the first is an increased energy-dependence of $\mu(E)$, for instance by a scattering mechanism that strongly depends on the energy of the charge carriers, and the second is an increased energy-dependence of *n(E)*, due to a local increase in *g(E)*. The second explains the Mahan-Sofo theory, provided that E_F of the semiconductor aligns properly in the range of the excess DOS in the band [24].
Therefore, it is possible to boost the TE efficiency by enhancing the Seebeck coefficient through a distortion of the electronic density of states. A successful implementation of this has been reported by Heremans *et al.* [31] through the use of the thallium impurity levels in lead telluride (PbTe). Such band structure engineering results in a doubling of *zT* in p-type PbTe to above 1.5 at 773 K.
An alternative approach, the Landauer formalism [50], has been widely used in mesoscopic thermoelectric studies and demonstrated by Kim *et al.*[49] that it could also apply to macroscopic thermoelectrics. They showed that the transmission *T(E)* and the number and distribution of conducting channel *M(E)* are the main factors establishing thermoelectric transport coefficients. Furthermore, the transport distribution being proportional to *T(E)·M(E)* and assuming *T(E)=1*(ballistic transport), they have shown how much more efficiently the modes are utilized in 1D systems than in 2D and 3D. With the Landauer formalism, the benefits from engineering *M(E)* into a Dirac function are analyzed. It is shown that for the same effective number of conducting channels, the improvement over a parabolic band in 3D is about 50%. Decreasing the dimensionality, the shape of *M(E)* resembles the one of a delta function. It doesn't necessary demonstrate that 1D is better than 2D or 3D, because the

magnitude of *M(E)* is also important. Thus, reduced dimensionality *per se*, does not determine a great improvement of the electronic part of the figure of merit. Engineering band structures through size quantization, strain, crystal orientation, etc., should be carefully explored in addition to the efforts to reduce κ_l.
Considering the low-dimensional materials approach, two trends are dominant. The first one points on the introduction of nanoscale constituents to induce quantum-confinement effects to enhance the power factor. The second one relies on the increasing of the number of internal interfaces to obtain a reduction of the thermal conductivity more than the electrical one, due to the difference in scattering lengths in relation to the phonons mean free path.
Regarding these two approaches it has to be taken into account that the recent investigations in this field don't focus on the exclusive attempt of improving one of them. Nowadays, the most successful bulk thermoelectric materials are host materials containing nanoscale inclusions, prepared by using chemical approaches [51]. In addition, materials systems with low dimensionality are now being synthesized as nanocomposites containing nanoclusters showing short-range low dimensionality embedded in a host material [52], in such a way to produce a bulk material with nanostructures and interfaces able to scatter phonons more effectively than electrons, and more in details to scatter more efficiently those phonons in the range of frequency and mean free path which contribute more to the thermal conductivity.
The new parameter introduced, the dimensionality *d* of the material (i.e. the thickness for a quantum-well 2D system, the diameter of a quantum wire for a 1D system or the dimension of a quantum dot for a 0D system), acts decreasing κ_l through three mechanisms [53]. The first one relies on designing the system dimensionality in such a way that the lattice thermal conductivity is reduced, without affecting the electrical conductivity. This is possible considering the different length scales of electron mean free path (Λ_{el} ~ few nanometers)[39] and phonon's one (Λ_{ph} ~ 200-300 nm [52] (distribution's peak of Si at room temperature)).
The second and third mechanisms are related to the enhancement of the Seebeck coefficient in low dimensional system due to size-quantization effects and electron energy filtering. Indeed, considering Mott's equation (2), it is resulting that any mechanism increasing the energy-dependence of the conductivity increases the Seebeck coefficient. The two ways to enhance this dependence are: enhancing the density of carriers energy-dependence *dn(E)/dE* or enhancing the mobility energy-dependence *dμ(E)/dE*. In other words, acting on the density of carriers, means acting on the density of states of energy, so the size-quantization effect plays the main role in this process [53]. The density of states dependency versus the energy is depicted in Figure 1.14.

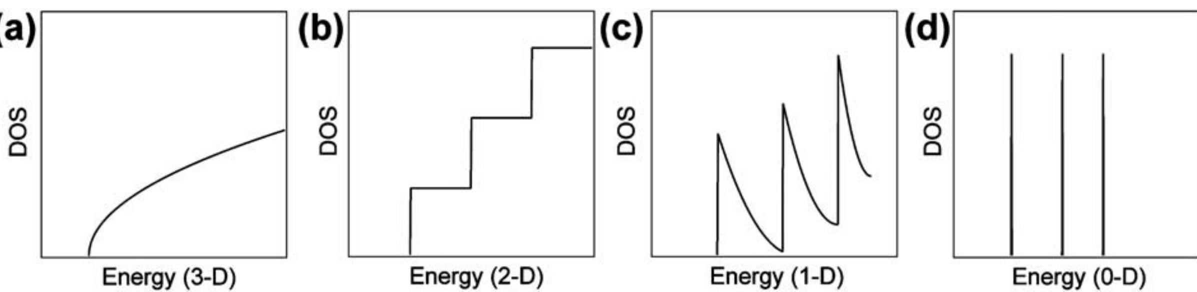

Figure 1.14 Schematic illustration of the density of states (DOS) as a function of energy for: (a) a bulk material (3-D), (b) a quantum well (2-D), (c) a nanowire (1-D), and (d) a quantum dot (0-D). The DOS at the band edge increases with decreasing dimension [54].

It is understandable that a sharp maximum of the DOS will correspond to an increased *S* [48], due to an augmented influence of carriers having flat dispersion behaviour. So, if an appropriate size tuning is performed to place sharp bands near the Fermi level, it would cause a marked increase in the thermopower. Thus, this approach results promising to boost the *zT,* which could be further enhanced by introducing dopants having appropriate resonant levels appearing in correspondence of the DOS spikes.
In addition, for energy filtering it is meant that the increased energy-dependency of the mobility, which leads to an augmented scattering time's energy dependence $d\tau(E)/dE$. Such a mechanism is summarized by the power-law dependence of the relaxation-time:

$$\tau = \tau_0 E^{\lambda - \frac{1}{2}} \tag{10}$$

taking in consideration that the relaxation time is the inverse of the scattering probability, which depends on the density of the initial state and the probability matrix element. It gives rise to E^{λ}, where λ is the scattering exponent (=0 for scattering of electrons on acoustic phonons, =1/2 for scattering of electrons on neutral impurities, =2 for scattering of electrons on ionized impurities) [55].
The next three paragraphs summarize the achievements and state-of-the-art of 2D, 1D and 0D nanostructured systems and underlines the improvements possible by lowering the dimensionality.

1.3.5.1 Superlattices

The use of artificially structured materials such as superlattices and nanowires, has demonstrated to be an effective way to increase the performance of thermoelectric devices. The first proof of the improved thermoelectric properties of a material with reduced dimensionality was presented by Hicks *et al.*[56], who demonstrated that it is possible to increase the *ZT* of certain materials by arranging them in the form of 2D quantum-well structures. They used $PbTe/Pb_{1-x}Eu_xTe$ superlattices grown by molecular-beam epitaxy, and found that an increase in *Z* over bulk values is achieved through quantum confinement effects using quantum-well structures. They obtained a good agreement between experimental results and theoretical predictions on the dependence of S^2n on the quantum well thickness (being *n* the carrier density).
Another experimental proof-of-principle of an enhanced thermoelectric figure of merit for such nanostructured materials is demonstrated in [57] using (001) oriented Si/Ge superlattices, modelled following the approach denoted as *"carrier pocket engineering"*. The resulting value of the experimental figure of merit at 300 K for a (001) oriented Si(20 Å)/Ge(20 Å) superlattice is 0.1, considering an in-plane thermal conductivity κ of 5 W K^{-1} m^{-1}, and achieving a seven time enhancement relative to the estimated value for bulk Si (*ZT*=0.014).
With respect to Bi_2Te_3/Sb_2Te_3 superlattices Venkatasubramanian *et al.* ([58], [59], [60], [61]) demonstrated that the scattering of phonons by the interfaces decreases the (lattice) thermal conductivity more than the electrical conductivity. This results yields to an enhancement of the *ZT* figure of merit greater than the one due to the increase of the product S^2n.

1.3.5.2 Nanowires

The enhancement of the figure of merit in one dimensional nanostructures is theoretically investigated by *Hicks and Dresselhaus* in [18]. They derived the expression for S, σ, κ for a general, anisotropic and one band material (conduction band assumed for convenience), assuming a constant relaxation time and parabolic bands.

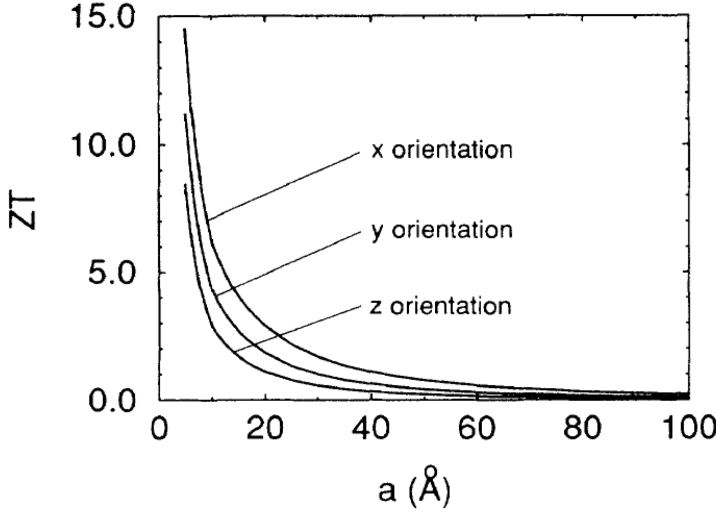

Figure 1.15 *ZT* versus the wire width *a* for 1D wired fabricated along the *x*, *y* and *z* directions [18].

The results reported show that *zT* depends strongly on the width *a* of the wire and that for widths narrower than the de Broglie wavelength of the carriers, it increases with the decreasing of *a.* Taking into account a good thermoelectric material as Bi_2Te_3, a *ZT* up to 14 is achievable for a cross section *a*=5 Å (Figure 1.15)[18]. For the mentioned results it has to be highlighted that the calculations are considering a layer thickness of a single lattice constant layer, which is not applicable under the practical point of view.

Under the experimental point of view, first interesting results have been shown by the group of P. Yang *et al.* [62], [63], [64], [65], [66] and A.I. Boukai *et al.*[67] from 2003 to 2008.

Li *et al.* [65] measured thermal conductivities of nanowires with different diameters, from 22 nm to 115 nm, using a microfabricated suspended device in a temperature range of 20-320 K. Their findings underline how the Debye T^3 law is well fitted for nanowires with larger diameters, suggesting that boundary scattering, which is frequency- and temperature-dependent, is the dominant phonon mechanism. Reducing this parameter, the temperature exponent decreases, suggesting that, besides phonon boundary scattering, other effects play a major role. The hypothesis to explain such a behaviour rely on the phonon confinement effect, happening for dimensionalities down to 10 nm, acting toward reducing the group velocity. In [62] NWs with diameters less than 30 nm have been measured in a temperature range from 20 to 100 K. The observed thermal conductance shows unusual linear temperature dependence at low temperatures, as opposed to the T^3 dependence predicted by the conventional phonon transport model. The work suggests that phonon-boundary scattering is a mechanism highly frequency dependent, and ranges from nearly ballistic to completely diffuse, which can justify the unexpected linear temperature dependence.

With a similar methodology [64], they investigated single crystalline Si/SiGe superlattice nanowires observing that the thermal conductivity shows comparable temperature dependence

as that of two-dimensional Si/SiGe superlattice films. Comparing with the thermal conductivity results of previously cited intrinsic Si nanowires, it is evidenced a more pronounced thermal conductivity-versus-diameter dependence. Thus, they concluded that alloy scattering of phonons in Si–Ge segments is the dominant scattering mechanism in these superlattice nanowires. The possible motivation is that while short-wavelength acoustic phonons can be scattered by atomic scale point imperfections in the SiGe alloy nanowire, long-wavelength acoustic phonons are scattered by its boundaries [64].
Hochbaum *et al.* [63] investigate the thermoelectric properties of silicon nanowires synthesized electrochemically with diameters ranging from 20 nm to 300 nm. Interestingly they found that, despite σ and S are not significantly modified with respect to doped bulk Si, for diameters lower than 50 nm, a 100-fold reduction in thermal conductivity was registered (κ_{latt} = 1.6 W K^{-1} m^{-1}, close to the amorphous limit), leading to a ZT = 0.6.

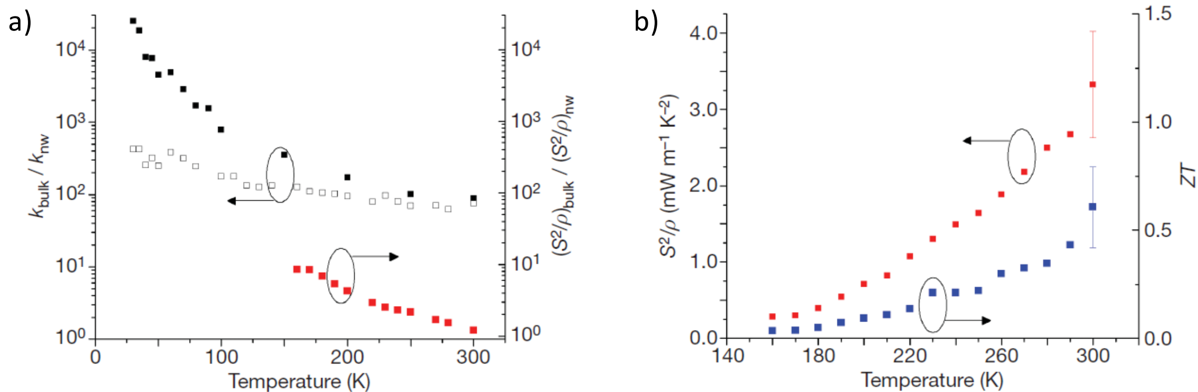

Figure 1.16 a) Ratio between intrinsic bulk silicon thermal conductivity and the one of highly doped Si nanowire, 50 nm in diameter. The ratio increases dramatically with decreasing temperature (solid squares). Comparison is done with highly doped bulk Si (As-doped, open squares). Red squares show the ratio of the power factor of optimally doped bulk Si relative to the nanowire power factor as a function of temperature. b) NW power factor (red squares) and *ZT* (blue squares). From [63].

The article underlines the advantages of such nanostructuration for thermoelectric applications, explaining that the difference in mean free path lengths between electrons (110 nm in highly doped samples [68], [69]) and phonons (300 nm [70]), at room temperature, allows to reduce the thermal conductivity without significantly affecting $S^2\sigma$ thanks to the incorporation of structures with critical dimensions/spacings below 300nm.
One of the most cited article in this field of the last year has been published by Boukai *et al.* in 2008 and it is entitled: *"Silicon nanowires as efficient thermoelectric materials"*[67]. The work investigates under a theoretical and experimental point of view different sizes and impurity levels of silicon nanowires. It demonstrated that semiconductor nanowires can be designed to achieve high *ZT* performing a proper tuning of the temperature of maximum efficiency by changing doping and nanowire's size. A record value of thermoelectric figure of merit has been found for ZT = 1 at 200 °C for these structures with NW 20-nm wide in diameter (Figure 1.19).

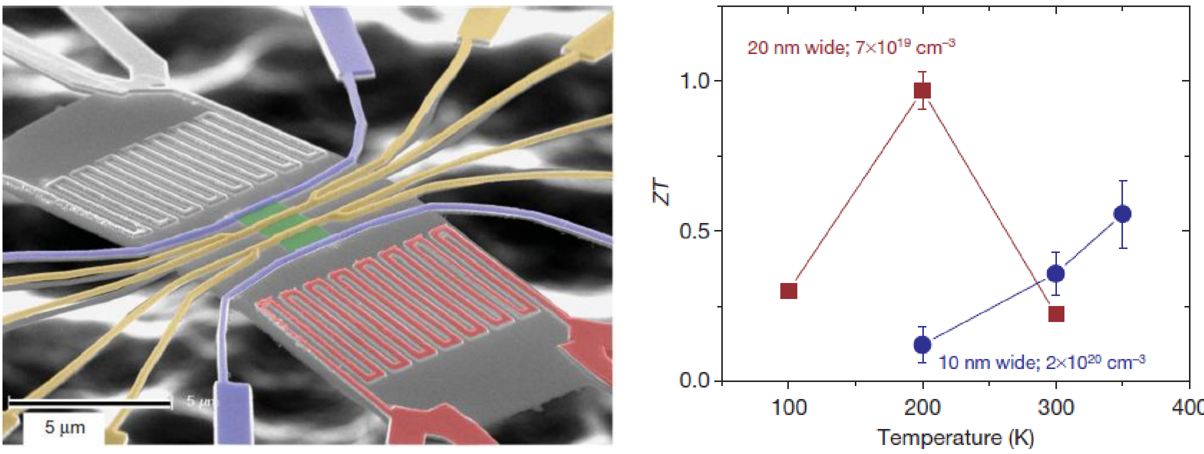

Figure 1.17 Left: The image of the suspended metrology platform showing the electrical connections. The central green area is the Si nanowire array. Right: *ZT* versus temperature for two different groups of nanowires. The cross-sectional area of the nanowires, and the p-type doping level, are given. The 20-nm-wide nanowires have a thermopower that is dominated by phonon contributions, and a ZT value ~1 is achieved near 200 K. The smaller (10-nm-wide) nanowires have a thermopower that is dominated by electronic contributions. [67].

Another method to reduce the thermal conductivity of crystalline silicon, presented by Lim *et al.* in 2012 [66], makes use of surface roughness. The work cited shows how the thermal conductivity can be reduced by frequency-dependent scattering down to 5 W K^{-1} m^{-1}. Furthermore, the quantitative relationship between three independent roughness parameters, σ, L, and α_p (with σ the root mean square, L the correlation length and α_p the coefficient obtained from power law behaviour of the roughness power spectrum at higher frequencies) has been measured and shown to have an important effect on the thermal conductivity of SiNWs, restricting the phonon transport below the Casimir limit. The obtained results could help to develop a more concrete theoretical understanding of phonon–surface roughness interactions and the role they play in designing next generation thermoelectric devices.
Another interesting approach is the one of investigating thermal conductivity reduction in nanowires under applied stress. Indeed, the experimental results cited show excellent agreement with computed results from Martin *et al.* [71],who calculated, with perturbation theory, frequency-dependent phonon scattering in order to model phonon-surface roughness scattering, predicting extraordinarily low thermal conductivity of 2 W K^{-1} m^{-1}. Such approach is suitable to be applied to the study of different materials, sizes and direction of thermal propagation. The first experimental measurements of the effect of spatially uniform strain and point defects on thermal conductivity of silicon suspended nanowires is performed by Murphy *et al.*[72] by Raman piezothermography, and κ is reduced by over 70% due to enhanced phonon scattering.

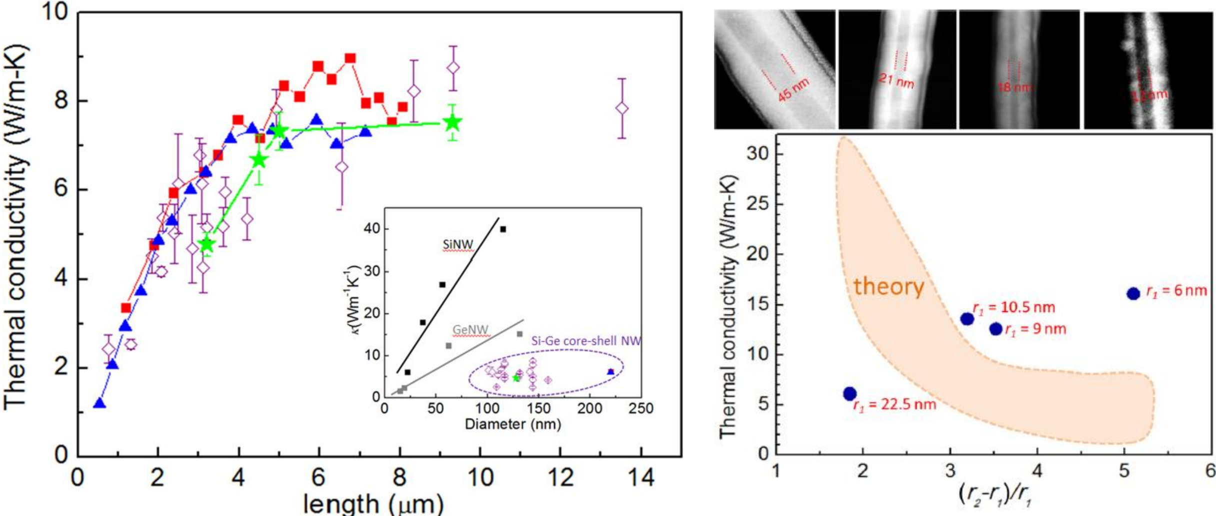

Figure 1.18 Left: κ vs L determined by three independent experimental methods. Method I (open diamonds) determines κ vs L for 20 Si-Ge core-shell nanowires of different lengths, diameters, and structures. Method II gives one set of data (green solid stars). Method III contributes two sets of data (red and blue solid symbols). (Inset) κ vs d relation for the investigated nanowires (data circled by the dashed line), Si nanowires (black squares) and Ge nanowires (gray squares). Right: (Top figures, from left to right) STEM images of four investigated nanowires with (r_1, r_2) =(22.5 nm, 64 nm), (10.5 nm, 44 nm), (9 nm, 45.5 nm), and (6 nm, 36.5 nm), respectively. (Bottom figure) κ vs $(r_2 - r_1)/r_1$ for the investigated nanowires and their respective r_1s. Due to the ballistic thermal conduction, here the κ data are compared at L = 3μm. The corresponding theoretical predictions (shaded area) for the given $(r_2 - r_1)/r_1$ and r_1 are shown for comparison. From [73].

Very recent reports from Hsiao *et al.* ([73], [74], [75]) illustrate with three different measurement methods that in silicon germanium nanowires ballistic conduction is present and persist over 8.3 μm with very low thermal conductivity and in a range of different structural variations and alloy compositions (Figure 1.18). Considering Si-Ge heterogeneously interfaced nanowires, they demonstrate that interfaces localize most high-frequency phonons and suppress the total thermal conductivity down to values lower than the ones of bulk Si or Ge. They found that nearly 99% of the phonons are filtered out by alloy scattering, so that only 0.1% of the low-frequency phonons carry out the heat conduction. Considering the same analysis on NW in Si or Ge, only 20-30% of the excited phonon modes lead to ballistic heat transport, according to theoretical calculations.

1.3.5.3 Quantum Dots

Mahan and Sofo [24] showed that sharp spectral features lead to high thermoelectric performance and high values of *ZT*. Nanoscale conductors such as quantum dots naturally provide these sharp spectral features. Thus, they are promising candidates for thermoelectric harvester devices.

A review by Sothmann *et al.* published in 2015 in *Nanotechnology* [76] details theoretical work on thermoelectric energy harvesting in multi-terminal quantum-dot setups. They firstly discuss several examples of nanoscale heat engines based on Coulomb-coupled conductors, focusing on quantum dots in the Coulomb-blockade regime, chaotic cavities and resonant tunnelling through quantum dots and wells. Secondly, they turn towards quantum-dot heat engines that are driven by bosonic degrees of freedom, pointing out how these systems provide interesting connections to spin caloritronics and circuit quantum electrodynamics.

It is known that strain can induce the growth of self assembled arrays of quantum dots at the interface between two slightly mismatched films. The cited technique is shown from

Springholz [77], [78] for lead chalcogenides, where PbSe QDs are grown with a uniformity in size distribution on a 4 μm-thin PbTe layer on Si.
In these systems two are the main mechanisms responsible of the *ZT* increase up to a value of 3 individuated by Heremans in [53]. The first cited is the reduction of lattice thermal conductivity, as indicated by Harman *et al.* [79] by a factor of 4 in n-type PbSeTe/PbTe quantum-dot superlattices (shown in Figure 1.19). The total thermal conductivity κ is measured, after the electronic contribution κ_e is calculated by Wiedemann-Franz law and then subtracted in such a way to obtain the value of the lattice part κ_{latt} ~ 0.33 W K^{-1} m^{-1}. The second mechanism is the boost of the Seebeck coefficient over that of the corresponding bulk material with the same carrier concentration.

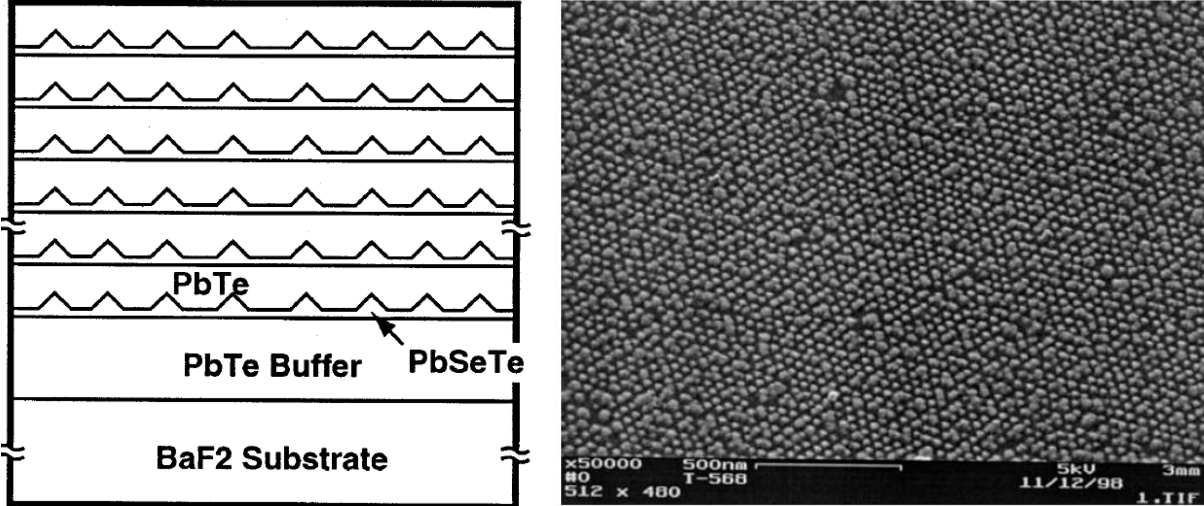

Figure 1.19 Left: Cross section of the QDSL structure investigated by Harman *et al.* [80]. Right: Field-emission SEM image of QDSL structure [80].

For a complete listing of the low-dimensional thermoelectric nanostructure at (quasi-)zero dimensionality it is worth to mention two others: $AgPb_mSbTe_{2+m}$ bulk alloys containing nanoscale inclusions and nanoprecipitates in bulk PbTe.
The first presents a *zT* factor up to 2.1 at 800 K ([51], [81], [82]). In these works Blic *et al.* point out that the material should be considered as a PbTe lattice with Ag and Sb inclusions. Ag introduces new states near the top of the valence band of PbTe, while isolated Sb atoms introduce resonant states near the bottom of the conduction band of PbTe. The Ag-Sb pairs result in an increase in the density of states, compared to the one of bulk PbTe. So, from Mott's equation, it is resulting an increase of the *S* coefficient and *zT* factor.
There are several other bulk materials containing nanoscale inclusions which solve the problem of limited quantities produced by MBE-grown films (previously cited in [79]) and limited power dissipation application. An example of these, presenting an interesting boost of the Seebeck coefficient, are: $CoSb_3$/fullerene composites [83] and sintered PbTe samples with nm-size grains [84].
For the bulk PbTe samples enriched with 6% Pb prepared by metallurgical heat treatment, the mostly cited mechanisms leading to a *S* increase are: an increase in the DOS such as could be induced by size quantization effects or by mechanisms similar to the ones reported previously for $AgPb_mSbTe_{2+m}$ alloys, or a change in scattering processes. To individuate the exact reason of this improvement Heremans *et al.* [84] used the *"method of four coefficients"*. They

considered that at each temperature there are four unknown parameters: carrier mobility, density of carriers, density of states effective mass and the energy dependence of the scattering. To determine those parameter they considered four experimental points: resistivity, Seebeck coefficient, Hall coefficient and transverse Nernst-Ettingshausen coefficient. Solving the related equations, they found that an enhancement in the energy dependence of the scattering time is at the origin of the increase in the Seebeck coefficient in samples that include Pb nanoprecipitates.

It can be concluded that QDSL have shown an increase of the zT figure of merit of a factor of two over the best bulk TE materials. So, the optimization of such TE materials involves the optimization of mainly three parameters: the electrical σ and thermal κ conductivity and the Seebeck coefficient S, which are interdependent. The mechanisms through which this optimization can happen are: by decreasing the lattice thermal conductivity or by increasing the Seebeck coefficient. The latter effect could be obtained by: size-quantization effect in quantum wires, enhancement of the LDOS in solids by nanometer size inclusions of $AgPb_mSbTe_{2+m}$ and electron energy-filtering on nano-precipitates of PbTe+6%pB metal.

1.3.5.4 Nanocomposites

From the study of regularly nanostructured material as nanolattices come out the discovery that to reduce the thermal conductivity it is not necessary required an atomically perfect interface or exact geometry. The finding that a high number of interfaces might lead to a big decrease of the thermal conductivity presents nanocomposites as a good solution to this aim. The advantage of this structure stays in its easy fabrication process, due to the reason that it doesn’t need a special geometry or structure. Indeed, the definition of nanocomposite is very broad, because several types of structures are called so. The main idea is of a structure composed by nanoparticles embedded in a host or a heterostructure geometry with nanoparticles of different materials adjacent to each other [16]. The fabrication process results easier and faster, by the fact the atomic layer deposition process is employed as methodology. The main challenge is represented by the need to produce a thermodynamically stable material which can retain its nanoscale structures while being integrated in a device, guaranteeing an enhancement of the ZT figure of merit. Nowadays, a commonly used methodology is ball milling and hot pressing, by creating nanograined materials by grounding into a nano-particle dust raw component elements, such as Bi and Te or Si and Ge ([19], [34], [85], [33]). Another way to fabricate bulk nanocomposites is to use thermal processing techniques to induce the formation of nanoscale precipitates, as detailed in the work presented by Kanatzidis’ group ([28], [29], [30]).

By reducing the dimensionality of the grains, the volume fraction of grain boundaries becomes comparable to the volume fraction of the investigated material, in this way the grain boundaries become another phase inside the host material. The challenge is represented by the theoretical interpretation of this reduction of thermal conductivity, because the properties of the overall material are determined not just by the scattering processes but by the presence of the grain boundary phase, whose properties are still unknown and difficult to be determined.

Indeed, the transport in nanocomposites is usually explained in terms of grain boundary scattering processes.
In the next section the heat transport phenomena and theoretical description of it are depicted, highlighting the developed models for nanoscale thermal transport which is interesting for the fabrication of nanodevices and the simulation of their properties.

1.4 Heat transport

The heat transport mechanism is fundamental to study material properties and their application in nanotechnology and microelectronics. The importance of a deep understanding of heat transfer at the nanoscale is given by two facts: the management of heat generated in devices to maintain the functionality and reliability of them and the use of nanostructures to manipulate the heat flow for thermoelectric and energy applications. The process is attributed to phonons, the quanta of lattice vibrations, that travel through the material and can carry the heat. The phonon transport is a topic that needs to be deeply investigated in order to obtain a better understanding of processes and mechanisms governing the thermoelectric behavior of devices.
At the macroscale, the heat conduction was firstly described by Fourier, who published a treatise *"Théorie Analytique de la Chaleur"* in 1822, where he sets the mathematical theory of heat conduction, describing the heat flux as linearly proportional to the temperature gradient by the thermal conductivity:

$$\vec{J} = -\kappa \cdot \vec{\nabla} T \tag{11}$$

where J is the heat current density.
The law is based on the continuum assumption, in a macroscopic continuum sense. Under a microscopic point of view, molecular and atomic motion (phonons) and free electrons are responsible for the heat transfer (as seen before: $\kappa = \kappa_{el} + \kappa_{phon}$). Indeed, the carriers diffuse, under the effect of the heat gradient, from a high temperature region to a low temperature one. On the other hand, the classical heat conduction theory may not hold when the specimen length scale approaches the mean free path. This is the case at low temperature when the mean free path rises up to the mm scale, or at room temperature for nanoscale systems [86].

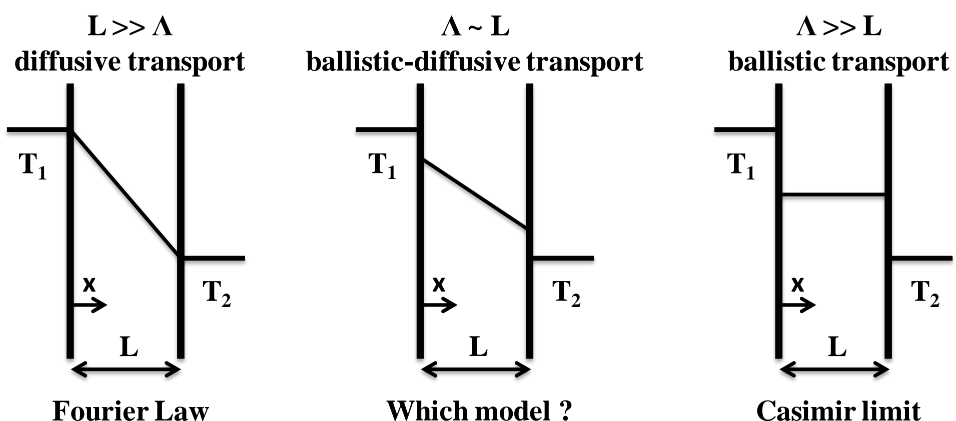

Figure 1.20 Comparison of the different dissipation methods and theoretical approach. Reproduced from [87].

Indeed, considering the size dimensionality of the sample Goodson and Flik individuated [88] the important size parameters that govern the heat transport in a specimen:

- the mean free path,
- the characteristic length of the material.

Thus, when the mean free path is bigger than the characteristic dimension of the system, the transport is said to be microscopic and Fourier law breaks down and the transport shifts from a partially diffusive-ballistic nature to a purely ballistic one (Figure 1.20).
At the ballistic limit it is noticed that the temperature at the boundaries governs the heat transport. Indeed, the situation at which boundary scattering dominates over intrinsic scattering is called “Casimir limit” [89] (Figure 1.20). For the sake of understanding, the length regime on which the interest of this research is focused is the one in which the dimension of the system approaches the phonon mean free path length, and the transport is at the limit between a ballistic and a diffusive one. The two ballistic and diffusive regimes are in competition for such dimensionalities. In the case of the molecular dynamic simulations performed, the discrimination between the two is not necessary, being the properties already embedded in the potential formulation chosen. Also the experimental measurements are not aiming to distinguish their origin, because those are providing results which already account for the phenomenon. Thus, given the scale and relaxation times, other equations are needed to investigate and explain at the nanoscale the phenomenon of heat transport in devices.
The first attribution of heat transport to lattice waves was given by Debye in 1914. He was the first able to explain the 1/T dependence of thermal conductivity at high temperatures [90].
The first attempt to modify the Fourier’s law to account for the time dependence of the heat transfer was done by Cattaneo [91] and Vernotte [92] who independently modified the equation to include the relaxation time, τ, of the system. They derived the Hyperbolic Heat Conduction (HHC) equation:

$$\tau \frac{\partial}{\partial t}\left(\rho c_p \frac{\partial T}{\partial t} \right) + \rho c_p \frac{\partial T}{\partial t} = \nabla \cdot \left(\kappa \nabla T \right) \tag{12}$$

Different solutions of the equation have been developed both numerical and analytical, but still the equation, improved over the Fourier’s law, is not able to predict conduction at micro and nano scale levels nor under extremely short transient heating times.
Considering that at these levels the length of the system becomes smaller than the mean free path of phonons [93], those carriers might be treated as particles, still having the structure size larger than the wavelength of vibration.
Under these condition it is possible to model the electron and phonon transport with the Boltzmann transport equation.
The Boltzmann transport equation (BTE) describes the time rate of change of the heat carriers distribution due to diffusion in presence of a heat gradient. In other words it deals with the probability of finding a phonon in time, real space, and phase space. It was introduced for phonons in solids by Peierls in 1929, including the complete anharmonic collision term.

$$\frac{\partial \Psi_\lambda}{\partial t} + \mathbf{v}_\lambda \cdot \nabla_{\mathbf{r}} \Psi_\lambda = \left(\frac{\partial \Psi_\lambda}{\partial t} \right)_c \tag{13}$$

where Ψ_λ is the desired distribution function, v_λ the group velocity and λ denotes a particular phonon mode of wavevector $\boldsymbol{q}$.

The equation can be solved under two approximations: considering a linearized collision term that accounts for inelastic three-phonons coupling, and with the single-mode relaxation time approximation (RTA) that neglects inelastic processes but yields a simpler collision integral suitable for computing transport dynamics.
For the first solution it has to be assumed that the temperature gradient is uniform, one-dimensional and the collision integral linearized [94], [95]. Considering only 3-phonon processes and neglecting the higher order ones (because they are much less likely to occur than 3-phonon and contribute little to the thermal resistance), solving the BTE equation under the cited assumptions and for a particular Ψ_λ, the thermal conductivity tensor $\kappa_{\alpha\beta}$ becomes:

$$\kappa_{\alpha\beta} = \frac{1}{V}\sum_{\lambda} \hbar\omega v_{\alpha\beta} n_\lambda^0 \left(n_\lambda^0 + 1\right)\left(\frac{-\Psi_\lambda}{\partial T / \partial x_\beta}\right) \tag{14}$$

where V is the volume of the crystal, ω the phonon frequency, $v_{\alpha\beta}$ the velocity in the direction x_α, n_λ^0 the Bose-Einstein distribution, T the absolute temperature. This solving methodology requires the knowledge of the phonon dispersion relation, the description of the phonon frequency ω_λ for different wavevectors $\boldsymbol{q}$ and polarizations j in the Brillouin zone and scattering matrices. While the dispersion relation is measurable with different approaches (i.e. neutron scattering), to determine the scattering matrices it is required to know the cubic force constants that describe the anharmonic component of the interatomic potential, a very difficult calculation. There is no methodology suitable to measure those matrices.
The second approach to solve the BTE equation is the one used from a longer period, considering the difficulties related to the knowledge of the 3-phonon scattering matrices. For the RTA method, the BTE becomes:

$$\frac{\partial \Psi_\lambda}{\partial t} + \mathbf{v}_\lambda \cdot \nabla_{\mathbf{r}} \Psi_\lambda = \frac{\Psi_\lambda - \Psi_\lambda^0\left(T_p(\mathbf{r},t)\right)}{\tau_\lambda} \tag{15}$$

where τ_λ is the total relaxation time for a phonon mode and $\Psi_\lambda^0\left(T_p(r,t)\right)$ the local equilibrium distribution, representing the distribution at which the phonons relax as function of space and time. The total relaxation time is calculated by Mathiessen's rule:

$$\tau_\lambda^{-1} = \tau_{\lambda,p-p}^{-1} + \sum_i \tau_{\lambda,ext,i}^{-1} \tag{16}$$

where $\tau_{\lambda,p-p}^{-1}$ is the relaxation time for phonon-phonon scattering [95]. This description of the relaxation time considers the scattering mechanisms independent of each other.
To establish a relationship between Ψ_λ and Ψ_λ^0 the energy conservation conditions have to be posed, summing over all the phonon modes:

$$\frac{\partial \mathbf{U}(\mathbf{r},t)}{\partial t} + \nabla \cdot \mathbf{q}(\mathbf{r},t) = 0 \tag{17}$$

where $\boldsymbol{U}(\mathbf{r}, t)$ is the local energy density and $\boldsymbol{q}(\mathbf{r}, t)$is the heat flux. So, given this expression for the heat equation, it leads to:

$$\sum_\lambda \frac{\Psi_\lambda(\mathbf{r},t)}{\tau_\lambda} = \sum_\lambda \frac{\Psi_\lambda^0\left(T_p(\mathbf{r},t)\right)}{\tau_\lambda} \tag{18}$$

where $T_p(\mathbf{r}, t)$ is the local pseudo-temperature, which differs from the thermodynamic one for the presence of the weighting factor τ_λ^{-1}. To solve the BTE, the equations (16) and (18) have

to be solved simultaneously. Considering the crystal isotropic, the thermal conductivity, under RTA, becomes:

$$\kappa = \frac{1}{3}\int C_\omega v_\omega^2 \tau_\omega d\omega \tag{19}$$

where C_ω is the frequency-dependent specific heat:

$$C_\omega = \hbar\omega D(\omega)\partial n_\lambda^0 / \partial T \tag{20}$$

with $D(\omega)$ the density of states. It is also known that the mean free path is $\Lambda_\omega = v_\omega \tau_\omega$. So that:

$$\kappa = \frac{1}{3}\int C_\omega v_\omega \Lambda_\omega d\omega \tag{21}$$

This solution of the BTE results easier with respect to the previous one because in this case the scattering matrices over the full Brillouin zone are not required. It results accurate to within 10% for semiconductor materials as Si, while it fails for diamond [96]. Still, the number of variables to integrate is high, which evidences the main challenge of thermal transport: the fact that all the properties of phonons are represented by averaging over all the population, neglecting the microscopic details.

Several analytical models for thermal conductivity have been developed based on the second solution proposed of the BTE, the so called single mode relaxation time (SMRT) approximation. In these models a single relaxation time is associated with each phonon mode. It describes the response to an excitation of that mode, considering all the others in equilibrium. The first to develop a successful low temperature SMRT model for Ge thermal conductivity has been Callaway in 1959 [97]. He assumes in his work that all the phonon scattering processes can be represented by relaxation times which are functions of frequency and temperature. The model considers the material is elastically isotropic. This approach uses the Debye approximation, because it assumes that there is no phonon dispersion in the vibrational spectrum and that the longitudinal and transverse polarizations behave identically. For the relaxation time of normal three phonon processes it is taken the one of longitudinal phonon processes in a cubic crystal. Considering that normal processes cannot themselves lead to a finite thermal conductivity, all the other scattering process are taken into account to obtain a correct formulation of the relaxation time. Thus, boundary scattering, normal three-phonon processes, impurity scattering and umklapp processes are contributing.

A more detailed formulation of the thermal conductivity is done by Holland in 1963 [98], who extended the work of Callaway by separating the contribution of acoustic phonons in a longitudinal (LA) one and a transverse (TA) one. Furthermore this formulation includes some phonon dispersion by splitting the different branches in two segments and uses different forms of the relaxation times. This approach shows a better agreement for silicon at high temperatures (1.7 to 1300 K) than with the Callaway model.

$$\kappa = \frac{4\pi/3}{(2\pi)^3}\sum_\lambda \int_0^{2\pi/a} \tau(k,\lambda) k^2 v_g^2(k,\lambda) C_{ph}(k,\lambda) dk \tag{22}$$

where a is the lattice constant $a=n^{-1/3}$ for a cubic lattice, v_g the group velocity given by the derivation of the phonon frequency with respect the wave number, C_{ph} the heat capacity:

$$C_p(k,\lambda) = k_B\left(\frac{\hbar\omega(k,\lambda)}{k_B T}\right)^2 \frac{\exp(\hbar\omega(k,\lambda)/k_B T)}{[\exp(\hbar\omega(k,\lambda)/k_B T) - 1]^2} \tag{23}$$

and τ the phonon scattering lifetime, which can be broken into three major components: Umklapp, impurity and boundary contribution. The inverse of those parameters are summed up following the Matthiessen's rule, as previously described.
Figure 1.21 illustrates the comparison between thermal conductivity experimental results from [99] and the simulated ones from models described above of Callaway, Holland and the Born – von Karman – Slack (BvKS) one for Si bulk and nanowires in a wide range of temperatures.

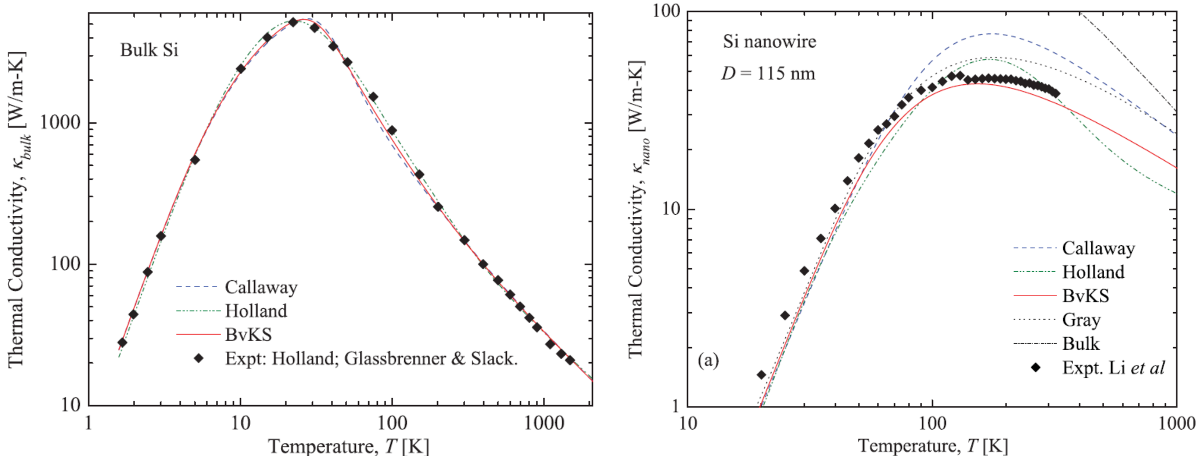

Figure 1.21 Comparison between thermal conductivity results obtained by three analytical models (Callaway [78], Holland [79] and Born – von Karman – Slack (BvKS)) and experimental values from Glassbrenner and Slack [99]. From [100].

It is clearly shown how those models reproduce correctly the experimental results found for silicon confidently, depicting a better agreement for bulk than for nanowires, being the nanostructuration a complication factor in simulations.
There are different numerical techniques to predict the phonons properties and thermal conductivity shown in the Boltzman transport equation. The approaches mostly used to calculate the silicon phonon parameters are: phenomenological models, lattice dynamics [101] and molecular dynamics [102], [103], [104], [105]. Molecular dynamics simulations with Green-Kubo method are in Chapter 2, as they are used to simulate the heat transport properties in bulk silicon, thin films and phononic structures.
Finally, looking at equation (21) it can be highlighted that phonon transport phenomenon is dependent on the mean free path, group velocity, heat capacity (intrinsic to the material) and scattering events. At low temperatures, the mean free path is longer and mainly limited by boundary scattering. Thus, the thermal conductivity is respecting the heat capacity's temperature T^3 exponential dependence, for temperatures much lower than the Debye's one. Increasing the temperature, phonon population increases, but scattering events are more frequent too. The thermal conductivity presents a peak in correspondence of the temperature at which the scattering events start to outweigh the impact of the increasing heat capacity. Figure 1.22 (from [89]) supports these facts by reporting experimental results of thermal conductivity for bulk and nanostructured silicon. The peak shifts toward higher temperature by nanostructuring the material (i.e. reducing the film thickness) and its intensity decreases. For high temperatures the thermal conductivity decreases as the temperature increases because of the lower mean free path. In this temperature range the exponential coefficient α, linking the thermal conductivity κ in a exponential dependence to the temperature *T,* in the

equation: $\kappa = \kappa_{300K}\left(\frac{T_0}{T}\right)^{\alpha}$ (where κ_{300K} is the thermal conductivity at T_0= 300 K), has been investigated to have a better insight of phonon processes in relation to nanostructuration, and it is discussed hereafter.

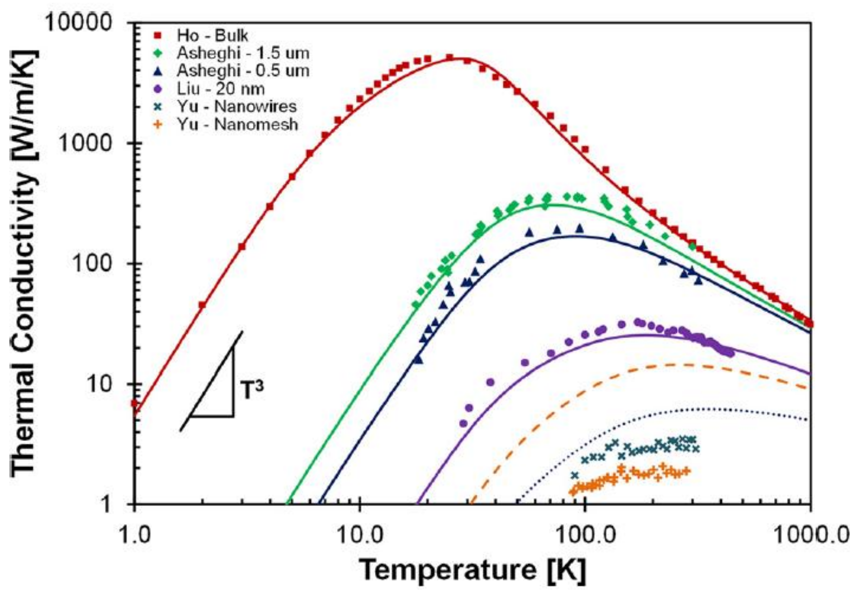

Figure 1.22 Temperature dependent thermal conductivity of several different SOI-based silicon structures. From [89]. Thin films results from [106], [107]; rectangular nanobeams and nanoporous films from [108]; bulk from [109].

Given the discussion above, the approach acting on the above cited parameters appears the opportune solution leading to thermal conductivity reduction.

1.5 Phononic Engineering, state of the art

Considering the dependence of lattice thermal conductivity on the group velocity and mean free path depicted in the models presented in the previous paragraph, it is possible to focus our attempts of reducing the thermal conductivity on these parameters. Thus, it is desired not to affect the electronic properties of the material, avoiding to degrade them. As detailed before, nanostructuring the material represents an efficient way to reduce the heat transport. The mechanisms leading to such a decrease are still debated and intensely investigated. One reason is the reduction of the thermal conductivity by phonon confinement in thin films or nanowires, or the modification of the phonon dispersion curve by an added periodicity, in superlattices or phononic crystals. Another relevant effect is the shortening of the mean free path due to the phonon scattering at the boundaries. Thus, the effect of hindering the phonon transport is increased as the membrane thickness is decreased down to values smaller than the phonon mean free path.

1.5.1 Membranes

The thermal properties of fully silicon suspended membranes have been widely investigated during the last years. The incredible reduction of the thermal conductivity down

to a factor of 10 with respect to bulk is a promising step toward the potential integration of the material into industrial scalable converters which are flexible, cost efficient and CMOS compatible.
The thermal conductivity behavior of silicon thin film membranes is reproduced by the Fuchs-Sondheimer model [110], [111].

$$\kappa_{membrane} = \kappa_{bulkSi}\left(1 - \frac{3(1-p)}{2\delta}\right)\int_1^{\infty}\left(\frac{1}{\xi^3} - \frac{1}{\xi^5}\right)\frac{1-\exp\left(-\frac{t}{\Lambda}\xi\right)}{1-p\exp\left(-\frac{t}{\Lambda}\xi\right)}d\xi \tag{24}$$

where t is the thickness, Λ the mean free path at 300 K and p the fraction of phonons specularly reflected at the boundaries.
In Figure 1.23 is reported a summary of the state-of-the-art of measured thermal conductivities obtained for membranes of different thickness. The solid line represents the Fuchs-Sondheimer model's behavior. The mean free path considered is the one of the silicon peak distribution at room temperature: Λ = 300 nm. The specularity parameter p is assumed to be 0.

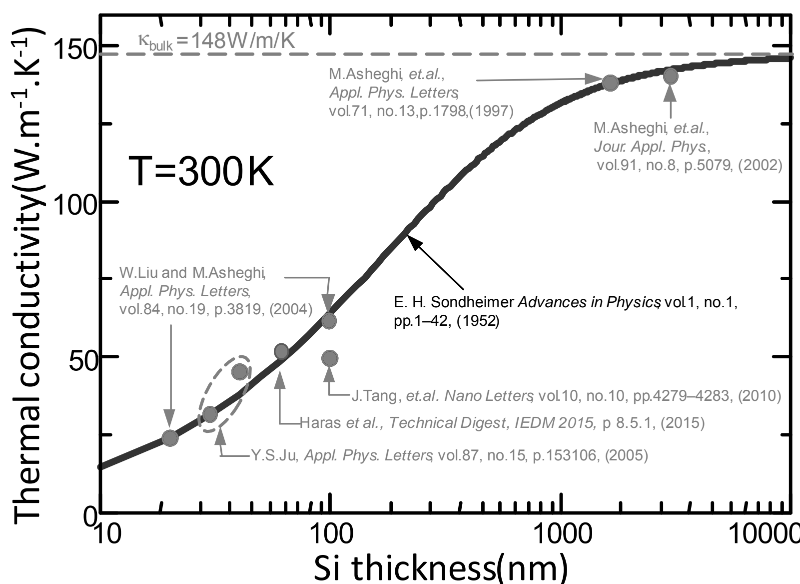

Figure 1.23 Thermal conductivity of silicon membranes, dots refer to state-of-the-art measurement values, solid line presents the Fuchs-Sondheimer model [110], [111]. Reproduced from [112].

A great variety of techniques have been demonstrated to measure the thermal conductivity of suspended crystalline silicon membranes. Table 1.6 summarizes the most interesting reports investigating the thermal properties of thin film suspended silicon membranes with different measurement methodologies [89].

Table 1.6 Thermal conductivity of various silicon thin film membranes at the state-of-the-art [89].

Reference	Year	Measurement configuration	Doping	Temperature range	Si thickness (nm)
Ju [113]	2005	On-substrate (steady state Joule heating, varying heater width)	p-type	RT	20 to 50

Reference	Year	Measurement configuration	Doping	Temperature range	Si thickness (nm)
Liu and Asheghi [106]	2004	Suspended heater bridge (steady state)	Undoped	20 to 300 K	20 to 25
Asheghi *et al.* [107]	1997	On-substrate (steady state Joule heating)	n-type	20 to 350 K	420, 830, 1600
Asheghi *et al.* [36]	2002	Suspended film (steady state Joule heating)	B or P (10^{17}-$3{\cdot}10^{19}$ cm^{-3})	15 to 300 K	3000
Chavez-Angel *et al.*[114]	2014	Raman thermometry	-	RT	9

Recently, Marconnet *et al.* [89] reviewed the last 20 years of results in the field of phonon transport using silicon-on-insulator technology. All the different factors influencing the phonon transport related to the material (silicon) are detailed. Firstly, the effect of thickness is studied using the previously cited model of Fuchs-Sondheimer (reported in Figure 1.23). Furthermore, the impact of temperature on thermal conductivity reduction is detailed for thin films and compared with bulk silicon, relating it to the parameters influencing (mean free path, group velocity, thickness). See Figure 1.22 for further details.
Considering the phonon dispersion curves (Figure 1.24) and knowing that the thermal conductivity is directly proportional to the group velocity, defined as the slope of the curve, it is evident that the phonons with higher velocities are the ones contributing more to the heat transport. Thus, the area highlighted in Figure 1.24 represents the region in which the phonons exhibit higher group velocity v_g and their density of states (DOS) results more important (right part of the figure). The branches interested are the ones of acoustic phonons in a range of frequencies between 3 THz and 7 THz, whose transport needs to be hindered to substantially decrease the thermal conductivity.
Moreover, the high density of state registered for phonons in optical branches at very high frequencies is not considered, having low group velocities.

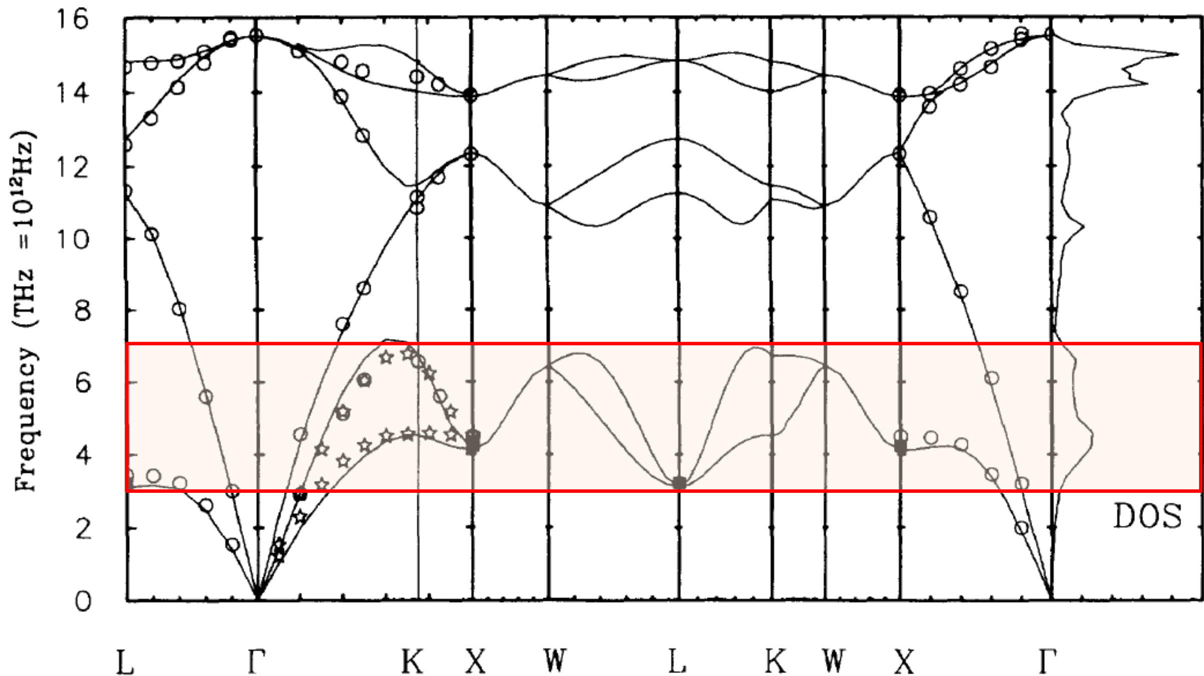

Figure 1.24 Phonon dispersion curve and density of states (DOS) for silicon, from [115]. The results are obtained with a plane-wave energy cut-off of 18 Ry. Solid lines are calculated results and experimental values are shown as circles [116] and stars [117].

An interesting point to stress is that, for silicon, at room temperature, the peak of the distribution of the lattice thermal conductivity carried "per unit MFP" is registered in a range of mean free paths around 200 - 300 nm (as shown in Figure 1.25). Thus, the heat conduction might decrease by hindering the phonon transport by material nanostructuration in such a range of dimensionalities. This approach is treated and detailed in the next subparagraph.

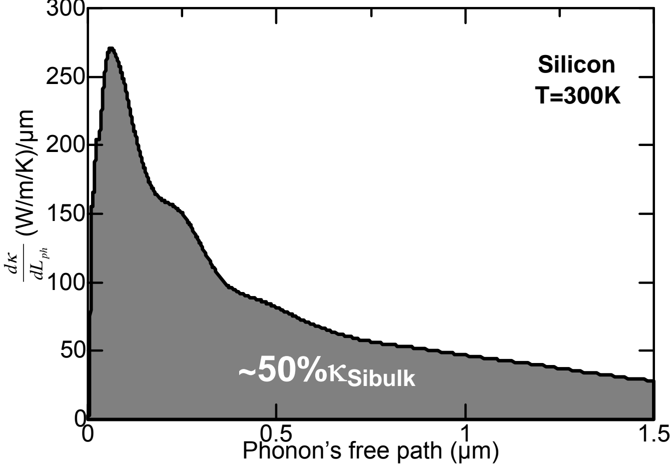

Figure 1.25 Thermal conductivity derivative as function of the phonon mean free path. From [118].

1.5.2 Phononic crystals

As previously anticipated, phononic crystals are fabricated by patterning regular and periodic identical features, which confers upon the material added properties that strictly

depend on its extrinsic characteristics (as: pitch, neck sizes, filling fraction, etc.) and intrinsic ones (as group velocity, mean free path, crystal anisotropies, etc.).

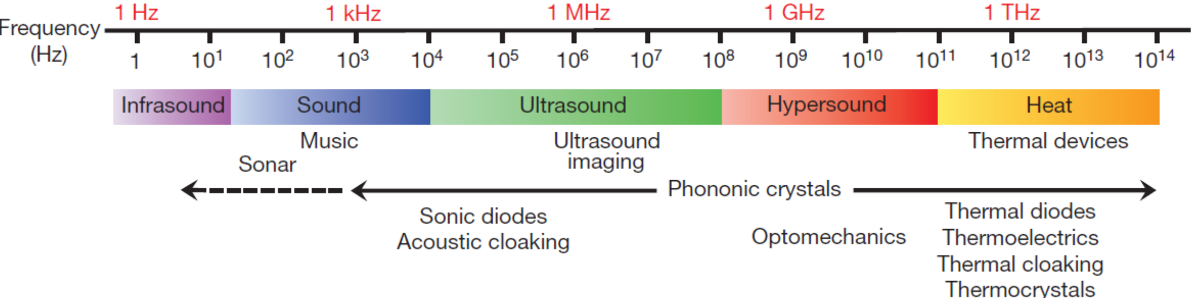

Figure 1.26 Phononic spectrum [119].

Being phonons described as the quantum of lattice vibration, able to transport sound and heat through the atomic lattice, it is important to detail the two phenomena, happening at different frequencies and wavelengths. Sound mostly oscillates at low frequencies: from few Hz (infrasound regime) up to 100 GHz (hypersound regime) and it travels for very large distances. Heat spans a range of higher frequencies (from 100 GHz up to 100 THz) and propagates for shorter distances (Figure 1.26). Therefore, nanostructuring the material it is possible to act on the phonon transport regime (playing with frequency and wavelength) to control heat [119]. Figure 1.28 shows 3 different examples of phononic crystals at different scales.

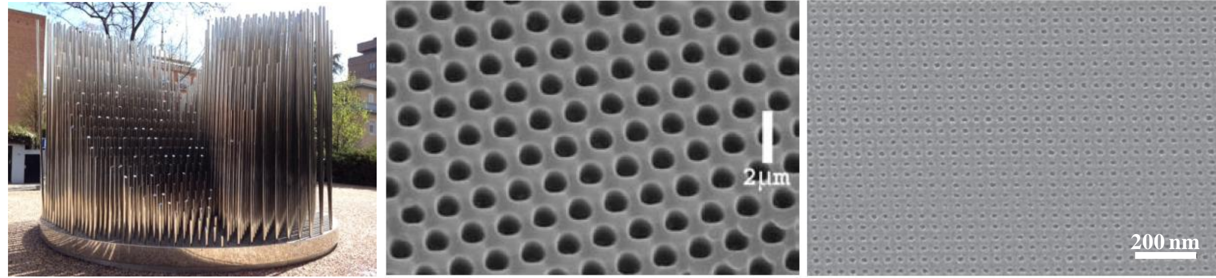

Figure 1.27 Left image: *Órgano*, sculpture by Eusebio Sempere, at the Juan March Foundation in Madrid. It is an example of a 2D phononic crystal, a periodic arrangement of structures — in this case, metal tubes — that can block sound waves (cm - kHz frequencies range). Central image: 2D phononic crystal in the hypersound regime (μm - GHz frequencies range) [120]. Right image: 2D phononic crystal in the heat regime (nm – THz frequencies range).

The works presenting phononic crystal patterned structures are summarized in Table 1.7.

Table 1.7 Thermal conductivity of various phononic engineered silicon thin film membranes at the state-of-the-art.

Reference	Year	Measurement configuration	Doping	Temperature range (K)	Si thickness (nm)	Pore diameter/pitch (nm)
Song and Chen [121]	2004	Suspended film (steady-state Joule heating)	n- type ($5 \cdot 10^{14}cm^{-3}$ - $5 \cdot 10^{15}cm^{-3}$)	50 to 300	4670	2300 to 10900/ 4000 to 20000
Hopkins *et al.* [122]	2010	Thermoreflectance	n-type	RT	500	300/500-600-700; 400/800
Yu *et al.* [108]	2010	Suspended heater thermometer	B ($2 \cdot 10^{19}$ cm^{-3})	80 to 320	20 to 25	11/34; 16/34; 270/385

Tang *et al.*[123]	2010	Suspended heater thermometer	Intrinsic or B ($5\cdot10^{19}$ cm^{-3})	25 to 300	100	32/55; 81/140; 198/350
Kim *et al.*[124]	2012	Suspended (steady-state Joule heating)	B (10^{16} cm^{-3})	RT	500	200 to 500/ 500 to 900
Marconnet *et al.* [125]	2012	Suspended heater thermometer	-	RT	196	110/385; 210/385; 280/385
Nomura *et al.* [126], [127], [128]	2015	Micrometer scale time domain thermoreflectance	B doped (lightly)	4 and RT	145	211/300
Alaie *et al.* [129]	2015	Suspended film (steady-state Joule heating)	-	RT	366	850/1100
Lim *et al.*[130]	2015	Suspended film (steady-state Joule heating)	B doped ($3.1\cdot10^{18}$ cm^{-3} to $6.5\cdot10^{19}$ cm^{-3})	50 to 300	340	26 to 44/60

The works attracting at the most the attention in the last year (2015) are the one published by Alaie *et al.* [129], claiming a coherent phonon scattering at room temperature (the *'hot'* topic still largely debated in the last years), and the one by Lim *et al.* [130], presenting a RT thermal conductivity as low as 1.8 W K^{-1} m^{-1}, obtained by measurements from 50 K to 300 K by suspended heater and sensor thermometers method, confirmed by Raman spectroscopy and also justified with Monte Carlo simulations and Boltzmann Transport Equation methods.
Recently, several groups, summarized in Table 1.7, concentrated their effort in demonstrating that patterning phononic crystal into suspended thin film membranes represents the most efficient nanostructuring methodology to markedly reduce the thermal conductivity.
The work by Yu *et al.*[131] compares thin film (TF), electron beam lithography devices (EBM), nanowires (NWA) and nanomesh devices (NM, different dimensionalities) registering the lowest thermal conductivity of 1.9 W K^{-1} m^{-1} for the phononic nanomesh structures (Figure 1.28). One of the main concerns posed by industry is the preservation of the electrical properties of silicon when patterned and integrated into thermoelectric device. For this scope, in the cited article, the electrical conductivity of two differently doped silicon nanomesh suspended membranes is measured. Both the devices exhibit values which are lower, but still comparable, with the ones of bulk thin films. These facts demonstrate that the phononic membranes are relatively defect-free and the bulk electrical properties are preserved in the high-doping range, guaranteeing an improved *ZT* figure-of-merit due to the lower thermal conductivity. Other reports by Tang *et al.* [123] and Hopkins *et al.* [122] investigated the thermal properties of holey silicon membranes. In the first, different holey silicon (HS) membranes are fabricated and the thermal conductivity of 55 nm pitch HS shown to be as low as 1.14-2.03 W K^{-1} m^{-1}. The result is explained in terms of "necking effect", indentified to be the main mechanism of reducing the thermal conductivity and leading to a figure-of-merit *ZT*~0.4 at room temperature.

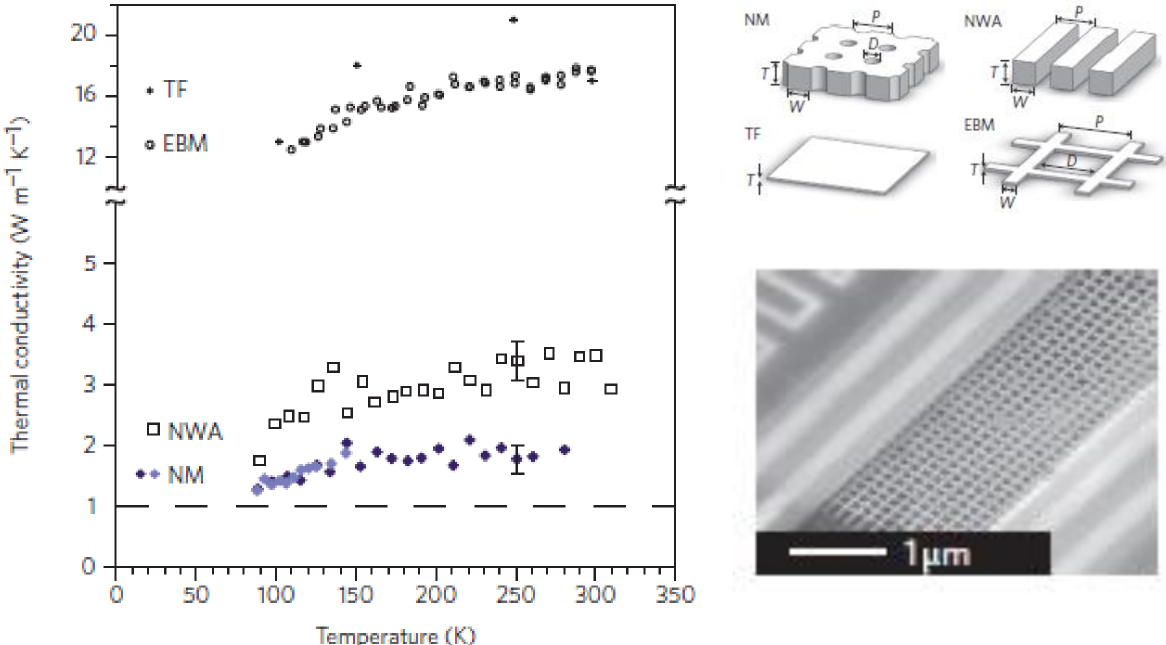

Figure 1.28 Left: Results obtained from Yu *et al.* for thermal conductivity measurements of different nanostructures: thin film (TF), electron beam lithography devices (EBM), nanowires (NWA) and nanomeshes (NM). Right top image: Schematic of the 4 structures measured. Right bottom image: SEM image of the suspended EBM device.

The work by Hopkins *et al.* [122] presents thermal conductivity measurements by time domain thermoreflectance technique of phononic crystalline patterned membranes. Thermal conductivities result reduced with respect to the bulk value of more than one order of magnitude, being as low as 4.81 W K^{-1} m^{-1} for PnCs with diameter of 300 nm and pitch of 600 nm. It is also demonstrated that the coherent, phononic effect in phononic crystals is leading to a further reduction of thermal conductivity beyond the effect of boundary scattering alone. To do so, two films: one patterned with PnCs and the other one unpatterned with the same limit dimension (neck size) are compared. The patterned one presents a thermal conductivity which is 3 – 4 times lower than the unpatterned membrane. It is justified in terms of change of silicon mode density and proved by plane-wave expansion (PWE) technique (Figure 1.29). Indeed, the spike of the 2D phononic crystal density of states in the inset in Figure 1.29 (right) is indicative of a large reduction in the phonon group velocity in the PnCs lattice. These facts confirm that the thermal energy in silicon follows a Bose-Einstein distribution and the majority of energy is carried by (acoustic) phonons in the 1 – 6 THz range.

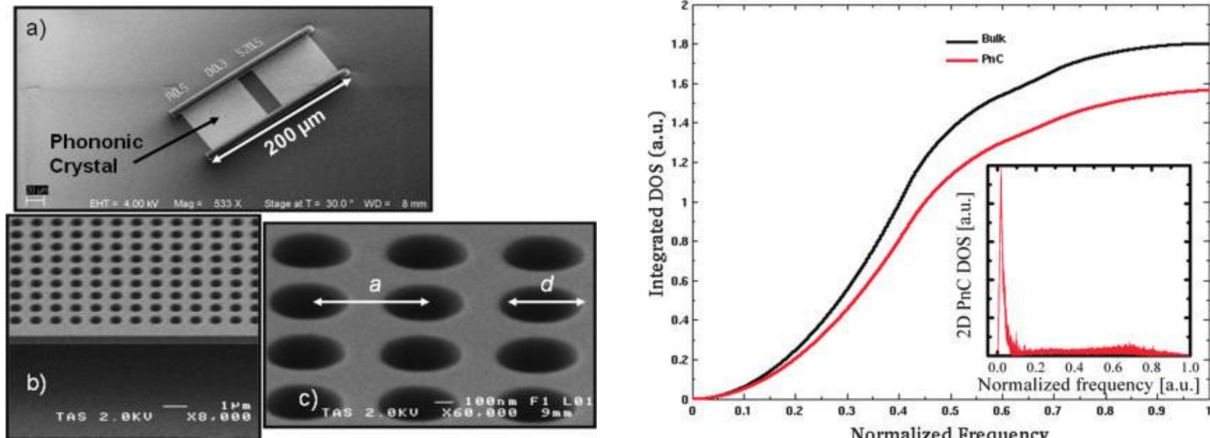

Figure 1.29 From [122]. Left: SEM image of the membranes containing PnCs (pitch a = 500 nm and diameter d = 300 nm): a) full device; b) side image showing the suspended part; c) closer image of Si/air PnCs. Right: PWE simulated integrated density of states as a function of frequency for bulk Si (black) and PnC lattice (d/a = 0.6). Inset shows the calculated DOS of the PnC.

A recent report by E. Dechaumphai and R. Chen [132] theoretically investigates thermal conductivity in terms of wave or particle nature of the phonons depending on their frequencies. They make use of Boltzmann transport equation and Finite Difference Time Domain (FDTD) modeling coupled with Plane Wave Expansion (PWE) method, to justify the experimental findings.

Phonons with a mean free path lower than the characteristic size of the structure (phononic crystal in this case) are treated as particles and their heat transport properties are formalized with the BTE, taking into account phonon boundary scattering. Thus, they are considered presenting incoherent regime and the dispersion relation can be the same as for bulk. MFP is modified due to the diffusive scattering at the interfaces. Phonons whose mean free paths are higher than the size individuated are treated as wave, their heat transport properties are treated with the Finite Different Time Domain (FDTD) method and planar wave equations (PWE) are applied to find the wave parameters. The phononic crystal periodicity is introduced by means of Bloch conditions. Considering those conditions, phonons are coherent and their dispersion is modified due to the *zone folding effect*. Such an effect is seen as the natural consequence of the imposed *new* periodicity of the crystal, whose bands, to respect energy and momentum conservation laws, fold inside the shrunk Brillouin zone. This band folding leads to a consequent reduction of the group velocity (being the slope of the dispersion curve being: $v_g = \frac{\partial \omega}{\partial k}$) and, in turn, a thermal conductivity reduction. Furthermore, interference effects due to the crystal periodicity might lead to the creation of new bands and phononic band gaps in the dispersion curve, even if this aspect has not yet been demonstrated experimentally and still results a controversy.

The size to take into account is individuated to be the *'neck size'* of the crystal. In other words, the space between two periodic holes which is the one the phonon has to travel before undergoing a boundary scattering event. A clear reduction of the thermal conductivity is registered in correspondence of lower neck sizes, validating the model [132], which agrees with experimental results [131], [123] [122], as shown in Figure 1.31. It is possible to tune the neck size in such a way to filter out by scattering as much phonons as possible. To that purpose in Figure 1.30 (left) the accumulated thermal conductivity is shown as a function of

the mean free path. It is understandable that about the 80% of the thermal conductivity is accumulated for mean free paths in the range of 10 nm to 10 µm. Thus, it could be sufficient to pattern phononic crystal with a neck size of the order of few tenths of nanometers to filter out the main portion of phonons contributing to the heat transport. Figure 1.30 (right) indicates the MFP of longitudinal and transverse acoustic modes as function of the frequency.

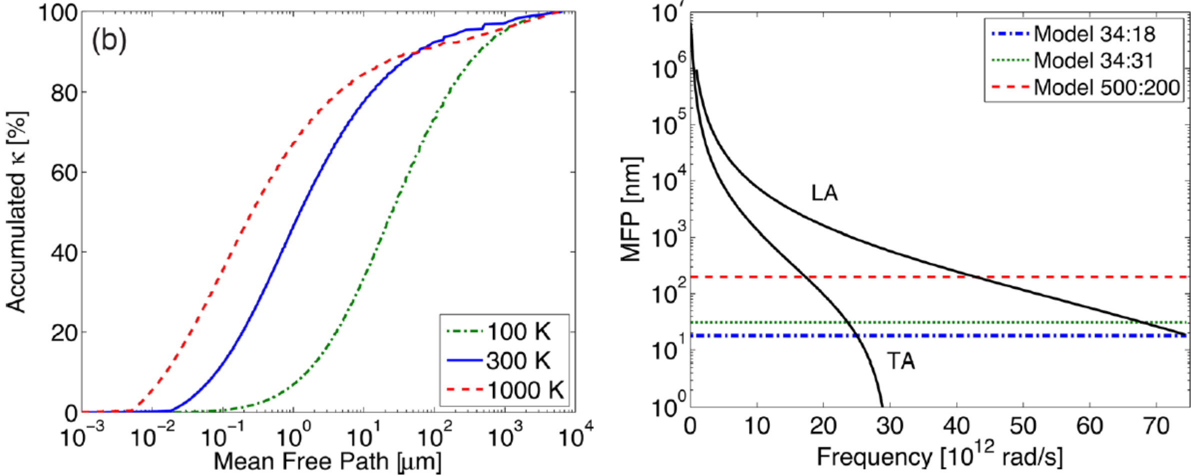

Figure 1.30 Left: accumulated thermal conductivity at different temperatures as function of the phonon mean free path. Right: Phonon mean free path for longitudinal and transversal acoustic modes as function of the frequencies for different phononic structured. From [132].

Considering the different dimensionalities, it is possible to individuate a cut-off frequency for particle/wave - like regime. Of course, in this case, it represents a unrealistic approximation, because more likely the change of regime happens in a frequency range more than for a specific value. It is important to underline that the LA phonons present a higher MFP compared to the TA modes for the same frequency value.

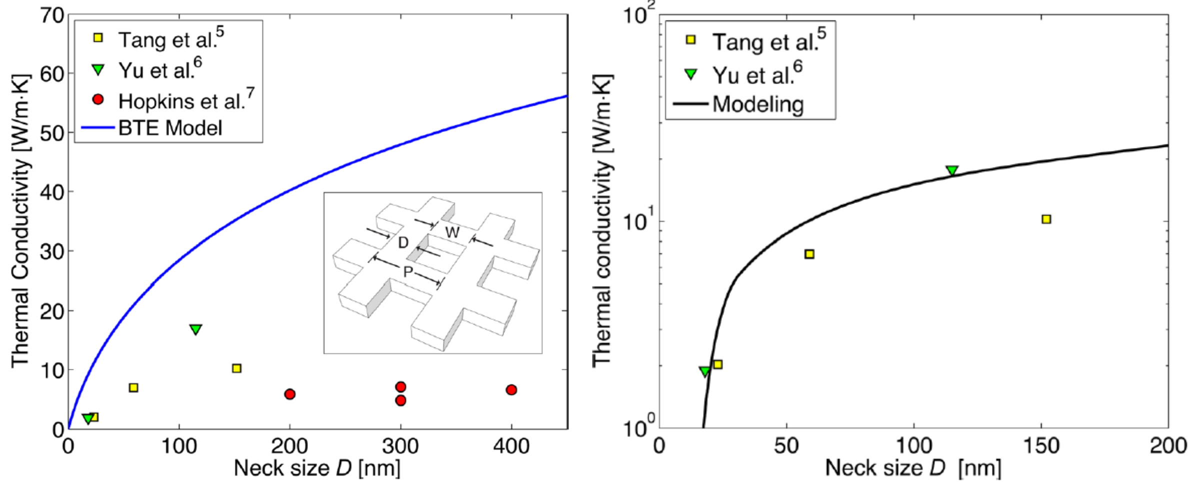

Figure 1.31 Experimental data [131], [122], [123] of silicon thermal conductivity as a function of neck size, compared with BTE model (left) and the one developed in [132](right). Reference [132].

Considering the cited reports, it is understandable that the reduction of phonon thermal conductivity for thermoelectric applications is a hot topic during the last years. The factors on which it is important to focus the attention in order to design the best phononic crystal

structure are: thickness of the active material (SOI thin film in this case), pattern filling fraction *ff*, pitch, neck size. The fabrication methodology (CMOS compatibility, material pollution and cost, etc.) are also aspects to not to neglect, because they could make the difference and drag attention among microelectronics industry.

1.6 Conclusions and perspectives

The research efforts made in the last 5 years demonstrated the concrete possibility of exploiting the silicon advantages (CMOS compatibility, good electron mobility and conductivity, high Seebeck coefficient, cost – efficiency, environment friendliness, etc.) to build a phononic engineered thermoelectric device which exploits the phononic properties of the nanostructured active media to reduce the naturally high lattice thermal conductivity of Si. The possibility of fabricating a Seebeck membrane generator with improved efficiency in a CMOS compatible material is proved by theoretical and experimental cited result. Thus, the boosting of the *ZT* figure of merit might be achieved by integrating into the thin film membrane a phononic crystal pattern able to further reduce the silicon lattice thermal conductivity by one order of magnitude, as previously depicted. The prospective study of a possible design is shown in Figure 1.32 were a phononic engineered membrane substitutes the plain thin film one. The heat flow directionality is meant to be further controlled by exploiting the phononic crystal patterns arrangement and dimensionality and the natural phononic dispersion curve anisotropy. The lateral generator design is of the same topology of the one designed and simulated in [40], depicted in Figure 1.14, with electrical contacts (blue metal: cold side; red dotted metal: hot side).

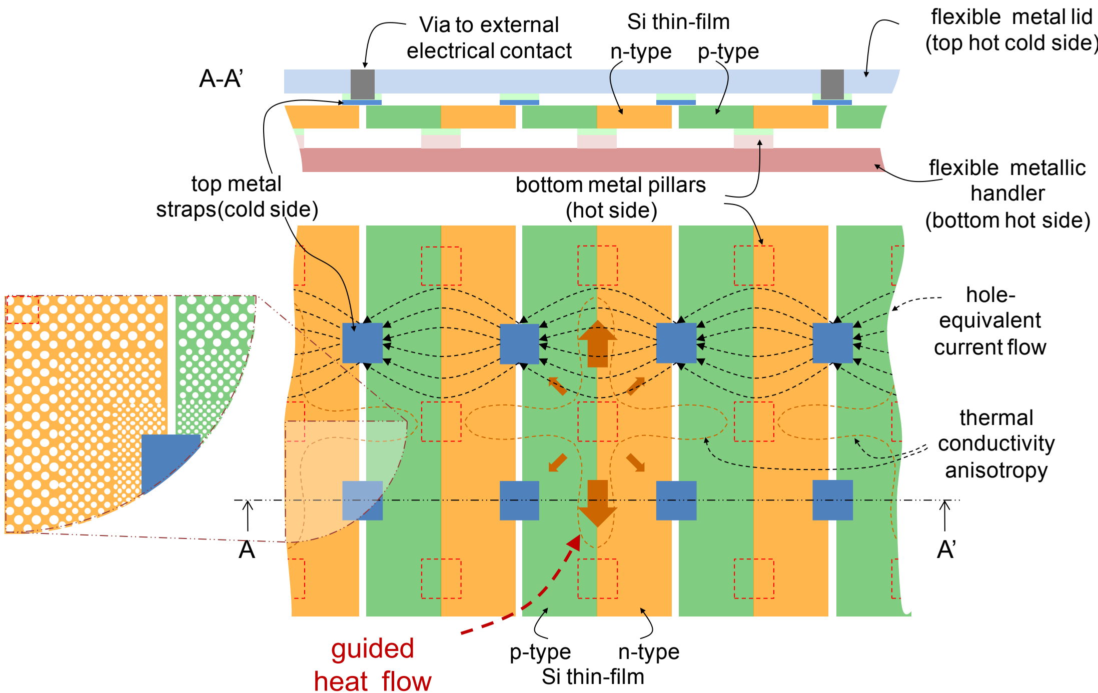

Figure 1.32 Cross section (top image) of the lateral Seebeck generators in series. Top view (bottom image) of a series of generators detailing the phononic engineered structure.

The advantages of phononic crystal patterning and the possible applications of their integration into devices are widely illustrated by different authors as shown in Table 1.7. Being sound and heat carried by phonons at different frequencies, macroscale microstructured materials are able to control and manipulate sound and hypersound (at very high-frequency sound, with f <1 GHz) frequencies, whereas to control heat, nanostructures are generally required [119]. The applicability of phononic engineered materials to thermoelectric energy harvesters has been widely and intensely studied during the last years, and expected to present the best results given the progresses recently registered. Indeed, it has been shown how the layout modifications and measurements techniques (detailed in Chapter 3 and 4) may lead to a complete metrology platform able to measure the thermal properties of nanostructured silicon devices for TE applications.

Chapter 2 **Molecular dynamics simulations**

Abstract

This chapter is devoted to a study and the investigation of the physics behind heat transfer, understanding, by means of Molecular Dynamics (MD) simulations with Green – Kubo method, how it is influenced by the atomic structure of the targeted material. Phonons are the main contributors to thermal conductivity in semiconductor and insulators, therefore, only the phonon-assisted heat conduction is described.

Considering the recent studies in the field of silicon nano-patterning for thermoelectric applications it is of great importance to reproduce the same phenomena in a simulation framework which allows the understanding of experimental results and prediction of future possible trends and achievements.

In this work, bulk, thin film membranes and phononic crystal ones in silicon have been simulated to put in evidence the impact of patterning topology on the material (and device) future performances. A comparative study has been performed, also listing the obtained results at the state-of-the-art for simulations (with same frame conditions) and experiments. Thermal conductivity reduction is confirmed for the material nanostructurations presented and paves the way for the integration of silicon into a CMOS-based thermoelectric energy converter with ameliorated properties related to the PnCs .

2.1 Introduction

The conducted study aims to establish for the first time a complete framework for Molecular Dynamics simulation of silicon nanostructured material, with the main goal of defining the guidelines to conceive and build an efficient thermoelectric device whose thermal characteristic are carefully improved with respect to the one of bulk silicon.

Recently, silicon nanostructuration techniques have been investigated from a novel point of view: thermoelectric (TE) generation. Silicon is known for being the most largely used material in information and communication technology, namely Complementary Metal Oxide Semiconductor (CMOS), but its high Seebeck coefficient, 400 $\mu V \cdot K^{-1}$ for 1.7×10^{19} cm^{-3} p-doped silicon [39], is rarely mentioned. On the other hand, silicon presents a very high thermal conductivity (148 $W \cdot m^{-1} \cdot K^{-1}$ @ 300 K) such that a sufficient heat gradient cannot be sustained across devices based on it, making silicon being a bad TE material. As an example, naturally disordered materials such as $Si_{1-x}Ge_x$ feature a 20 times lower thermal conductivity [133] and are used in high operating temperature TE generators. Considering the phonon mean free path distribution and taking into account that it is peaked around 200-300 nm for Si, it is understandable that nanoscale periodic patterning could yield to a decrease of the thermal conductivity by means of phonon confinement, interferences and scattering. The artificially induced κ modulation won't affect the electron transport, being the electron mean free path way smaller than the artificial crystal dimension (few nm at 300 K) [39].

Several works have demonstrated phononic crystals (PnC) effects in thin-films [134], nanowires [67] and holey membranes [123][122]. In 2012, Yu *et al.* published a thorough study of various silicon based nanostructures among which a periodic holey membrane exhibits the lowest conductivity around 2 $W \cdot m^{-1} \cdot K^{-1}$ (two order of magnitude lower than the bulk one) with low electric properties degradation (one third with respect to the one of bulk silicon) [135]. The developed artificial crystal, combined with an efficient membrane design integrated converter, is expected to push silicon among state-of-the-art TE materials [40]. To succeed with this goal, some challenges have to be faced. First of all, an efficient and predictive modeling tool for the correct design of the artificial material has to be established. As a matter of fact, the origin of the 100-fold reduction in the membrane phononic crystals by itself is still debated. While some authors claim that band folding effects (frequency band gaps, group velocity reduction) sometimes named "coherent effects", play a major role in thermal conductivity reduction [129], [134], [136] others state that the introduction of inclusions, which scale as the bottom of the thermal conductivity accumulation curve, is the main explanation [123], [122], [135]. Indeed, thermal phonons with mean free paths comprised between 40 nm and 40 µm account for 80% of silicon thermal conduction [132]. A second challenge to face is the limitation in computation time. Thus, the simulation of experimental-like dimensions results difficult. The simulations presented in the following paragraphs are performed thanks to the resources made available by Genci, owning the Curie supercomputer, operating into the TGCC owned by CEA (See Appendix related).

2.2 Heat transport

First of all, a proper model for heat transport mechanism and thermal conductivity analysis needs to be individuated.
Thermal conductivity is described at the macroscopic scale by the Fourier law:

$$\vec{q} = -\overline{\overline{\kappa}} \cdot \vec{\nabla} T \tag{25}$$

where $\vec{q}$ is the heat flux, $\vec{\nabla} T$ is the spatial gradient of temperature, and $\overline{\overline{\kappa}}$ is the thermal conductivity tensor. The thermal conductivity is a second-order tensor, but in case of cubic isotropy, it is reduced to a scalar. Combining Fourier's law, energy conservation equation and considering that, at equilibrium and fixed temperature, the thermal conductivity κ is not space-dependent, it is obtained:

$$\kappa \Delta T = \rho C_V \frac{\partial T}{\partial t} \tag{26}$$

where ρ is the mass density, C_v the specific heat and t the time. Those equations are the basis for describing heat transfer.
Heat transfer at the microscopic scale is described by phonon propagation. The quanta of lattice vibrations propagate under the effect of temperature gradient, which results in a local non-equilibrium distribution. This phenomena is described by the Boltzmann transport equation (BTE):

$$v_g \cdot \nabla T \frac{\partial f_t}{\partial T} = \left(\frac{\partial f_t}{\partial T} \right)_{coll} \tag{27}$$

where v_g is the phonon group velocity, f_t is the phonon distribution function, and the right-hand side term is the partial derivative of f_t. The latter term refers to the system's evolution under the influence of collision processes and can be written as the sum of an equilibrium distribution function and a fluctuating part:

$$f_t = f + f' \tag{28}$$

To simplify the difficulty of describing collisions, the single relaxation-time approximation is applied to simplify the task, in such a way to write the collision term as:

$$\left(\frac{\partial f_t}{\partial t} \right)_{coll} = -\frac{f'}{\tau} \tag{29}$$

where τ is the phonon lifetime.

Considering a detailed analysis of the relaxation time assumption for the BTE [94], we can apply the Matthiessen's rule to sum up all the contributions coming from the various collision processes, each one with its characteristic decay time.

$$\frac{1}{\tau} = \frac{1}{\tau_{ph}} + \frac{1}{\tau_e} + \frac{1}{\tau_d} + \frac{1}{\tau_b} \tag{30}$$

where τ_{ph} is the phonon-phonon scattering decay time, τ_e is the phonon-electron scattering decay time, τ_d is the phonon-defect scattering decay time and τ_b is the phonon-boundaries decay time.

In MD simulations electron-phonon scattering processes are neglected and the crystal is considered as defect-free. For a nanostructured material, the phonon-hole inclusion scattering is considered. In the case of phononic crystals the latter would be the scattering against the periodic arrangement of these inclusions.

From the Fourier's law, substituting the collision term in the BTE, the thermal conductivity becomes:

$$\kappa = \sum_{\kappa} \sum_{\nu} c_{ph} v_g v_g \tau \tag{31}$$

where c_{ph} is the phonon volumetric specific heat. The summation is over all the phonon branches ν with κ vectors in the first Brillouin zone of the lattice. At each temperature, the main parameters in thermal conductivity modulation are phonon group velocity and lifetime. Thus, a reduction of the phonon group velocity would lead to a thermal conductivity reduction. Such a result shows that it is possible to act on the phonon dispersion curve, for example creating a periodic structure typical of phononic crystals that, in turn, could be the origin of other phonon-phonon collisions, leading to a modification of their lifetime.

2.3 Green Kubo Molecular Dynamic (GK-MD)

There exist several methods to properly calculate the phonon thermal conductivity κ from atomic interaction distribution [137], [101]. The mostly cited methods are: Green-Kubo (or Equilibrium) Molecular Dynamics (GK-MD)[138], [139], Non Equilibrium Molecular

Dynamics (NMD, also known as direct method)[140], Approach to Equilibrium Molecular Dynamics (AEMD) [141], Boltzmann Transport Equation (BTE) [94] and Lattice Dynamics (LD) [101].

Thermal conductivity can be derived from the Boltzmann transport equation (BTE) as anticipated, but it requires to make assumptions over the phonon dispersion curves and/or the use of *ad hoc* semi-empirical models for the computation of phonon lifetime distribution. It is possible to calculate the band structures of PhCs by Plane Wave Expansion (PWE) and Finite Elements Methods (FEM). However, the linear elasticity hypothesis cannot account for phonon-phonon interactions that result from anharmonicity and give its finite value to the thermal conductivity [132]. An alternative methodology is Lattice Dynamics, which requires to calculate the dynamical force constant matrix that describes the interactions between atoms and the successive neighbors in the unit cell, in order to calculate the dispersion curves. At this step it is possible to compute phonon lifetimes by means of the perturbation theory and used them as input for the BTE [101]. This methodology is hardly suitable for large and complex simulation cells since the dynamical matrix has to be determined by another method first.

Considering the interest of studying a naturally periodic systems we chose to apply Molecular Dynamics with Green-Kubo method exploiting the periodic boundary conditions to our advantage. MD simulation can provide a deep insight of the mechanisms responsible for phonon transport in nanostructured materials. The method has been intensely used in studying thermal transport in nanoscale interfaces. Furthermore, it doesn't require details related to phonon-phonon interaction, because those are already embedded in the specific potential formulation. Thus, it is assumed that the system under study behaves classically (starting from Newton's second law to describe the forces exerted on the molecule by the others in the system), presents diffusive energy carrier transport and its material properties are known.

Molecular Dynamics relies on the use of an interatomic potential to solve the classical motion equations and gather statistical thermodynamic data. This method encompass all the effects of the anharmonic part of the potential. Especially, all the changes induced in the phonon lifetimes and group velocities can be described with no further assumptions. In our work we choose Molecular Dynamics combined with Green-Kubo method for predicting silicon lattice thermal conductivity. MD simulations are performed using the LAMMPS software [142], [143].

The MD approach permits to describe classically an ensemble of N-atoms, considering each one of them as a point of mass M constant, proper position $\vec{r}$ and velocity $\vec{v}$, whose motion is described by Newton's second law. For the fluctuations-dissipation theorem, at each step, the positions and velocities of each atom can be computed as function of the time and used to calculate the system thermal conductivity by Green-Kubo method:

$$\kappa = \frac{1}{3k_B V T^2} \int_0^{\infty} \langle \vec{J}(t) \cdot \vec{J}(0) \rangle dt \tag{32}$$

where V is the system volume, $\left\langle \vec{J}(t) \cdot \vec{J}(0) \right\rangle$ the heat current autocorrelation function (HCAF). The latter is averaged over a defined time span for a single simulation, then the same set is repeated for simulations with different randomized initial conditions (*seeds*).

The heat current $\vec{J}$ can be obtained from:

$$\vec{J} = \sum_i E_i \vec{v}_i + \frac{1}{2}\sum_{i,j}(\vec{F}_{ij} \cdot \vec{v}_i)\vec{r}_{ij} + \frac{1}{6}\sum_{i,j,k}(\vec{F}_{ijk} \cdot \vec{v}_i)(\vec{r}_{ij} + \vec{r}_{ik}) \tag{33}$$

where E_i is the i-th atom's energy, $\vec{v}_{ij}$ is its velocity, $\vec{F}_{ij}$ is the two-body force between atoms i and j, $\vec{r}_{ij}$ is their relative position vector, and $\vec{F}_{ijk}$ is the three-body force between atoms i, j and k. The first term in (33) corresponds to the convective heat current, and the second and third terms account for heat conduction due to two- and three-body interactions.
An exact definition of E_i only exists for pair interactions between identical atoms, but more than 30 different potential formulations have been defined considering three-body interactions such as Stillinger-Weber, Tersoff, Environmental-Dependent Interatomic Potential (EDIP) and others.

2.4 Molecular Dynamics procedure

The following section details the Molecular Dynamic Green-Kubo procedure, explaining step-by-step the strategies adopted and choices made.

2.4.1 Heat current autocorrelation function (HCAF)

Considering the preciously detailed theoretical treatment, inserting the EDIP potential in equation 33, a value of heat current is computed each s=200dt time steps by trapezoidal integration method. The autocorrelation function is then calculated (equation 32) each d=sxp=200x4000=800000dt intervals, where p is the number of correlation time windows to accumulate. A set of 25000dt dump intervals has been collected to reduce the confidence interval and assure the equilibrium for the value of thermal conductivity found.
For a precise result of thermal conductivity a closer look has to be taken to the convergence of the heat current autocorrelation function (HCAF), in such a way that the integral in equation 32 takes into account a sufficient number of accumulation time windows, until the oscillations of the HCAF are fully dumped and go to zero.
For each simulation performed, a same number of 25000dt time steps has been collected to obtain the HCAF. To individuate an appropriate accumulation time it is needed to carefully evaluate the autocorrelation function's convergence, being the thermal conductivity proportional to the area underneath.

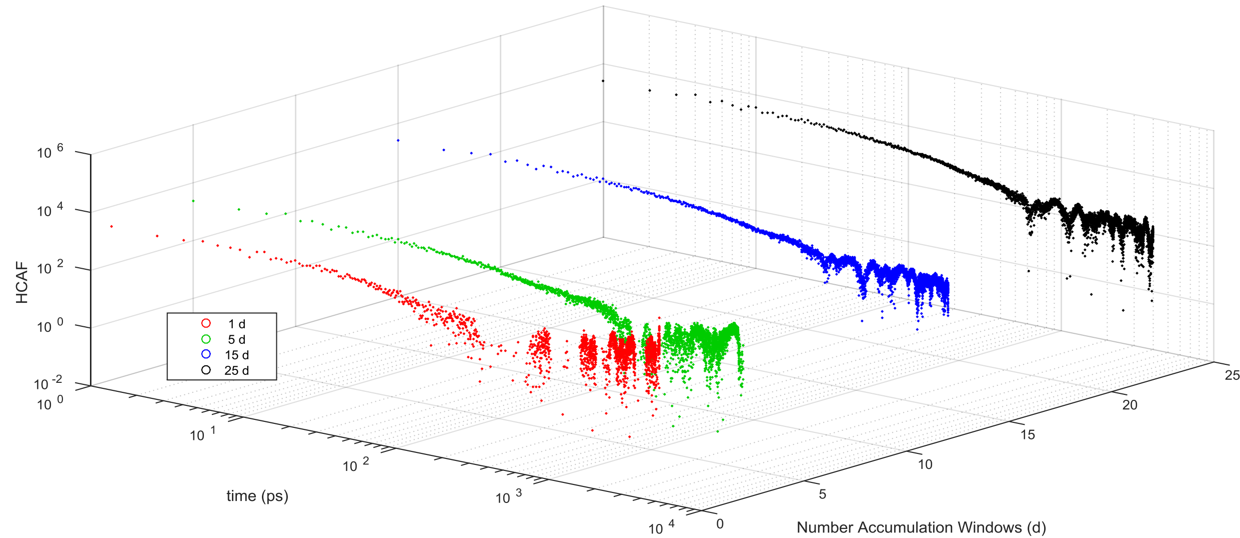

Figure 2.1 Heat function autocorrelation function for different accumulation time.

As it is noticeable from Figure 2.1 the HCAF converges already after 15 time windows *d* accumulated , 6 ns, and doesn't present significant difference with respect to the one accumulated for 10 ns (25 *d*). The red and green points in the figure are related to accumulation times of 0.4 ns (1 *d*) and 2 ns accumulated, too low to guarantee a sufficient and acceptable conversion of the HCAF.

Considering the normalized HFAC (34) of a thin film membrane, and comparing its oscillations for the x-y coupled directions with the ones of z, it is noticeable that the function oscillates around zero in a confined way along the z direction.

$$Norm_HCAF = \frac{\left\langle \vec{J}(t) \cdot \vec{J}(0) \right\rangle}{\left\langle \vec{J}(0) \cdot \vec{J}(0) \right\rangle} \tag{34}$$

The results are compared in Figure 2.2 for two different simulation *seeds* (random initial conditions) for thin film membranes. Thus, for the HCAF calculation, in the case of thin film membranes, only the x and y contribution are taken into account to properly evaluate the function convergence to zero and, consequently, the thermal conductivity κ.

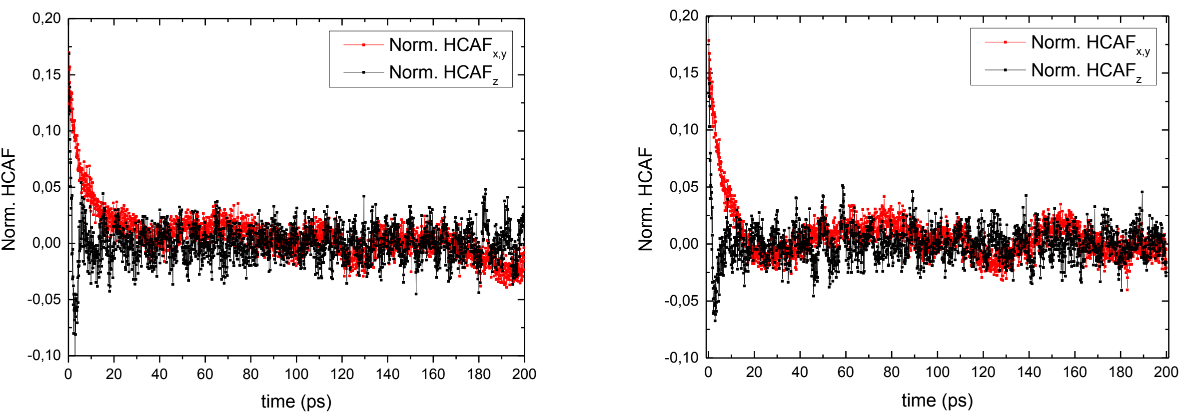

Figure 2.2 Thin film membrane at 500K with cell dimension 8x8x20 lattice constants, 2 different simulation results (different initial conditions 'seeds') showing the same behavior for the z axis.

Indeed, the value of thermal conductivity resulting from the integration of the normalized heat current autocorrelation function (Norm. HCAF) for the *z* direction, of the two *seeds* shown in Figure 2.2, is clearly around zero.

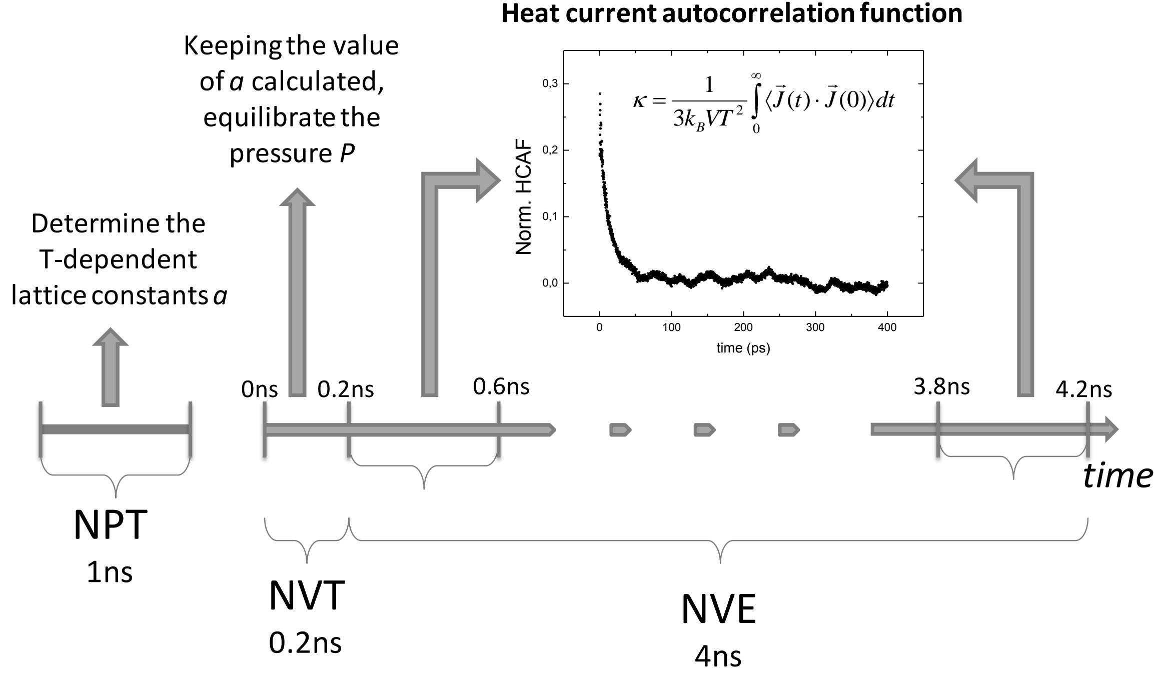

Figure 2.3 Time line showing schematically the Molecular Dynamics procedure adopted and the simulations steps and times.

Figure 2.3 details in a time-line all the simulation steps performed and described in the paragraph.

2.4.2 Cell Geometries

The simulation cells geometries are aimed at describing bulk, membrane, phononic crystal (PnC) and phononic membrane (PM) and are schematized in Figure 2.4. The bulk cell is a 8×8×8 silicon lattice constants cube with periodic boundaries in all the three directions. The cell dimension is chosen after simulating different cells and choosing the one opportune to reach the equilibrium of κ. The membrane cells are 8×8×N parallelepipeds with N=15, 20 and 30, boundaries are periodic in the x and y directions and shrink-wrapped in the z direction. The PnC cells are N×N×N boxes with periodic boundary conditions in all directions, a cylinder of radius R lattice constants depending on the size N is extruded. This cell describes a 2D N-periodic array of cylinders etched in bulk. Finally, the PM cell combines the N×N×N geometry and the shrink-wrapped condition in the z direction. The geometrical filling fraction (ff), which is a conventional comparison value for phononic structure is equal to $\pi R^2/N^2$. All the parameters (N, R, ff) are reported in Table 2.3.

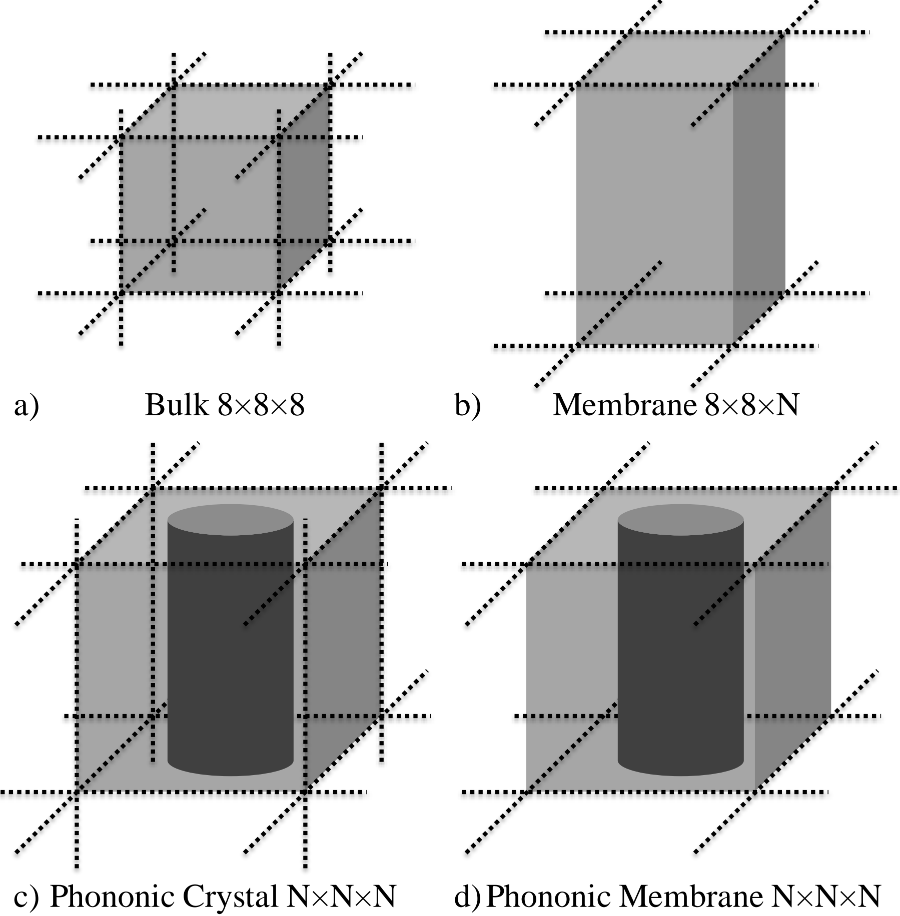

Figure 2.4 MD simulation cells used in this work to describe: a) Bulk silicon b) Membranes c) Phononic Crystals with infinite z-axis dimensions and d) Phononic Membranes. The figures X×Y×Z denotes the cells dimensions in terms of silicon lattice constants.

These dimensions were chosen as a tradeoff between reasonable computation time and meaningful dimensions. Indeed, the 15 lattice constants correspond to a thickness of 8.5 nm which is the experimental state-of-the-art for ultrathin silicon membranes [144]. However, the lateral dimensions are still low as compared to actual phononic materials for which pitch scales as 40 nm at very best [135], [105]. All the cell and dimension details are summarized in Table 2.3.

The simulation time step is 0.5 fs. A first simulation stage, using NPT ensemble with a Nosé-Hoover thermostat at T=300, 350 and 400 K and barostat at zero pressure, aims at finding the equilibrium configurations. Indeed, the interfaces introduce local stress which need to be unclenched before further analysis. During this stage, the cell dimensions are averaged in all directions until equilibrium is reached (from 5 to 10 ns) in order to determine the lattice constant at different targeted temperatures. The value obtained results in agreement with the one cited in literature (5.431 Å [145]).

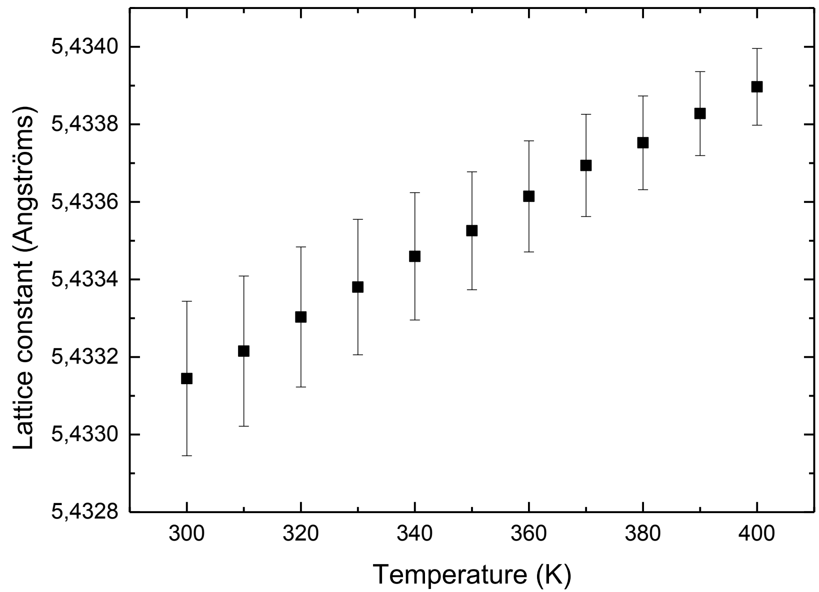

Figure 2.5 Lattice constant as funstion of the different temperature at which it is relaxed.

In the bulk case, the three dimensions are coupled to simulate a hydrostatic pressure tensor. In all other cases, since the cells have different boundary conditions along the z axis, the x and y dimensions are coupled while the z dimension is independent. Having obtained an equilibrium configuration, after the NPT stage, the velocities are then randomized following a Gaussian distribution, in order to simulate ten independent systems for each set of initial parameters and compute satisfactory statistics. An additional NVT 10 ps run is then applied before the NVE ensemble (constant number of atoms, volume and energy) is established to accumulate the heat current autocorrelation function following the Green-Kubo formalism until sufficient convergence (10 ns). More details about this methodology can be found in [146].

2.5 Molecular dynamics state of the art comparison

Several authors have computed the thermal conductivity κ for silicon, using the Green-Kubo equation with different potentials. The most commonly used potentials are Stillinger-Weber (SW) and Tersoff. Both take into accounts three-body interactions, leading to slightly different results for κ, but always consistent with the trend. Considering the different size domains and integration time, a careful analysis of the results has been performed, in such a way to compare the obtained results with the state of the art, to individuate the optimal simulation parameters.

Regarding the simulation size, a good convergence is obtained for cells of size 8 unit cells (uc). The value used is confirmed in simulations performed by Henry *et al.*[147], Schelling *et al.*[140], Sellan *et al.*[103].

Simulations are performed with SW and EDIP potentials, and compared with state of the art and experiments. In Table 2.1 and Table 2.2 are summed up and compared the results for simulations performed with SW, EDIP potentials.

Table 2.1 Results of Molecular Dynamics simulations performed by Green-Kubo method with Stillinger-Weber (SW) potential.

TEMPERATURE	Stillinger - Weber	
	κ (W.K^{-1}.m^{-1})	Author
300	350	*Goicochea et al.* [148]
	344	**This work**
500	206	*Howell et al.*[146]
	231	*Schelling et al.*[140]
	202	**This work**
1000	51	*Howell et al.*[146]
	62	*Schelling et al.*[140]
	60	*Sellan et al.*[103]
	62	**This work**

Table 2.2 Results of Molecular Dynamics simulations performed by Green-Kubo method with Environment Dependent Interatomic Potential (EDIP).

TEMPERATURE	Environment Dependent Interatomic Potential	
	κ (W.K^{-1}.m^{-1})	author
300	160	*Henry et al.*[147]
	165	Sun et al. [149]
	165.7	**This work** [105]
500	80	*Henry et al.*[147]
	81	Sun et al.[149]
	61	**This work** [105]
1000	25	*Henry et al.*[147]
	30	*Sun et al.*[149]
	31	**This work** [105]

The results in Figure 2.6 are compared with state of the art of MD simulation, for SW and EDIP potentials, and with experimental points from Glassbrenner [99] and Fulkerson [150].

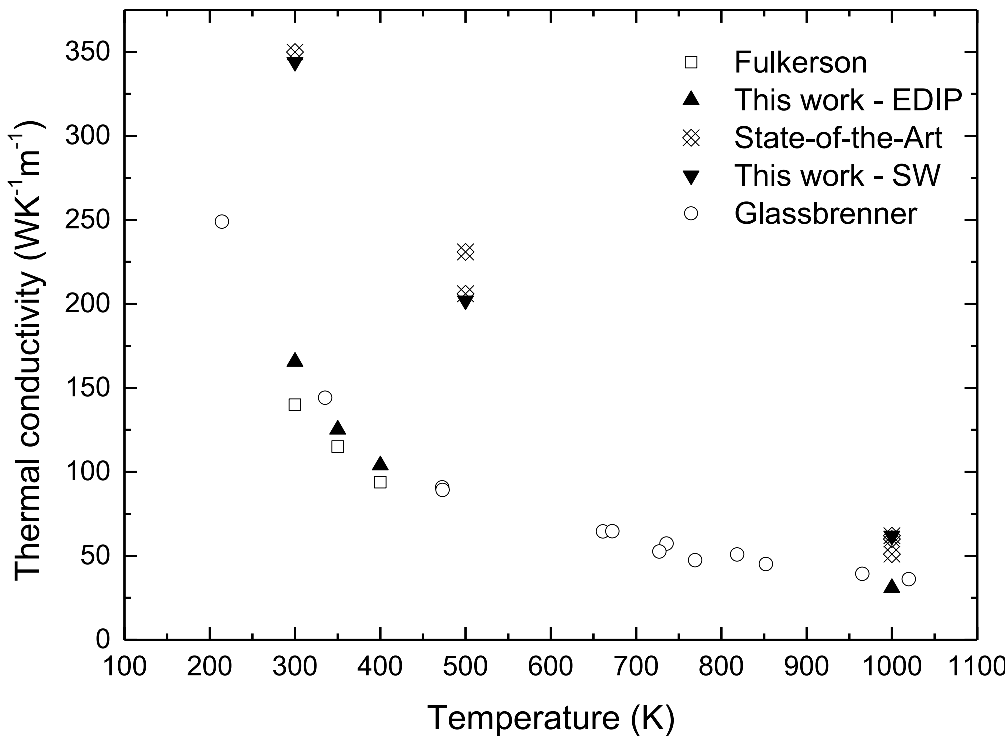

Figure 2.6 Comparison of results obtained from MD – GK with SW and EDIP potentials in our simulations and state-of-the-art ones (in Table 2.1 and Table 2.2) and experimental points from Fulkerson [150] and Glassbrenner [99].

Considering its better ability to reproduce thermal conductivity of bulk silicon with respect to other models, the EDIP potential was chosen for such simulation set. A full demonstration of how EDIP is suited to study Silicon bulk thermal conductivity is provided in [147], where the frequencies extracted from MD simulations and calculated from lattice dynamics are compared with experimental values.

2.6 Results

The simulated structures are summarized in Table 2.3 and Figure 2.8, a comparison with experimental results from [99], [150] is indicated.

Table 2.3 Cell dimension, filling fractions and results MD simulations thermal conductivity at 300K.

Type / Boundaries	Size N	Radius R	*ff* (%)	κ (W/m/K) *p p p*	κ (W/m/K) *p p s*
Bulk 8×8×8	-	-	-	165.7	-
Membrane 8×8×N	15	-	-	-	44.9
	20	-	-	-	54.2
	30	-	-	-	59.3
PC & PM N×N×N	15	3	12.6	19,8	12,0
	15	4	22.3	9.51	7.22
	15	5	34.9	5.76	4.11
	15	6	50.3	2.24	2.36

The data in Figure 2.8 are fitted according to the model described by the power law for thermal conductivity of semiconductors [68]:

$$\kappa = \kappa_{300K} \left(\frac{T_0}{T} \right)^{\alpha} \tag{35}$$

where κ_{300K} is the thermal conductivity at T_0 = 300 K. Equation (35) has been plotted using the coefficient α= 1.65 from Palankovski's work [151], whose study's results are reported in Figure 2.7.

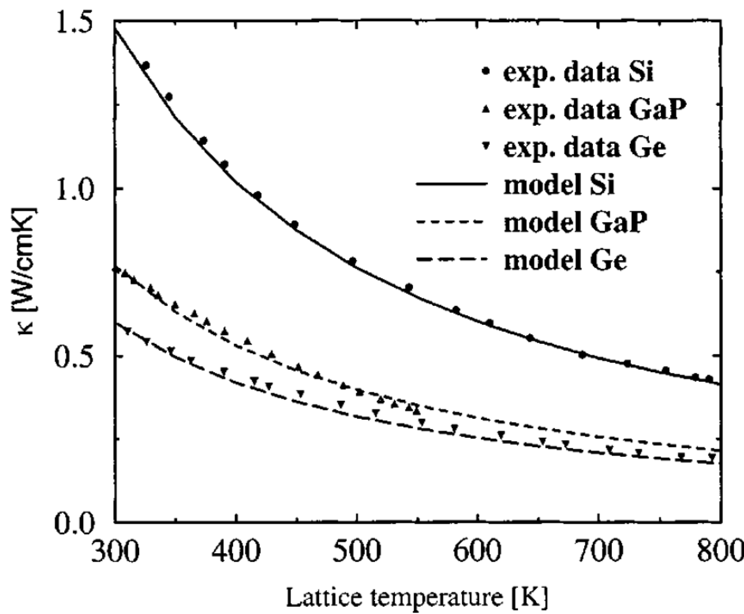

Figure 2.7 From Palankovski *et al.* [151], comparison between experimental data and models for Si, Ge and GaP for thermal conductivity as function of the lattice temperature.

A good agreement between simulation and the developed model is obtained for bulk (see Figure 2.8). For the membranes and phononic crystals the accordance remains within the error bars. With the temperature increase, an effect is clearly seen that flattens the thermal conductivity curve. This effect is remarkably known for low dimensional structure [89] and it is accounted for by the simulation procedure. A precise fitting of the results is possible by tuning down the α coefficient as shown in Figure 2.8. The value of α is governed by the third and fourth order anharmonic part of the potential [152], so the procedure provides information about the way in which the structure dimensionality affects anharmonic processes.

A decrease of thermal conductivity is shown in Figure 2.8 from bulk to thin film geometry (44.9 $W.m^{-1}.K^{-1}$) and phononic crystal geometries (5.76 $W.m^{-1}.K^{-1}$). It is noticeable that, despite the phononic crystal being infinite along the z axis (periodic boundary conditions applied), this configuration achieves a 30 times reduction of κ with respect to bulk. The same order of magnitude is obtained for all phononic crystals whatever the pitch. This result supports several experimental observations of reduced thermal conductivity in relatively thick silicon membranes [122] and is of great relevance for practical use in the framework of micro-integrated thermoelectric devices [40], [147]. A further reduction is registered for periodically patterned membranes (4.11 $W.m^{-1}.K^{-1}$) which underlines that both these effects can cumulate in such systems. This last finding is of great relevance because it takes into account and

evaluate the respective contributions of the thin film geometry and the phononic structure with no need for further hypothesis or *ad hoc* parameter.

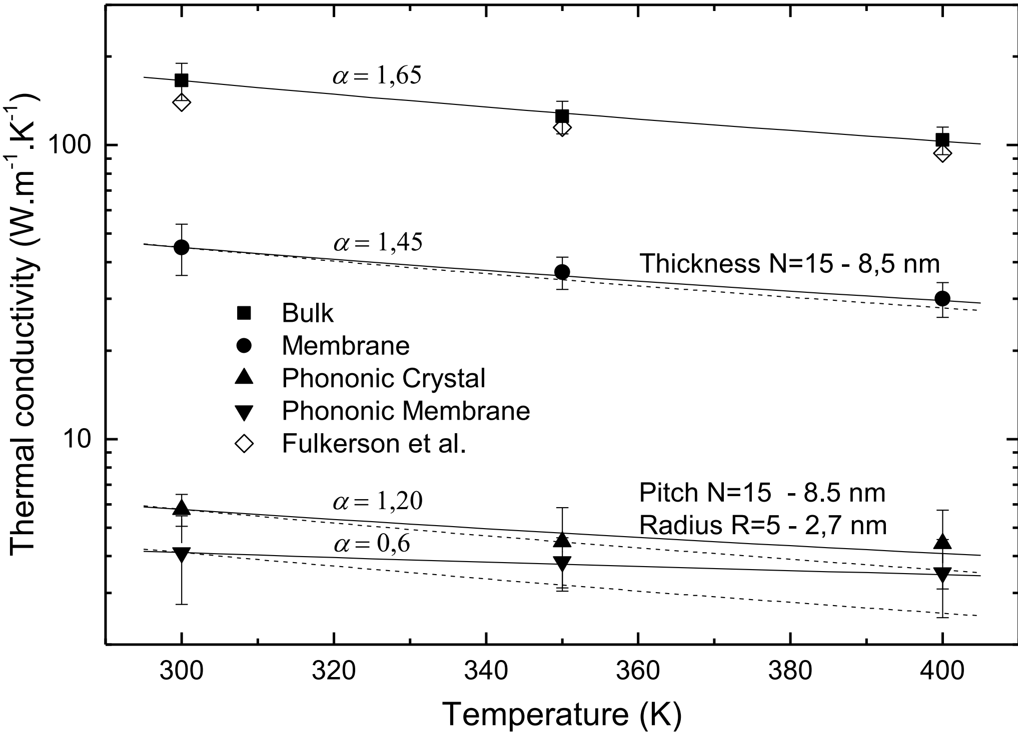

Figure 2.8 Simulated thermal conductivity by MD Green-Kubo as a function of temperature (plain symbols). The results are fitted according to the power law in equation . A comparison experimental results from [150] is shown.

Figure 2.9 shows detailed results for plain membranes, confirming that the thermal conductivity decreases reducing the membranes' thickness. The common explanation presented is that phonon confinement effects and surface scattering phenomena limit the phonon mean free path. This trend is reproduced using the Fuchs-Sondheimer model [150], [68]:

$$\kappa_{membrane} = \kappa_{bulk} \cdot \left(1 - \frac{3(1-p)}{2\delta}\right) \cdot \int_1^{\infty} \left(\frac{1}{\xi^3} - \frac{1}{\xi^5}\right) \cdot \frac{1 - e^{-\frac{t}{\Lambda}\xi}}{1 - pe^{-\frac{t}{\Lambda}\xi}} \cdot d\xi \qquad (36)$$

where t is the thickness, Λ = 300 nm the mean free path at 300 K [21] and p = 0.75 the fraction of phonons specularly reflected at the boundaries.

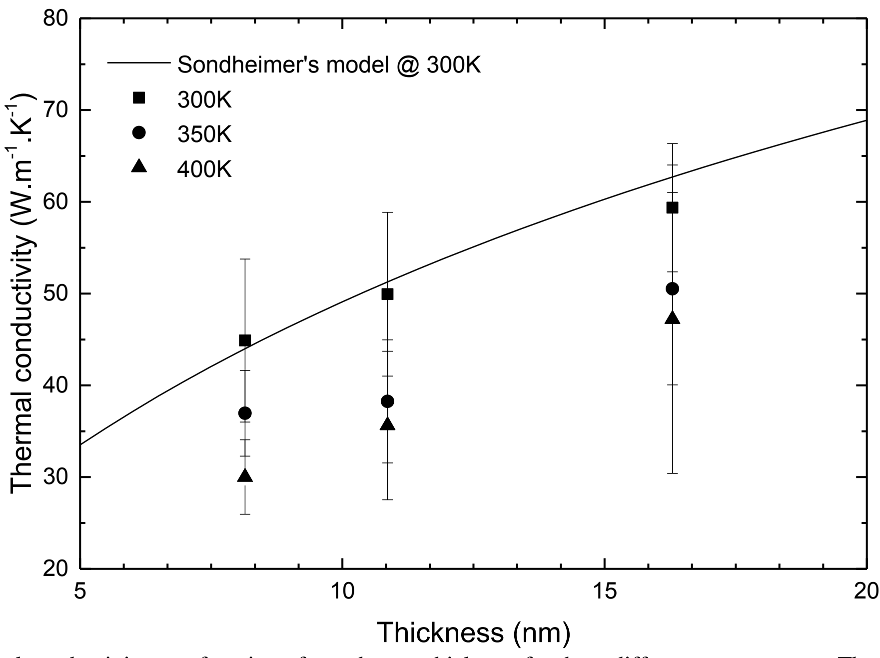

Figure 2.9 Thermal conductivity as a function of membranes thickness for three different temperatures. The results for 300 K are fitted using the Fuchs-Sondheimer model [110], [111] for a mean free path of 300 nm and a value of the specularity parameter p = 0.75. The value of p chosen is in agreement with calculation and experimental measurements [134].

In Figure 2.10 the effect of periodical patterning on the thermal conductivity are evidenced. It is interesting to notice that increasing the filling fraction (enlarging the enclosures, decreasing the *neck size*) a further reduction of κ is registered. The Green-Kubo methodology provides quantitative information from a statistical analysis and it doesn't discriminate the microscopic processes leading to the conductivity reduction. The commonly cited effects producing a reduction of the thermal conductivity are: band gap opening, group velocity reduction due to band folding and increased diffusion on boundaries. Band gaps usually arise in the lower frequency range of the band folded dispersion curves. Thus, even a pitch as low as 8.5 nm would not produce a gap above 1 THz. It is unlikely that the structures studied here exhibit any phononic band gap. Furthermore, the consequence of local disorder (defects) in the periodic structure is the introduction of propagating modes dragged in the band gap and would reduce its efficiency. Another common interpretation is given in terms of reduced limiting dimensions (neck size - distance between two consecutive holes) of the structure [132]. Indeed, as the radius increases, the space between two enclosures forms a bottleneck. The reduced *neck size* entails an increase of scattering events and the consequent decrease of the phonon mean free path. Finally, the mostly cited effect provoking a 2-order of magnitude decrease of κ is the band folding and flattening due to the Brillouin zone shrinking, related to the artificial crystal periodicity [132].
The “phononic” effect is considered as the hinder of phonon transport by means of the thin-film confinement, the cylindrical holes inclusions and the cumulative contributions of these two structures. In this extent, the procedure doesn't discriminate between periodic "coherent" effects and diffusive effects, for which a specific simulation framework is required.

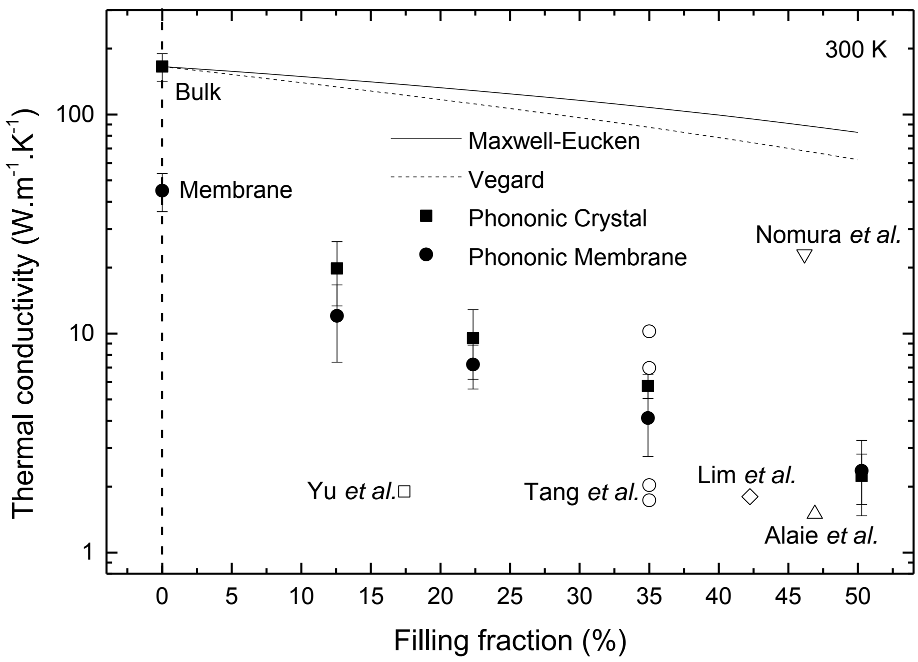

Figure 2.10 Thermal conductivity as a function of filling fraction *ff* for periodic patterns in bulk (squares) and thin film membranes (circles) at 300 K. Maxwell-Eucken and Vegard models of porous media are indicated and clearly show that phononic engineering is far more efficient than the sole material removal effect. A comparison to several experimental results from literature is shown [135], [123], [130], [129], [127] (white symbols).

Considering the results' order of magnitude, a reasonable matching is exhibited with respect to findings of Yu *et al.* (1.9 $W{\cdot}m^{-1}{\cdot}K^{-1}$) [135], Tang *et al.* (from 1.73 to 10.23 $W{\cdot}m^{-1}{\cdot}K^{-1}$) [123], Lim *et al.* (1.8 $W{\cdot}m^{-1}{\cdot}K^{-1}$) [130] and Alaie *et al.* (1.5 $W{\cdot}m^{-1}{\cdot}K^{-1}$) [129], even though little discrepancies hold between experimental and simulated results.
Taking into account the simulation cell dimensions, being limited by computational availability, the discrepancies between experiments and the systems studied in the paper are justifiable.

2.7 Conclusions

Finally, we can remark that the Green-Kubo MD methodology using the EDIP potential reproduces confidently the reduction of thermal conductivity of nanopatterned silicon. Furthermore, the results highlight the suitability of MD toward quantitative comparison to experimental values. The methodologies does not require any assumption on the phonon distribution and the transport mechanism and it is demonstrated to reproduce different experimental trends such as temperature and dimensionality effects which permit to shed light onto the thermal transport in nanoscale systems. The results underlay that the phononic structure effect accounts for a significant part of the thermal conductivity reduction with respect to the thin film geometry one. This fact is in agreement with several experimental works and it is of crucial importance for application in designing thermoelectric devices.
Interestingly, all the other effects that could be introduced to refine the simulated cell should further hinder the phonon transport and reduce the thermal conductivity.

In a future perspective, disposing of a higher computation time, the simulation of bigger system is envisaged along with the design of cells not perfectly periodic to study the influence of periodicity on thermal conductivity reduction.
Another aspect to consider is that, for temperature lower than Debye's one, quantum effects may occur, Green-Kubo methodology provides a classical description of specific heat for those temperature ranges, then slightly overestimates the thermal conductivity and could be compensated by quantum corrections. Those corrections would improve the agreement between simulation results and experimental ones.
Other factors that lead to a thermal conductivity reduction and not simulated in this work are: defects, impurities, isotopic composition and surface native silicon dioxide.

Appendix - THE CURIE SUPERCOMPUTER

The simulations were performed thanks to the resources offered by Curie supercomputer, owned by GENCI and operated into the TGCC owned by CEA . It is the first French Tier0 system open to scientists through the French participation into the PRACE (Partnership for Advanced Computing in Europe) research infrastructure. Curie is offering 3 different fractions of x86-64 computing resources for addressing a wide range of scientific challenges and offering an aggregate peak performance of 2 PetaFlops. Curie Thin nodes machine has 5040 B510 bullx nodes, and for each node: 2 eight-core Intel® processors Sandy Bridge EP (E5-2680) 2.7 GHz, 64 GB, 1 local SSD disk. The processors are 10080 eight-core x Intel® Xeon® Next Generation, for a total of 80640 cores.

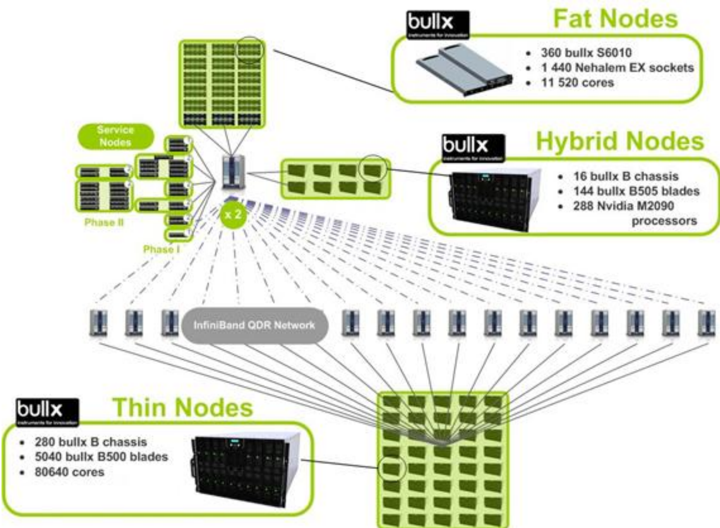

Figure 2 Schematic description of the Curie supercomputer at the CEA.

The computational time they supplied us is of 50000 hours, and it allowed us to run all the simulations to achieve our goal for the article published [105].

Figure 2.11 Photo of the Curie supercomputer at the CEA.

Chapter 3 **Device design and fabrication**

Abstract

The aim of this third chapter is to describe the methodology developed to realize phononic engineered suspended metrology platforms. My focused objective is to measure the thermal conductivity using different strategies depicted in the following section.

The first part of this chapter will deal with the study of the relevant methodology to realize dense patterns with a very high resolution and a low defect level. A particular emphasis is put on the following process steps: the lithography technique and the etching methodology. After investigating the different options, it is shown that phononic crystals (PnCs) are best patterned with a combination of *'dots on the fly'* lithography and Cl_2 reactive ion etching (RIE).

The second part of the chapter details the different steps necessary to realize the suspended metrology platform, integrating the phononic engineering processes with the technique developed by our group for the suspension of thin film plain membranes [112].

The whole fabrication process is satisfactorily developed for different device generations (different geometries) and presents a remarkable reliability and repeatability in the realization of all the steps.

3.1 Phononic Crystals (PnCs) patterning

Previous chapters have highlighted the effect of periodically patterning the thin film membrane to further reduce the thermal conductivity in silicon, preserving the electrical one and globally increasing its thermoelectric efficiency.

The patterning of highly dense and defects-free phononic crystals represents the main challenge for the fabrication process of such a periodically arranged structure. The dimension of the repetition period, the so-called 'artificial' lattice constant or pitch of the phononic crystals is established by two parameters: the phonon wavelength (λ ~ 2 nm) and its mean free path (Λ_{ph} ~ 100 nm). To guarantee an efficient reduction of the thermal conductivity κ without affecting the electrical one σ_{el}, the pitch has to be larger than the electron mean free path (Λ_{el} ~ 2-3 nm) at room temperature. In such a way the scattering of the acoustic phonons by the period array of inclusions is promoted without leading to a sensible degradation of σ_{el}, as demonstrated by Yu *et al.*[131]. Indeed, phonons that most contribute to the thermal conductivity have a wavelength in 1–100 nm range. Thus, the period repetition a is fixed by phonon parameters to values in the range of tenths of nanometres.

The main variables to tune during the fabrication process are the lithographic electron-beam (e-beam) impinging dose, the resist minimum resolution and etching parameters (concentration and pressure of reactive gas in the chamber as well as power and time).

Firstly, to achieve the best resolution and sensitivity, different electron beam lithography methodologies have been explored, and will be depicted in the next subparagraphs. Secondly,

to ensure an efficient pattern transfer, several Reactive Ion Etching (RIE) recipes and techniques have been tested and will be further described.

3.1.1 Electron Beam Lithography methodology

Electron beam (e-beam) lithography allows achieving a very high pattern resolution, without the need of hard masks and without resorting to complex mask fabrication, thereby enabling short optimization loop. Still the low writing speed and relatively high cost represent a drawback of the methodology from an industrial applicability point of view. Taking into account those considerations, different e-beam lithography techniques [153], [154] have been explored to fabricate dense enclosures and to find the best efficiency in terms of writing time, cost and pattern resolution.
Although limited by proximity effects and low throughput, e-beam lithography can reach the desired resolutions for dense and very small-pitch patterns to open regular arrays of cylindrical holes on the silicon surface.
The critical dimension (CD) in optical lithography is described by the Rayleigh equation $CD = k\lambda / NA$, where k is a numerical factor, which depends on the state-of-the-art and the used tool, λ the wavelength of the light and NA the numerical aperture. In the same way, a quality factor for the EBL could be described as *k·(spot size)*, where the spot size is the diameter of the Gaussian beam.
The selected resist for PnCs patterning is the positive-tone ZEP 520, which assures high resolution and sensitivity, high stability in time and good plasma etch resistance [155]. The pattern transfer through the film of ZEP 520 (positive resist by ZEON Corp. [156]) is realized by Cl_2 chemico-physical plasma anisotropic etching (30 sccm, 30 W, 5 mTorr, Plasmalab System 100, Oxford Instruments). The resist is developed with ZED N-50 [157] and cleaned with a 20 min double bath of PG Remover [158], preceded by 10 min of UV light exposure.

3.1.1.1 Conventional Method and "Overdosage" trick

The first methodology is based on a classical use of the electron beam lithography with the aim of writing highly dense periodic enclosures closely spaced. In a conventional method, a grating equivalent to the beam step size (BSS) of the machine is designed. Indeed, each dot is corresponding to a shape and one pixel. By the fact that every dot is considered one shape, the machine's pattern generator is called for every step and thus for every dot. The electron beam impinges on one dot, and after, making use of the main field deflection, moves to the following ones. The sketch of this adopted strategy is shown in Figure 3.1.

Figure 3.1 Right: sketch of a conventional layout design; left: after exposure. Normally, shot pitch is small and fills up the drawn pattern.

To reach very high pattern resolutions, we use the trick of *"overdosing"* the square patterns sized at a minimal 2 x 2 nm^2 BSS of the e-beam equipment Vistec EBPG 5000+ [159]. The electron dose ranges from 50000 $\mu C/cm^2$ to 150000 $\mu C/cm^2$ using a current of 300 pA.

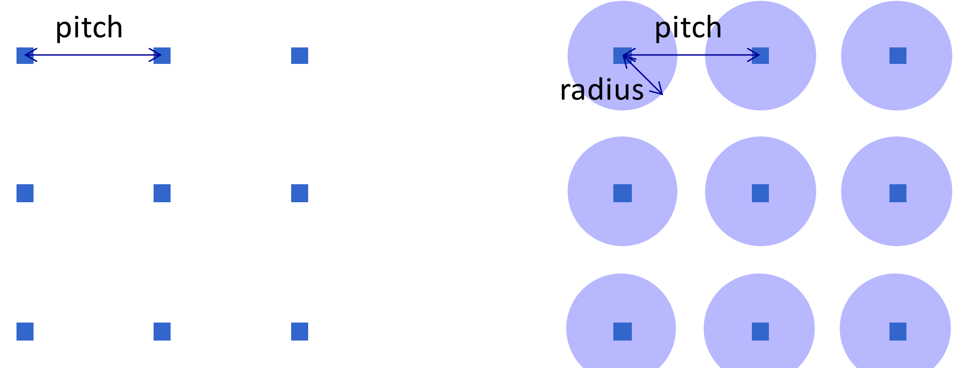

Figure 3.2 On left: sketch of a conventional layout design with minimal squares (1BSS = 2 nm), to perform the "overdosage" technique; on right: after exposure, the high dose entails the opening of a circular area larger than the designed one.

The electron beam size is estimated to 10 nm according to the aperture of 400 µm. The resulting exposed area features circular patterns of diameter directly related to the electron impinging dose. Following this principle, it is possible to achieve very dense and highly resolved patterns, as depicted in the sketch in Figure 3.2. The drawback is represented by the exposure time, which is dramatically high for large area dense patterns and centimetre to wafer-scale writings. The respective dimensions of the BSS, pitch and beam size are summarized in Table 3.1 in subparagraph 3.1.1.3.
Figure 3.3 shows the results related to the methodology calibration, analyzing the diameter achieved as function of the desired pitch for different doses. As expected, for lower pitches, proximity effects entail a larger diameter, which further increase as the electron dose increases.

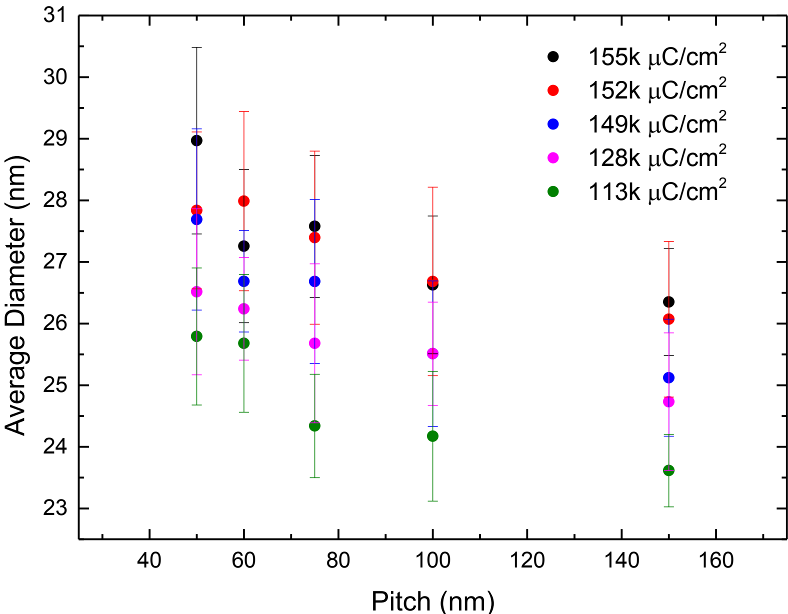

Figure 3.3 Average diameter as function of the pitch for the investigated doses. It is shown how increasing the impinging dose contributes to enhance the diameter of the enclosures.

In Figure 3.4 (left), it is presented an example of pattern regularly opened for a pitch of 44 nm and a dose of 77000 μC/cm² using the *'overdosage'* technique. The dose is sufficient to open regular and dense patterns. In the right figure the same pitch has been targeted to be written, but with a dose of 152000 μC/cm² this time. Clearly, the dose is too high and proximity effects lead to the over exposure of the resist, destroying the pattern regularity.

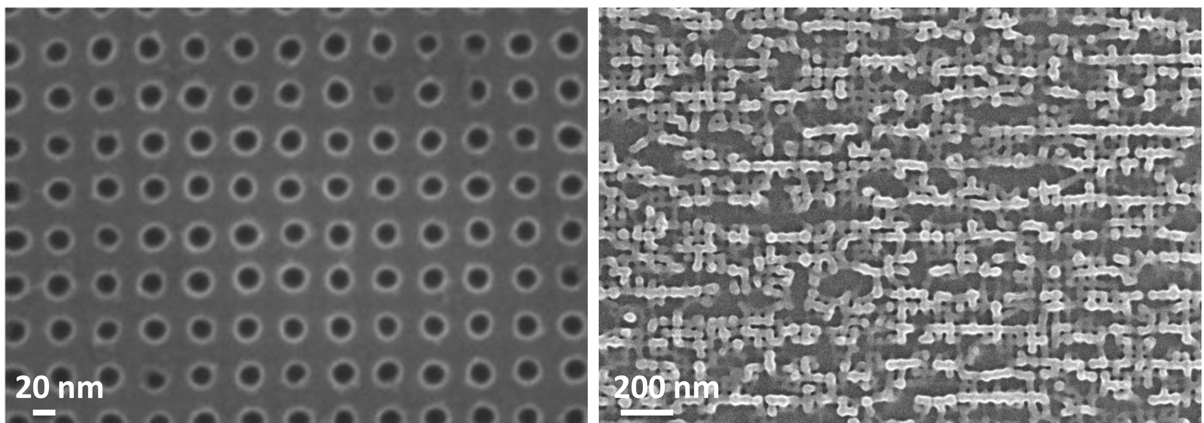

Figure 3.4 SEM images of periodically patterned enclosures for two different electron doses chosen: left : dose of 77000 μC/cm², the patterns appear regular and well featured, and right: dose of 152000 μC/cm², the electron dose is too high, patterns are destroyed.

This kind of study has been repeated for different pitches in a range of doses between 50000 μC/cm² and 150000 μC/cm², in order to identify the right dose to select, considering the trade-off between low dose (lower porosity, smaller diameter) – high dose (high porosity, high diameter, risk of merging holes and breaking of the periodicity).

Figure 3.5 shows the different pitches opened with the methodology described. It is interesting to notice how it is possible to reach minimal dimensionalities as low as the actual state of the art for the used resist [155] and realize patterns with a repetition path of 38 nm (Figure 3.5, a).

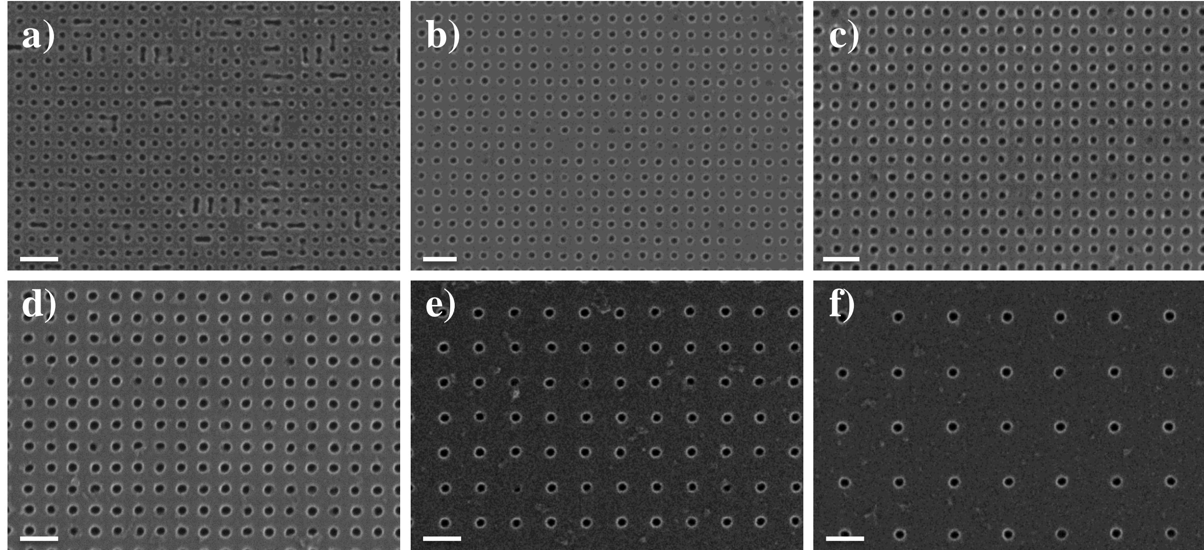

Figure 3.5 SEM images of different pitches written with the *overdosage* method (different doses in order to achieve the best writing quality): a) 38 nm, b) 44 nm, c) 50 nm, d) 60 nm, e) 100 nm, f) 150 nm. Scale bar is 100 nm.

3.1.1.2 Dots on the fly

The second investigated approach, sometimes referred to as ‘‘dots on the fly’’ (DOTF), aims to get rid of the time limitations imposed by the pattern generator, improving the lithography throughput. The methodology relies on increasing the BSS up to the desired pitch, using higher currents (10 nA) and lowering the electron dose (10–80 μC/cm^2) in order to obtain regularly spaced pixels. The minimal doses to provide the lithography machine sufficient to open the features are indicated in Figure 3.6. Each pixel corresponds to the distance between the dots. Indeed, the *trick* is to draw a simple geometry (i.e. a large square pattern) Figure 3.**7** (left), so as to generate the pattern only once, but to not to provide it the sufficiently high dose and small BSS to perform the desired writing of the full feature. The image obtained appears as a *“pixelization”* of the desired object. The technique works because the electron beam size is about 12 nm for the required current, whatever the BSS.

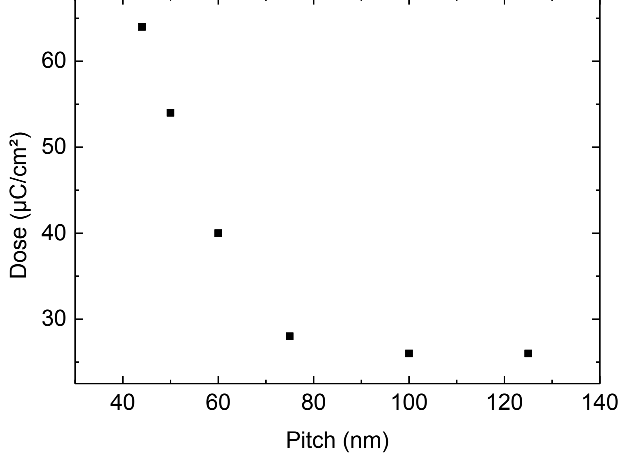

Figure 3.6 Minimal dose required to open the pitch for the DOTF technique.

The number of electrons per surface unit in a single dot has to be constant for higher doses once the shape diameter is equal (or higher) to the spot size [160]. For smaller diameters the amount of electrons per area unit is higher. Indeed, for lower pitches the required dose is higher because, having a BSS equal to the pitch (and almost no proximity effects (PE)), a higher number of electrons is required to impinge in order to open denser patterns. This behaviour is opposite with respect to the one registered for the conventional and *'overdosage'* techniques. Indeed, for those massive proximity effects and high doses entail the opening of smaller pitches with lowest doses, to avoid the PE degrade features (Figure 3.4, right).

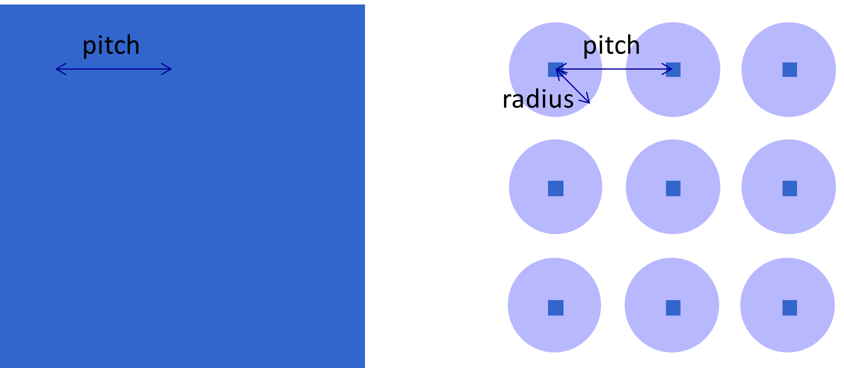

Figure 3.7 On left: sketch of a conventional layout design for the DOTF technique (one object), to perform the *"dots on the fly"* technique; On right: after exposure, the low dose entails the opening of a circular area, but does not allow the writing of the full squared pattern.

Following this approach, a sensible increase of the writing speed is obtained and the fabrication of highly dense and resolute PnCs patterns (Figure 3.7, right) is possible. The only drawback is represented by the shape of the design area, which is limited to rectangular arrays of dots within a single exposure step. To build different complex geometries, several layouts and steps need to be aligned.

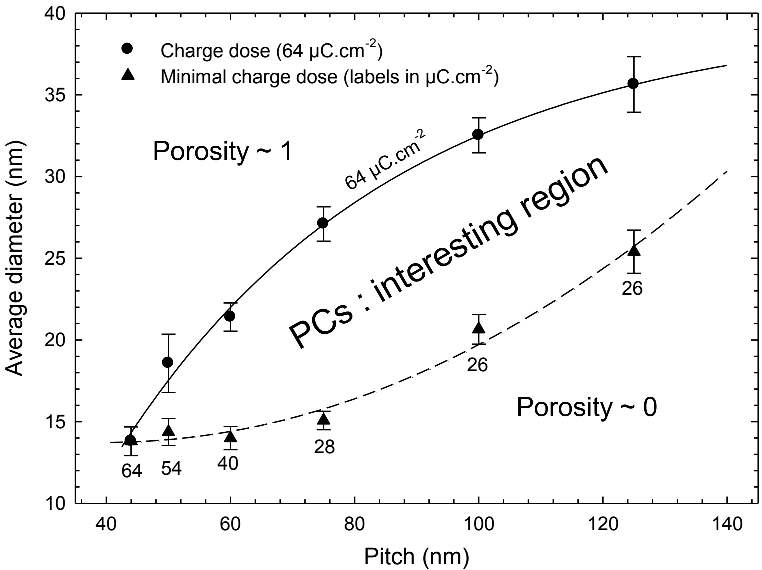

Figure 3.8 The "dots on the fly" trends for diameter versus pitch are plotted. The lower curve represents the diameter opened for each pitch by the lowest possible efficient dose. The upper one is plotted for the higher dose (64 μC/cm²) tested, sufficient to open all the pitches.

Exploiting the advantages of this technique is possible to establish the lithography guidelines to write very high resolution patterns at the limit of the resist minimal resolution. The ZEP resist used presents a minimal resolution of 14 nm.
Indeed, in Figure 3.8, the diameters of holes are plotted as a function of pitches for two different doses: an arbitrary medium-high dose (64 μC/cm²) and the minimal required dose over the impinging area to open the holes (which varies depending on the pitch desired). The collected data enlighten the presence of a region in between the experimental curves where the patterns are precisely opened. The point reached for a dose of 64 μC/cm² for the minimal pitch, corresponds to a minimum diameter of 14 nm. The graph clearly shows how it is possible to adjust the machine dose in order to open features for targeted characteristics (diameter / pitch). Of course, lower doses are sufficient to open the largest pitches. Increasing reasonably the dose, the diameter is consequently increased (i.e. Figure 3.8, points for pitch of 125 nm for dose at 26 μC/cm² and 64 μC/cm²).

3.1.1.3 Conclusions

An analytical MATLAB model developed to consolidate the results confirms the experimental trends and estimates the enclosures optimal diameters. Beam shape, electrons diffusion, proximity effects and pattern periodicity were taken into account to correctly simulate the proximity effects. The electron beam is assimilated to a Gaussian distribution. The model provides useful guidelines to predict holes diameter depending on the parameters previously cited. In such a way, it is possible to perform an *a-posteriori* analysis starting from the desired characteristics of the pattern to be designed.
Proximity effects are responsible of the holes enlargement for the lithography techniques, mostly for the *"overdosage"* technique. The complexity of the analysis lies in the simulation of the periodical patterning methodology and the different estimation of the dose for surface unit for the two techniques.
The code considers a grid of 400 points in x and y directions and centres the electron beam at the (0,0) vertex, which is considered the center of the hole. Therefore, a Gaussian function is centered at the same point and the dose is accumulated considering the proximity effect contribution of the first 5 neighbours (37).

$$I = \int_{surface} A \cdot Dose \cdot e^{-r^2/w^2} \tag{37}$$

where the matrix *Dose* is firstly filled accumulating the different contribution of the 5 close neighbours for all the grid points. The beam full amplitude is centred on the grid vertex and expressed in μC/cm², *r* is the distance of influence of the considered close neighbour from the point established as the centre of the hole, *w* is the waist parameter of the beam and *A* is the global dose amplitude.
The difference for the two methodologies stays in the global dose amplitude for surface unit *A* evaluation and it is depicted in Figure 3.9. For the *overdosage* method, it is considered to be the effective machine high dose impinging, which is selected and focused on a square with the same dimensions of the BSS of 2 nm. The high dose, the proximity effects, the beam shape and diameter entail the opening of the desired circular feature. For the *DOTF,* the dose

considered to open the enclosure has to be weighted by the surface unit of interest, considering the correspondent amount necessary to write a defined feature of known diameter and pitch (equal to the BSS).
For the *dots on the fly* methodology, to respect the same dose delivered to a given surface for each pattern, we calculated the dose range according to the following equation:

$$\alpha = \frac{\beta \cdot \left(\frac{L}{BSS} \right)^2}{L^2} = \frac{\beta}{BSS^2} \tag{38}$$

The dose over area α is calculated. The number of squares (of side BSS) contained in the designed layout square of side L is multiplied by the dose impinging on a single circle pattern and divided by the total area (layout square). Fixing the dose β (around 15k μC), it is therefore possible to calculate the dose that we have to use for each BSS.

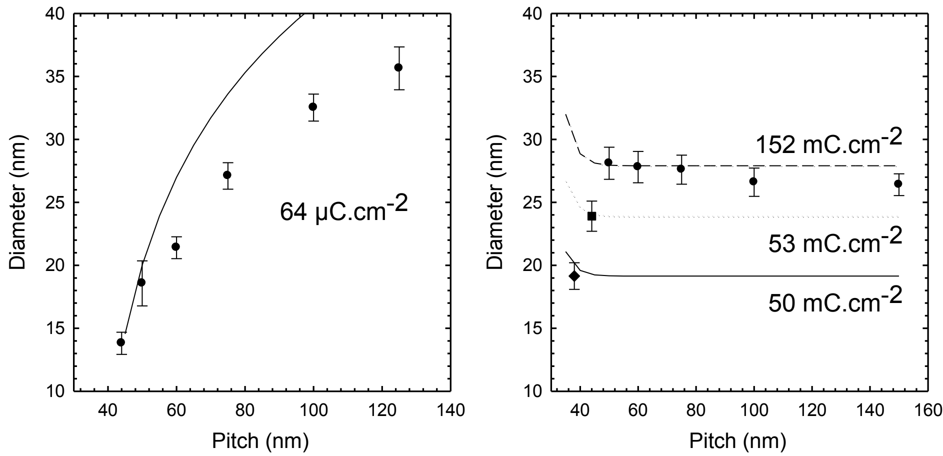

Figure 3.9 Diameter of the cylindrical holes as a function of the pitch a for the ''dots on the fly'' (left) and the conventional methodology (right).

A good agreement is reached between the experimental results and the simulated ones, demonstrating the correct modelling of the key parameters determining the holes diameter. Considering the dots on the fly strategy (Figure 3.9, left) the model overestimation is due to the fact that no defects are simulated in the film to obstacle the electron path nor backscattered electrons are considered. Thus, the real diameter dimensions are reduced by these factors which are not taken into account in this model. For the conventional method, it can be observed that, lower doses over the enlightened area are required to open smaller pitches (38 and 44 nm) to avoid the influence of massive proximity effects, which expose intensively the resist, causing breaks in the patterns or extremely high porosity.
A Monte Carlo simulation has been performed with Sceleton™ (Synopsis®) to have a better insight into the electrons spread inside the resist layer and individuate the optimal waist parameter.

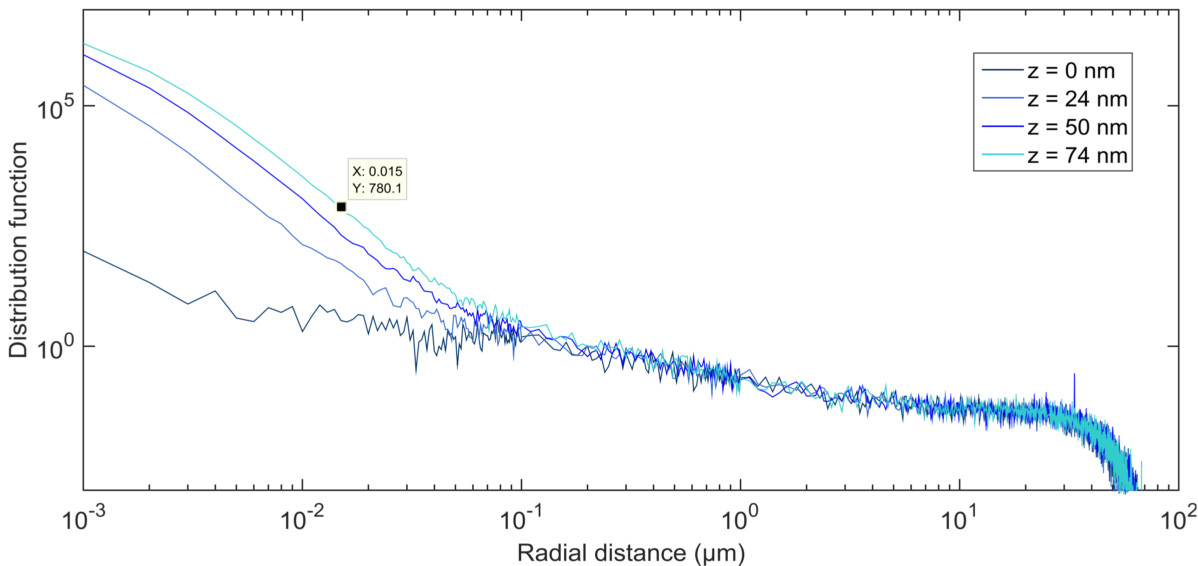

Figure 3.10 Scheleton simulation to evaluate the waist parameter to consider for analytical simulations at different resist depths *z*.

The simulation has been run considering a stack of layers corresponding to the one used for the electron beam lithography. The electron energy is 100 keV and the number of traced electrons is 2 millions. The applied mesh is 1 nm for the lateral direction and 2 nm in the vertical direction. Different vertical sections have been extracted at a depth of 0, 24, 50, 74 nm.
The waist parameter corresponds to the value at which the distribution function of the electrons in the resist drops of a value of 1/e. The correspondent waist at 1/e is 15 nm, which is consistent with the minimal resolution achievable with the used ZEP520A resist (ZEON CHEMICALS, [156]) and the minimal diameter we succeeded to open. The effect of impinging electrons in the resist is cumulated differently depending on the investigated methodology, considering the specific machine beam step size (BSS) and the electron-beam impinging dose. The dose accumulation contribution is neglected after a distance of 5 neighbours (5 lattice constants *a*).
The strategies described are summarized in Table 3.1 with a comparison between the diameter of the obtained cylindrical holes and the respective optimal electron doses as a function of the pitch *a*.
The main advantage presented by '*dots on the fly*' relies on the sensible increase of the surface writing speed to values 3 orders of magnitude larger when compared to the average speeds for the previous method (from 10^{-5} cm^2/min up to 10^{-2} cm^2/min). There are three main components of writing time: shape time, beam time and stage time. Shape time is the required one to write individual shapes on a vector scan tool and includes disk read time and beam settling time. By using the DOTF strategy, this contribution can be reduced to zero. Beam time is the time to effectively expose the resist. Making use of higher currents results in a decrease of the writing time [153]. Furthermore, using a resist which requires lower writing doses (as ZEP520, instead of PMMA), the beam time is further reduced. Stage time is the one needed to move the stage from one field position to the successive one and it is dependent on the field size. Larger is the field, lower is the stage time and higher the beam deflection. Anyways, too high deflection lead to a loss in beam quality and therefore in the pattern

resolution. Finally, the decrease in writing time is mainly attributed to the suppression of the electron beam blanking time for the DOTF methodology, leading to a considerable hardware time reduction. Indeed, the dose per pattern only depends on the resist intrinsic contrast curve, thus it is equal for both the approaches. However, in this case, the gain resulting from current variation is at the best of a factor of 33 (10 nA vs. 300 pA), while the total difference between the two methods is of three orders of magnitude.
The analytical behaviour of the exposure time required to write the patterns is given by equation (39):

$$time = \frac{Dose \cdot A \cdot ff}{I} \tag{39}$$

where *time* is the exposure time needed to write the patterns, *Dose* is the minimal dose in µC/cm², *ff* is the filling fraction of the exposed area equal to $\frac{\pi r^2}{(pitch)^2}$ with *r* the average radius of the enclosures and *I* the required writing current.
The potentialities of the DOTF technique have been investigated to explore resolution limits and optimal doses for different pitches.

Table 3.1 Comparison of lithography techniques: : conventional overdosing the pixel area and *"dotf on the fly"*.

Method	Overdosing a pixel area	"Dots on the fly"
Resist	ZEP 520, positive resist, 80 nm	
Dose	High (~130000 µC/cm²), lower for small pitches, focused on a BSS² spot	Very Low (~50 µC/cm²), increasing with pitch.
Current	Very Low (300 pA)	High (10 nA)
Writing speed	Very Low, 10^{-5} cm²/min	High, 10^{-2} cm²/min (no e-beam blanking time)
Layout		
Latent Image		
Etching	Cl2 plasma etching: 30 sccm, 5 mTorr, 30 W	

3.1.2 Reactive Ion Etching of phononic patterns

The next step to improve the feature resolution and achieve dimensionality as low as possible with respect to the phonon mean free path is the definition of a proper etching technique. Two methodologies have been explored to find the best pattern etching results.
It is necessary to point out that, after trials with PMMA resist (EL13%MAA8.5%), the ZEP 520 [155] was presented as the best resist solution for its high sensitivity (from 2 to 10 times higher than the PMMA). Indeed, lower voltages and xylene based developers (n-Amyl Acetate, commercially ZED-N50 [157]) permit to achieve the greatest sensitivity. Furthermore, the chosen resist features a very good stability in time (no resolution loss after 6 months), higher plasma etch resistance (from 2 to 4 times better than PMMA for C_2F_6 or SF_6 gases, due to the α-methylstyrene group) and it has a comparable (or better) resolution with respect to PMMA. The latter, in fact, presents lower sensitivity and poor etch resistance and it is not compatible with Chlorine-based etchants.

3.1.2.1 *SF_6 + Ar recipe*

This etching recipe has first been tested to etch dense periodic patterns making use of PMMA resist and the conventional lithography technique. The etching parameters are depicted in Table 3.2.

Table 3.2 Etching recipe for SF6 + Ar

SF_6 rate	Ar rate	Pressure	Power	Etch Rate
10 sccm	10 sccm	3 mTorr	30 W	70 nm/min

The tool used for the etching is a reactive ion etching (RIE) Plasmalab system 80plus Oxford [161]. Having chosen the ZEP 520 resist, the pattern resolution and wall slope were observed to be more degraded for this recipe with respect to the one depicted in the next paragraph. Despite the achievement of the same pitches for the two recipes, the etch selectivity between ZEP and silicon is lower. Accounting for their effect, chlorine etching has been selected given its better etching anisotropy (see next subparagraph).

3.1.2.2 *Cl_2 recipe*

Chlorine etching presents a better anisotropy according to a higher physical component. Furthermore, it is compatible with ZEP, but it forms non-volatile components that redeposit if performed over PMMA resist. The etching parameter set for the process are indicated in Table 3.3.
The tool used for the etching is a reactive ion etching (RIE) Plasmalab System 100 OXFORD [161].

Table 3.3 Etching recipe for Cl_2.

Cl_2 rate	Pressure	Power	Etch Rate

10 sccm	5 mTorr	30 W	50 nm/min

3.1.2.3 Conclusions

Given the better quality of the Chlorine etching approach, this solution has been selected and combined with the high resolution of ZEP. Following this strategy, periodical and dense enclosures with minimal pitches are patterned. Figure 3.11 shows two examples of patterned enclosures with minimal dimensions. It could be noticed that the 38 nm-sample still presents few defects due to the merging of adjacent holes. It is due to the fact that the minimal resist resolution has been reached and that the dose could be slightly decreased to avoid proximity effects.

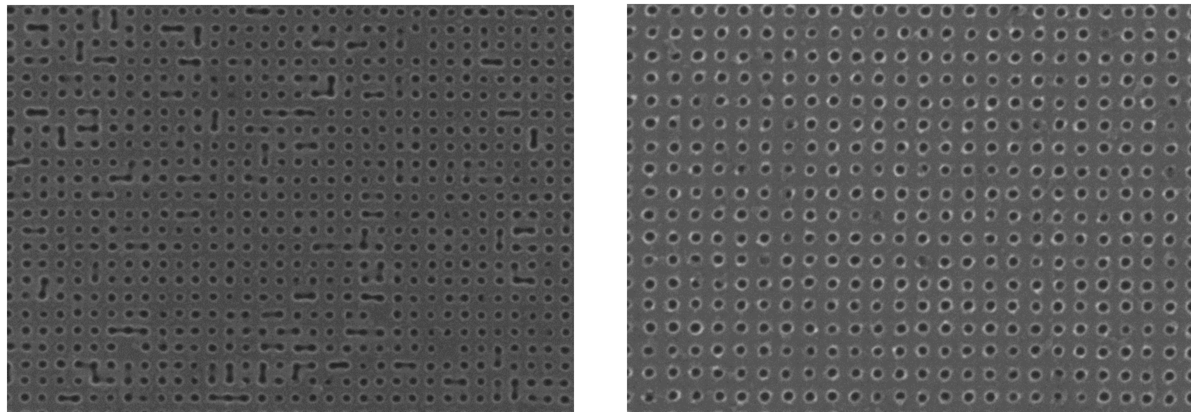

Figure 3.11 SEM images of samples etched by Cl_2 recipe: 38 nm pitch (left), 44 nm pitch (right).

3.1.3 Patterning results and conclusion

The complete fabrication of a phononic periodic patterns on silicon for the integration into the devices presented in the next paragraph has been performed combining the listed advantages of the *dots on the fly* lithography methodology and the capabilities of chlorine reactive ion etching (RIE).

The achieved results show very high resolution and dense patterns in silicon-on-insulator (SOI) substrates. Being the substrate used for the devices a SOI [162] with 145 nm of buried oxide (BOX) and a 72 nm silicon layer (SOI), the necessary resist mask to ensure a complete opening of the enclosures and an efficient masking of the underneath silicon layer, presents a thickness of 170 nm, as measured by profilometer and ellipsometer.

The spin coated resist is, as anticipated, ZEP 520A, diluted with Anisole (solvent, in a ratio 1:0,5). The determined recipe is 1800 revolutions per minute (rpm) speed, 1000rpm/sec acceleration, for a duration of 15 seconds.

Being a thicker resist than the one used to test the methodology capabilities and performance, the expected results in terms of best achievable resolution will be worse. Thus, the minimal pitch opened for such resist and SOI thicknesses is limited to 50 nm.

Table 3.4 Description of the phononic patterns fabrication process on SOI.

Step description	Parameters

Step description	Parameters
ZEP520 spin coating	1800 rpm, 1000 rpm/sec, 15 sec
Electron beam Lithography	*Dots on the fly* technique
Development	ZED-N50, 1 min
Etching	Cl_2 30 sccm, 5 mTorr, 30 W, ER_{Si}: 50 nm/min
Resist stripping	20 min UV exposure, Remover PG @65°C 30 min

3.2 Integration of PnCs into suspended membranes

After describing the full pattern fabrication process of phononic crystals and the different methodologies tested, the device fabrication process is illustrated hereinafter.

Substrate

The used substrates for the fabrication of the device are purchased from SOITEC [162]. The stack is composed of a SOI layer of 72 nm (p-doped with B, and resistivity between 14 and 18.9 Ω·cm), a BOX of 145 nm and a 800 µm – Silicon substrate, p – doped.

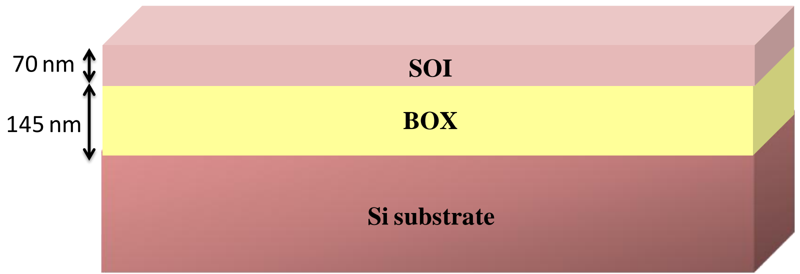

Figure 3.12 Stack of the wafer used for the process. SOI layer is 70 nm, BOX layer is 145 nm.

Wafer cleaning

The SOI wafer purchased are 8 inches and cut by laser. The protective resist layer used for the cut needs to be removed before starting the process. The removal process consists in a preliminary exposure under UV for 20 minutes to soften the cross-linked resist. Successively, 2 baths of Remover PG [158] at 65 °C of 20 minutes and 60 minutes respectively are performed, both followed by Acetone and IPA rinse and nitrogen blow drying (Table 3.5).

Table 3.5 Description of the wafer cleaning steps, before starting the fabrication process.

Step description	Parameters
Shipping resist removal	UV exposure, 20 min Remover PG @65°C 20 min, acetone, IPA, dry Remover PG @65°C 40 min, acetone, IPA, dry
Piranha cleaning	$H_2O_2 : H_2SO_4 = 1:1$, 10 min
HF wet etching	HF 5%, 1 minute

The cleaning of all the organic residues off the substrate is performed by piranha wet etching, a 1:1 mixture of sulfuric acid (H_2SO_4) and hydrogen peroxide (H_2O_2) for 10 minutes. After this step, the removal of native oxide from the silicon surface is performed by wet Hydrogen fluoride (HF) 5% diluted in water, for 1 minute.

Markers

After wafer cleaning, the first step to carry out is the patterning of markers for the future alignment of the layers to write. The resist used for the process is MMA copolymer [163] (MMA(8.5)MAA, formulated in the solvent ethyl lactate (EL13%)) and the writing is performed by electron beam lithography. The used tool is a VISTEC EBPG5000PlusES [159] (the same for all the successive lithography steps) installed in the cleanroom facility of the IEMN. Table 3.6 summarizes the steps to perform. Firstly, the resist is spin coated and post-baked for the following e-beam lithography.

Table 3.6 Description of the markers lithography process.

Step description	Parameters
Spin coating	MAA8.5EL13% : 1000rpm, 1000rpm/sec, 12sec Post bake, rump up: 80°C for 2', 100°C for 2', 140°C for 2', 180°C for 10'. Thickness: 1.8 µm (mechanical profilometer)
Markers lithography	Dose 500 µC/cm², Current 25nA, Resolution 0,025µm
Resist developing	MIBK:IPA=1:2, 1 min
Markers etching	SF_6/Ar=10sccm/10sccm, 30W, 10 mTorr : SOI etching (1 min) CF_4/N_2/O_2=40/40/5 sccm, 100 W, 10 mTorr : BOX etching (14 min) SF_6/Ar=10/10 sccm, 30W, 10 mTorr : Si etching (about 12 min)
Resist stripping	UV exposure for 20 min Remover PG @65°C 40 min, acetone, IPA, dry

Figure 3.13 shows the layout for the alignment markers. The four crosses are used to align the sample horizontally and vertically with the optical microscope before inserting in the lithography machine. The microscope is combined with a x-y positioning systems indicating the coordinates of the spotted points to set as markers in the lithography machine. The coordinate systems are regulated to match to each other. Furthermore, the optical microscope is provided with an interferometric laser for checking the tilt of the wafer on the holder.

In Figure 3.13, the numbered squares are the layer markers. Each one is related to a layer which will be written during the successive lithography steps. Two of them are back up markers just in case a lithography needs to be repeated. The square in the top right part of the layout is used as end point detection window to detect, by laser interferometry, the end of the etching process, in other words, the moment when the last layer (in this case the silicon substrate) has been fully etched and the process stopped.

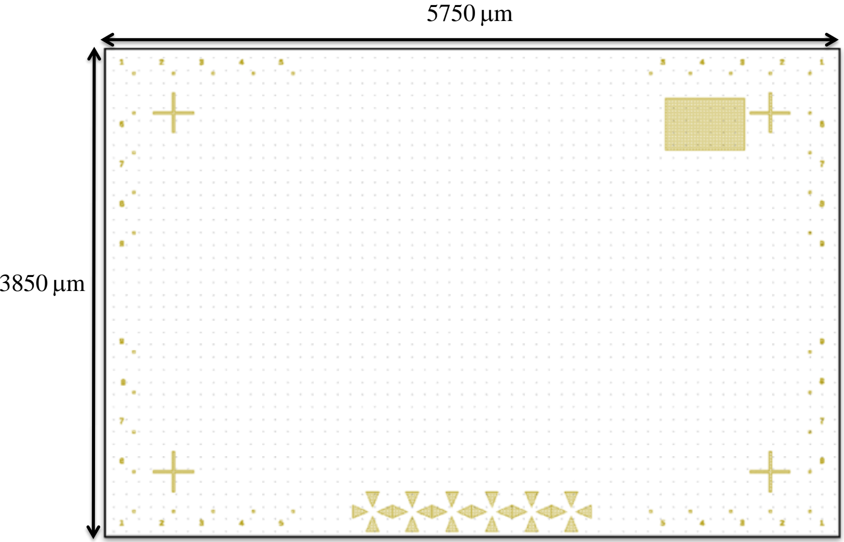

Figure 3.13 Layer marker's layout in L-Edit [164].

After e-beam exposure, the development is performed and the markers are subsequently etched by Reactive Ion Etching with the recipe listed in Table 3.6. The markers need to be deep enough to be clearly visible during the successive lithography steps, in order to correctly align all the layers. To succeed, it is opportune to perform an etching down through the 70 nm-SOI, 145 nm-BOX and few micrometers deep into the substrate.
The etching is performed in a Reactive Ion Etching apparatus (Plasmalab 80plus OXFORD [165]) and monitored by mean of an end point detection system. Indeed, the DC bias potential is monitored, while holding the RF power constant. Considering that the voltage-power dependence is related to the chemistry of the plasma, a change in their relationship occurs when the plasma contribution from the etching layer is no longer present. Thus, the intensities of spectral lines emitted from the plasma change when the etching layer is totally removed. A camera with an integrated laser apparatus is pointed and focused on the end point detection square (in Figure 3.13) and, by interferometry, indicates the changes in reflection due to the different layers etching and the etch rate. The intensity of the laser reflected off a thin layer oscillates. Oscillations occur because of the phase interference between the light reflected from the outer and inner interfaces of the etching layer, which has to be optically transparent to observe it [166].
The etching curve can also be simulated using KinMod (Kinetic Modeller, by HORIBA Jobin Yvon SAS [167]), knowing the different layers etching rate, thickness and refractive index. The tool allows to predict the etching curve shape, in such a way to stop the process at the opportune moment. Simulating the markers etching, the curve obtained is the one shown in Figure 3.14.

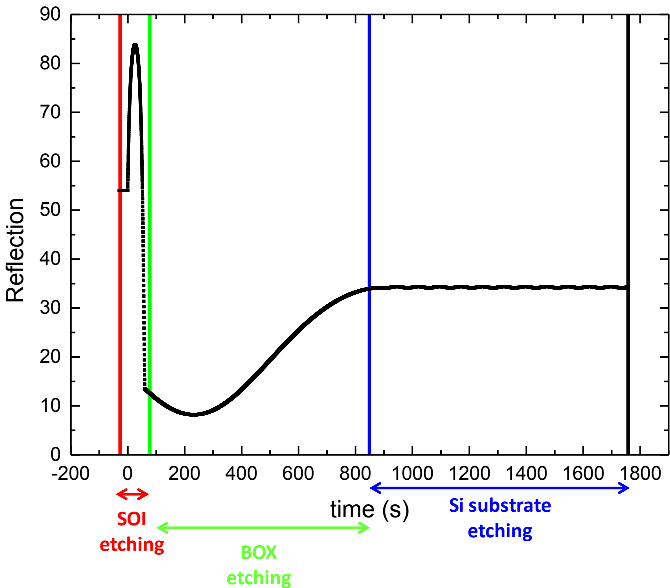

Figure 3.14 Markers' etching curve simulated by KinMod [167].

The etching curve obtained by laser interferometry is detailed in Figure 3.15.
The etching process is detailed in Table 3.6. Before the introduction of each gas in the chamber, a pumping step of 1 minute is performed. Successively, a purge step lasting 20 seconds is launched to fill up the chamber with the required gas (without applying RF power) to recondition it.

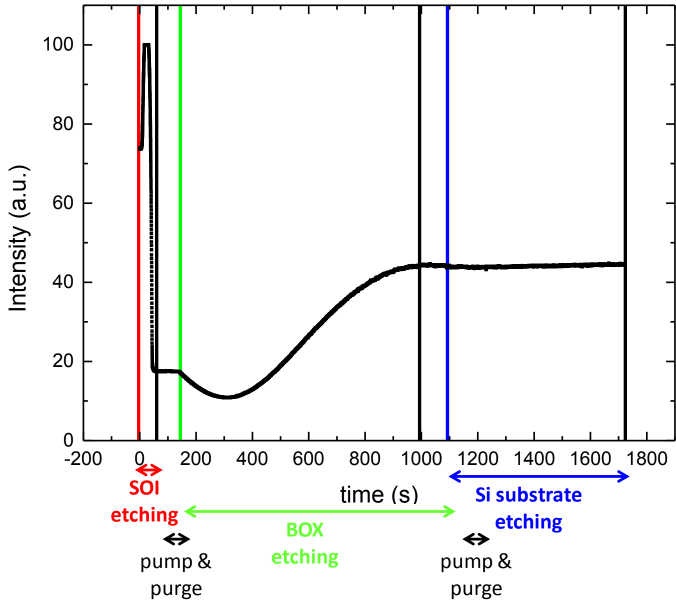

Figure 3.15 Laser interferometry graph of the etching process for the markers.

For the etching of the superficial SOI layer the recipe used is SF_6 10 sccm mixed with Ar 10 sccm. The etching rate is well controllable, being of about 70 nm/min. After the pump and purge steps, the etching of the BOX is performed by CF_4 40 sccm, N_2 40 sccm, O_2 5 sccm with an etch rate of 10 nm/minute (about 14 min totally). The following etching, always preceded by pump and purge steps, is performed again by a mixture of SF_6 and Ar (same parameters as before) to engrave markers deep in the silicon substrate (about 12 min).

As it could be noticed from Figure 3.14 and Figure 3.15 the curves' profiles are very well in accordance. It has to be pointed out that the pump and purge steps are not simulated in KinMod.
The resist is removed performing an UV exposure (20 minutes) and 1 bath of Remover PG at 65 °C for 1 hour.
Mechanical profilometer differential measurements, performed before and after resist stripping, indicate a markers depth of 1.5 μm.

Phononic Crystal patterning
As detailed in section 3.1, the phononic crystals (PnCs) patterning is a crucial step of the device fabrication. The different methodologies have been investigated and analyzed to achieve the best results in terms of pattern resolution, density, etching and time. For the reason listed in the dedicated paragraph 3.1.1.2, the chosen technique of lithography is the *dots on the fly* and the selected electron beam resist is ZEP 520.

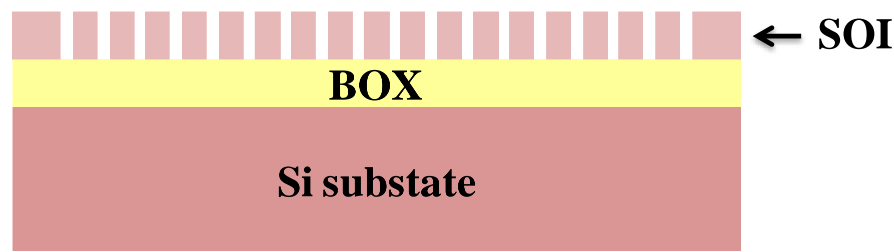

Figure 3.16 Schematic of the patterned SOI with the periodic enclosures.

Regarding the presented device, the patterns are designed exclusively on the suspended membrane. On each device, the cells are reproduced in a grid of 4x4. The SEM images in Figure 3.17 below show the patterned enclosures on the membranes (not yet suspended at this process step). The pitches are 50 nm, 55 nm and 60 nm. The etching is performed with Cl_2 and the resist removed with the same recipe listed in the section 3.1.2.2.

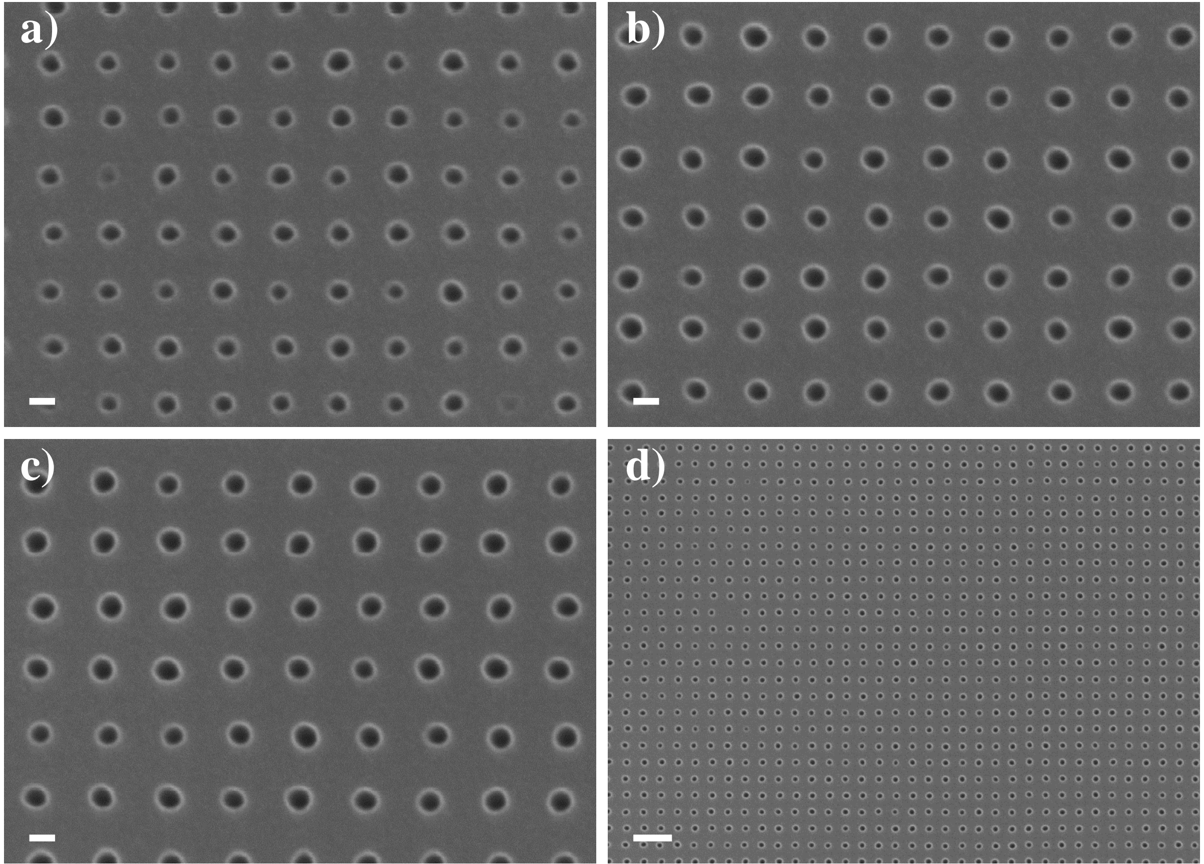

Figure 3.17 SEM images of different pitches for the device presented: a) 50 nm, scale bar of 20 nm ; b) 55 nm, scale bar of 20 nm ; c) 60 nm, scale bar of 20 nm ; d) 60 nm, scale bar of 100 nm.

SiO_2 and SiN deposition

The thermal oxidation step to obtain 12 nm - thick SiO_2 thermal oxide is processed in wet ambient at 850°C. It is necessary for the following etching of the SiN to act as a sacrificial etch stop layer for the SiN removal process. Thus, the wet SiO_2 works as etch stop layer. The oxidation, preceded by a HF wet etching to remove the native silicon dioxide (naturally growing on silicon surfaces when exposed to air), is performed in a horizontal furnace tube. Firstly, N_2 is introduced at a temperature of 500°C with a rate of 2 l/min. Secondly, the temperature is ramped up for 35 min at the same rate up to a temperature of 850°C. The successive step is the oxidation. O_2 is introduced at a rate of 1.5 l/min and H_2 with a rate of 2.5 l/min. The temperature is kept constant at 850 °C for 6 minutes. The last step is the ramp down, from 850 °C to 500 °C under N_2 flow at 2 l/min.

To assure electrical insulation from the underneath SOI layer a low stress 100 nm - thick SiN layer is deposited by low pressure chemical vapour deposition (LPCVD) in a horizontal tube furnace at 800°C and a pressure of 100 mTorr. The gases used for the process are: SiH_2Cl_2 20 sccm and NH_3 10 sccm reacting in the following way:

$3\ SiH_2\ Cl_2\ (g) + 4\ NH_3(g) \rightarrow Si_3N_4(s) + 6\ HCl(g) + 6\ H_2(g).$

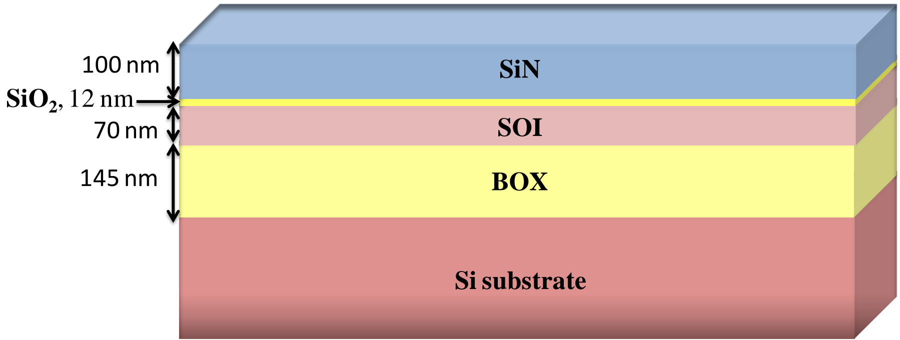

Figure 3.18 Stack of the described wafer after the silicon oxidation and SiN deposition.

Furthermore, the covalent bonding between low-stress SiN_x and Si pads results in a low thermal resistance at the SiN_x/Si interface, and consequently the continuity of the thermal conductivity measurement is improved. The SiN layer could also act as a mechanical support layer in the case of a fragile layout. This is the case of the first device's design generation, which will be depicted in the next chapter.

Cavities

Once the stack is ready, the process of cavities opening can start. The objective is to etch access cavities to be able to fully suspend the SOI membranes during the last steps of this fabrication process.

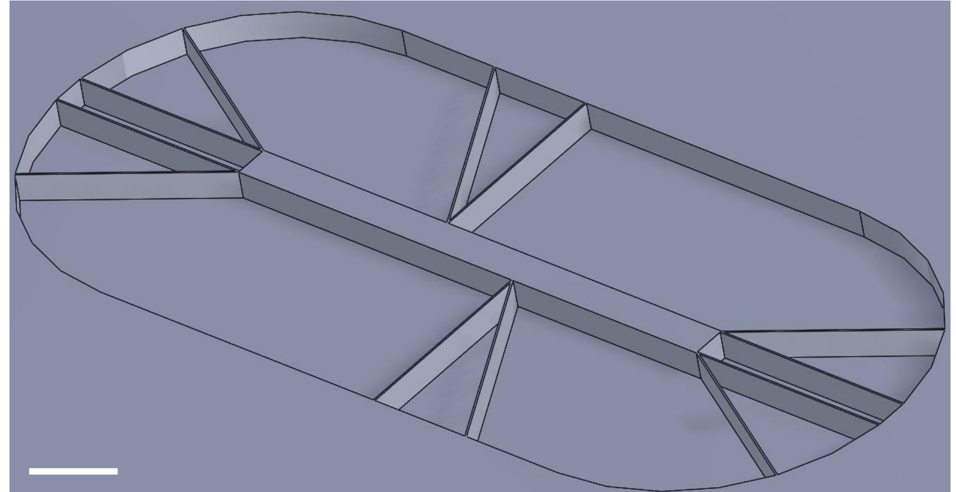

Figure 3.19 3D tilted view of the device after the etching of the cavities to access the substrate. Scale bar of 20 µm.

The final device comprises a central heater and two lateral and symmetric sensing serpentines (3D tilted view in Figure 3.19). The cavities are designed on the two sides of the heater, to facilitate its suspension, including membranes and arms (Figure 3.20: right, layout of cell; top left : detail of a 60 µm x 10 µm cavity layout; bottom left: SEM image of the same cavity).

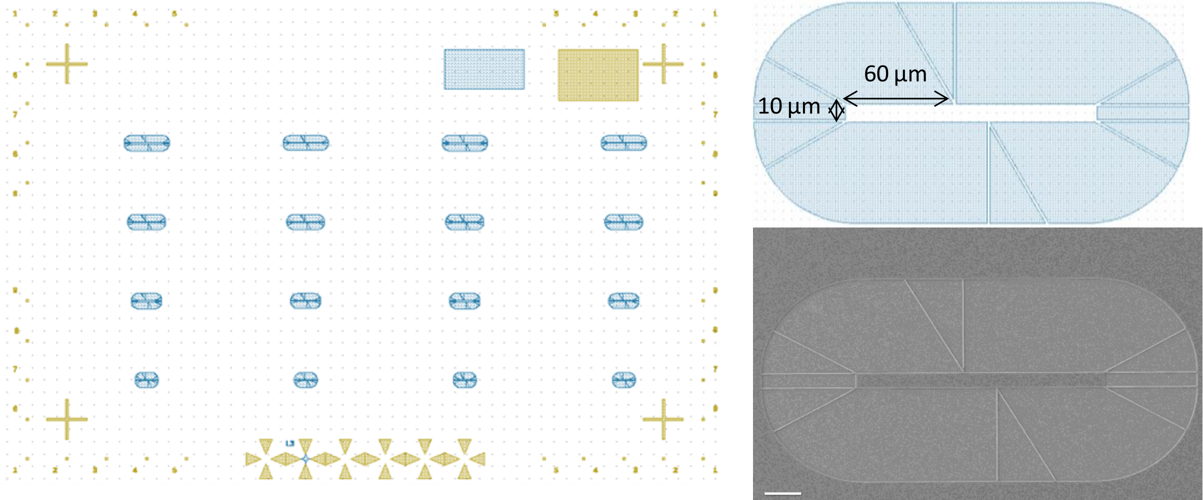

Figure 3.20 Left: cavities layout for electron beam lithography (in blue). The blue square is the end point detection window for the related etching. . Right: up, layout detail of the cavity; down, SEM image of the cavity after etching (scale bar 20 µm).

Different cavities have been designed, the details will be reported in the chapter dedicated to the results. The resist used for the lithography is MAA copolymer [163] (the same used for markers lithography and for the subsequent lithographies), the spin coating is performed with a speed of 1000 rpm, acceleration of 1000 rpm/sec for 12 seconds, to assure a thickness of 1.8 µm (checked at the profilometer). The development is performed by dipping the sample in a mixture of IPA:MIBK=2:1. Firstly, 60 ml of IPA and 30 of MIBK are stirred together in a beaker for 5 minutes to guarantee full mixture. The sample is developed for 1 minute, with a 100 rpm rotating stirring.
The successive cavity etching is performed with the same gases used for the markers etching, as summarized in the following Table 3.7.

Table 3.7 Description of the cavities lithography and etching process.

Step description	Parameters
Spin coating	MAA8.5EL13% : 1000 rpm, 1000 rpm/sec, 12sec Post bake, rump up: 80°C for 2', 100°C for 2', 140°C for 2', 180°C for 10'. Thickness: 1.8 µm (mechanical profilometer)
Cavities lithography	Dose 500 µC/cm², Current 25 nA, Resolution 0,025 µm
Resist developing	MIBK:IPA=1:2, 1 min
Cavities etching	SF6/Ar=10/10 sccm , 30W, 10 mTorr: SiN + SiO_2 + SOI etching (7min) CF4/N2/O2=40/40/5 sccm, 100 W, 10 mTorr : BOX + Si etching (14+1 min)
Resist stripping	UV exposure for 20 min Remover PG @65°C 40 min, acetone, IPA, dry

The cavity etching is performed through the SiN windows deposited by LPCVD, the thin wet thermal oxide and the BOX, down to the substrate (etched for 1 minute to assure the BOX is fully removed and silicon exposed). A schematic cross section of the device is shown in

Figure 3.21. The central part (layout in Figure 3.20) is the membrane to suspend. Laterally the cavities are etched.

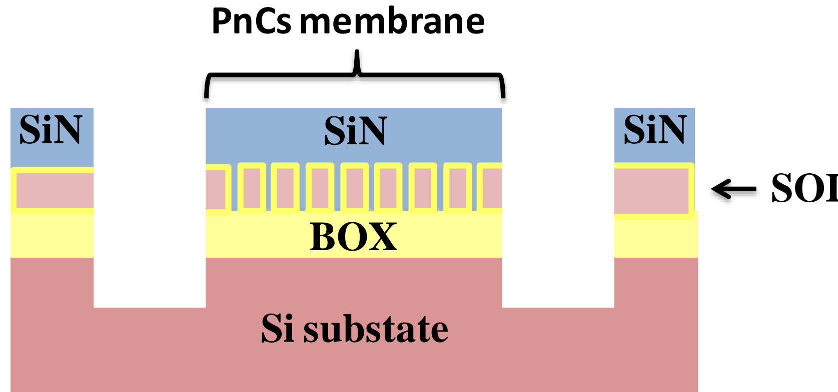

Figure 3.21 Schematic image of the etched cavities through the SOI, BOX until the silicon substrate.

SiN removal from membranes

The SiN has the function of mechanical support for the arms (only for the first generation of devices, as detailed in the following chapter) and electric insulation, because Pt metallic thermometers will be deposited above it. The SiN has thus to be removed from the suspended membrane, composed of the material which alters the thermal conductivity (the nominal value for its bulk thermal conductivity is 77 W K^{-1} m^{-1}.

Table 3.8 Description of the silicon nitride removal process.

Step description	Parameters
Spin coating	MAA8.5EL13% : 1000rpm, 1000rpm/sec, 12sec Post bake, rump up: 80°C for 2', 100°C for 2', 140°C for 2', 180°C for 10'. Thickness: 1.8 µm (mechanical profilometer)
Markers lithography	Dose 500 µC/cm², Current 25nA, Resolution 0,025µm
Resist developing	MIBK:IPA=1:2, 1 min
Markers etching	SF_6/Ar=10/10 sccm, 30W, 10 mTorr : SiN etching(6 min)
Resist stripping	UV exposure for 20 min Remover PG @65°C 40 min, acetone, IPA, dry

The etching is performed until the signal of the end point detection system drops, indicating that the etching of the silicon nitride is completed and the exposed surface corresponds to the wet thermal SiO_2. The schematic of this process step is presented in Figure 3.22.

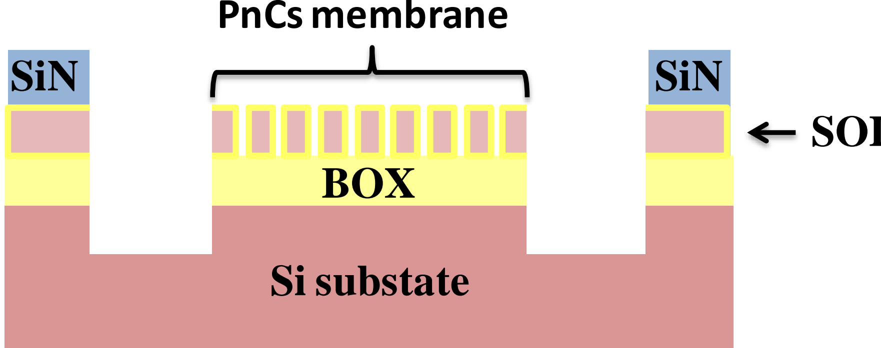

Figure 3.22 Schematic image of the step of SiN removal from the membranes.

Sidewalls protection by oxidation

Once the cavities have been etched and the silicon nitride has been removed from the membrane an inconvenient as to be face out. The SOI inside the cavities has been laterally exposed (as shown in Figure 3.23 (left)), and it could be attacked during the successive substrate etching to suspend the membrane. As detailed below, the substrate etching for the suspension is performed by XeF_2, which rapidly etches silicon and could remove the SOI layer. To circumvent this problem an ulterior silicon thermal oxidation (wet thermal oxide, 12 nm thick) is performed, with the same process previously described.

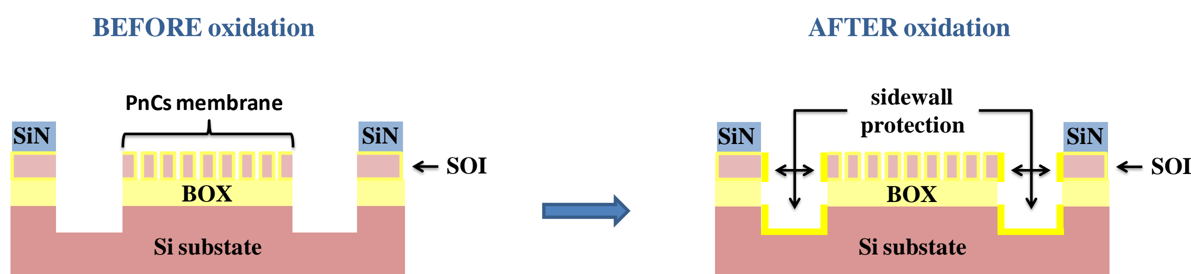

Figure 3.23 Before and after the oxidation of the SOI exposed on the cavities wall.

This steps allows to oxidize the laterally exposed SOI layer and the inner surface of the cavities. Doing so, the following step of etching the substrate by XeF_2 will not affect the SOI layer.

Pt metallization

The fabrication of platinum thermometers is the follwing steps of the depicted process flow. It is done with the goal of performing electro-thermal measurements to obtain the thermal conductivity of the suspended membranes, by means of temperature-induced resistance variation of metallic heating and sensing serpentines. The platinum has been selected as the worth material to realize such serpentines, given its good electrical conductivity with a linear resistance-versus-temperature characteristic. Firstly, the same copolymer resist MAA used for the previous lithography is spin-coated and the e-beam exposure is performed to define the area of the thermometers. After resist development, the metallization of platinum is performed (Figure 3.24).

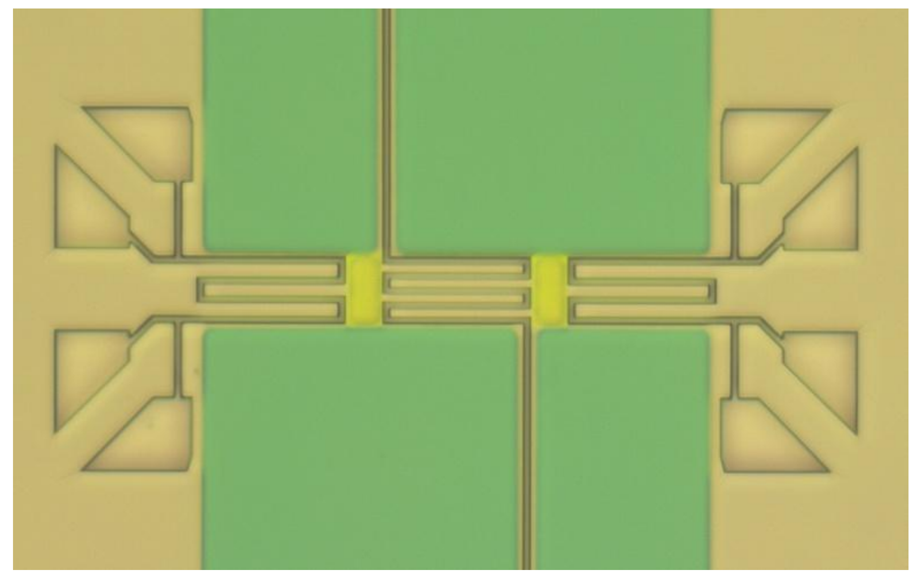

Figure 3.24 Optical microscopy image of the device after developing for the metallization of the platinum heater and sensor serpentines. The MAA copolymer resist is still present. The picture is related to the first generation of the device realized.

A lift-off is necessary to remove the metal from the area not devoted to the serpentines, by removing the resist underneath the metal and, by consequence, the metal which is deposited above. The thickness of the Pt deposited is 50 nm. The process is detailed in Table 3.9.

Table 3.9 Description of the process of Pt metallization.

Step description	Parameters
Spin coating	MAA8.5EL13% : 1100 rpm, 1000 rpm/sec, 60 sec Post bake, rump up: 80°C for 2', 100°C for 2', 140°C for 2', 180°C for 10'. Thickness: 807 nm (mechanical profilometer)
Pt lithography	Dose 500 µC/cm², Current 10 nA, Resolution 0,025 µm
Resist developing	MIBK:IPA=1:2, 1 min
Pt lift-off	1 hour in Remover PG @65°C

A schematic image of the process and the SEM picture of this step are shown in Figure 3.25.

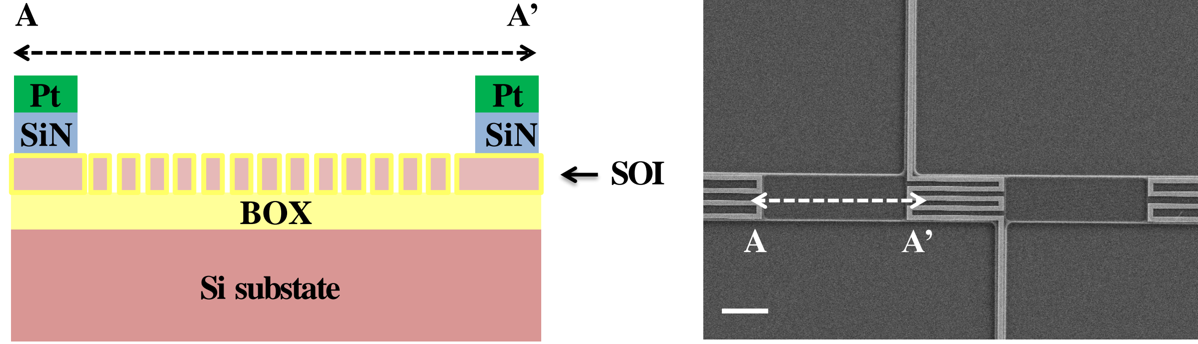

Figure 3.25 Left: Section view of the A-A’ cut. Right: SEM image of the platinum metallization for the serpentines. Scale bar: 10 m.

The scanning electron microscopy images (Figure 3.26) show the Pt serpentines after the lift-off process (first generation device) and a detail of the membrane side with the serpentine.

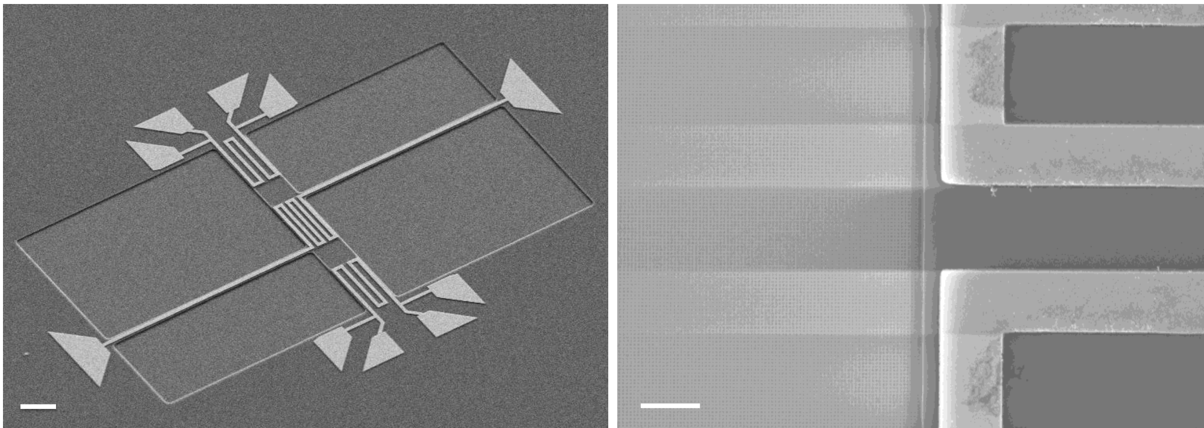

Figure 3.26 SEM imagines of the platinum thermometers after lift-off (left) and detail of the PnCs patterned membrane and platinum serpentine. Scale bars: 10 µm (left), 1 µm (right). 1st device generaion.

The phononic crystal patterns are clearly visible in Figure 3.27. The pitch is of 60 nm.

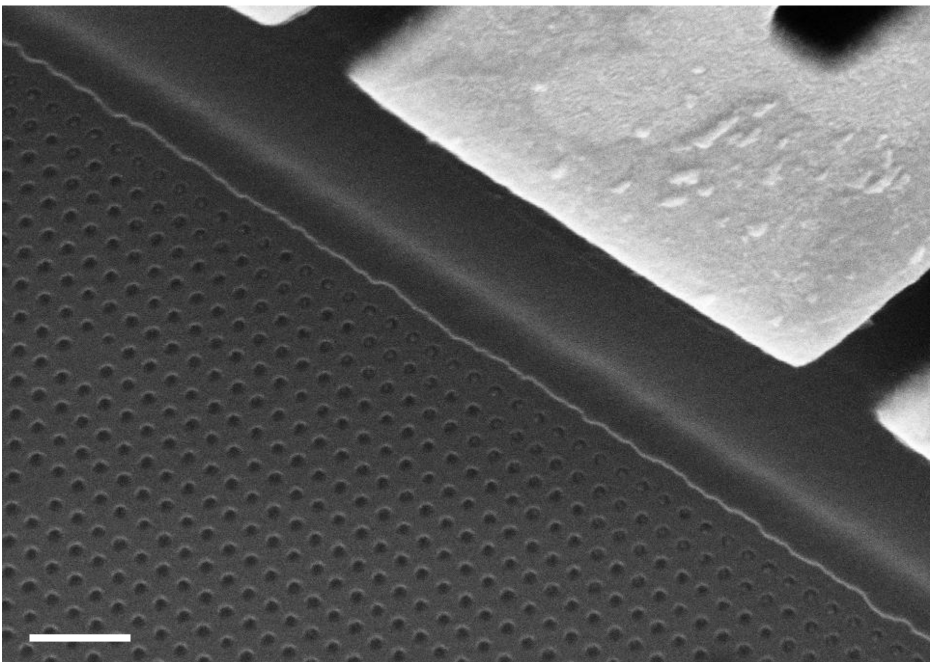

Figure 3.27 SEM image of the PnCs patterned on the side of the mebrane. The Pt serpentine is also visible. Second generation device. Scale bar: 200 nm.

Au metallization

For the thermo-electric measurements metal contacts are needed to place the electrical probes. Thus, for their fabrication, gold has been chosen as the best material given its softness and ductility. This step is similar to the previous one used for platinum, except for thickness, lithography current and metallization parameters.

Table 3.10 Description of the process of Au metallization.

Step description	Parameters

Step description	Parameters
Spin coating	MAA8.5EL13% : 1000 rpm, 1000 rpm/sec, 12 sec Post bake, rump up: 80°C for 2', 100°C for 2', 140°C for 2', 180°C for 10'. Thickness: 1.8 µm (mechanical profilometer)
Au lithography	Dose 500 µC/cm², Current 50 nA, Resolution 0,025 µm
Resist developing	MIBK:IPA=1:2, 1 min
Au lift-off	2 hours in Remover PG @65°C

The thickness of the gold layer is 400 nm to assure a good contact of the sensing probes during measurements.

Oxide removal from cavities bottom

Before moving to the membrane suspension step, it is necessary to remove the thermal oxide previously grown at the bottom of cavities during the sidewall protection step. For that sake, another electron beam lithography is performed. The details are summarized in Table 3.11.

Table 3.11 Description of the process of oxide removal from the cavities' bottom.

Step description	Parameters
Spin coating	MAA8.5EL13% : 1000rpm, 1000rpm/sec, 12sec Post bake, rump up: 80°C for 2', 100°C for 2', 140°C for 2', 180°C for 10'. Thickness: 1.8 µm (mechanical profilometer)
Markers lithography	Dose 500 µC/cm², Current 25nA, Resolution 0,025µm
Resist developing	MIBK:IPA=1:2, 1 min
Markers etching	$CF_4/N_2/O_2$=40/40/5 sccm, 100W, 10mTorr : SiO_2 etching (1 min)
Resist stripping	UV exposure for 20 min Remover PG @65°C 40 min, acetone, IPA, dry

The chemical etching step is very fast (1 minute) and allows the exposition of the silicon substrate at the bottom of the cavities. This step is fundamental because the XeF_2 vapour used for the Si substrate etching, for the membrane's suspension, is a very selective gas respect silicon oxide. To avoid the growth of an ulterior layer of native oxide, it is suggested to perform the etching of cavities bottom right before the XeF_2 vapour etching.

XeF_2 vapour etching

The silicon substrate etching is performed with vapour XeF_2. This gas presents the advantages of high selectivity to silicon dioxide (around 1000:1), CMOS compatibility and a high etching rate of silicon (few µm/min, depending on pressure and temperature) [168], [169]. It consists in a pulsed etching technique. Firstly, an expansion chamber is filled with the gas up to a given pressure. The etchant is subsequently expelled in the etching chamber, toward the sample, until the target pressure is reached. After exposure to XeF_2, the chamber is filled with nitrogen and pumped down again, evacuating a gas phase byproduct, namely SiF_4. Then, a second pulsed etching can be started. The tool used is a XETCH (Xenon Difluoride Etching

System – X3 Series) by Xactix® XeF2 Release Etch System by SPTS [170]. A schematic cross section of the process step is sketched in Figure 3.28.

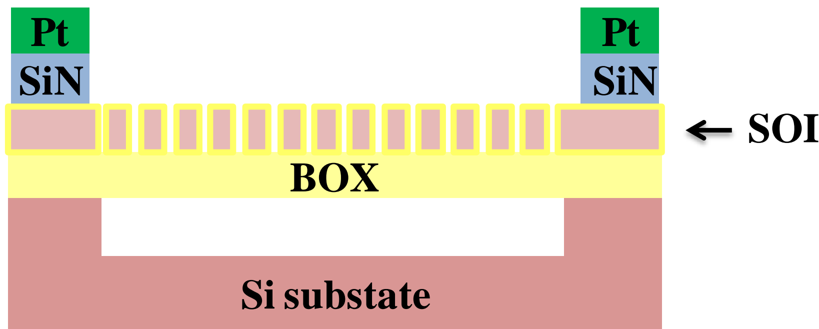

Figure 3.28 Sketch of the device after the XeF_2 vapour etching step.

Optical microscopy (a, b, c) and scanning electron microscopy (d) images of the suspended membranes after XeF_2 are shown in Figure 3.29.

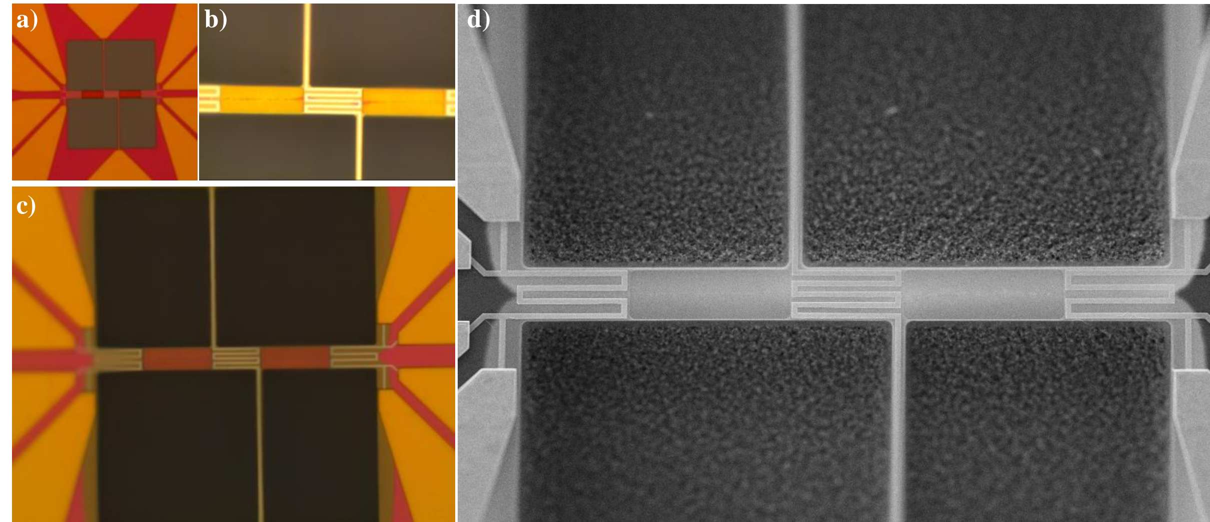

Figure 3.29 Optical and Scanning electron microscopy images of a 30 μm x 10 μm membrane: a) before suspension; b) after 3 cycles of XeF2 vapour etching, the suspension is not completed (the silicon substrate is still connected at the centre of the membrane); c) Fully suspended membrane after 3.5 cycles; d) SEM image of the same membrane suspended.

The etching pressure is 3 Torr, with a pump out pressure of 0.8 Torr. The performed cycles last 10 seconds. The number of cycles needed to fully suspend the membrane is strictly correlated to the time passed from the last etching step. Indeed, it is dependent on the thickness of the native oxide to etch (very low etch rate for XeF_2), before reaching the substrate. Therefore, a number of cycles between 3 and 12 could be necessary to fully suspend the membranes. The etching cycles are performed by 2, in such a way to check how etch proceeds with optical microscopy.

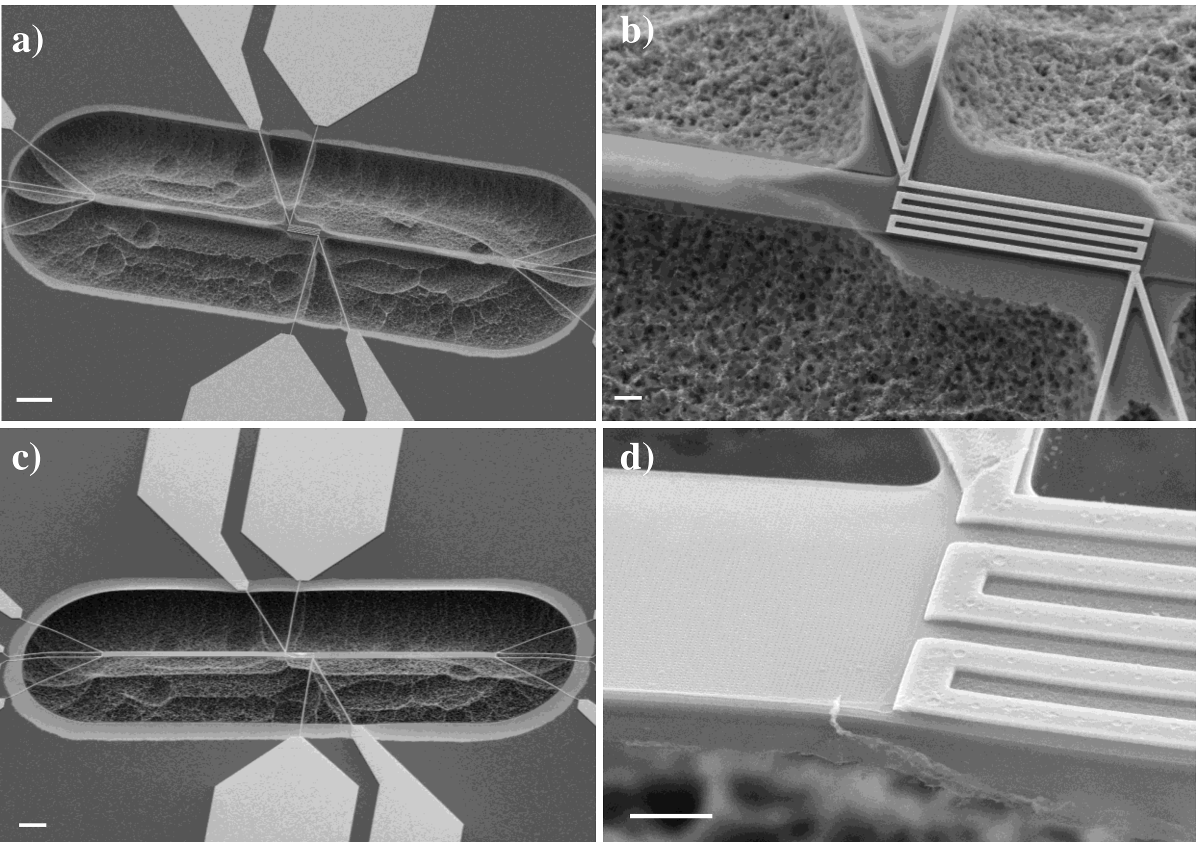

Figure 3.30 SEM images of the device after XeF2: a) and b) after 8 cycles of etching, membrane of length 120 and width 10 not fully suspended. c) Fully suspended membrane of length 120 and width 5 µm. d) Detail of the membrane fully suspended, PnCs are visible. The oxide at the borders appears hanging over the border due to the lateral substrate etching in d).

HF etching

Once the membrane is suspended by etching the silicon substrate (under the BOX layer), it is possible to remove the 145 nm-thick buffered oxide (BOX).

The commonly chosen methodology is to perform HF etching. There are two possibilities: a wet etching (1 minute, 5% mixture concentration of HF in water) or a vapour phase HF (in a dedicated apparatus [170]).

The wet etching is the mostly widespread technique to release micrometer devices by silicon dioxide etching. Unfortunately, this solution presents the disadvantage of increasing stiction problems, by pulling the free-moving microstructures together which adhere to each other, reducing device yields. Another potential issue with wet HF etching is that it will corrode any exposed metals, most notably aluminium, on the wafer. So, only few membranes are damaged during this step and break down. A super critical drying might be performed to reduce the stiction.

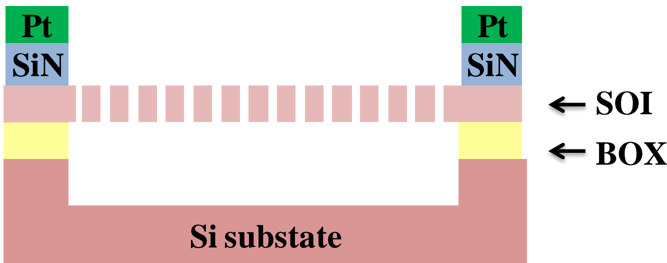

Figure 3.31 Sketch image of the device after the HF vapour etching of the 145 nm - BOX.

The vapour phase HF etching represents the best solution with a device yield of 100%. Furthermore, it provides repeatable, stable performance with a wide process window, it is compatible with a large range of metals, it doesn't pose issues of complex waste management and has low cost of ownership.
An optical interferometric profilometer comparison is done on the same device after XeF_2 (before HF) and after the HF process. It shows that the membrane presents a different bending, from 6 µm to 1.6 µm (for a 200 µm long and 20 µm wide membrane), due to the released stress after the BOX complete etching.

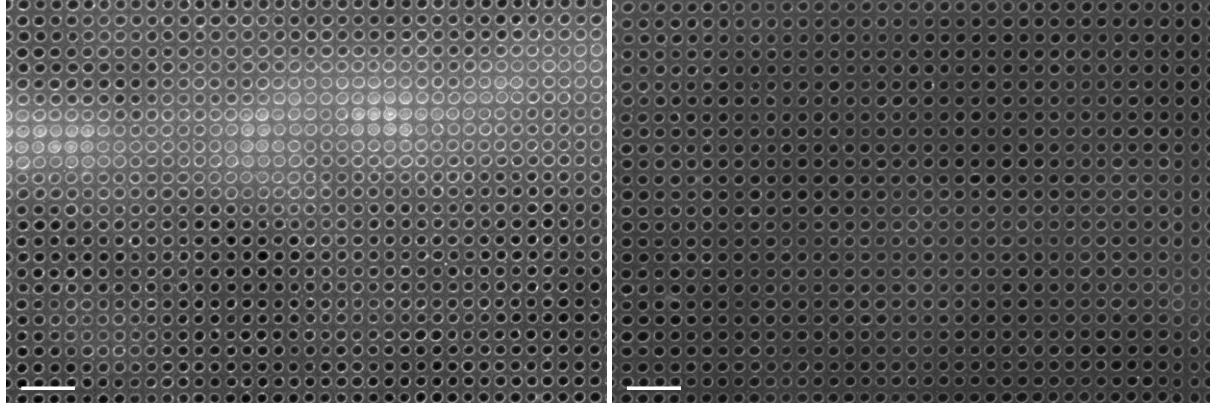
Figure 3.32 SEM images of two membranes with PnCs (60 nm pitch). Left: the BOX has not fully etched under the SOI membrane of 60 nm. Right: fully etched BOX underneath the SOI. The bottom of the cavity is visible through the patterned holes. Scale bar 200 nm.

The process is performed in the apparatus from SPTS [170]. A gaseous etchant penetrates smaller features more easily and allows longer undercuts. Alcohol (A) ionises the HF vapour and acts as a catalyst:

$$SiO_2\,(s) + 2HF_2^-\,(ads) + 2AH^+\,(ads) \rightarrow SiF_4\,(ads) + 2H_2O\,(ads) + 2A\,(ads)$$

Water, a by-product of the reaction, also acts as a catalyst and must therefore be carefully controlled and removed from the system. The apparatus SPTS (patented Primaxx HF/Alcohol process) employs a reduced pressure, thus a gaseous phase environment for the isotropic etch removal of sacrificial oxide layers.
The process is generally carried out at pressures around 130 Torr providing controlled, residue-free etching. Typical vertical and lateral oxide etch rates are in the 0.1-10 µm/min range. To fully etch the 145 nm buffered oxide, 1 cycle of 5 minutes of etching is performed with 190 sccm HF and pressure of 125 Torr. The etching rate of the selected recipe is about 37.4 nm/min (anisotropic etching), with an uniformity of 0.8%.

The SiN is a critical material during the HF vapour etching, it might swell and create bumps which may degrade the device or break the suspended membrane. A solution envisaged is the post etching bake at 255°C for 2 minutes, which reduces the SiN stress and limits the issue [171]. In Figure 3.32 two SEM images of the membrane (2nd device generation, specified in the next section) show the device before and after the etching of the buffered oxide. It is noticeable that in the left one the buried oxide is not yet fully removed under the silicon, and it is visible as a white layer under the SOI suspended membrane. The right image shows the SOI layer suspended, without BOX underneath (etching completed).

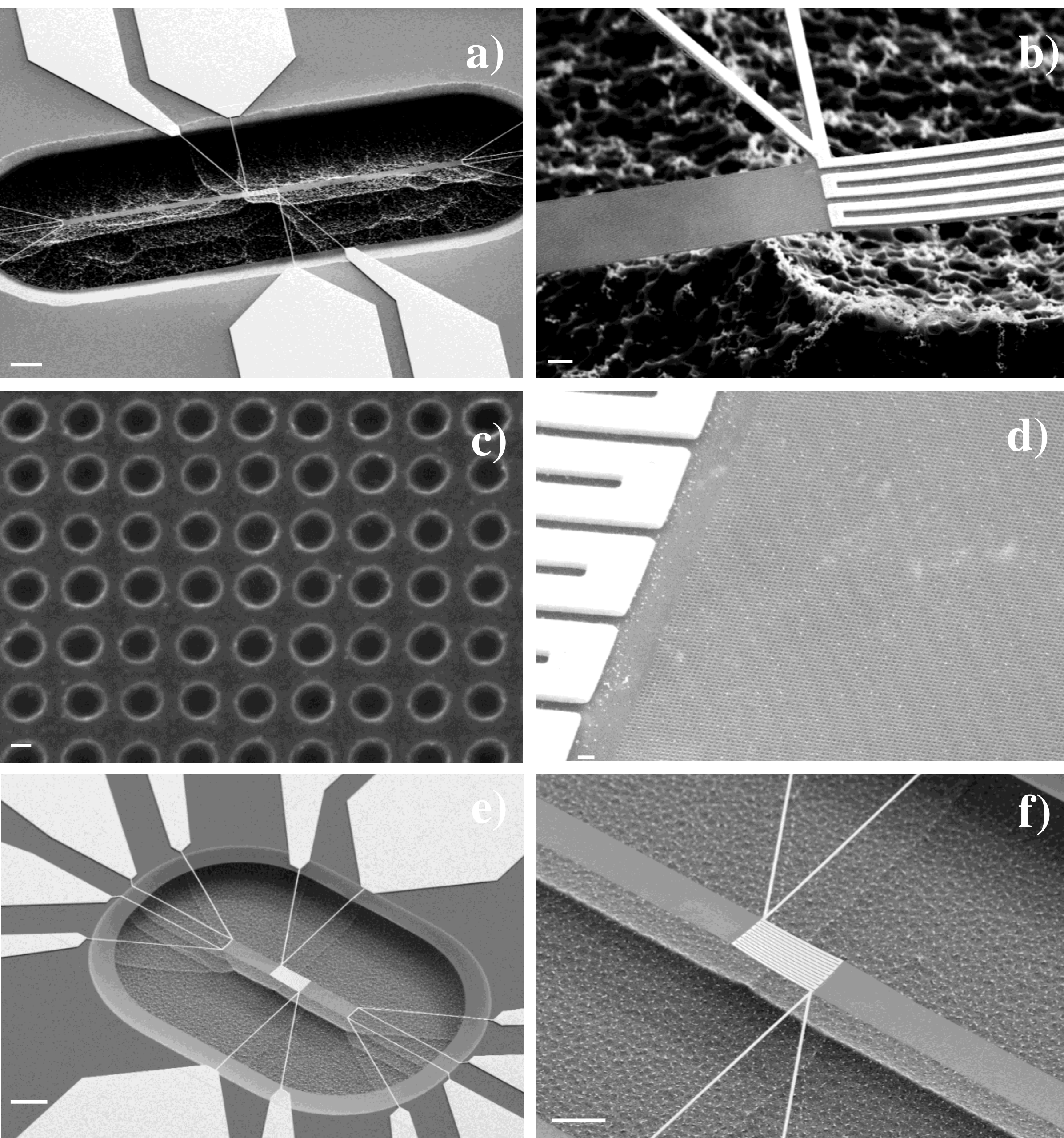

Figure 3.33 SEM pictures of the fully suspended phononic membranes after HF etching (2nd generation). a) membrane of length 120 µm and width 10 µm, scale bar of 20 µm. b) Magnified picture of the same membrane in a), scale bar of 1 µm. c) PnCs patterns after HF etching, pitch 60 nm, scale bar 20 nm. d) Patterns etched, the bottom of the cavity is visible in transparency. e) A 30 µm x 10 µm membrane (scale bar of 20 µm). f) Detail of the central heater serpentine of a membrane of width 10 µm. Scale bar of 10 µm.

3.3 Description of the different device generations

The PhD work carried out focused initially on the integration of the phononic engineered structure developed (paragraph 3.1) onto the measurement metrology platform to obtain the final device described in paragraph 3.2.

The first device fabricated and characterized (see Chapter 4 for further characterization details) is referred to as 1st generation. Layout design and structural improvements have been applied to the fabrication of the successive device, 2nd generation. The next subsections show the main differences between the two designs.

Another device typology has also been fabricated to perform Raman measurements and is presented in the third subsection of this paragraph.

3.3.1 1st generation device

The first layout realized presents 16 different devices on the same cell, reproduced twice on Figure 3.34. The main characteristic of such a design is the fact that the membrane is suspended between the central heater and the sensor serpentine which is not fully suspended, but deposited on the silicon nitride at the edges of the cavities. The dimensions of the devices fabricated are summarized in Table 3.12.

Table 3.12 Dimensions of the 1st generation device.

Element	Thickness (nm)	Length (µm)	Width (µm)
Heater Serpentine	30	206 (for width 5 µm) 244 (for width 10 µm)	1
Sensor Serpentine	30	47 (for internal, width 5 µm) 90 (for internal, width 10 µm) 61 (for external, width 5 µm) 104 (for external, width 10 µm)	1
Membrane (suspended)	61	5 – 10 – 20 – 30	5 – 10

Thus, the sensed temperature at the serpentine's extremity is the same of the regulated chuck when there is no voltage applied. A detail to underline and take into account is the fact that the heater is suspended and connected to the contacts through two arms (Figure 3.34 c), d)). Therefore, 6 probes measurements, with 4 probes positioned on heater, are not possible for this design, making the temperature detected for the heater affected by parasitic resistance's contributions.

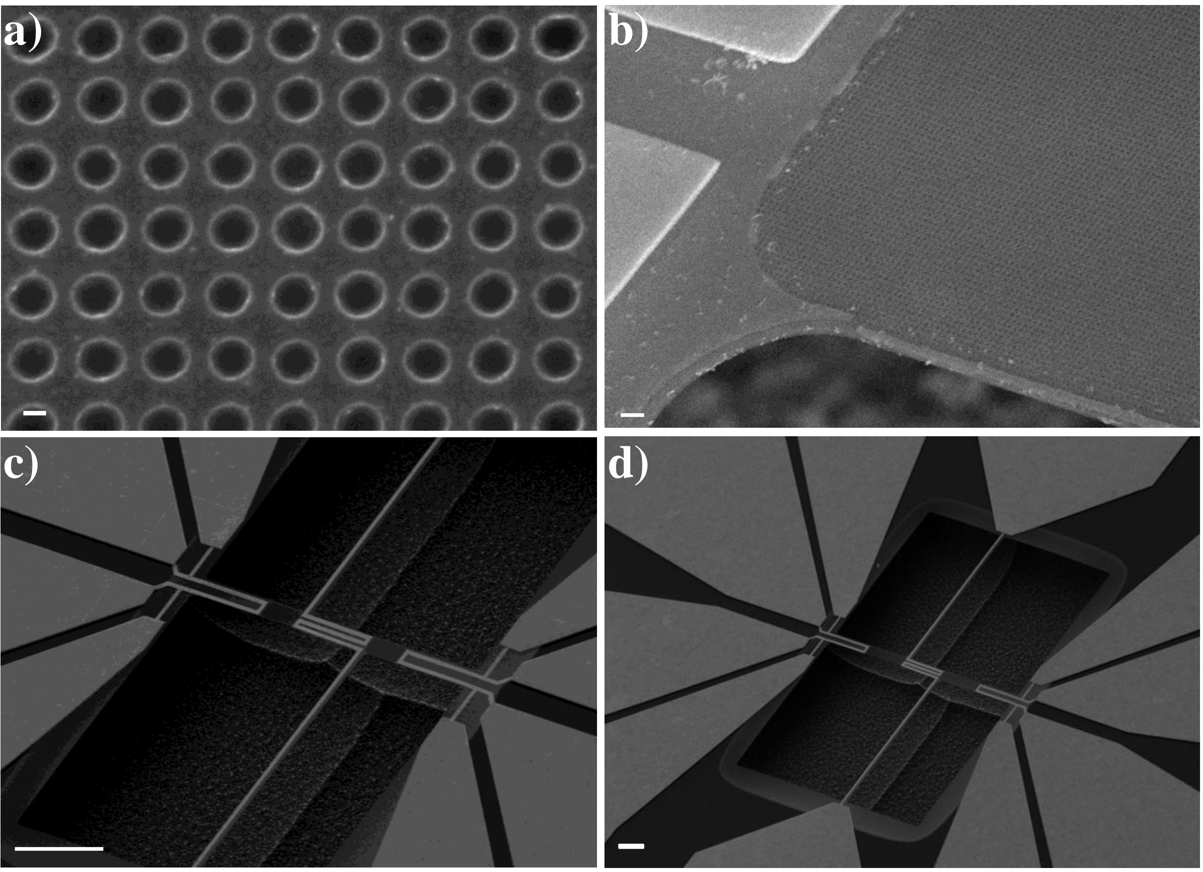

Figure 3.34 SEM pictures of the first device generation: a) detail of the PnCs patterned in SOI, pitch 60 nm and scale bar 20 nm; b) side view detail of the suspended membrane, scale bar 200 nm; c) suspended membrane 10 µm x 5 µm, scale bar 20 µm; d) Full cavity and contacts picture of a 20 µm x 5 µm suspended membrane, scale bar 20 µm.

3.3.2 2nd generation device

A second design has been realized due to the necessity of fully suspending the sensor serpentine to have a proper isolation from substrate and thus reduce thermal losses. Another interesting modification has been the adding of two more arms to the heater to properly detect the heater's temperature and resistance getting rid of parasitic and arms resistance contributions. Furthermore, the cavities design presents a higher symmetry, having a rounded shape around the central heater.

Table 3.13 Dimensions of the 2nd generation device.

Element	Thickness (nm)	Length (µm)	Width (µm)
Heater Serpentine	50	100 (for internal, width 5 µm) 257 (for internal, width 10 µm) 237 (for external, width 5 µm) 395 (for external, width 10 µm)	1
Sensor Serpentine	50	4.5 (for internal, width 5 µm) 9.5 (for internal, width 10 µm) 142.5 (for external, width 5 µm) 147.5 (for external, width 10 µm)	1
Membrane (suspended)	57	30 – 60 – 90 – 120	5 – 10

The 2nd device generation is designed with plain membranes (with no phononic patterning), with one pitch (of 60 nm) and with three pitches to study the possibility of a cumulative effect in thermal conductivity reduction of the different phononic patterns (pitches of 50 – 55 – 60 nm).

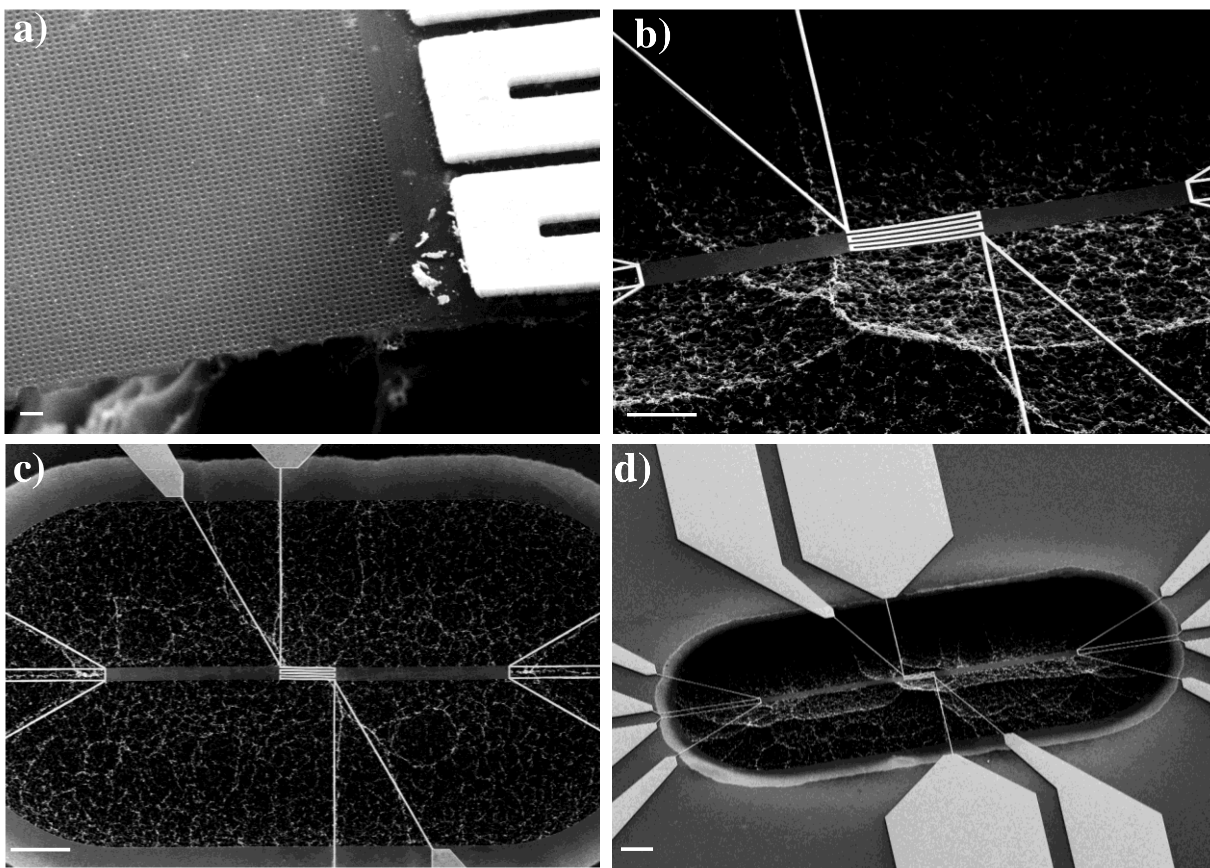

Figure 3.35 SEM pictures of the second device generation: a) detail of the PnCs patterned SOI membrane (side view), pitch 60 nm and scale bar 200 nm; b) tilted view of the suspended membrane, scale bar 10 µm; c) top view of the suspended membrane 60 µm x 5 µm, scale bar 20 µm; d) Full cavity and contacts picture of a 20 µm x 5 µm suspended membrane, scale bar 20 µm.

Figure 3.35 shows images of the suspended second generation device. The pictures clearly show the sensor fully detached from the substrate and the four arms which are used to sense the heater temperature exactly. In Figure 3.35 a) the phononic patterning and the thin film membrane are magnified to demonstrate the regularity of the periodic structure.

3.3.3 Device for Raman measurements

A third device design has been realized in order to measure the thermal conductivity by Raman spectroscopy. The followed methodology is depicted in the next chapter, and it is worth underlining that metallic contacts are not needed Figure 3.36. Thus, the fabrication procedure is much shorter by skipping the silicon nitride deposition with related removal etching and the two metallization steps with related lift-offs.

Table 3.14 Structure realized for the Raman spectroscopy experiments.

Element	Thickness (nm)	Length (μm)	Width (μm)
Membrane (suspended)	53 – 61	50 – 100 – 150 – 200	5 – 10 – 20 – 30

The device have been realized with plain membranes and with phononic engineered ones (with pitches of 60, 80 and 100 nm).
The device thicknesses varies depending on the cell considered, because for few of them the final suspension has been performed after a second lithography and sidewall protection oxide etching process, in order to remove the native oxide.

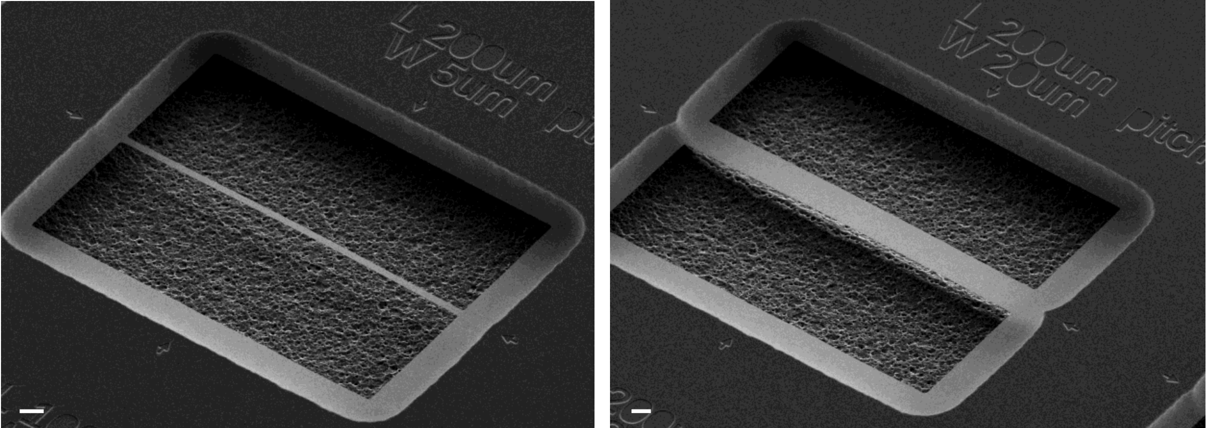

Figure 3.36 SEM image of suspended membranes designed for Raman spectroscopy. Left: length 200 μm and width 5 μm. Right: length 200 μm and width 20 μm.

First of all, it is worth to specify that the depth of the cavities is strictly related to the XeF_2 etching recipe and varies a lot with the number of cycles performed and their length. For instance, an etching by Xenon difluoride performing 3 cycles, a check and 3 more cycles results different with respect to the one counting 5 cycles continued, check at the microscope and one more cycle. The main difference is given by the fact that taking out the sample from the XeF_2 vacuum chamber new native oxide grows upon the cavities during the check at the optical microscope, resulting an added element which slows down the successive cycle of XeF_2 etching if needed.

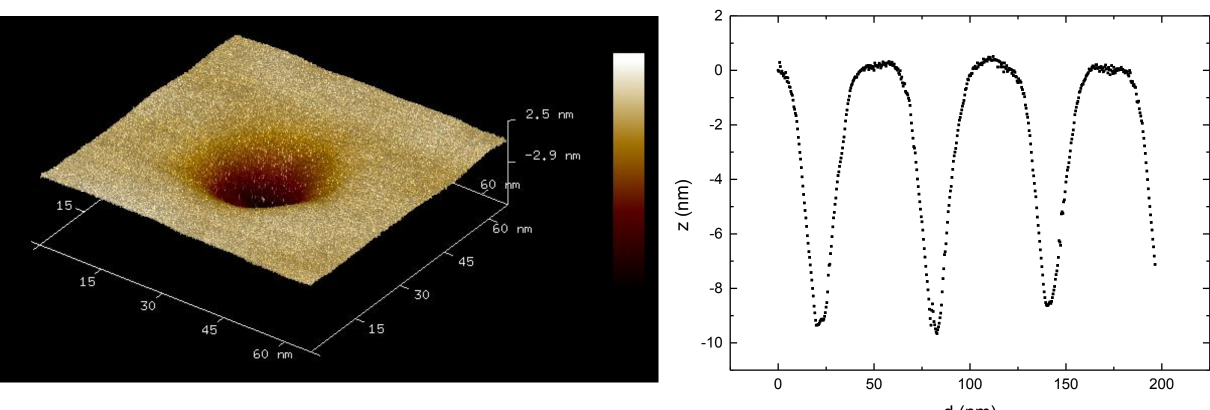

Figure 3.37 Left: detail of one enclosure of 60 nm pitch, radius about 38 nm. Right: Plot of AFM point depth as function of the scan direction.

AFM measurements have been performed to evaluate the sample's topography and roughness. A detail of one enclosure and the scan trace are shown in Figure 3.37. The tip used has a radius of few nanometers, thus it is not providing information about the depth of the enclosures. It is interesting to notice that the roughness of the surface between holes is about 0.2 nm for the three different membranes (three different pitches) analyzed. Figure **3.38** presents AFM images of three different membranes of pitches 60 nm, 80 nm and 100 nm. The top view AFM scan and 3D one are shown for the three.

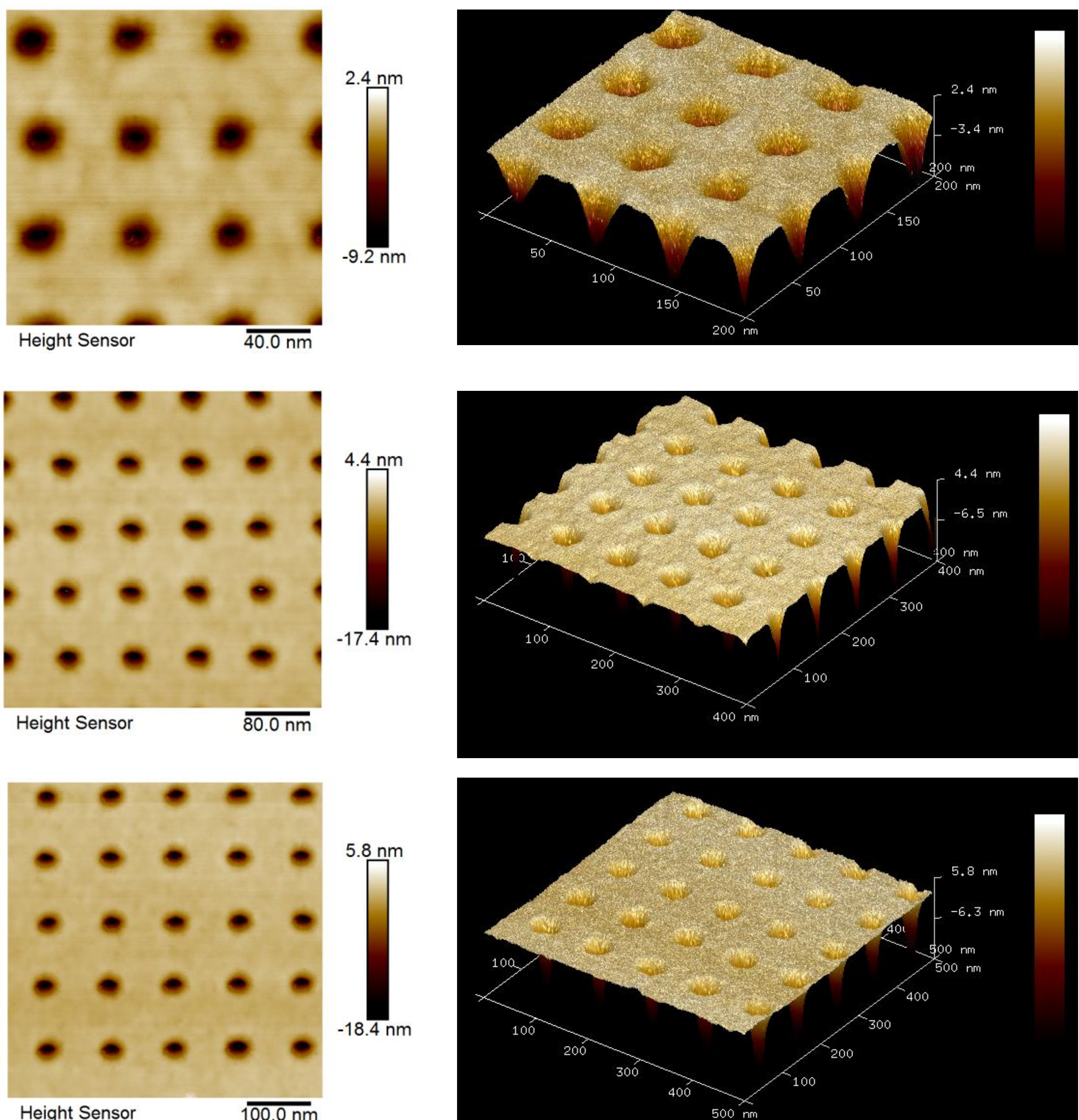

Figure 3.38 AFM images of area topography in top view (left) and 3D tilted view (right) of silicon membranes of 60 nm pitch, roughness of 0.20 nm (top), 80 nm pitch, roughness of 0.21(central) and 100 nm pitch, roughness of 0.24 nm (bottom).

Optical profilometry has been performed on cavities after etching by XeF_2 to verify the depth of them and the bending of the membranes. The bending results more important for devices with longer membranes and thinner ones (Figure 3.39). Membranes of width of 30 µm present a zero or negative bending, due to the weight of the structure and the stress of the bilayer due

to the presence of the BOX underneath. Anyways, the bending is reduced after the vapour HF steps, which removes the underneath BOX, releasing the membrane stress (from 6 µm to 1.6 µm of maximum bending after vapour HF etching, for length of 200 µm and width 20 µm).
All devices analyzed are on the same cell processed. Thus, they underwent the same process flow and conditions. The cavity depth is deeper for larger (and longer) cavities (i.e. membranes of length 200 µm).

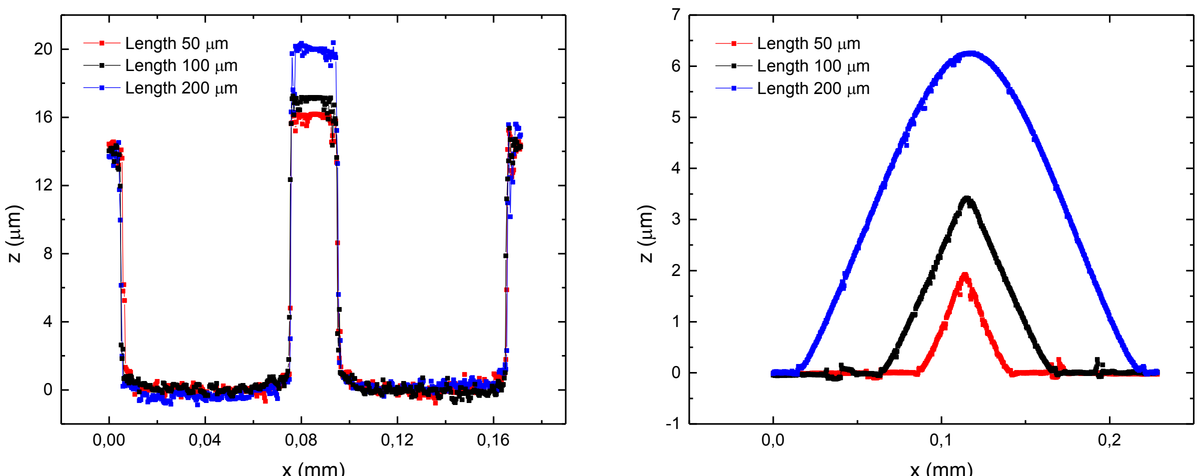

Figure 3.39 Curves of the suspended membranes taken by optical profilometer showing the depth of the cavities (left) and membranes bending (right). All the membranes have a width of 20 µm and lengths of 50 µm (red), 100 µm (black), 200 µm (blue).

3.4 Conclusions

This third chapter illustrated the device fabrication process developed during this work. The first part of it presented the different fabrication options. It focuses on the lithography methodology chosen, frequently referred to as *dots on the fly* and the etching process by Cl_2 RIE. The realized patterns are dense, defect-free and present a very high resolution. The dimensionality reached is the actual state of the art for etched periodical enclosures with the ZEP520 resist. A very precise control of the lattice constant for periodical enclosures is possible thanks to the developed patterning process.
The second part of the chapter is devoted to the description of the whole process of integration of PnCs patterned film into suspended micrometric platforms for thermal conductivity metrology.

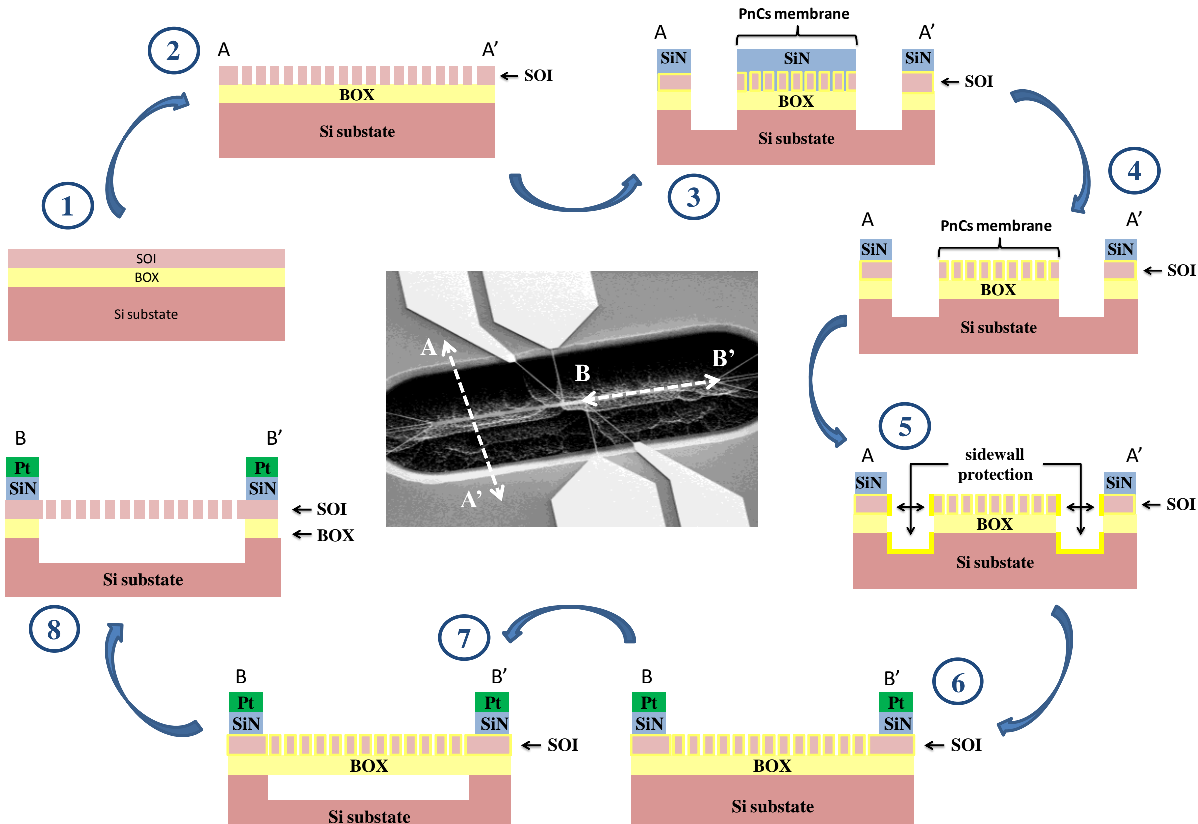

Figure 3.40 Summary of the principle steps of the fabrication process flow. 1) SOI wafer(2.2.1); 2) PnCs patterning (2.2.4); 3) SiN deposition and cavities' etching (2.2.5 – 2.2.6); 4) Si removal from membranes (2.2.7); 5) Silicon oxidation to protect sidewall; 6) Pt metallization (2.2.9); 7) XeF_2 vapour etching (2.2.12); 8) HF vapour etching (2.2.13). At the center an SEM image of the device, indicating the different cuts of the illustrations (AA' and BB').

The process flow (detailed in 3.2) is summarized in Figure 3.40 (from different points of view, AA' and BB').

The SOI membrane is fully suspended. The final thickness of the latter is around 62 nm (after the oxidation process which happens at the surface between the silicon and the BOX). The phononic patterns do not present degradation (as confirmed by scanning electron microscopy). After the vapour phase HF etching the yield of unbroken membranes is 100%. The process developed has the main advantage of being fully CMOS compatible, because it doesn't make use of metallic hard mask or materials which could pollute the surfaces. Furthermore, it is fully repeatable and it could be easily integrated in a converter type design (performing implantation and slight changes in the layout). Adding windows through the silicon nitride down to the SOI and additional electrical contacts it could be also possible to measure the electrical conductivity and the Seebeck coefficient. The very thin membrane lends the device good flexibility, envisaging possible future applications in flexible electronics.

Chapter 4 **Thermal characterization**

Abstract

The following chapter is devoted to the description and analysis of the results obtained for the devices whose fabrication process and characteristics are described in Chapter 3. The typology of the different measurements performed on the devices is illustrated and detailed. To study the thermal conductivity κ of phononic patterned membranes different methodologies are adopted. The interest in performing several characterizations is due to the fact that measuring thermal conductivity in nanostructures remains an open challenge. Our samples offer the opportunity to calibrate and check several techniques and try to obtain a quantitative agreement. The first subchapter introduces the thermal characterization methods. The second one describes the Electro-Thermal technique to measure the κ of suspended micro-engineered membranes by exploiting the resistance's variation as function of the temperature of suspended Pt thermometers. The second subchapter presents the results of measurements obtained using the Raman spectroscopy. For this technique the temperature dependent shift of the silicon Raman peak is detected and related to the temperature difference established across the membrane. Thus, Finite Element Method simulations allow the extraction of the thermal conductivity. The last part introduces a third measurement technique: the Scanning Thermal Microscopy (SThM). The last two characterizations are performed in the framework of the ongoing collaboration established with Pierre-Olivier Chapuis, Jean-Marie Bluet and Mouhannad Massoud of the *Institut national des sciences appliquées* (INSA, Lyon), *Institut des Nanotechnologies de Lyon* (INL, Lyon) and the *Centre d'Energétique et de Thermique* (CETHIL, Lyon).

4.1 Thermal characterization: methods

There are several methodologies to measure the thermal conductivity, developed since the late 1980s. Among them three are treated in this chapter, and two others merit to be mentioned in order to have a view of the topic. Even if not used during this PhD work, the 3ω method is one of the now very well established techniques to evaluate a device's thermal properties, and it is well described by Cahill *et al.* in [172] and Shi *et al.* in [173]. Its basic principle relies on the fact that an electrical current flows at angular frequency *ω*: $I = I_0 \cos(\omega t)$, causing a Joule heating in DC and at *2ω*: $P(t) = R \cdot I(t)^2 = \frac{RI_0^2}{2}(1+\cos(2\omega t))$. By the fact that the response in the thermal domain is linear, this *2ω* heating causes temperature fluctuations also at *2ω*: $T(t) = T_0(t_0) + \Delta T \cos(2\omega t + \varphi)$, with an amplitude and phase dependent on the thermal properties of the system. This perturbs the heater's electrical resistance at *2ω*: $R(t) = R_0(1+\alpha \Delta T(t)) = R_0 + \alpha R_0 \Delta T \cos(2\omega t + \varphi)$, which when multiplied by

the driving current at ω causes a voltage signal across the heater at a frequency 3ω, which strictly depends on material's thermal properties:
$U(t) = R(t) \cdot I(t) = [R_0 + \alpha R_0 \Delta T \cos(2\omega t + \varphi)] \cdot I_0 \cos(\omega t)$. Developing, it becomes: $U(t) = R_0 I_0 \cos(\omega t) + \frac{\Delta R I_0}{2} \cdot [\cos(3\omega t + \varphi) + \cos(\omega t + \varphi)]$ with the 3ω component: $U_{3\omega} = \frac{\Delta R I_0}{2} = \frac{\alpha R_0 \Delta T I_0}{2}$. Indeed, with lock-in amplifiers, it is possible to filter and measure the 3-omega-component of the voltage signal and the phase dependency. The advantages of this method are the fact that it can measure with accuracy the layer's thermal conductivity and presents a very low noise thanks to the lock-in scheme [174].
Another widespread methodology is the Time Domain Thermoreflectance, which exploits the change in reflectance of a film, when it heats up, to derive its thermal properties, using a pump – probe laser set up. This contactless method works on the basis of a system consisting of two lasers with different beam paths or one laser with two split beams. A pump beam is directed onto the sample's surface which is heated as result of the laser beam power absorption. Thus, the heat diffusion and temperature on the surface of the sample are dependent on its properties. The reflectivity is influenced by the temperature. So, the surface temperature can be determined by a laser probe beam that falls onto the sample surface after the pump beam with a time delay of Δt. Indeed, this probe beam reflected can provide information about the surface temperature and thermal properties, by falling on a photodiode which allows retrieving the measurements information. The advantage of the TDTR methods lies in its ability to characterize both individual layers and multilayer coating system with layers of thickness from few nanometers to millimetres. Moreover, any kind of material can be measured and samples preparation is straightforward [175].
Among all the possible methodologies to measure κ, in the following section the Electro-Thermal measurement, Raman spectroscopy and Scanning Thermal Microscopy techniques are introduced and applied.

4.2 Electro-Thermal

As previously introduced, thermal conductivity κ of silicon is dominated by phonon distribution. The κ of thin films is smaller than the one of their bulk counterparts. It is explained in terms of scattering of phonons with boundaries, imperfections, impurities and electrons. Thus, the thermal conductivity of silicon thin film membranes is a relevant parameter to study the material-device complete integration. Indeed, the study of the thermal conductivity in thin crystalline silicon films provides an opportunity to more directly determine the distribution of phonon mean free paths in this material, exploiting the conductivity reduction due to the phonon boundary scattering. The thermal conductivity of phononic engineered membranes (2-dimensional periodically patterned materials) has been studied across a range of dimensions [121], [131] and, given the promising results, merits more attention. The structure fabricated with integrated PnCs onto suspended SOI membranes presents an interesting opportunity to examine the impact of holey geometry and boundary

scattering on thermal transport. In the following section the DC Electro-Thermal measurement technique is introduced and applied.

4.2.1 Methodology description

Electro-thermal method is chosen for its simplicity (easy theoretical background, methodology and equipments) which enables the maintaining of high measurement accuracy. The requirements influencing the structure design are: low thermal leakages (through the substrate, resistances, etc.), linear temperature distribution along the membrane (to properly extract the characteristic behaviour), temperature sensitivity (related to the electronic equipment's sensitivity, which allows thermal conductivity measurements sensitivity for low temperature differences).
The thermal conductivity of the silicon suspended membrane is characterized using a 4 or 6 probes steady-state electro-thermal measurement technique, inspired by the work of Liu and Asheghi [176], [177]. The measurement technique is detailed in the next subparagraphs.

4.2.1.1 Theoretical background

Chapter 3 details the fabrication procedure of the suspended micro-platform used for the characterization of the thermal conductivity. It is worth to specify that the device has been realized in order to guide the heat flux transfer only in one direction and simplify the problem of heat flux estimation from a three-dimensional to a one-dimensional problem. Furthermore, to eliminate the issue related to convection losses which are crucial for nanometer-size devices, the measurements are performed under vacuum.
As described in the third chapter, firstly a 30 or 50 nm (depending on the device's generation) Pt thin film is deposited on the SiN layer in such a way to work as a thermometer serpentine (heater or sensor). The choice of platinum as metal for the thermoresistive is done considering the linearity of its Resistance-vs-Temperature characteristic, which allows a precise determination of the temperature coefficient of resistance α. Secondly, Au contacts for the electrical probes are fabricated. The metal is chosen taking into account its softness, and the fact that the electrical probes can easily scratch its surface, leading to a reduced contact resistance and higher surface contact.
In Figure 4.1 several strategies exploiting the SOI structure integrated onto a platform to measure the thermal conductivity of the silicon layer have been developed. Before detailing the different strategies, it is worth mentioning the common methodology allowing the extraction of the thermal conductivity.
In metals, it is well known that the resistivity (and resistance) increases with temperature due to the decrease of carriers lifetime associated to electron-phonon collisions. The increase in electrical resistance R is expressed by:

$$R = R_0 \cdot [1 + \alpha \cdot \Delta T] \tag{40}$$

where R_0 the resistance at RT and α the temperature coefficient of resistance. Given the linearity of the R-vs-T characteristic of platinum, it is possible to extract the α coefficient by sweeping the temperature (at constant steps) and, consequently, registering the correspondent

resistance values. This step is later referred to as serpentine's *calibration*. It is performed twice: for heater and sensor, in order to evaluate properly the α of both (slightly different due to the metal deposition process imperfections). At this point it is possible to relate the temperature variation to the applied voltage in the inverse procedure, which is referred to as *coupling*. The law governing the temperature distribution along the membrane is Fourier's one:

$$\vec{q} = -\kappa \nabla T \tag{41}$$

where q is the heat flux density and ∇T the temperature gradient in the device.

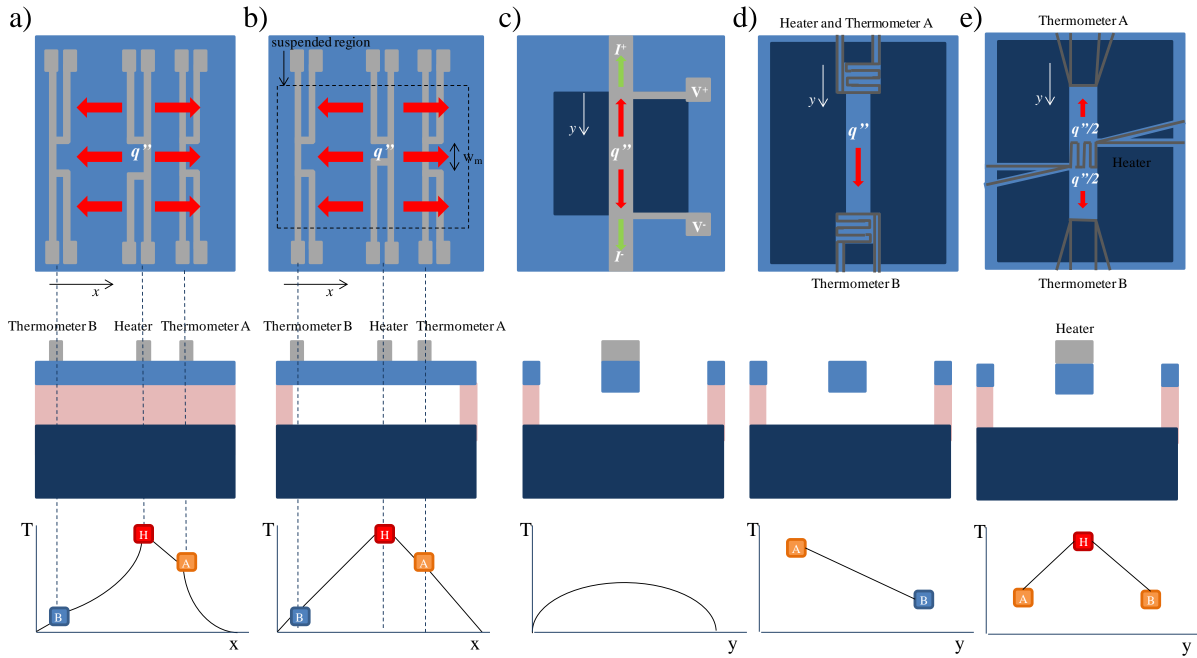

Figure 4.1 SOI Electro-Thermal measurement structures [89]. a) On-substrate steady-state Joule heating structure. b) Suspended steady-state Joule heating structure. c) Suspended heater bridge structure. d) Suspended heater-thermometer structure. e) Fully suspended heater structure with two symmetric suspended thermoemeters.

In all cases, the principle of Electro-Thermal measurement of thermal conductivity relies on Joule heating of a resistive metallic heater to generate a heat source *Q*. The metallic heater generates heat when current is flowing through it. The temperature variation is measured at a defined distance (*L*) from it, and its distribution is linear (in vacuum). The precise model developed for the extraction of the thermal conductivity is detailed in the following sections related to the specific membrane's design and geometry.

As sketched in Figure 4.1 a) the first measurements of SOI wafers were performed using three resistive elements taking advantage of the on-substrate steady-state electro-thermal configuration [178], [179]. The central element works as a heater. By applying a voltage, Joule effect generates heat that laterally flows through the membrane to the two sensor elements. Thus, the temperature profile results not linear due to the lateral thermal conduction in the oxide, which needs to be small compared to the one in the silicon layer. Furthermore the silicon vertical thermal resistance is required to be much smaller with respect to the one of the oxide and the silicon substrate beneath the BOX almost isothermal (as detailed in [178], [179]). In the work of Aubain and Bandaru [180], [181] the same experiment is proposed, but

combined with scanning thermoreflectance to measure the in-plane thermal conductivity, which is extracted using a Finite Element Method software.
Other designs present a configuration with a fully suspended bridge to confine the heat flow in the SOI plane. In this way, the BOX underneath the silicon is used as an etch stop layer to allow the full suspension of the silicon layer under study. Figure 4.1 b) presents the same layout as a), but with fully suspended heater and sensors thermometers. In this way the temperature profile along the membrane is linear and symmetric with respect to the heater. Therefore, the heating power and the geometry of heater and sensor being known, it is possible to extract the thermal conductivity by temperature measurement. An example of this structure is presented in the works [182], [183], integrated onto a complete thermo-generator device.
Figure 4.1 c) presents the design of a suspended bridge coated by a metallic heater. The temperature profile along the beam can be extracted from the heat diffusion equation. As for the other designs, the electrical resistance of the heater being dependent on the temperature, the thermal conductivity can be obtained by measuring the resistance variation as a function of the applied current (or voltage). For this typology, the heat generated is distributed over the whole structure to be characterized, resulting in a non-linear temperature curve. Thus, the metallic heater fully covering the bridge implies a possible device pollution due to this strip and the need for a supplementary modelling of the heat equation to extract the thermal conductivity from the measurements.
Designs in Figure 4.1 d) and e) represent the improvement of the one in b) and c) but with one or two fully suspended sensor elements. Specifically, the one in e) is the one realized during this work (referred to as 2nd device generation) which presents a heater and two suspended symmetric sensors lithographically patterned. The κ of the silicon membranes is measured by applying a power to the heater and detecting the resistance variation between the resistive elements (heater and sensor) which is related to the thermal drop along the membranes. The structure is fully suspended to ensure that the heat generated is injected into the membranes laterally and not evacuated through the support and substrate. The listed characteristics and advantages of the e) structure design (fully suspended sensors, symmetric structure, central heater with four arms for four probes connections, ..) lead us to chose this design for the work described in the following part.

4.2.1.2 Apparatus

The tool used to characterize the suspended membranes is a six (or four, depending on the device generation) DC point probes measurement set-up, equipped with a vacuum chamber (down to $4 \cdot 10^{-6}$ Torr). Performing the measurements under vacuum justifies the hypothesis of negligible air conduction mechanisms, which represent the bigger source of losses for this typology of measurements.
Originally, the chamber came with 4 DC probes and 2 RF coplanar probes which have been modified (2 ground contacts cut and point rubber sheath removed) in order to perform 6 probes DC measurements (as detailed in the following section, concerning the 2nd device generation). An HP4155c semiconductor parameter analyzer is connected to the probes to

power the device and measure the current/voltage. A picture of the apparatus is shown in Figure 4.2.

Table 4.1 Measurement and analysis parameters setting for the Semiconductor Parameter Analyzer (Agilent Technologies 4155C/4156C) [184].

Parameters	Description
Measurement mode	Single sweep
V_{heater}	Variable
Start	0 V
Stop	0.5 V
Step	$5 \cdot 10^{-3}$ V
Delay time	10 s
Hold time	0 s
Compliance	100 mA

The voltage supplied to the heater (V_{heater}) is swept from 0 to 0.5 V, with constant steps of 5 mV. A delay time is applied at each step for 10 seconds. Voltage sources (for heater and sensor) are SMU (Source Measurement Units). The output signals sensing the potential drop V across the Pt serpentine are VMU (Voltage Measurement Units). Performing the four probes measurements it is possible to get rid of the contact resistances and of the resistance due to the part of the Pt wire lying on the beams.

The sample is mounted on a copper plate using a silver glue and positioned in the chamber, where the vacuum is made. A pressure of $4 \cdot 10^{-6}$ mbar is obtained by reaching firstly a low vacuum (10^{-1} mbar) with the primary pump (Figure 4.2, left) and after turning on the turbo-molecular (Figure 4.2 right) , able to reach the vacuum level desired.

The sample and support temperature can be tuned by using a temperature controlled chuck. During the calibration step the temperature is increased step by step and the resistance measured to get the linear curve and extract the temperature coefficient of resistance (α). During the coupling steps the temperature is kept constant (controlled at RT) to ensure the same conditions of measurement, and the voltage is swept in order to detect the resistance-dependent temperature variation on the sensor dependent on the heat transferred through the membrane.

The complete apparatus is shown in Figure 4.2.

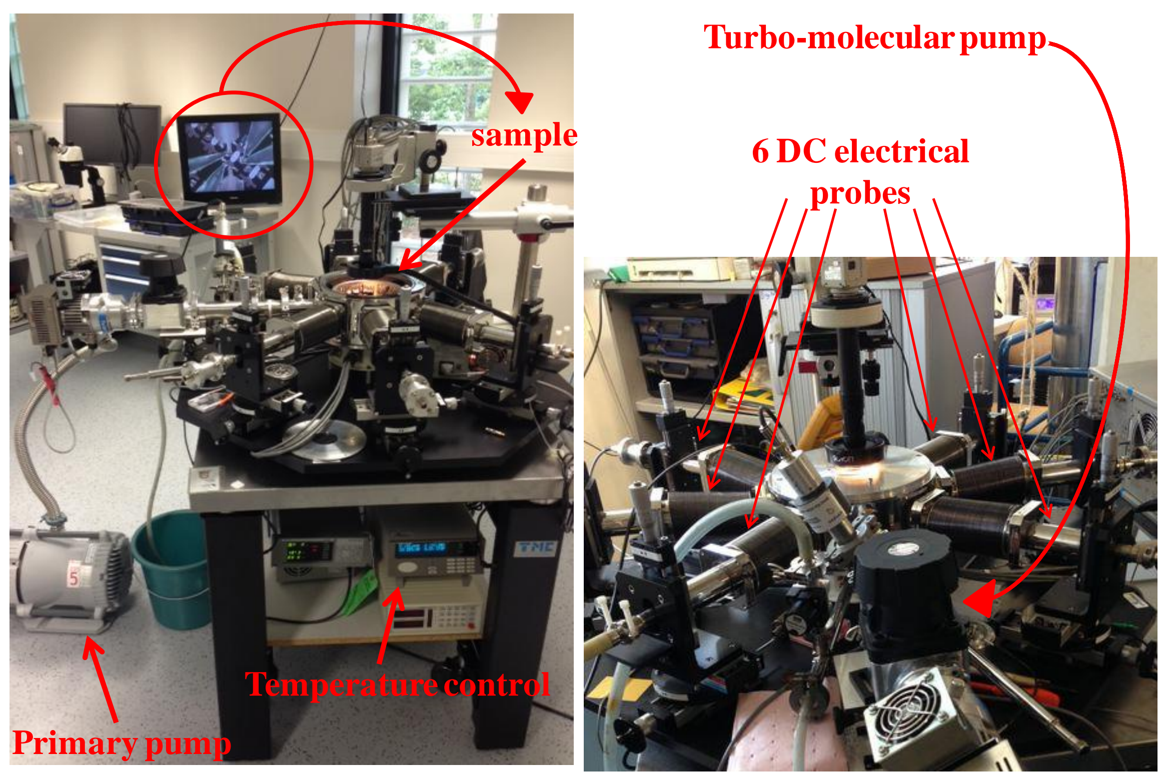

Figure 4.2 Left: Full picture of measurement set up. Right: Detail of the vacuum chamber and arms for electrical probes.

4.2.2 Results

The experimental results are analyzed and explained in the next two subsections for the Electro-Thermal method. It is worth considering the measurement's technical background depicted above and the device different typologies (*generations*) detailed in the previous chapter for a better understanding. The devices designed and fabricated for the Electro-Thermal measurements are two. Thus, the procedures of extracting the thermal conductivity are different, given the different physics underneath. The main point to carefully take into account is that the sensor serpentine is fabricated on the substrate, where the metal is deposited, for the first generation, and fully suspended, with a different temperature respect the chuck's one, for the second generation.

4.2.2.1 1st device generation

The first device designed with phononic engineered patterns is introduced in the previous chapter, along with its fabrication procedure. The details related to the device measured are depicted in Table 4.2.

Table 4.2 Dimensions of the 1st generation device.

Element	Thickness (nm)	Length (µm)	Width (µm)
Heater Serpentine	30	206 (for width 5 µm) 244 (for width 10 µm)	1
Sensor Serpentine	30	47 (for internal, width 5 µm) 90 (for internal, width 10 µm)	1

Element	Thickness (nm)	Length (μm)	Width (μm)
		61 (for external, width 5 μm)	
		104 (for external, width 10 μm)	
Membrane (suspended)	61	5 – 10 – 20 – 30	5 – 10

The first part of the measurement consist of calibrating the serpentine in order to extract the coefficient α. The methodology consist in stepping the temperature of the chuck (T_{chuck}) from 25 to 80°C and registering, at each step, when in steady state, the correspondent resistance value. A small voltage is applied to the sensor (not the VMUs) for 10 seconds to allow the measure. The sensor is supplied by Source Monitor Unit (SMU) from the semiconductor parameter analyzer HP4155c. SMUs are programmable current or voltage sources (when the voltage is specified, the output current is measured). The voltage drop along the sensor serpentine is measured using Voltage Measurement Unit (VMU), two units are available and more precise for voltage measurements) (see Figure 4.3, left). Figure 4.3 depicts the wiring configuration for this step.

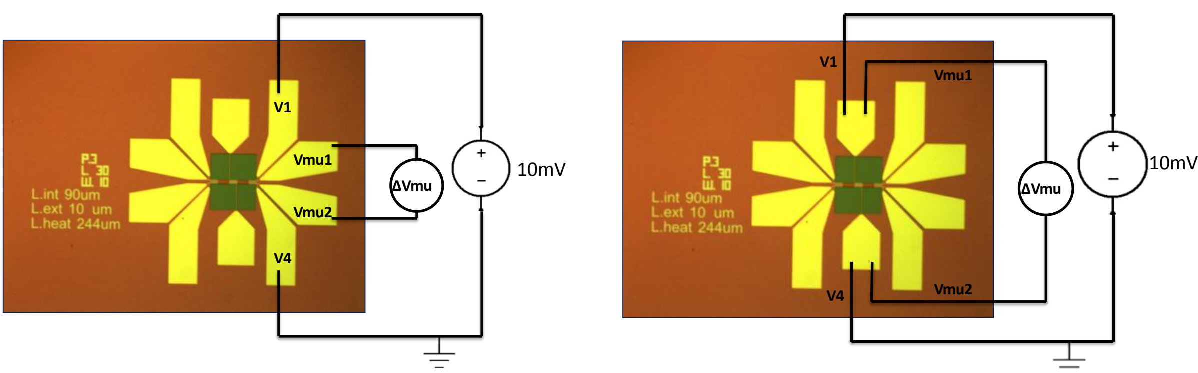

Figure 4.3 Left: Optical microscopy image showing the measurement set up and contacts needed to perform serpentine calibration. A voltage of 10 mV is applied to the sensing serpentines to detect the external resistance, while the chuck temperature is increased step by step and, at each, the correspondent resistance is registered. The measurement is performed averaging 10 seconds of measurement and after having kept the temperature constant for 10 minutes. Right: Measurement set up to perform heater calibration. The measurement principle is the same of the one described above.

The coefficient α is extracted using the equation:

$$\alpha = \frac{\frac{R(T)}{R_0} - 1}{T - T_{chuck}} . \qquad (42)$$

where $R(T)$ is the one correspondent to the temperature T and R_0 relative to the temperature T_0 set at the measurement start (RT).

$$R(T) = \frac{V_{MU1} - V_{MU2}}{I} . \qquad (43)$$

Figure 4.4 reports the linear fit of the resistance experimental points to estimate α, temperature coefficient of resistance, for the suspended membranes (two different widths implies a slightly different Pt serpentine length, thus two different values of α).

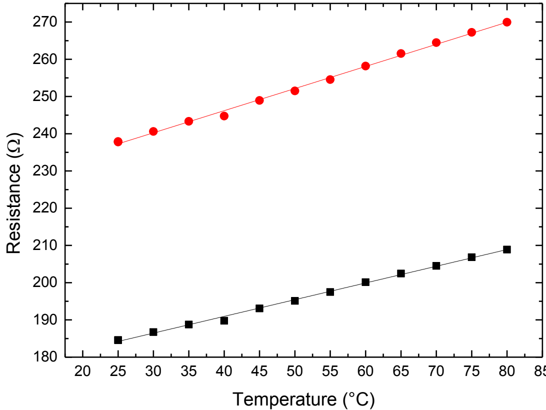

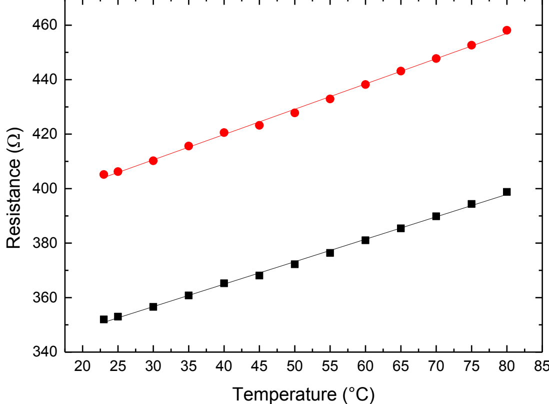

Figure 4.4 Determination of α coefficient for sensor serpentines for membranes of width 5 µm (left) and 10 µm (right). The measurements are performed with four probes under vacuum. Red dots are related to the external resistance measured (SMUs), affected by losses, black dots indicate the internal resistance (R_{int}).

Thus, the values obtained are very similar, as envisaged: α = 0.00256 K^{-1} for the 10 µm width membrane and α = 0.00253 K^{-1} for the 5 µm width one.

Once the two elements are calibrated, the temperature (resistance) variation of the heater needs to be linked to a corresponding temperature (resistance) variation on the sensor serpentine. Thus, another calibration is performed on the heater serpentine. A voltage is swept on the external contacts (V_1 and V_4 in Figure 4.3) in a range from 0 V to 0.75 V with a step time of 5 milliseconds and a delay time of 10 seconds between two measurements. During the measurements, the chuck's temperature is kept constant. The heater being connected to two pads only, it is necessary to place the probes (SMU and VMU) on the same pad.

The variation of resistance is recorded and, given the previous calibration (knowing the temperature coefficient of resistance), the temperature variation as function of the voltage Figure 4.5 is found.

The temperature is extracted, knowing α, with equation (44).

$$T(V) = T_{chuck} + \frac{\frac{R(T)}{R_0} - 1}{\alpha} \tag{44}$$

The relation is parabolic and understandable considering the Joule power released in the heater resistance when the current is flowing. The relation to consider is:

$$P = \frac{V^2}{R} \tag{45}$$

where V is the swept voltage and R the heater's serpentine resistance. Thus, little variation of the applied voltage entails a considerable change of the power released as heat in the resistor and of its resistance value.

The last calibration allows to perform the successive step (*coupling*) of the measurements, the one in which the voltage swept on the heater induces, by Joule heating, a resistance increase on the sensor, which is directly linked to the temperature variation due to the heat transferred through the membrane.

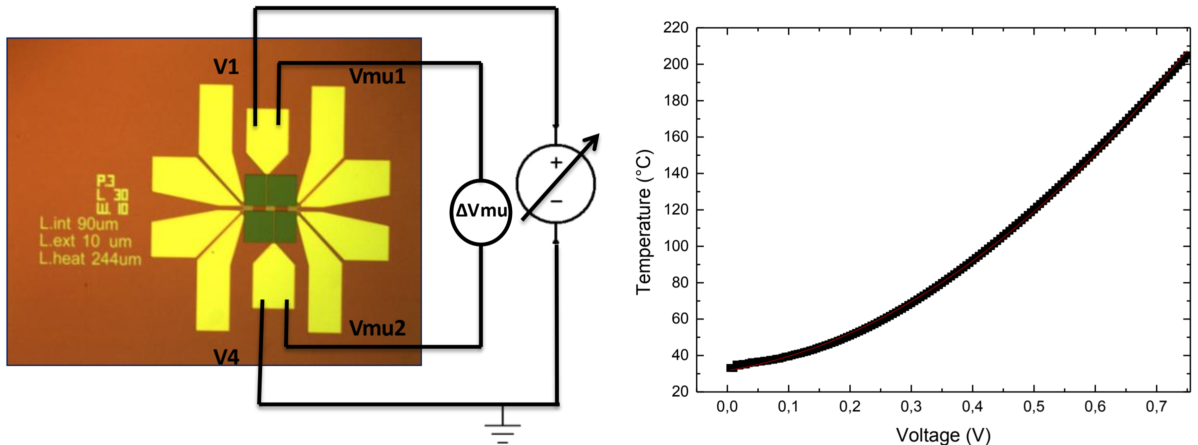

Figure 4.5 Left: Optical microscopy image showing the measurement set up and contacts needed to find the quadratic relation of temperature as function of applied voltage swept on the heater. Right: Temperature as function of voltage supplied to the heater (parabolic fit gives equation (46)).

The equations (46) obtained are different for the two serpentines (due to the different width of the membranes, as mentioned before).

$$T_{heater_10\mu m} = 31{,}75367 + 54{,}28097 \cdot V + 240{,}3097 \cdot V^2 \qquad (46)$$
$$T_{heater_5\mu m} = 30{,}16237 + 90{,}86994 \cdot V + 278{,}4565 \cdot V^2$$

Combining the results obtained for the last calibration (Figure 4.5) with the ones for the sensor's calibration (Figure 4.4) the temperature of the sensor (T_{sensor}) correspondent to a defined voltage applied at the heater can be determined.

Therefore, as anticipated, the *coupling* step is the decisive one allowing the extraction of the temperature gradient established between the sensor and the heater, directly related to the heat transport mechanism trough the membrane and its thermal conductivity κ.

The thermal conductivity is obtained from the Fourier law (equation (41)), considering that the heat injected by the heater serpentine ($V_{HEATER} \cdot I_{HEATER}$), in the two symmetric identical membranes, for Joule effect, is equally transferred in the two directions to the sensors. Moreover, the losses at the heater's arms are subtracted from the total heat flux knowing the nominal resistivity of Pt and the arms' dimensions and estimated with the equation:

$$P_{heater's_arm} = R_{HEATER} \cdot I_{HEATER}^{\ 2} = \frac{L_{beam}}{w_{serp_Pt} \cdot t_{serp_Pt}} \cdot I_{HEATER}^{\ 2} \qquad (47)$$

The formulation of the thermal conductivity equation for this device topology is:

$$\kappa = \frac{V_{HEATER} \cdot I_{HEATER} / 2 - \rho_{Pt} \cdot \dfrac{L_{beam}}{w_{serp_Pt} \cdot t_{serp_Pt}} \cdot I_{HEATER}^{\ 2}}{\Delta T \cdot w_m \cdot t_{m_SOI}} \cdot L_m \qquad (48)$$

where V_{HEATER} is the voltage applied to the heater, I_{HEATER} is the measured current flowing in the heater, ρ_{Pt} is the platinum resistivity, L_{beam} the length of the heater's arms, w_{serp_Pt} the width of the platinum serpentine and t_{serp_Pt} its thickness, L_{membr} the length of the silicon-on-insulator membrane, w_m its width and t_{m_SOI} its thickness. The effect of taking into account the heat dissipated at the heater's arms is depicted in Figure 4.6.

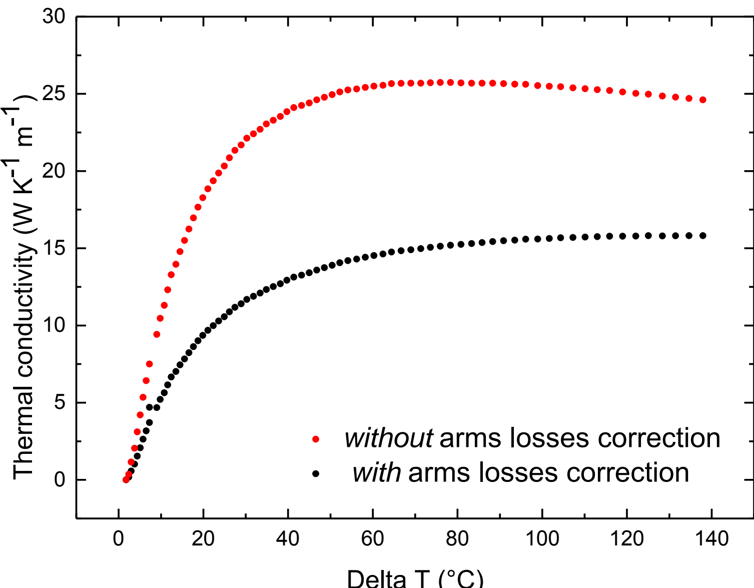

Figure 4.6 Thermal conductivity comparison with and without correction for the heat dissipated trough the heater's arms as function of the temperature difference. Membrane of width 10 µm and length 10 µm.

The coupling measurements are performed on different membranes (lengths and widths), in thermal steady state. The results are given by summing up the contributions of the calibrations previously described.

The wiring configuration for this step is the same as depicted in Figure 4.3 (left), with the difference that the heater is supplied with a DC voltage which is stepped range from 0 V to 0.75 V with a step time of 5 milliseconds and a delay time of 10 seconds between two measurements (as for the heater's calibration step) and the sensor with 10 mV to allow the measurement (small in order not to induce a sensor's resistivity change). The resistance at each step is registered and the correspondent temperature on sensor (T_{sensor}) and heater (T_{heater}) are extracted.

In Figure 4.7 the obtained temperatures on heater and sensors, for all the membranes lengths, are presented as function of the voltage applied on the heater. T_{heater} is much higher than T_{sensor}.

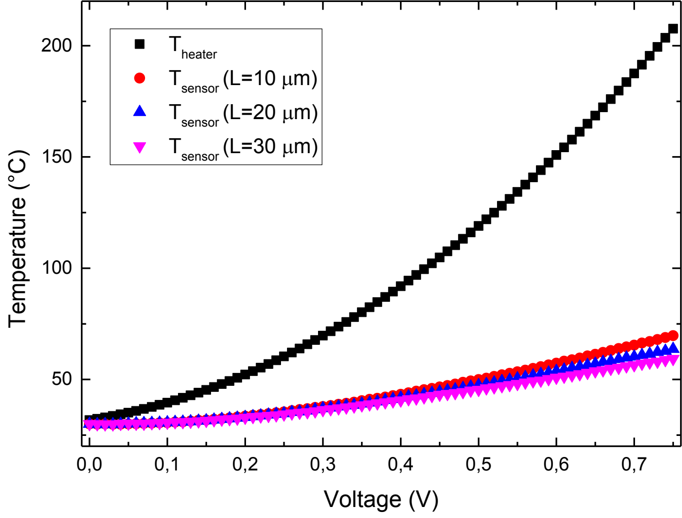

Figure 4.7 Temperature of heater and sensors for three different membranes of length 10 µm, 20 µm and 30 µm.

Figure 4.8 reports the temperatures of heater and sensor for two membranes with same length and different width. The membrane of 5 μm width presents a maximum temperature difference of 170.5°C while the one of width 10 μm a difference of 138 °C. This result leads to different thermal conductivities of κ = 25.170 $WK^{-1}m^{-1}$ for the first of width 5 μm, and κ = 15.816 $WK^{-1}m^{-1}$ for the membrane of 10 μm. The limited number of probes available (2 VMU and 2 SMU) doesn't allow to perform a four-probe measurement on the sensor, which would have resulted in a better accuracy (no VMUs are used, but only SMUs).
The temperatures registered in Figure 4.8 for heater and sensor show that for low heater's voltages not a big sensing is noticed, being the values related to the Joule heating effect of the Pt thermometer. Indeed, when the heat power injected is too small, the resistance variation on the sensor is not significant to be registered.

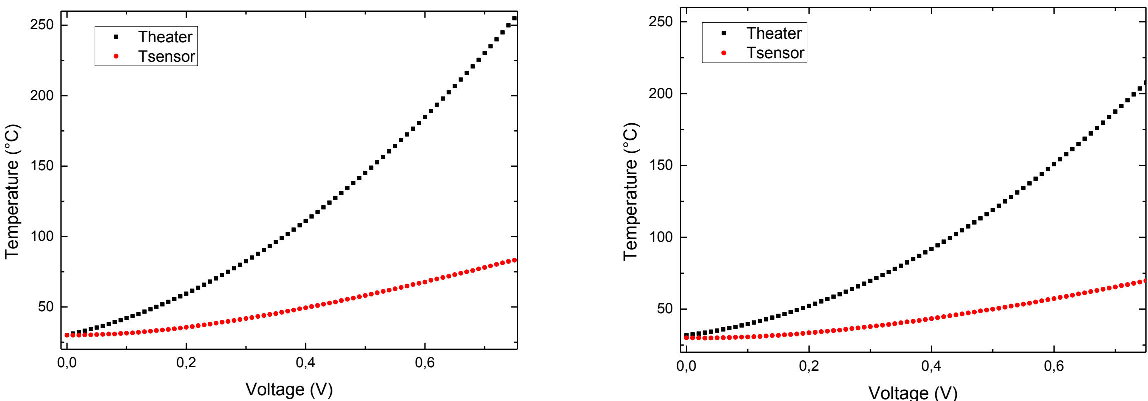

Figure 4.8 Temperature of heater and sensor for a membrane of length 10 μm and width 5 μm (left) and 10 μm (right).

The graphs in Figure 4.9 report the results of thermal conductivity for two devices of this 1st generation for the shorter and longer membranes. It is worth to specify that the thermal conductivity extraction has been performed applying equation (48). Furthermore, the full suspension of the membrane and the performing of measurement under vacuum (no convection affecting) allows the linearization of Fourier's law, as previously described. This operation is also justified considering that the thermal conductivity should be determined in the limit of thermal delta tending to zero ($\Delta T \rightarrow 0$), thus for the lowest possible temperature differences across the membrane.

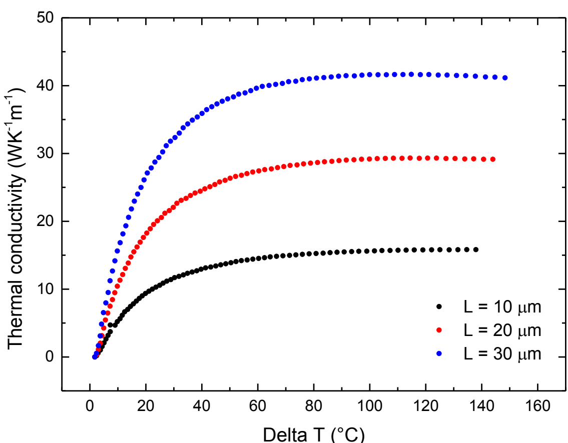

Figure 4.9 Thermal conductivity versus temperature difference of three membranes of width 10 μm and lengths 10 μm (black), 20 μm (red), 30 μm (blue).

The value of κ is linearly extrapolated for low temperatures. The diverging value of thermal conductivity for low temperatures is explained in terms of low sensitivity, a too small ΔT the heat power doesn't allow to sense a electrical resistance variation on the sensor. Reducing the distance between the heater and sensor (membrane length) this decay is faster than for longer membranes (Figure 4.9).

A stronger coupling is established between the heater and sensor for shorter membranes, which implies an "artificially" lower temperature difference. Moreover, the sensor's serpentine laying on the cavity's side, doesn't ensure a good thermal isolation from the underneath layers. Thus, dissipation through the substrate are affecting the sensor's measured temperature and this is the reason why the 2nd device generation was designed. Indeed, errors affect the measurements performed on this device generation which could be due to the heat leakage from the arms of the heater to the substrate (whose estimation is shown in equation (47)) and from the sensor serpentines to the substrate (being the sensor not fully suspended), which justifies the stronger coupling of shorter membranes with respect to long ones.

Figure 4.10 shows the device under IR camera for different voltages applied to the heater, but in air conditions. As anticipated and marked here, low voltages (0.1V), in air conditions, don't guarantee a sufficient sensitivity to evaluate the thermal conductivity and the heat flow, in this case, is also evacuated through the arms to the substrate. For voltages of 0.25 V and 1 V, higher temperatures can be observed on heater serpentine.

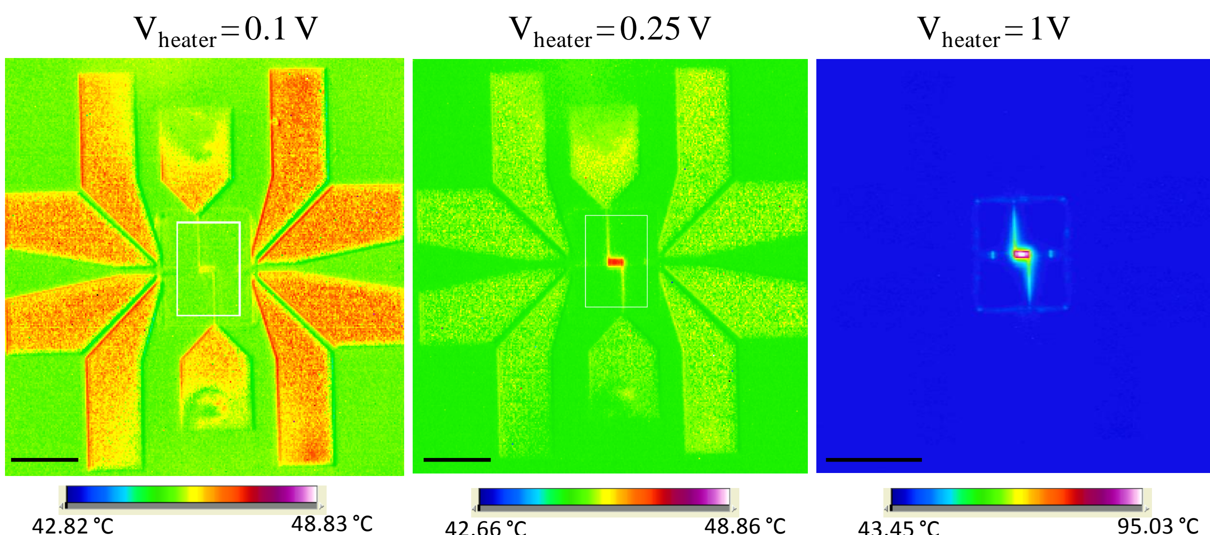

Figure 4.10 IR camera images of the first generation device wit heater supplied by different voltages (0.1 V – 0.25 V and 1 V). Scale bar 90 µm.

Another error which could influence the results is the consideration of the heater as a punctual heat source, which is demonstrated to not be the case. In fact, heater and sensors have not a uniform temperature in the centre with respect the border. The verification of this statement is done by Infrared camera (not in vacuum), whose results are presented in Figure 4.11, for a voltage supplied to the heater of 0.5 V. It is worth to underline that the temperature effect is observable on Pt serpentines, and not on Si, which is transparent to infrared light.

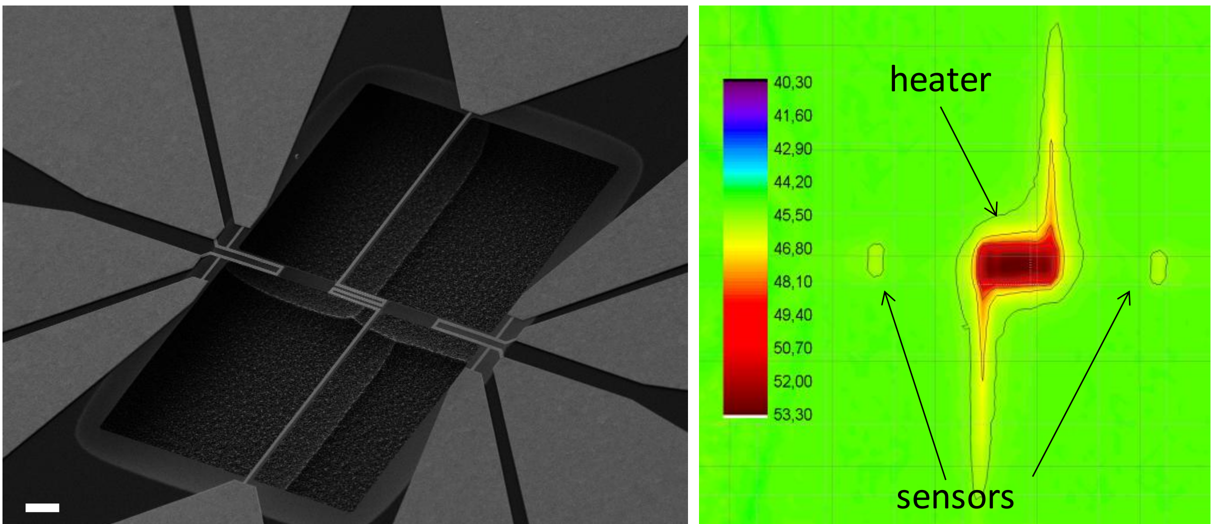

Figure 4.11 Left: SEM image of the full device suspended. Right: IR camera image of the heat distribution when current (0.5 V) is flowing in the heater serpentine. Scale bar 10 μm.

Other errors which are not considered are the ones coming from neglecting the possibility of radiative heat transfer. Moreover, systematic errors due to the equipment are always present, such as contact resistances and accuracy of the measurements device (improved for VMU measurements).
To overcome the cited problems, the first design has been improved and modified, as described in the previous chapter, leading to a second generation device which is described and characterized in the following subparagraph.

4.2.2.2 2nd device generation

Fully suspended wire-like sensor, wider cavities, four-arms connection of the heater, reduced (from 1 μm to 0.5 μm) Pt serpentines' width, more turns for the heater's serpentine (to approximate it to a punctual heat source) and different membranes dimensions are the main characteristics of this second design. The reasons of those modifications along with its details are mentioned in Chapter 3 and recalled herein. In Table 4.3 are depicted the dimensions related to the device measured.

Table 4.3 Dimension of the 2nd generation device.

Element	Thickness (nm)	Length (nm)	Width (nm)
Heater Serpentine	50	100 (for internal, width 5 μm) 257 (for internal, width 10 μm) 237 (for external, width 5 μm) 395 (for external, width 10 μm)	0.5
Sensor Serpentine	50	4.5 (for internal, width 5 μm) 9.5 (for internal, width 10 μm) 142.5 (for external, width 5 μm) 147.5 (for external, width 10 μm)	0.5
Membrane (suspended)	57	30 – 60 – 90 – 120	5 – 10

The methodology adopted to extract the temperature coefficient of resistance α is the same applied to the 1st generation device. The thickness of the platinum layer is augmented from 30

nm to 50 nm, to guarantee a better serpentine resistance to membrane's bending and prevent any breaking problem during the resist stripping phase.

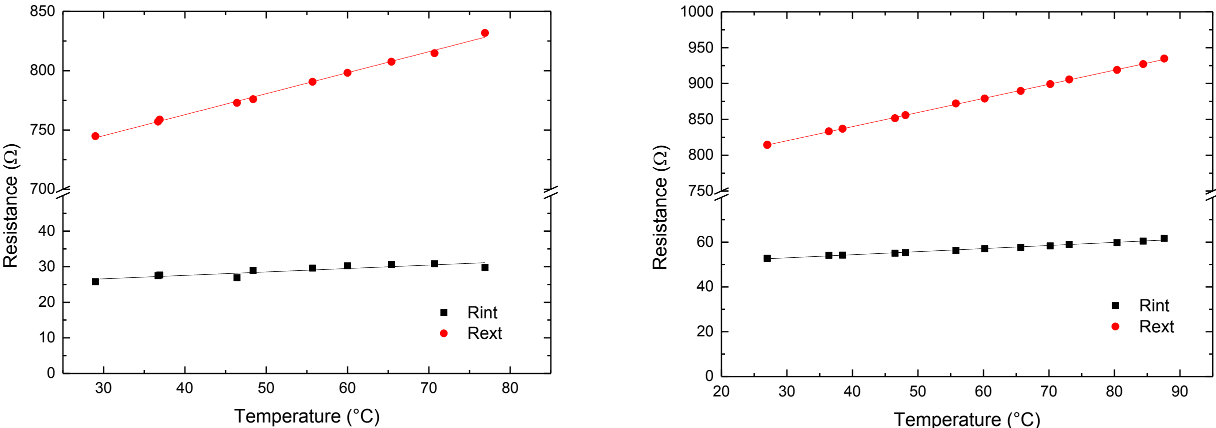

Figure 4.12 Determination of α coefficient for sensor serpentines for membranes of width 5 µm (left) and 10 µm (right). The measurements are performed with four probes under vacuum. The black points show the internal resistance R_{int}.

The value found for the temperature coefficient of resistance for the heater and sensor of membranes of width 5 µm and 10 µm are summarized in Table 4.4.

Table 4.4 Temperature coefficient of resistance for membranes of width 5 µm and 10 µm. *Value higher than expected one.

	α (K^{-1}) for W = 5		α (K^{-1}) for W = 10	
	Heater	Sensor	Heater	Sensor
R_{int}	0.00255	0.00407*	0.00265	0.00283
R_{ext}	0.00259	0.00255	0.00254	0.00259

The resistances used to extract the temperature differences across the membranes are the ones called R_{int} (internal resistances), which are not affected by losses. The measurement schematic set-up is presented in Figure 4.13 (right) with the connections drawn for the 4-probes heater serpentine calibration.

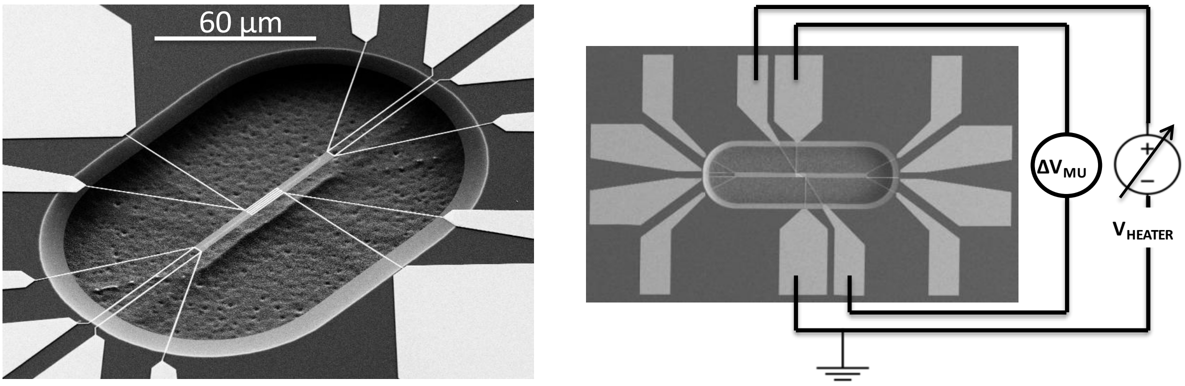

Figure 4.13 Scanning Electron Microscopy (SEM) image of the device (left) and SEM with schematic draw of wiring connections for: 4-probes connections for heater serpentine calibration (to extract the *α* as explicated before) (right).

Considering the symmetry of the device, with two identical membranes (Figure 4.13), Electro-Thermal measurements have been performed on the two sides of the membranes to verify that the temperature differences established at the two extremities of the sensor serpentines are comparable. The set-up for 6-probes Electro-Thermal measurement is

sketched in Figure 4.14 (left), with the two supplying connections placed on the heater serpentine (for V_{HEATER}) and the 4-probes sensing ones on the right side sensor.
The established temperature difference between heater and sensor is the needed data to extract the thermal conductivity of the membrane. The value is obtained repeating the same measurements of resistance with four probes on heater (with two probes on sensor) in such a way to find the exact heater's resistance, getting rid of losses in current conducting arms, thus extracting the arm's resistance value, and on sensor, to establish the sensor resistance without losses (repeated on the two symmetric sensor).
The model built to extract this parameter implies the values of the electrical resistances (R_{H_int}, R_{H_ext}, R_{S_int} and R_{S_ext}) obtained to extract, by using the calibration, the temperature differences.
To better understand the model it is worth to specify that for the R_{int} extraction, in both the cases of heater and sensor serpentines, the values are fitted with an order 2 polynomial at low voltages, in such a way to better estimate the intercept value (R_0).

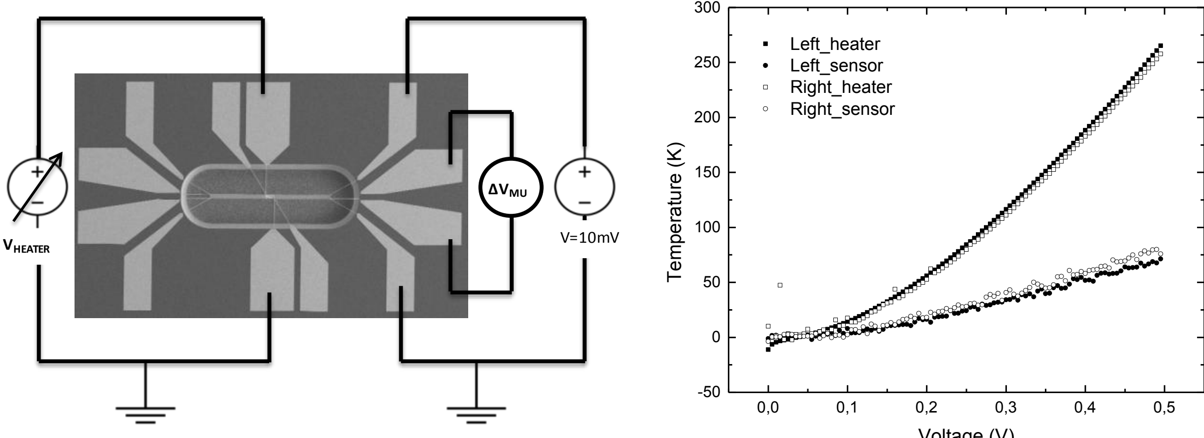

Figure 4.14 Left: 6-probes connection for Electro-Thermal coupling between heater and sensor serpentine (to extract the temperature delta), right: temperatures measured by 6-probes Electro-Thermal method for heater and sensors (both the sides).

In the right graph presented in Figure 4.14 the temperatures extracted for heater and sensors are drawn (T_H: heater's temperature, T_S: sensors' temperature and T_0: chuck's temperature). It is worth to specify that the *coupling* measurement is performed with two probes on the heater serpentine, and four on the sensors ones, the left and right one. The graph highlights that the membranes conduct the heat in the same way, presenting the same temperature at the opposite serpentines. Few degrees of temperature disagreement are tolerated for this results and related to structure differences, as: probe displacement from one contact to the other, different positioning of the probe on the contact (with a different incident angle), Au contacts imperfections (relative to the metal deposition process, metal scratch or degradation), Pt serpentines imperfections (due to the deposition process). Thus, the main error results from the slight asymmetries of the system that can arise from fabrication process imperfections, which are critical for the investigation of any kind of heat flow influenced by Joule effect.
Once the temperature difference are individuated, it is needed to find the correct device modelling which allows the extraction of the thermal conductivity taking into account all the parameters and losses.

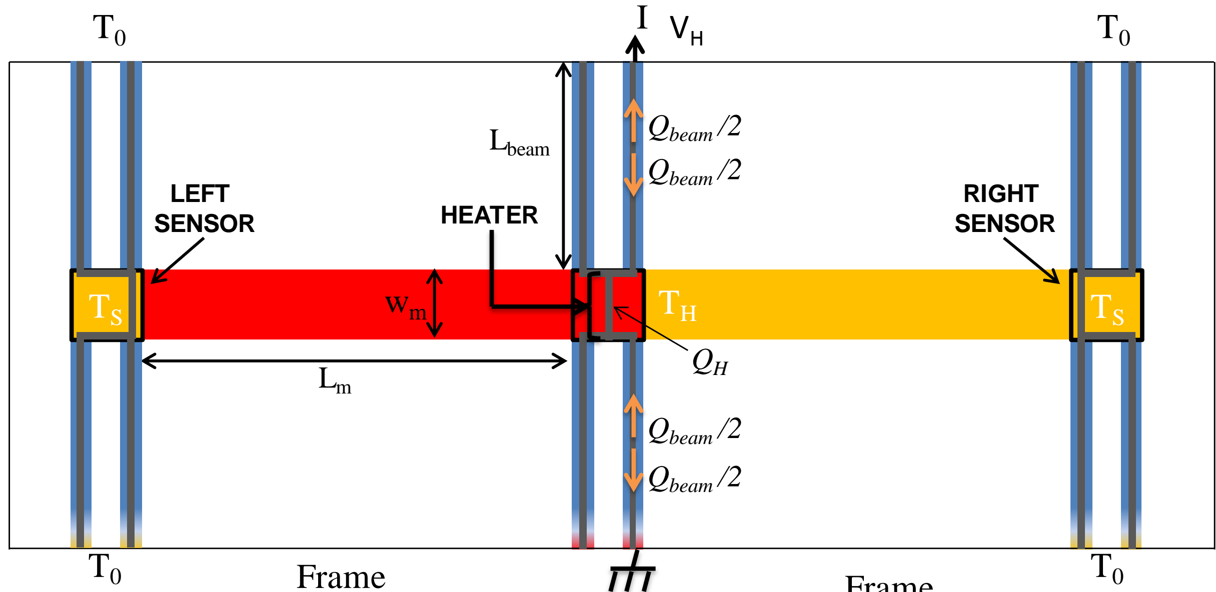

Figure 4.15 Schematic draw of the suspended platform, with central heater and symmetric sensors.

The starting equation to obtain the thermal conductivity formulation is the Fourier's law :

$$\vec{Q} = -\kappa \cdot \vec{\nabla} T \tag{49}$$

with Q the local heat flux entering the membrane (delivered at the heater), κ the membrane's thermal conductivity, ∇T the temperature gradient between heater's temperature T_H and the sensor's one T_S.

Considering the fact that the membrane in this design (in Figure 4.15) is fully suspended and the sensors have a different temperature with respect to the one of the regulated chuck (frame), two others temperature deltas are introduced:

$$\Delta T_H = T_H - T_0 , \tag{50}$$

for the heater, with ΔT_H the heater's temperature difference respect the chuck's one;

$$\Delta T_S = T_S - T_0 , \tag{51}$$

for the sensor, with ΔT_S the sensor's temperature difference respect the chuck's one.

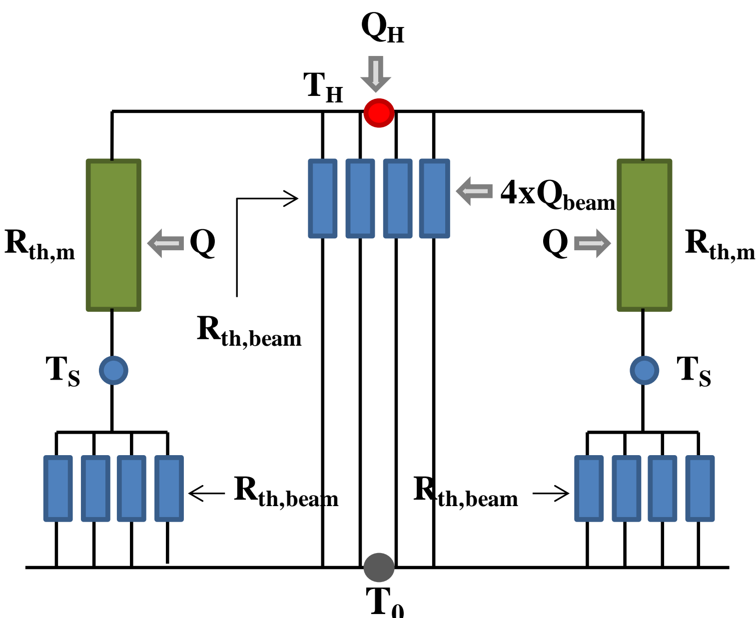

Figure 4.16 Thermal circuit model of the measurement platform.

The membrane conductance G_m is:

$$G_m = \frac{Q}{T_H - T_S}, \tag{52}$$

At the heater serpentine's side the energy conservation gives:

$$\frac{Q_{beam}}{2} + \frac{Q_{beam}}{2} + Q_H = 2 \cdot Q + 4 \cdot G_{beam} \cdot \Delta T_H, \tag{53}$$

where the left terms are related to the heat entering the heater serpentine, getting rid of the beam losses. The first two terms ($Q_{beam}/2$) are related to the heat conducted from the beams in which the powering current flows, in the two directions. Q_H is the heat injected through the heater. The sum of the terms at the left-hand side of the equation is equal to the electric power delivered to the heater is equal to:

$$\frac{Q_{beam}}{2} + \frac{Q_{beam}}{2} + Q_H = (R_{H_int} + R_{beam})^2 \cdot I. \tag{54}$$

The right terms sum up the heat flow contribution exiting form heater to the membranes and to the heater beams.

At the sensor serpentine's side the energy conservation gives:

$$Q = 4 \cdot G_{beam} \cdot \Delta T_S. \tag{55}$$

Thus, merging equation (52) and (55):

$$G_m = \frac{4 \cdot G_{beam} \cdot \Delta T_S}{T_H - T_S} \tag{56}$$

and

$$G_{beam} = \frac{G_m \cdot (T_H - T_S)}{4 \cdot \Delta T_S}. \tag{57}$$

Substituting (54) on the right-hand side of equation (53) and (55) on the left-hand side:

$$(R_{H_int} + R_{beam}) \cdot I^2 = 2 \cdot 4 \cdot G_{beam} \cdot \Delta T_S + 4 \cdot G_{beam} \cdot \Delta T_H, \tag{58}$$

the equation of the membrane's conductance is obtained:

$$G_m = \frac{\left(R_{H_\text{int}} + R_{beam}\right) \cdot I^2 \cdot \Delta T_S}{\left(2 \cdot \Delta T_S + \Delta T_H\right)\left(T_H - T_S\right)} = \frac{V_{HEATER} \cdot I_{HEATER} \cdot \Delta T_S}{\left(2 \cdot \Delta T_S + \Delta T_H\right)\left(T_H - T_S\right)}. \quad (59)$$

Once the heat conductance is calculated, the membrane's thermal conductivity comes from:

$$\kappa = G_m \cdot \frac{L_m}{w_m \cdot t_{SOI}}. \quad (60)$$

Therefore, the final equation for the extraction of the membrane's thermal conductivity is:

$$\kappa = \frac{\left(R_{H_\text{int}} - R_{beam}\right) \cdot I^2 \cdot \Delta T_S}{\left(2 \cdot \Delta T_S + \Delta T_H\right)\left(T_H - T_S\right)} \cdot \frac{L_m}{w_m \cdot t_{SOI}}. \quad (61)$$

It is possible to apply systematically the previous modelling in order to extract κ of the membranes. Indeed, if no losses are present ($4 \cdot G_{beam} \cdot \Delta T_H = 0$), the general equation used for the first device generation is retrieved $\kappa = \frac{V_{HEATER} \cdot I_{HEATER} / 2}{\Delta T \cdot w_m \cdot t_{m_SOI}} \cdot L_m$). It is worth mentioning that all the measurements were performed on heater and sensors, in order to extract the exact contribution from the sensor arms. However, the heater's arms being almost identical for every device, the contribution of the resistance (parasitic) of each one is roughly the same (verified from the left and right side measurement extraction):

$$R_{beam} = \frac{R_{HEATER_ext} - R_{HEATER_\text{int}}}{2} \approx 340\Omega.. \quad (62)$$

The obtained values of heater's resistance (R_{HEATER_int}) are summarised in Table 4.5. It is remarkable that, given the same dimensionalities of heater's arms, the value obtained for the resistance is the same for different membranes.

Table 4.5 Internal resistance of heater extracted for different membranes (equation (62)).

Membrane	R_{HEATER_int} – Left (Ω)	R_{HEATER_int} – Right (Ω)
L30W10	336	358
L60W5	343	359
L120W10	351	335
L60W10	332	349
L90W10	337	341

The thermal conductivity has been calculated for all the membranes. Moreover, considering that the fabricated cells present membranes with different length, their results are presented in Figure 4.17, which shows the thermal conductivity as function of the swept voltage on the heater, for three different membranes with different lengths and same periodic phononic patterning. Membranes of 30 µm, 60 µm and 90 µm are compared, along with their thermal conductivity of 43 W K^{-1} m^{-1}, 41 W K^{-1} m^{-1} and 40 W K^{-1} m^{-1}, respectively. It is necessary to underline that membranes of different length exhibit the same thermal conductivity, confirming the hypothesis that the second designed structure solves the problem of length dependence of κ and losses.

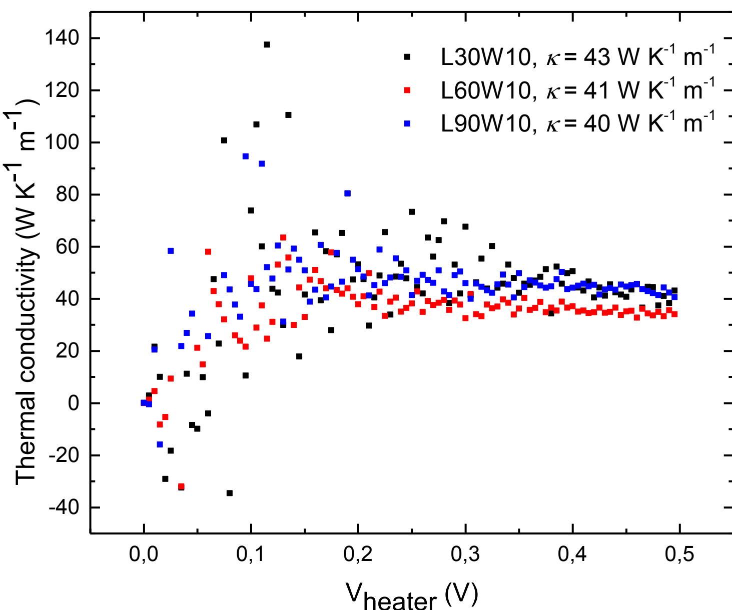

Figure 4.17 Thermal conductivity comparison between membranes of same width (10 µm), but different lengths (30 µm, 60 µm and 90 µm) and three pitches.

The heater and sensor calibrations steps previously described, allow to relate the V_{heater} to the Temperature difference between heater and sensor. The heat gradient is linear on the membrane and its average temperature is considered being: $\frac{T_H + T_S}{2}$. Thus, the thermal conductivity can be plotted as function of the average temperature of the membrane (as in Figure 4.18).

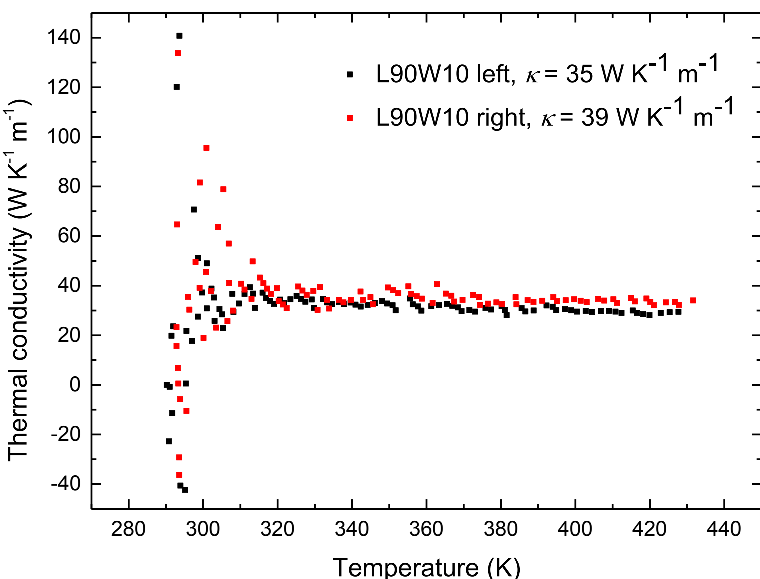

Figure 4.18 Thermal conductivity comparison between left sensing serpentine measurement and right one for a membrane of pitch 60 nm, length 90 µm and width 10 µm.

In Figure 4.18 the membrane's thermal conductivity is measured on the left and right sensors and plotted. The membranes (at the two sides of the same symmetric device) exhibit a similar

value of κ, confirming the hypothesis made on the heat symmetrically injected from the heater in the two membranes and its transport mechanism to the sensors.
The thermal conductivity results obtained for the temperature range 297 K – 430 K are plotted in Figure 4.18 for the same holey membrane of pitch 60 nm. The thermal conductivity results equal to 35 W K^{-1} m^{-1} for the measurements performed with 4 probes on the left sensing serpentine, 39 W K^{-1} m^{-1} for the one with the probes positioned on the right one. Besides the membrane length shouldn't influence its thermal conductivity, still it is notable that small degrees of temperature difference, even if on the two sides of the same device, as shown in Figure 4.14 (right), entail different thermal conductivity results. This is the case shown for the three different lengths on Figure 4.17.
As detailed in Chapter 3, the second generation device's design presents membranes with periodic patterns of pitch 60 nm and membranes with three different pitches aligned: 50 nm, 55 nm and 60 nm. The idea of etching three different pitches on the same membrane comes from the interest in studying the cumulating effect of phonon filtering. Indeed, hindering the phonon transport in a range of different lengths (pitches), would correspond to obstacle the travel of phonon with different mean free paths, thus a bigger population of the spectrum.
In Table 4.6 are reported the results for thermal conductivities of different devices measured.

Table 4.6 Summary of the thermal conductivity results for membranes of different dimensions and nanostructure. *Value lower than the expected one.

Thickness (54 nm)	Length (μm)	Width (μm)	κ (W/m/K)
Plain	120	10	69
1 pitch (60 nm)	90	10	37
	30	10	32
	90	5	20*
	90	5	24*
3 pitches (50/55/60 nm)	90	10	40
	60	10	41
	30	10	43
	60	5	23*

As highlighted in Table 4.6 the phononic period patterning of the thin film membranes leads to a decreasing of the thermal conductivity with respect to the one measured for plain ones. Considering the patterned periodic structure, not a considerable difference is registered for membranes with one pitch repeated and those with the three different ones assembled. The reason advanced is that, being the difference in neck size (limit parameter for the structure typology) of the three pitches (50 nm, 55 nm and 60 nm) small (few nm), the cumulative effect of phonon filtering, with respect to their mean free patch, is not remarkable.
It is remarkable that the cited reduction of conductivity is 50% with respect to the one registered for thin film membranes. The incredible phononic effect observed by recent works ([131], [129], [130], [185], [122]) is not of the same order for the designed membranes here shown. It has to be taken into account that the measurement methodology is different along with the membrane's thickness and periodic patterns dimensions (pitches, neck sizes, filling fractions). The results obtained by Electro-Thermal method are compared with state-of-the-art ones in Figure 4.19 (plain triangles). The results presented are from first and second

generation and are agreeing with the fitted model and the experimental values shown and already discussed.

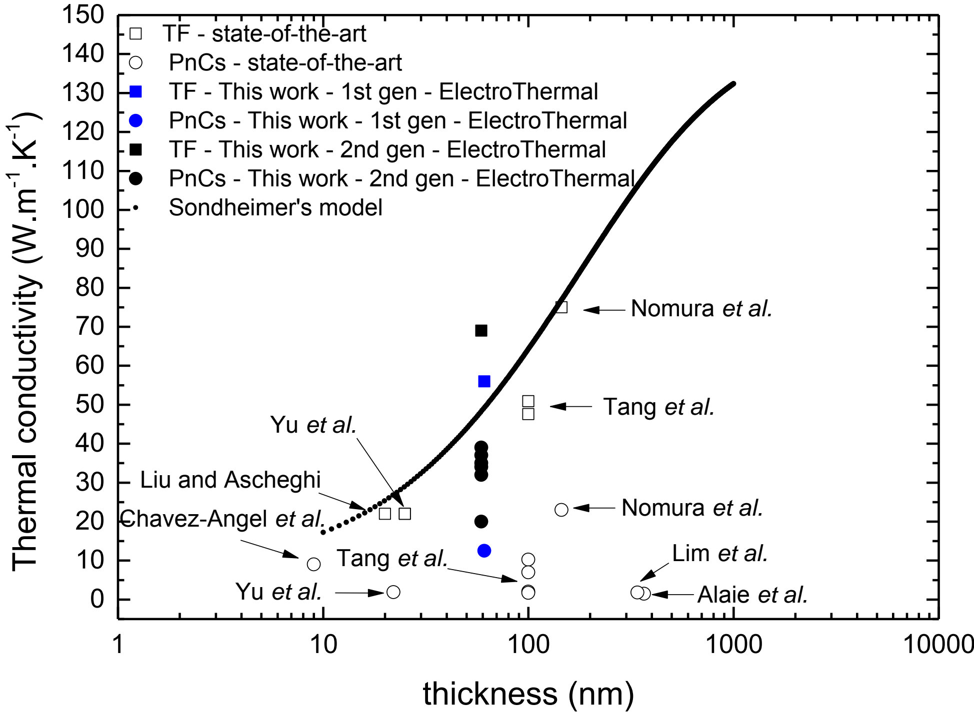

Figure 4.19 Thermal conductivity of thin film membranes (TF) and Phononic crystal ones (PnCs) for this work and for state-of-the-art results.

4.3 Raman thermometry

Raman thermometry is a thermal conductivity characterization method that makes use of Raman spectroscopy. Indeed, the working principle is based on Raman scattering, the inelastic scattering of monochromatic light, usually from a laser in the visible, near infrared, or near ultraviolet range. The laser light interacts with optical phonons in the material, resulting in the energy of the laser photons being shifted up or down. The shift in energy corresponds to the optical phonon frequency and thus is specific of the material and can be modified by local strain due to temperature.
Considering that the goal of our measurements is the finding of the membranes thermal conductivity, the laser is used as a thermal heat source, which is absorbed and dissipated through conduction in the membrane. Thus, the consequent increase of temperature can be measured locally by Raman thermometry. The laser source has then two functions: it acts as heat source and as a thermometer.
Furthermore, Finite element method simulations allow to relate the temperature variation found for the specific geometry of membrane to the heat dissipation, determining its thermal conductivity, as described in the following paragraph. Another method used, involving Raman scattering, is the Two-Laser Raman Thermometry, which exploit a laser as pump (heating) and another as temperature probe in a contactless methodology [186].
For the experiments described below the device conceived for Raman spectroscopy, detailed in Chapter 3, has been used.

4.3.1 Overview of the procedure

Experimental studies of the inelastic scattering of light by crystals can provide information about the optical modes of lattice vibration at the center of the Brillouin zone. In pure materials it is well known that both the line center and the linewidth vary with the temperature. The temperature dependence can be attributed to the anharmonic terms in the vibrational potential energy.
For Silicon-On-Insulator structures, a typical spectrum is shown in Figure 4.20 [187]. The typical silicon peak at room temperature is marked.

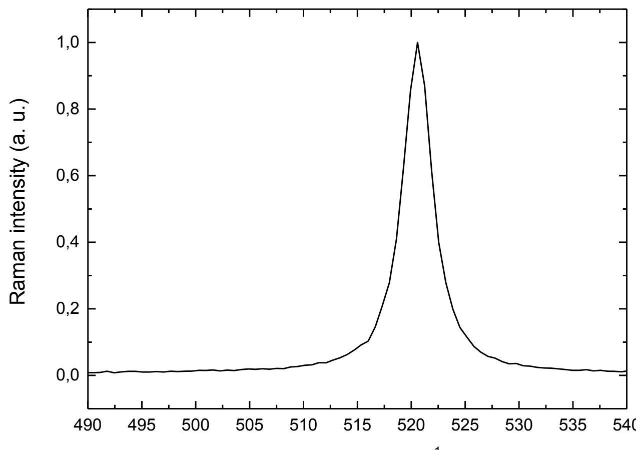

Figure 4.20 Spectrum of SOI structure with the Si characteristic TO peak targeted during Raman measurements at 522 cm^{-1}.

Laser power is 0.01 mW.

The membrane thermal conductivity is extracted by the knowledge of the incident power, absorbed one and, from the 2D heat equation, the temperature rise at the focusing spot can be determined. The heat propagation equation, in the case of a laser impinging on the membrane is:

$$\nabla^2 T = \frac{P_A}{(\kappa \pi a^2 t) e^{-(r/a)^2}} \tag{63}$$

In (63) P_A is the absorbed power, a the spot radius and t the membrane's thickness.
When the device's geometry is straightforward it exists an analytic solution for the heat equations which links directly the heat source to the thermal conductivity. In our case, being the sample's geometry complex, it is necessary to use FEM modelling to solve the heat equation. Thus, once the temperature differences have been evaluated from Raman spectroscopy (in section 4.3.2), it is possible to compare them to the ones simulated by FEM methods to deduce the thermal conductivity of the membrane. To do so, firstly the membranes absorption for targeted thickness and laser wavelength is estimated, after, the thermal conductivity is found by opportune FEM modelling of the structure under study.
The main steps, detailed in the next subparagraphs, are :

- Shine laser on the membrane and deduce the temperature from peak's shift,
- Determine the sample's optical absorbance in order to evaluate P_A,
- Solve heat equation analytically or model with FEM the membrane's geometry and tune κ in order to reproduce the measured temperature.

4.3.2 Detailed methodology

The following section is devoted to the description of the Raman technique approach and the main steps characterizing the measurements. Firstly, the shift from the main silicon optical phonon peak has to be identified. Secondly, this shift needs to be related to a temperature difference across the membrane. At this point, a Finite Element Method (FEM) model of the device under test has to reproduce the same heat transport condition. The thermal conductivity in the model is systematically tuned, in such a way to obtain the same temperatures found experimentally. To build a proper FEM model (by COMSOL), the nanopatterned material absorption properties need to be evaluated by Rigorous Coupled-Wave Analysis (RCWA).

4.3.2.1 Membrane scanning

The temperature variation is obtained from the shift values found experimentally. In Balkanski *et al.* [188] the damping constant (Γ) and frequency shift (Δ) are investigated as a function of temperature (between 5 and 1400 K), being proportional to the real and imaginary parts of the proper self-energy. The approach is based on Klemens model [189]. In the treatment, three and four phonon processes are taken into account to avoid any discrepancies with experimental results at high temperatures. Indeed, damping constant (Γ) and frequency

shift (*Δ*) are the sum of contribution arising from the cubic, quartic and higher order terms in the anharmonic Hamiltonian.
The damping constant as function of temperature is calculated from:

$$\Gamma(T) = A\left[1+\frac{2}{e^{x}-1}\right] + B\left[1+\frac{3}{e^{y}-1}+\frac{3}{(e^{y}-1)^{2}}\right] \tag{64}$$

with $x = \hbar\omega_0/2k_BT$, $y = \hbar\omega_0/3k_BT$, A = 1.295 and B = 0.105 (anharmonic constants from [188]) [190].
The resonant frequency *Ω(T)* determines the scattering line position as a function of *T* and is shown to fit the data of [188] specified by the expression:

$$\Omega(T) = \omega_0 + \Delta(T) \tag{65}$$

with

$$\Delta(T) = C\left[1+\frac{2}{e^{x}-1}\right] + D\left[1+\frac{3}{e^{y}-1}+\frac{3}{(e^{y}-1)^{2}}\right] \tag{66}$$

with ω_0 the shift at 0 K, equals to 528 cm^{-1}, *C* and *D* are constants with the values -2.96 and -0.174 cm^{-1}, respectively. Also, it is simplified: $x = \hbar\omega_0/2k_BT$ and $y = \hbar\omega_0/3k_BT$.
The D term represents the 4 phonons contribution which allows a better fitting at high temperatures.
Above room temperature the relationship between Raman shift and temperature is typically linear. Expanding expressions for the thermal expansion and anharmonic coupling effects [188], [191] in a Taylor series and cutting off at linear terms, the slope for this relationship is given by:

$$\left(\frac{d\omega}{dT}\right) = -3\omega_0\gamma\alpha + \frac{k_B}{hc\omega_0}\left[4A+9B\right] \tag{67}$$

with γ the Grüneisen parameter, α the coefficient of linear thermal expansion, and *A* and *B* are the cubic and quartic anharmonic constants, respectively [191].
Alternatively, deriving the line position-shift dependent equation (65), with respect to the temperature, and substituting the room temperature value (300 K) the parameter $\chi_T = \partial\omega/\partial T\big|_{T=300K}$ is obtained. From our calculations, χ_T equals -0.022, which is in good agreement with previous reports.

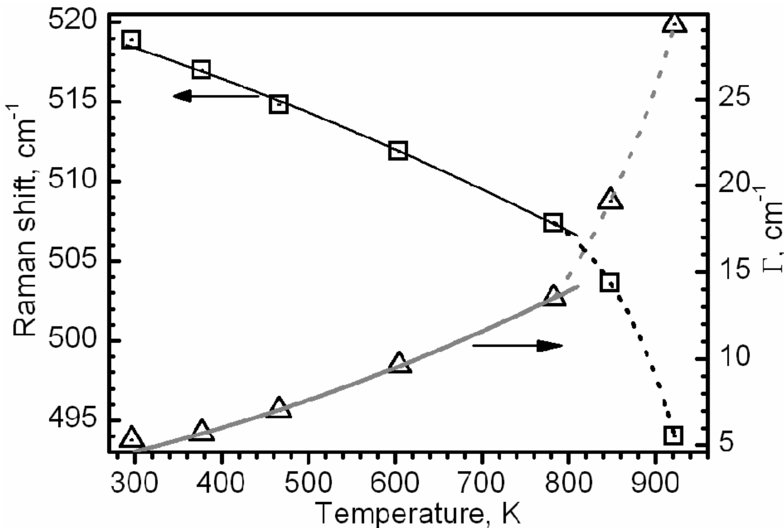

Figure 4.21 Raman shift and damping factor Γ of silicon nanocrystals as a function of temperature [25].

In Figure 4.21 the Raman shift (left axis) and the damping factor (right axis) are plotted as a function of the temperature. The displacement of the silicon peak toward lower frequencies is linked to the decrease of thermal conductivity in the membrane. Indeed, on bulk the heat is efficiently evacuated, thus the peak doesn't shift. In the case of suspended thin films, the heat is evacuated with difficulty, therefore the membrane temperature increases.

Several measurements and tests have been conducted before defining the best methodology to systematically find the highest temperature point at the center of the membrane. A scanning of the whole membrane has been performed, making use of the mapping function of the Horiba Jobin-Yvon Raman Spectrometer [192], to individuate the temperatures along the membrane length.

Firstly the membrane is aligned in the scan direction and the zero of the coordinate system is positioned in the middle of the membrane. An opportune power density is chosen, in such a way not to burn the membrane, therefore, the scan is performed along its length and extended over 50 µm outside the suspended part, in order to collect sufficient baseline points to calculate the shift.

Figure 4.22 (right) presents the Raman peak shift as function of the wave number for different power densities (D). The densities are related to the nominal laser power (P_0) by the equation:

$$P = P_0 \cdot 10^{-D}. \tag{68}$$

From the figure it can be remarked that the peak is moving towards lower wave numbers and enlarged in accordance with the increase of the power. Furthermore, it is registered a displacement of the non–linear part of the spectra and, for higher power, a "side low peak" appears at the normal frequency of the Si (pink) due, maybe, to a substrate background influence (as will be shown, the membrane is partially transparent at this wavelength). Once the shift from the main silicon peak (522 cm^{-1} for silicon at room temperature) is determined, a Lorenzian fit is performed on the baseline of Raman shift to get the reference shift outside of the membrane.

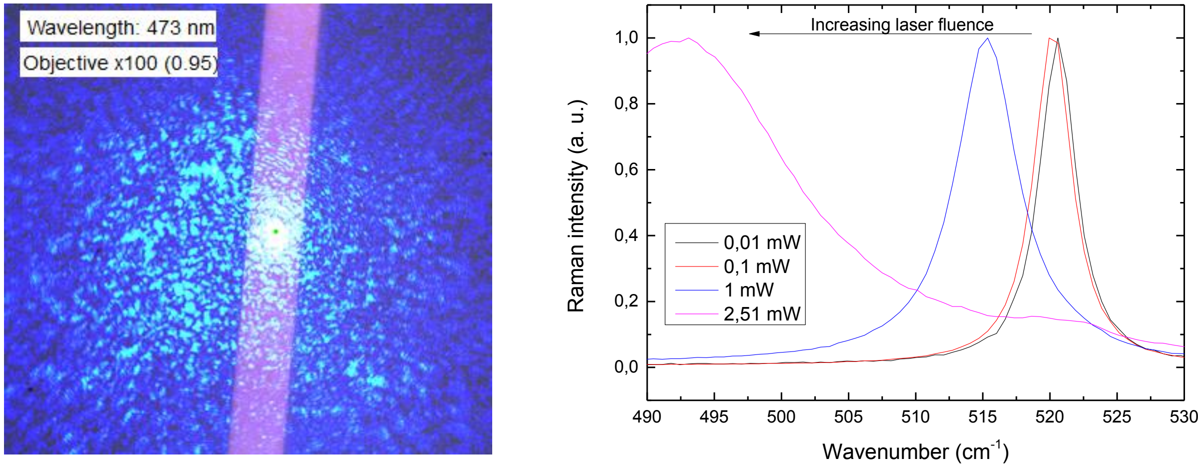

Figure 4.22 Left: Laser light (wavelength 473.11 nm) focused on the membrane. Right: Raman peaks shift as function of the wavenumber for different power densities. Powers are: P1 = 0.01 mW, P2 = 0.1 mW, P3 = 1 mW, P0.6 = 2.51 mW and nominal power P_0 = 10 mW.

The color map in Figure 4.23 clearly shows the shift of the Raman peak along the membrane, confirming the parabolic shape of the curve found for different membranes (listed below) and analysing it in a range of 8 µm of width (1 interval = 1 µm).

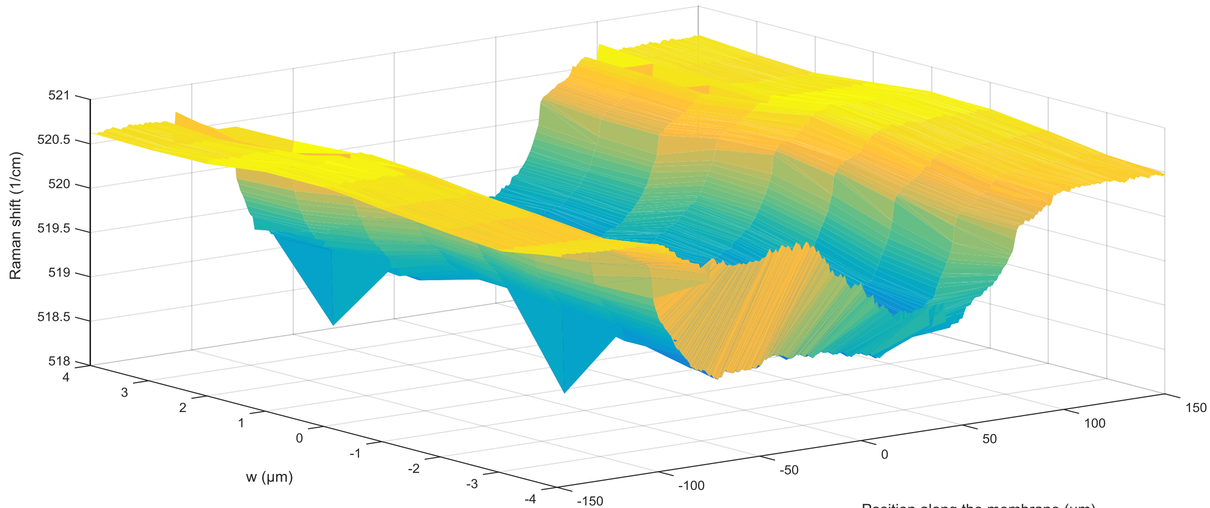

Figure 4.23 3D color map showing the peak's shift as function of membrane length (position along the membrane) and width.

The temperature variation can be extracted by applying the coefficient found by the equation:

$$T = \frac{\Delta(T) - baseline}{\chi_T}. \tag{69}$$

In Figure 4.24 are summarized the cited results: the temperature difference as function of the position on the membrane is plotted for three membranes of different lengths (50 µm, 100 µm and 200 µm).

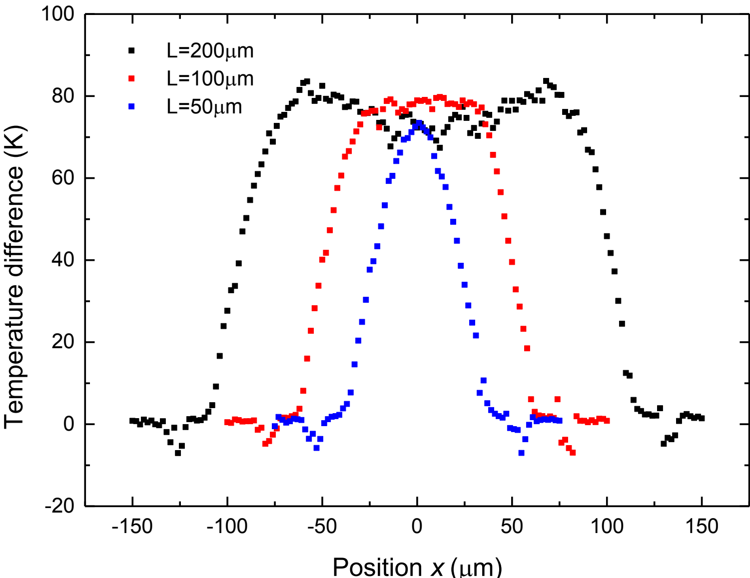

Figure 4.24 Results of Raman spectroscopy on three different membranes of lengths 200 µm (black), 100 µm and 50 µm (d, e, f). The temperature variation with respect to the spot position on the membrane, obtained following the procedure previously depicted, are shown.

The difference in the curve shape for the three membranes considered is justified by their different lengths. It is worth to underline that the temperature registered at the center of the membranes is the parameter to consider to successively extract the thermal conductivity. As expected, the central point corresponds to similar temperature for the three membranes analysed (respectively : 74 K for the membrane of length 200 µm, 79 for the one of 100 µm and 73 for the one of 50 µm). The lateral decay is due to the heat dissipation at the borders and its shape is dependent on the membrane’s length.
Figure 4.25 reports two different membranes measured on the the two different devices. The left graph reports the results of suspended thin films of length 200 µm and width 10 µm. The graph on right shows the results for the same devices, but length 50 µm and same width of 10 µm.

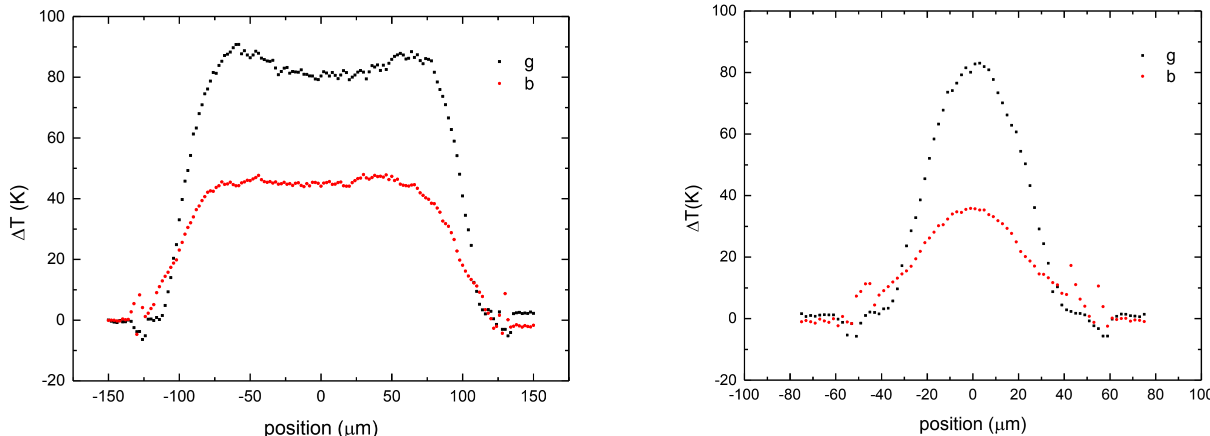

Figure 4.25 Comparison between the temperature gradients measured on the two different devices (*b* and *g*) for two different membranes lengths: 200 µm left and 50 µm right (same width of 10 µm).

The temperature increase at the sides of the membranes with respect to their center, appearing in Figure 4.24 and Figure 4.25 for longer membranes (200 µm), is justified by a possible

slight misalignment of the membrane scan. Indeed, hot spots are present at the extremities, outside of the suspended part, as shown in Figure 4.23.
The different temperature levels are accounted for a different silicon thickness and filling fraction (due to the different diameters of the PnCs). The repeated oxidation and HF vapour etching are the cause of those differences. It is interesting to underline that the thinner device (g) exhibits a higher temperature variation on the membrane.
Once the temperature differences are extracted from the Raman shifts for the suspended membranes on both the devices, it is possible to simulate the membrane by Finite Element Method (using Comsol) to reproduce the same temperature gradients as function of different thermal conductivities fixed on the membrane. Therefore, the best fitting simulation results reproducing the experimental conditions provide us the correct value for the thermal conductivity of the structure.

4.3.2.2 Absorption estimation

The advantages of a contactless method (i.e. Raman thermometry, time-domain thermoreflectance (TDTR), frequency-domain thermoreflectance (FTDR), thermal transient grating (TTG), etc.), to determine the thermal properties of silicon membranes, rely on the absence of errors related to thermal boundary resistances, contact resistances, heat spreading in thermometers (heater or sensor), heat leakage in the underling BOX.
As a drawback, to obtain the thermal conductivity it is required to know the reflectance and the transmittance of the sample, by the fact that not the totality of the laser power is absorbed. Thus, knowing the membrane's absorbance and the power impinging it is possible to obtain the heat flowing in the membrane to later extract its temperature.
First of all, it is required to know the devices thickness and refractive index. The samples accurately measured by Raman (and simulated) are two (named *b* and *g*). Both underwent the same process flow, but the *g* one was oxidized twice (given the low thickness of the oxide, which was not sufficient to protect the SOI during the final suspension etching by HF). Thus, the thickness of the two samples along with the refractive index are measured by Ellipsometry. The results are different, due to the added oxidation and successive etching. Figure 4.26 reports the results obtained for refractive indexes used for the successive FEM simulations.

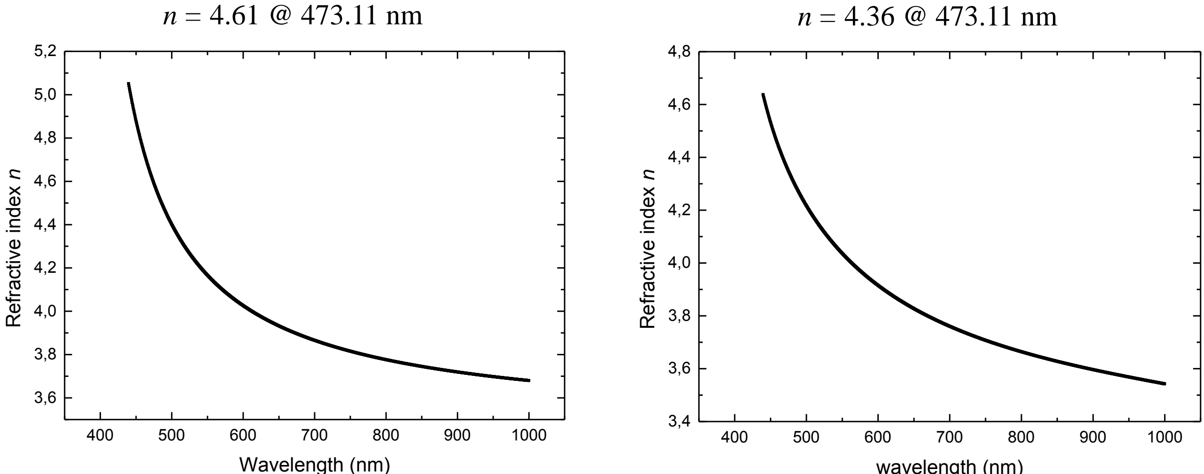

Figure 4.26 Refractive index *n* of the samples studied (b on left and g on right) as function of the wavelength. The laser used has a wavelength of 473.11 nm.

The silicon-on-insulator (SOI) layer for *b* presents a thickness of 59 nm, the SOI layer for *g* measures 53 nm.

The thin film behaves as a Fabry-Pérot optical cavity. For this reason, the power coefficients of absorption (A), reflection (R) and transmission (T) present an oscillatory behaviour (and not monotonous as for bulk silicon). With a Matlab simulation of a Fabry-Perot cavity, the absorption coefficient for a silicon thin film membrane is determined for the thickness targeted. The laser's incident light wavelength is 473.11 nm (for the Raman spectrometer used during the experiments). Transfer matrices are solved with iteration for thicknesses from 9 nm (state-of-the-art) to 209 nm. The thicknesses we are interested in are 59 nm and 53 nm (for the devices under study). The graph used for the R, T and A parameter extraction is reported in Figure 4.27.

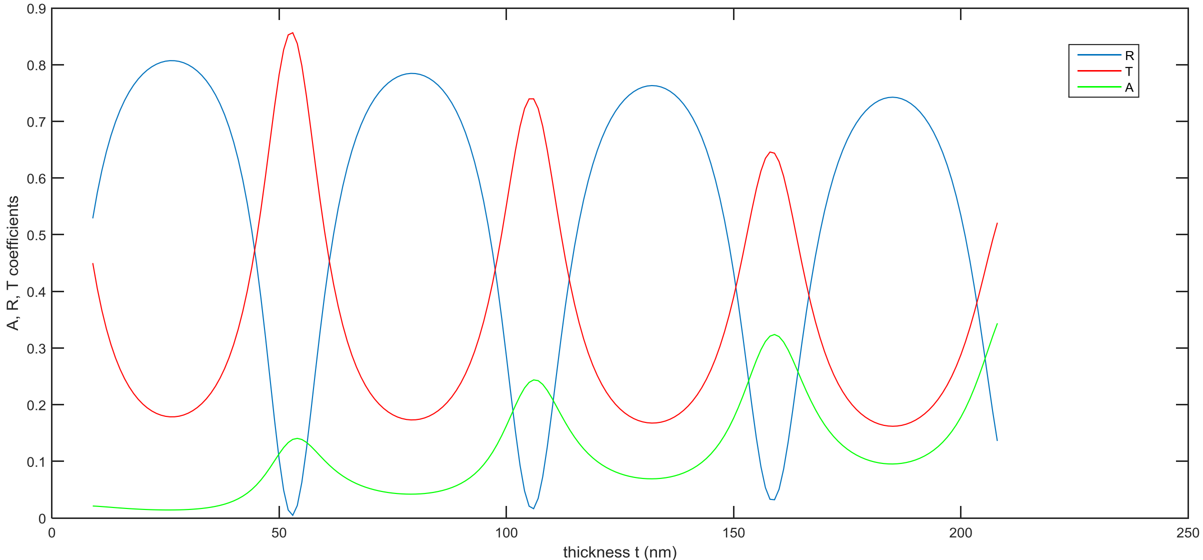

Figure 4.27 Absorption (A), Reflection (R) and Transmission (T) coefficients of a thin film silicon membrane behaving as a Fabry-Perot interferometer when a monocromatic laser light (473.11 nm) is shed on.

The calculated absorption A for such a thickness is 11%.

Once the absorption is calculated for plain thin films, it is worth to consider that, introducing periodic patterning , a photonic effect might rise and should be considered as well. Therefore,

another method, Rigorous Coupled-Wave Analysis (RCWA) is used to find the absorption in holey membranes. The calculations were conducted by Mouhannad Massoud, in the frame of a collaboration with the Institut des Nanosciences de Lyon (INL) and Centre d'Energétique et de Thermique de Lyon (CETHIL). The RCWA is a method mostly applied to solve scattering from periodic dielectric structures. It is a Fourier-space method based on the Floquet's theorem [193]. In Figure 4.28 we report the results obtained for the cited RCWA simulations as a function of the membrane thickness and the holes radius.

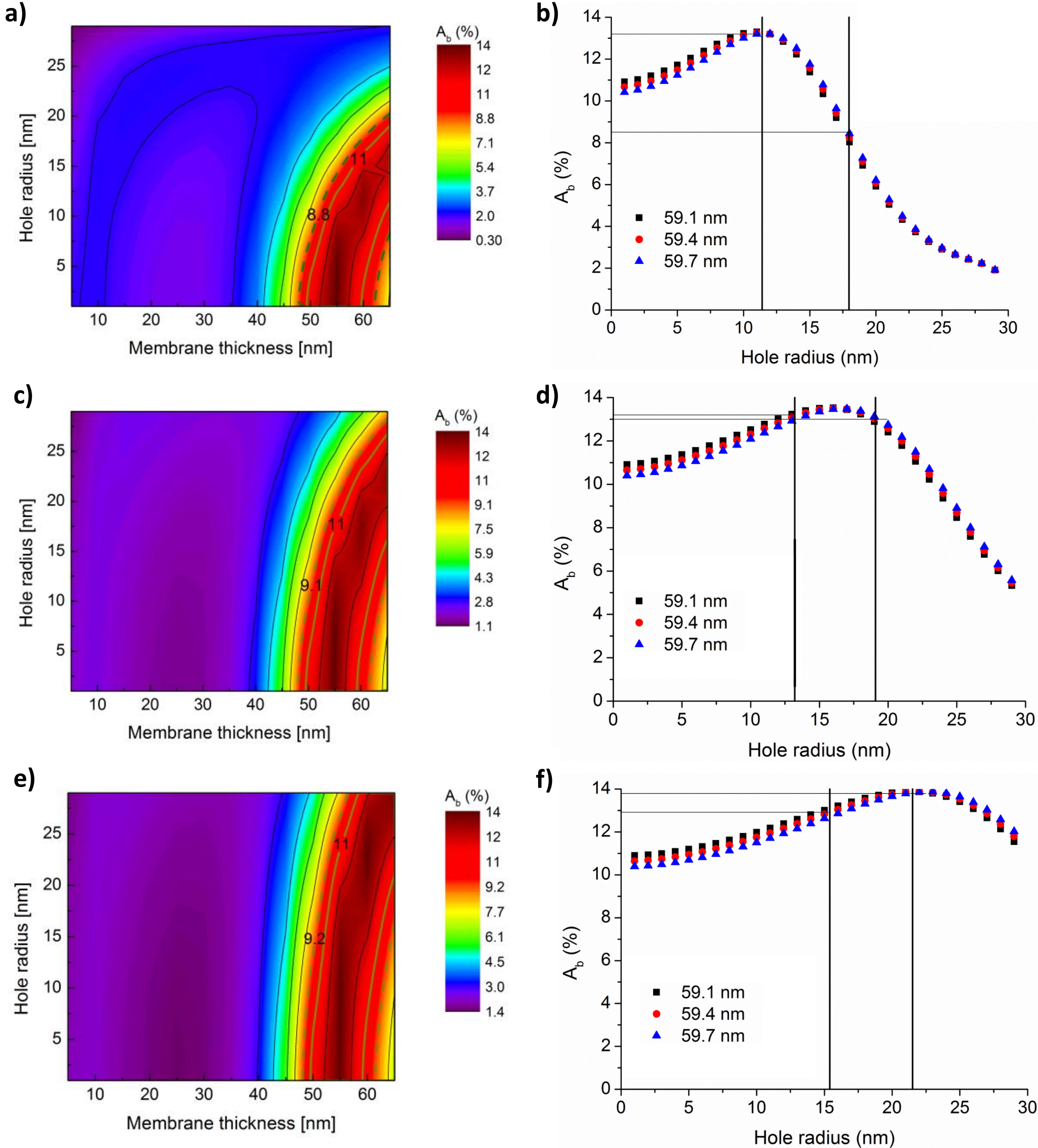

Figure 4.28 a), c), e) Absorption coefficients calculations by RCWA method, holes' radius as function of the membrane thickness. Pitch: a) 60 nm, c) 80 nm, e) 100 nm. b), d), f) Absorption for the three thicknesses previously targeted, as function of the hole's radius. Pitch: b) 60 nm, d) 80 nm, f) 100 nm. The lines draw are corresponding to the two radius targeted.

The main effect on the absorption variation is highlighted in graph b) in Figure 4.28 for the 60 nm pitch. Indeed, a small variation of the radius of the hole (range of variation marked with

the black continuous lines) entails a considerable difference in the membrane absorption, thus a sensitive variation of the thermal conductivity simulated, as it is detailed in the next part.
The absorption is strictly related to the radius of the periodic holes of the structure, thus a study has been performed to determine the exact value of it. The Scanning Electron Microscopy images have been analyzed and, as shown in Figure 4.29, the nature of the white part inside the circle has been determined to guarantee the correct result. Two are the cases: the first is identifying the white part as an absorbing material (i.e. silicon or amorphous silicon), the second is identifying it as a transparent material (i.e. air or silicon dioxide).

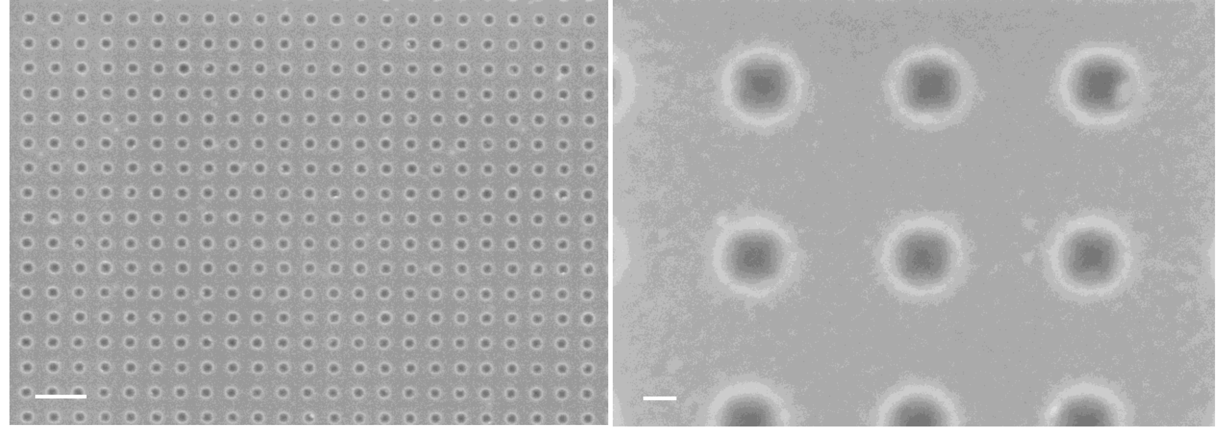

Figure 4.29 Scanning Electron Microscopy image of periodic patterned nano-holes in silicon. Scale bar: left 200 nm, right 20 nm. The nature of the white circle is of primary importance for the estimation of laser absorption.

The value of absorption at the laser's frequency (473.11 nm) is needed to correctly simulate the membrane's heat transport in the Comsol model for known laser power and membrane's dimensions and layout.

4.3.2.3 Finite Element Modelling

The heat transport in the structure, given the complex geometry, has been simulated by FEM to evaluate the temperature difference through the membrane as a function of the thermal conductivity. Then, comparing the deltas obtained from Raman measurements, the thermal conductivity of the membrane is determined.
The FEM model has been realized by Mouhannad Massoud, in the frame of the collaboration with the INL and CETHIL of Lyon. The structure's geometry and boundary conditions applied are depicted in Figure 4.30 in cross sectional view and top view.

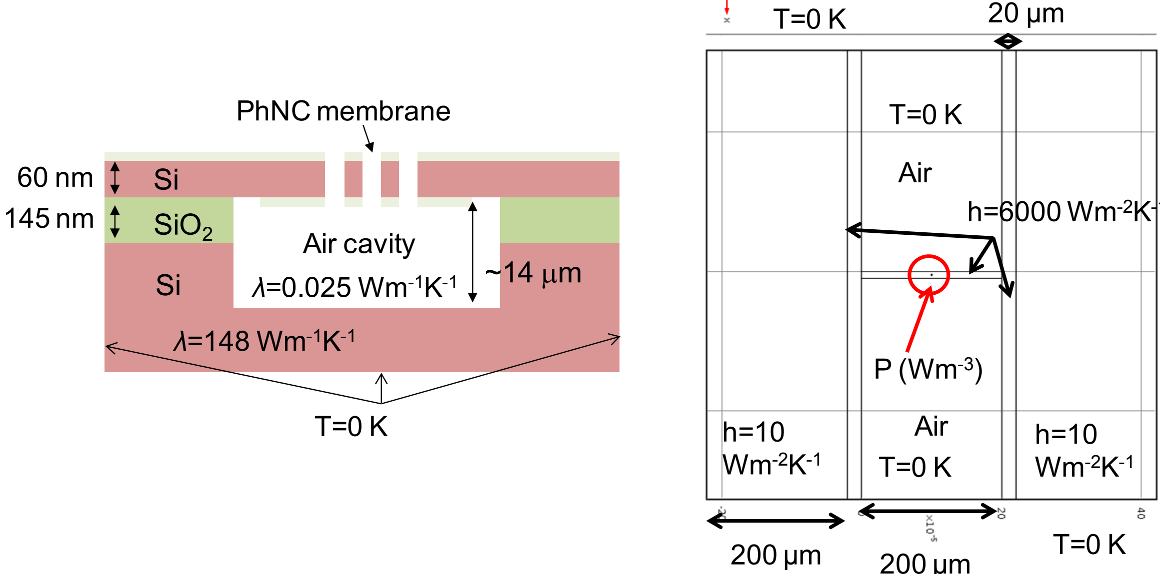

Figure 4.30 Geometry and boundary conditions of the simulated structure. The parameters are related to one of the sample measured. Left: Cross section view of the suspended membrane. Right : Top view of the suspended membrane.

First of all, Raman measurements have been performed (at IEMN) to evaluate the heat transfer coefficient h_m to insert in the simulations (indicated in Figure 4.31). The value has been obtained repeating the same Raman measurement in air and in vacuum on several membranes and for different laser's powers and combining the obtained data with the FEM results. The membrane is firstly simulated in vacuum-like conditions, considering h=0, no heat transfer, in order to reproduce the same temperature gradients obtained experimentally under vacuum (as in Figure 4.32). Secondly, the simulation reproduces air-like conditions, aiming to obtain the same gradients and h coefficient for the membrane (referred to as h_m) tuning the thermal conductivities.

$$h = \frac{q}{\Delta T} \tag{70}$$

where q is the amount of heat transferred (heat flux).

The membrane model built is shown in Figure 4.31. Room temperature boundary conditions are applied at the sides and the h_m of the membrane is determined, as previously explained. The other h values are taken from literature.

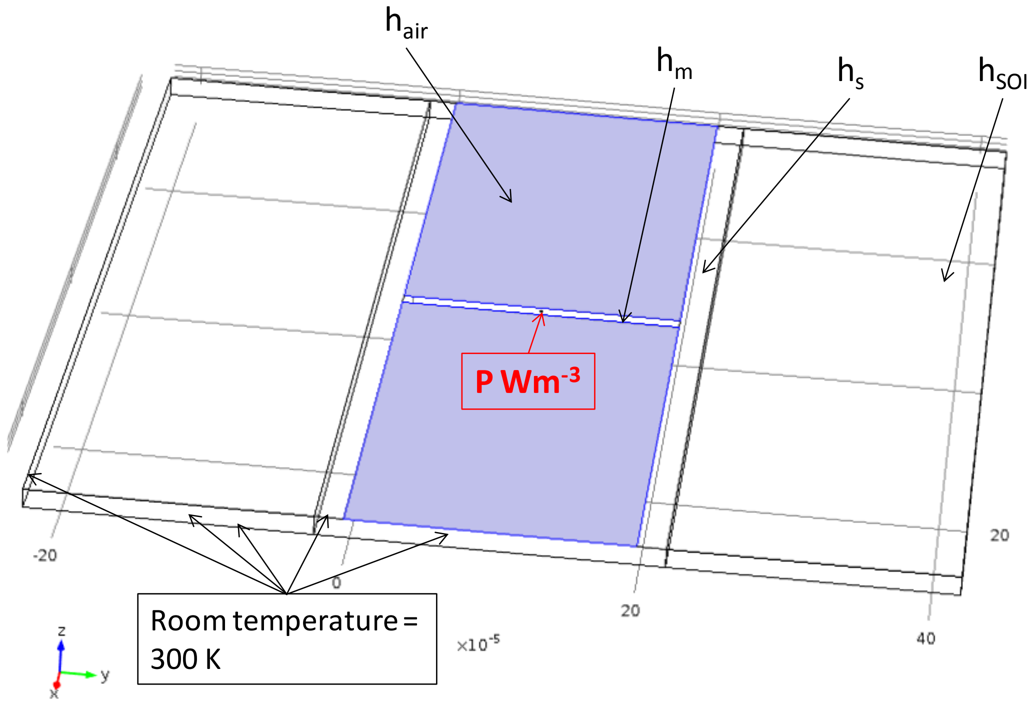

Figure 4.31 Comsol model of the suspended membrane realized by Mouhannad Massoud (INSA – CETHIL, Lyon).

In Figure 4.32 (left) the different temperature fields as a function of the position on the suspended membrane are registered for different impinging laser powers. The used densities (D = 1, 1.3, 1.6 and 2) are indicated in legend for air and vacuum experiment. For D1 the experiment was not performed under vacuum to avoid a membrane burn due to the high temperature established. Figure 4.32 (right) reports the temperature obtained in air and under vacuum as function of the laser power, showing the linearity of the relation between the two parameters.

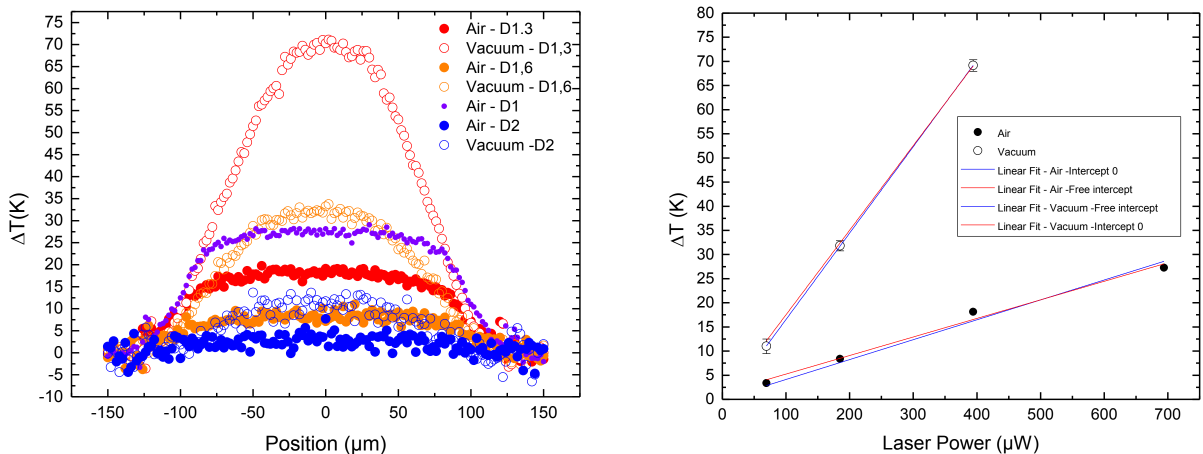

Figure 4.32 Left: Temperature difference measurements for the same membrane (plain), with 3 different laser powers under vacuum and in air, as function of the position on the membrane, in order to estimate the heat transfer coefficient of the membrane, h_m. Right: Temperature differences measured under vacuum and in air as function of the maser power used.

The h loss coefficient is properly composed by two different terms dependent on the membrane's geometry: a part taking into account losses from the membrane bottom, another

considering the losses from the top of the membrane, which influence differently in the two cases. Both the heat transports modelled are conducting-convective. Experimentally, the average h value is measured, and tuned with the FEM model to find the two different components.
The measures under vacuum are performed using different laser powers (65 μW, 185 μW and 394 μW) and the relative thermal conductivities are extracted.

Table 4.7 Thermal conductivities (from FEM simulations) calculated for the 3 different laser power densities in the range of thickness of the membrane (the one measured by Raman is 59.4 ± 0.3 nm thick, length of 200 μm and width of 10 μm).

Thickness (nm)	κ (W·m^{-1}·K^{-1}) (69.4 μW)	κ (W·m^{-1}·K^{-1}) (185 μW)	κ (W·m^{-1}·K^{-1}) (394 μW)
59.1	64.5	59.5	58.5
59.4	62.5	58	56.5
59.7	61	56.5	55.5

From the experimental values of thermal conductivity obtained simulating the membrane condition under vacuum (Table 4.7) and comparing with air ones, the values of h_m can be extracted. The average of the resulting h values for the powers used is the value of h_m considered for the simulation scope. Thus, the value obtained for the heat transfer coefficient is around 2500.

4.3.3 Results

The measurements, performed over a membrane of length 200 μm and width 10 μm, with a thickness of 59.4±0.3 nm (sample called *b* previously), present an average value of κ around 59.5 W·m^{-1}·K^{-1} for plain ones, 30.5 W·m^{-1}·K^{-1} for membranes with a pitch of 60 nm, 32.5 Wm^{-1}K^{-1} for pitch of 80 nm and 39.5 W·m^{-1}·K^{-1} for a pitch of 100 nm . The results, which confirm expectations and theoretical trend, are reported in Table 4.8.

Table 4.8 Thermal conductivities for the membranes (length 200 μm and width 10 μm) plain and holey (different pitch) measured.

Thickness (nm)	κ (W·m^{-1}·K^{-1}) plain	κ (W·m^{-1}·K^{-1}) pitch 100 nm	κ (W·m^{-1}·K^{-1}) pitch 80 nm	κ (W·m^{-1}·K^{-1}) pitch 60 nm
59.1	61.5	40	33	34.5
59.4	59.5	39.5	32.5	30.5
59.7	58	38.5	29	30

The findings are in agreement with the ones obtained by Electro-Thermal method (for the same pitch of 60 nm and membrane's thickness: 30 Wm^{-1}K^{-1}), confirming the method's reliability (their comparison is shown in conclusions at the end of this chapter). Considering the results obtained for plain membranes, with the electro-thermal method it has been

obtained a value of 56 $Wm^{-1}K^{-1}$ [112] for the first design and 69 $Wm^{-1}K^{-1}$ for the second one, which is comparable with the value obtained from Raman spectroscopy of 59.5 $Wm^{-1}K^{-1}$. Thus, the value obtained are in the error range of variability. Such an error is difficult to be estimated, being dependent on different parameters. As explicated the methodology is complex and relies on different estimations and modelling (Comsol, RCWA, exact hole's diameter estimation). Thus, all those parameters can contribute to the error. The machine systematic error and resolution also generate incertitude on the results obtained.

4.4 Scanning Thermal Microscopy

The Scanning Thermal Microscopy (SThM) measurements are performed at the Centre d'Energétique et de Thermique de Lyon (CETHIL), in the frame of a collaborative project with Mouhannad Massoud (who materially performed the analysis), Pierre-Olivier Chapuis and Jean-Marie Bluet.

The following part of this chapter provides an overview of the SThM technique adopted and presents the thermal conductivity results obtained for the devices whose fabrication process is detailed in Chapter 3.

4.4.1 Introduction

The continuous nanotechnology improvements in the last years in the field of thermoelectricity and heat transport study require precise thermal measurements at very small scales (few tenths of nanometres). As detailed in previous chapters, the mechanisms governing the energy transfer at the nanoscale are not deeply understood so far.

A technique allowing the nm-scale thermal measurement, imaging and study of thermal transport phenomena is Scanning Thermal Microscopy (SThM). The main advantage of this methodology relies in the fact that it is not limited in lateral resolution by optical diffraction at few hundreds of nm. Indeed, being a technique based on scanning probe microscopy (SPM), its spatial resolution depends on the characteristic lengths associated to the heat transport between the tip (thermal probe) and the sample.

4.4.2 Technique

The Scanning Thermal Microscopy (SthM) is a technique based on Atomic Force Microscopy (AFM). The deflection of a cantilever is probed by an impinging laser beam on a reflective part of the probe tip, which mirrors it toward a photodiode. The deflection generates an electrical signal that is detected and, through a feedback control loop, the contact tip-sample force is adjusted while the tip scans laterally.

The probe attached at the cantilever's extremity is a metallic thermo-resistive probe. The thermal image contrast provides information about the change in the amount of heat exchanged between the tip and the sample. The cantilever used is made of a Wollaston [194] wire consisting of a silver shell of $\kappa = 429$ W m^{-1} K^{-1}and a diameter of 75 µm. The wire's core is made by an alloy of Pt_{90}/Rd_{10} presenting a $\kappa = 38$ W m^{-1} K^{-1} and a diameter of 5 µm. The cantilever's tip is bent in a V-shape and a part of 200 nm is etched to expose the Pt_{90}/Rd_{10} core (Figure 4.33).

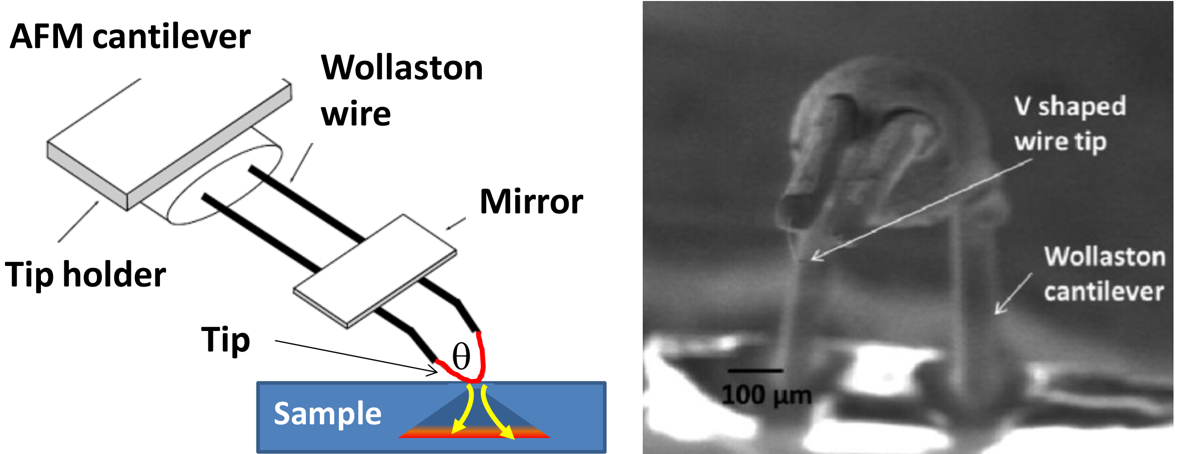

Figure 4.33 Left: Schematic image of the Wollaston wire probe used for SThM measurements. Right: Scanning Electron Microscopy image of the Wollaston wire probe [195].

The active mode use of the resistive metallic probe allows the measure of thermo-physical properties of materials, such as thermal conductivity. The tip resistance is given by:

$$R_{tip}(T_{tip}) = R_{tip}(T_0)\left[1+\alpha(T_{tip}-T_0)\right] \tag{71}$$

A large current (order of mA) is passed through the probe, resulting in a sample's Joule heating. Thus, the heat flowing into the sample depends on: tip temperature, contact force, contact area, sample temperature and its thermal conductivity κ.

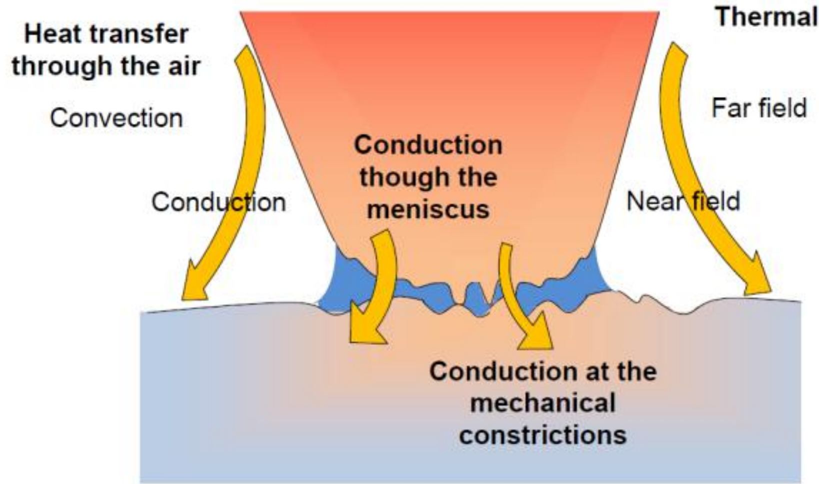

Figure 4.34 Heat transfer mechanisms playing a role in SThM measurements (Chapuis, INL-CETHIL present.).

As depicted in Figure 4.34 the heat transport mechanisms involved are: solid-solid conduction, solid-liquid conduction (if any), conduction through air and near field radiation. The dominant process is the conduction through air, being the measurement in air and not performed under vacuum.

The measure of thermal conductivity is possible by relating κ to the temperature of the probe. Before starting the analysis on a targeted sample, a reference bulk one (of known thermal conductivity) needs to be measured, in order to compare the values. This calibration step consists in specifying the link between the electrical resistance (resistive probe, equation (71)) and the temperature of the sample. A DC current is used to heat up the tip by mean of Joule effect, thus its resistance is monitored with a balanced Wheatstone bridge.

The thermo-resistive probe is one of the four elements of the Wheatstone bridge. The bridge is balanced while the probe is far away from the sample, resulting in a constant current of order of magnitude of a couple of mA in the probe. Thus, the probe is hot. When the probe is approached toward the sample's surface, heat exchanges occur that cool down the probe resulting in the Wheatstone bridge imbalance. From this point the setup can be used in two different ways. The first modality is making use of the voltage drop as a temperature measurement of the tip (ΔT/T). For the second way, the symmetric resistance of the Wheatstone bridge is tuned to balance the bridge (the current is increased), in order to keep the probe temperature constant (ΔP/P). The first modality is the one adopted for the measurements performed and described hereafter.

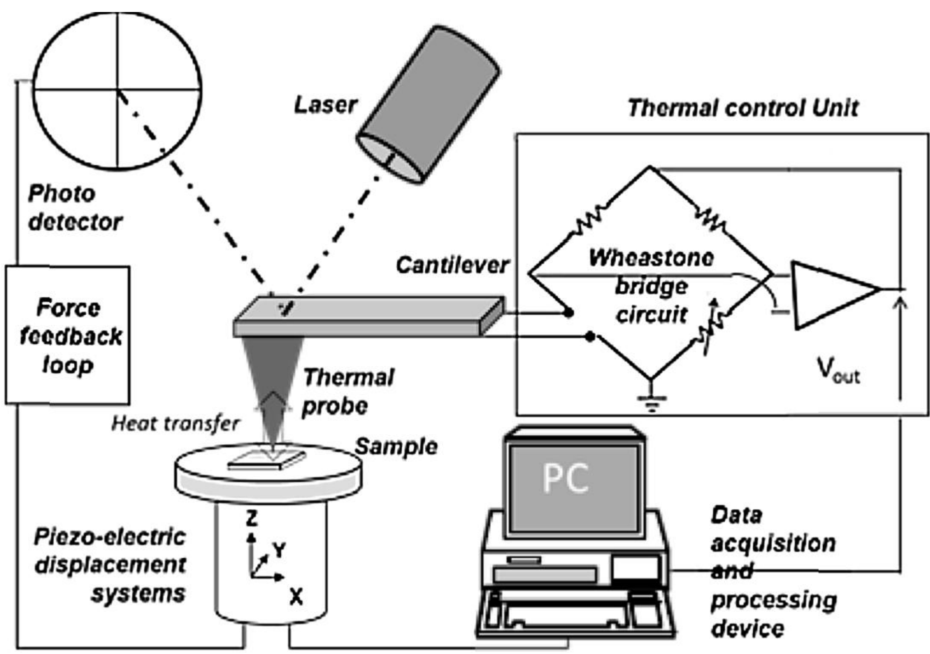

Figure 4.35 Set-up of an AFM-based SThM system. A balanced Wheastone bridge can be used to maintain the probe mean temperature at a constant value, while the output signal is the voltage V_{OUT} [196].

4.4.3 Measurements

The devices measured are the one described in the previous chapter: 1st generation (with Pt serpentines) and the samples designed for Raman measurements (without Pt and Au metals).

A Comsol model of the tip 3D geometry has been realized in CETHIL by Mouhannad Massoud in order to take into account its geometry and inclination angle to simulate the membrane scanning and related temperatures. The mesh and geometry are illustrated in Figure 4.36.

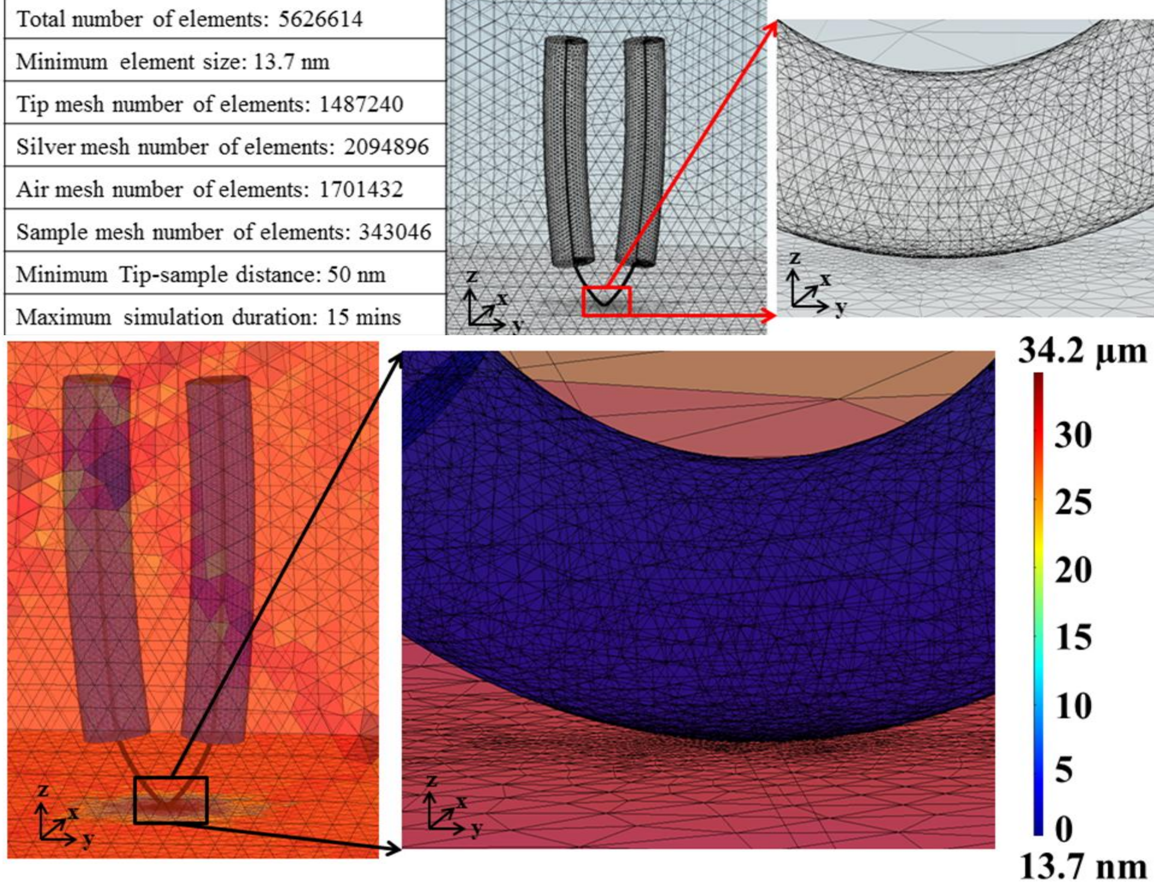

Figure 4.36 Full geometry and Finite Element Method mesh of the tip and surface used for SThM at the CETHIL.

4.4.4 Results

The analysis of the results is done in collaboration with the CETHIL (Lyon) and still object of study. Herein, preliminary results of the measurements performed are shown and commented.

Considering the resistive thermometry equation (71), and that $V = RI$, the relation between voltage drop and temperature variation is a direct proportionality:

$$\Delta V \propto \Delta T \tag{72}$$

Stated that ΔT depends on the sample's thermal conductivity, Figure 4.37 shows the sensed voltage profile as function of the position on the membrane for different lengths (left) and different a comparison between plain and holey ones (right).

At a first glance, from Figure 4.37 it can be said that the temperatures follow the expected theoretical order. Furthermore, the flat part of the curve can be justified by the lateral heat losses (membrane's borders).

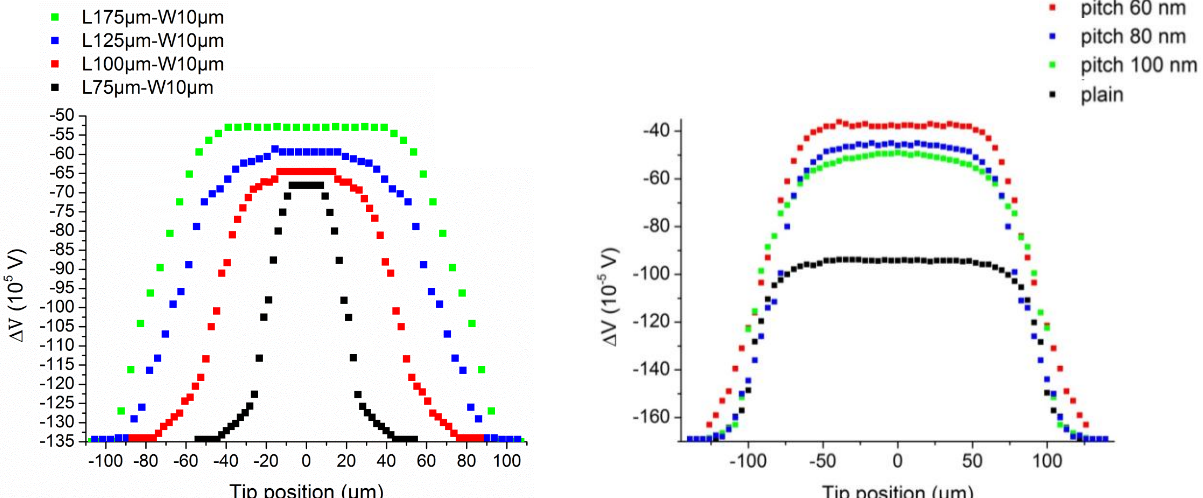

Figure 4.37 Left: Sensed voltage profile (proportional to the temperature difference) for different lengths of membranes. Right: Comparison between membranes with different membrane nanostructuration (different PnCs pitches and plain one).

As previously anticipated, the analysis of SThM's results consist also in comparing them with the ones of calibration samples of known thermal conductivity *κ*. In a first analysis, Figure 4.38 show the results obtained for the four different membranes analysed.

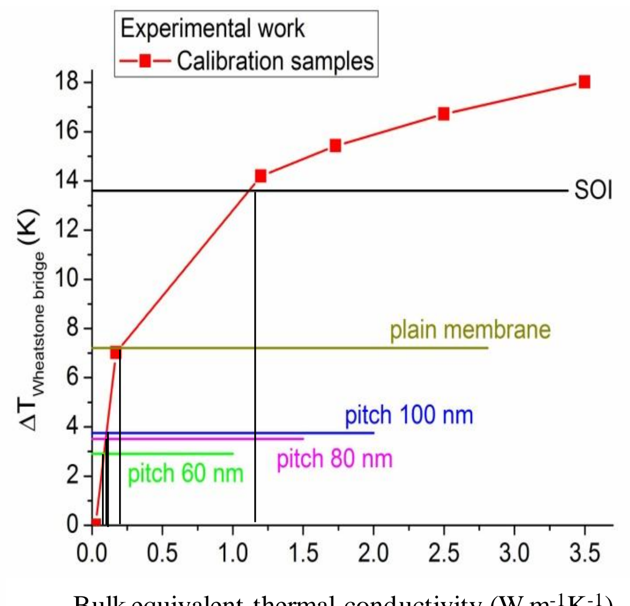

Figure 4.38 Measured effective thermal conductivity of plain membranes and holey ones. The ΔT is equivalent to a decrease in temperature for a bulk sample.

The temperature difference obtained for plain and patterned thin film suspended membranes is investigated by SThM and compared with the ones of calibration samples of know thermal conductivity. Figure 4.38 presents the temperature differences of various bulk samples as a function of their bulk equivalent thermal conductivity. The samples plain and patterned with PnCs present bulk equivalent thermal conductivities which are in the exact expected order with respect to their geometry. Indeed, the ratio between the differences of temperatures established for the different membranes types follows the one of *κ*. Being the collaboration

ongoing, still improvements in the SThM tip-substrate interaction and model can be done and the presented results need to be confirmed to extract the exact values of thermal conductivity.

4.5 Conclusions

The chapter presented the three characterization methodologies adopted to measure the thermal conductivity of the suspended membranes. The first characterization presented is the DC-Electro-Thermal. It exploits the advantage of measuring indirectly the thermal conductivity using the heating and sensing Platinum Resistance Thermometers (PRTs). The variation of the sensor PRT's resistance, dependent on the temperature, is registered and linked to the heat transported through the suspended membrane. This is the methodology on which we mostly focused our attention (a dedicated metrology platform, detailed in Chapter 3, has been fabricated for that goal) being versatile and easy to be readapted to other typology of measurements (presented in the Perspectives part). An interesting reduction of thermal conductivity, with respect to bulk silicon and plain membranes, has been registered for the first device designed with nanopatterned PnCs.

Considering the necessities of performing more precise four-probes measurement on heater and fully suspend the sensor serpentine to avoid thermal losses in the silicon substrate, a second device generation has been developed. Different periodic nanopatterned membranes have been produced on this second device, and characterized. The thermal conductivity obtained for this new layout results reduced with respect to the one of plain membranes and more precise in terms of methodology adopted. The values are not affected by dependences on device's dimensions, which were considered being the most important issue of the first device generation. The results obtained for plain membranes (69 W K^{-1} m^{-1}) are in agreement with the ones found in literature (and following the theoretical model of Fuchs-Sondheimer, see Figure 4.39). For this second design, PnCs membranes exhibit lower thermal conductivity respect unpatterned films, confirming the predominance of diffusive boundary scattering in thermal conductivity reduction at room temperature. At this temperatures, a clear evidence of coherent phonon transport cannot be claimed, indeed the interpretation of the phenomenon under this point of view is not possible in this range of temperatures and still intensely debated. The results pave the way for the direct integration of periodically patterned membranes into metrology platform device with reduced thermal conductivity respect the bulk one.

Another characterization methodology has been adopted in order to verify the results obtained by Electro-Thermal and perform contactless optical Raman measurement on the phononic patterned membranes without using the PRTs. The collaboration established with the CETHIL (Lyon) allowed the building of a COMSOL model for the simulation of the membrane's heat transport and a deeper understanding of the results. The obtained values of thermal conductivity by Raman thermometry are in agreement with the ones of Electro-Thermal measurements and confirming the reliability of the methods adopted. A value of κ = 59.5 W K^{-1} m^{-1} has been obtained for plain membranes. Periodically nanopatterned membranes of pitch 60 nm exhibit a thermal conductivity of 30.5 W K^{-1} m^{-1} and the result obtained by Electro-Thermal measurements is 29.5 W K^{-1} m^{-1}, confirming the expectations. Other pitches of 80 nm and 100 nm shown slightly higher thermal conductivity, which is the correct expected trend, being the phonon transport hindered by a larger limiting dimension. Figure 4.39 shows a comparison of Electro-Thermal method and Raman spectroscopy,

underling the agreement of the obtained results for the same 60nm-pitch patterned silicon membrane.

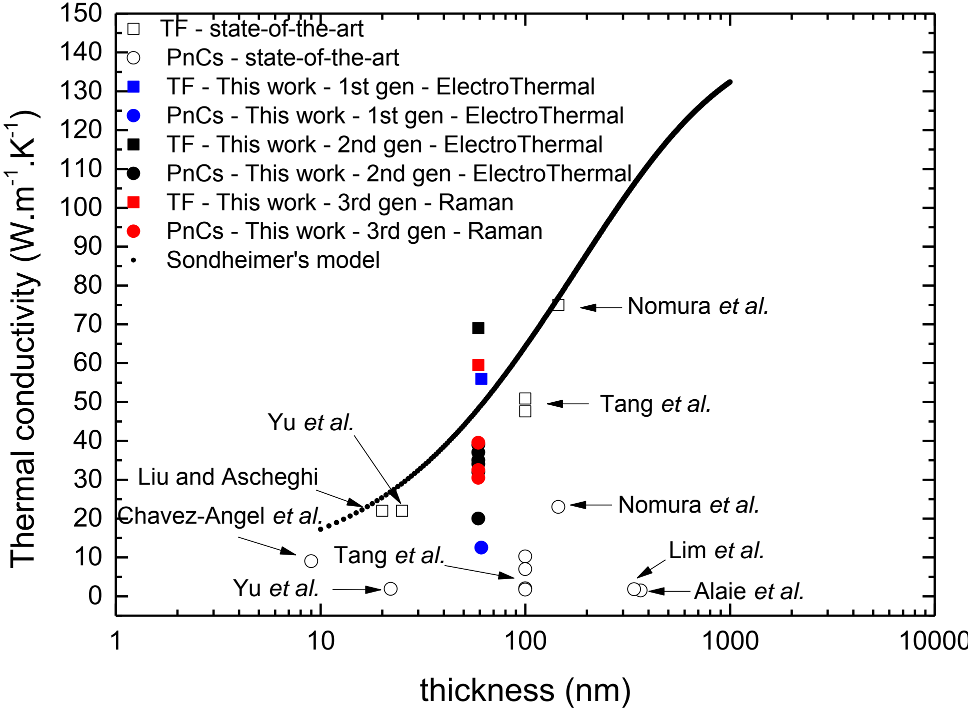

Figure 4.39 Thermal conductivity of thin film membranes (TF) and Phononic crystal ones (PnCs) for this work (by Electro-Thermal method and Raman-Spectroscopy) and for state-of-the-art-results

Scanning Thermal Microscopy (SThM) is the third technique adopted to investigate the transfer of heat through the silicon nanostructured membranes. The experiments, performed at the CETHIL in Lyon, demonstrate a reduced thermal in the expected order with respect to the membranes geometry. The findings need to be confirmed by a refined Finite Element Method model.

Conclusions

This thesis work focuses on the study of the thermal transport mechanisms in silicon phononic engineered nanostructures. The main goal of the PhD project is the demonstration of lattice thermal conductivity reduction in silicon periodically patterned nano-films membranes, for the integration into a thermoelectric converter device.
In a first place an exhaustive framework for Molecular Dynamics simulations by Green-Kubo method (MD-GK) has been established in order to study the heat transport mechanism in nanostructured devices and the phononic effect, to provide a tool for predictive structural device design. The simulations performed well reproduce the impressive reduction of silicon thermal conductivity due to nanoscale periodic patterning. Furthermore, the results highlight the suitability of MD toward quantitative comparison of obtained results to experimental values. The method adopted presents the advantage of not requiring assumptions on the phonon distribution nor on the transport mechanisms, already embedded in the potential formulation. The results demonstrated a reproduction of the experimental trends, such as temperature and dimensionality effects, shedding light onto the thermal transport in nanoscale systems. Finally, the findings confirm that the phononic structure accounts for a significant part of the thermal conductivity reduction with respect to the thin film geometry. This fact is of crucial importance for application in thermoelectric device design.

The second task tackled has been the conception, design and fabrication of a phononic engineered thin film metrology platform to measure the thermal conductivity. First of all, a robust fabrication process has been developed to pattern silicon phononic crystal structures using the *''dots on the fly''* technique. A simple layout, an Electron-Beam Lithography writing time consistently reduced by 3 orders of magnitude with respect to the conventional lithography methodologies, an anisotropic Cl_2 reactive ion etching (RIE) recipe are the decisive advantages of this methodology, contributing to the realization of periodic and dense patterns with pitches comparable to the actual state-of-the-art. Therefore, the use of silicon, along with industrial compatible materials (SiN, Pt and Au) for the complete device fabrication, guarantees compatibility with CMOS technologies and enables the integration of PnCs nanopatterned structures in thin film thermoelectric energy converter. Furthermore, the developed process preserves surfaces from contamination by avoiding metallic hard masks deposition. The integration onto thin suspended membranes conveys flexibility to the device, envisaging possible application in flexible electronics fields. Indeed, the device architecture and the choice of fabricating Pt thermometers for heating and sensing comes from the interest in re-adapting the structure for successive measurements of Seebeck coefficient and electrical conductivity (see Perspectives section).

Once the device process has been established, the thermal conductivity is measured. The first characterization is performed by Electro-Thermal method, exploiting the heating and sensing Platinum Resistance Thermometers (PRTs), in the case of first and second device generation. A consistent reduction of thermal conductivity has been registered for the first

device designed. Considering the necessities of performing more precise four-probes measurement on heater and fully suspend the sensor serpentine to avoid thermal losses in the silicon substrate, a second device generation has been developed. Systematic measurements of thermal conductivity on different membranes and with different periodic patterns arrangements have been performed. The thermal conductivity obtained for this new layout results reduced with respect to the one of plain membranes. The results obtained for plain membranes are in line with the one present in literature (and following the theoretical models). PnCs membranes exhibit lower thermal conductivity, confirming the predominance of diffusive boundary scattering in thermal conductivity reduction at room temperature.
The second characterization performed is Raman thermometry. It has been adopted in order to verify the results obtained by Electro-Thermal and perform a contactless optical measurement on the phononic patterned membranes without using the PRTs. Collaborating with the INL and CETHIL (Lyon) it has been possible to build a COMSOL model for the simulation of the membrane's heat transport and provide a deeper understanding of the results. The measurements of κ confirm the ones performed with the Electro-Thermal method, falling in the same range of values, both for plain and patterned membranes. It is interesting to point out that the two different methods, based on different physical behaviours, are in agreement. To our knowledge, this is the first direct comparison of the two methodologies for thermal conductivity evaluation.
Scanning Thermal Microscopy (SThM) is the third technique adopted to investigate the transfer of heat through the silicon nanostructured membranes. The experiments, performed at the CETHIL, are still ongoing. A preliminary analysis of the results highlights a conductivity in the same order of the ones obtained with the Electro-Thermal method. It has to be pointed out that the device measured is from the first generation, thus the values of the measurements are agreeing.

Perspectives

The research conducted during this PhD work represents a step toward the fabrication of complete measurement platform integrating a phononic engineered silicon membrane and allowing a deeper understanding of heat transport mechanisms at the nanoscale. The argument is of great interest among the community.
Given the results provided and expected improvement, in a short term it is envisageable to fabricate phononic engineered membranes with different pitches (similar to the ones presented as second device fabrication), but with dimensions more differentiated in order to intercept and hinder the transport of a wider range of phonons. The statement is justified considering the mean free path distribution of silicon at room temperature, which interests dimensions from hundreds of nanometers to few micrometers. Thus, creating larger pitches next to small ones should allow the blocking (by cumulative effect) of phonons with different mean free paths.

Although this manuscript has shown preliminary results obtained in our group of PnCs membranes patterning and integration into devices for thermal conductivity measurements, electrical conductivity and Seebeck coefficient are argument of great interest for the field.
Future work in this direction envisages in a short term the fabrication of a fully integrated phononic engineered metrology platform for the characterization of thermal conductivity (κ), electrical conductivity (σ) and Seebeck coefficient (S) to pave the way for the introduction of silicon into the list of the candidate materials for thermoelectric low-power applications. Few modifications, hinted in Figure – Perspectives 1, of the fabrication process (already detailed in Chapter 3) would allow the re-adaptation of the structure to this scope.

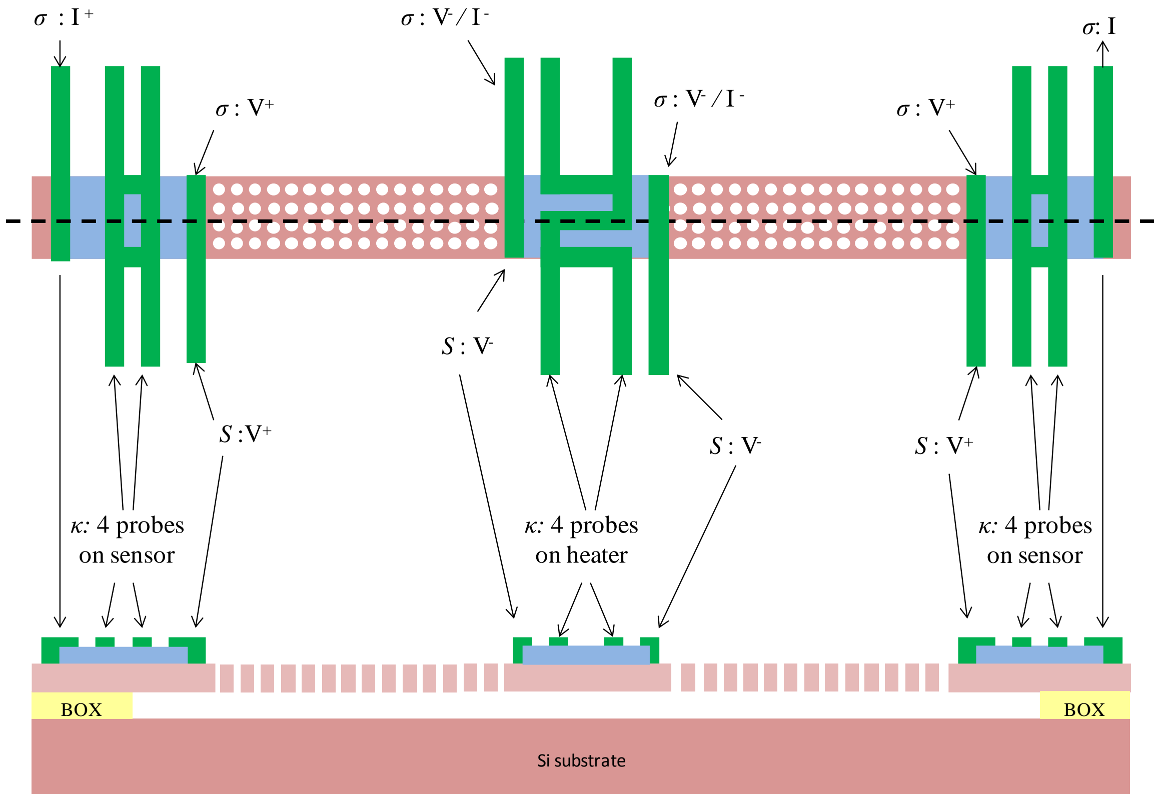

Figure – Perspectives 1 Sketch of the measurement platform with phononic engineered membrane. Two contacts have been added on the sensor and heater sides to allow the measurement of Seebeck coefficient (S) and electrical conductivity (σ). Dopants implantation (p and n for the two membranes) and activation by annealing are the main steps to add at the beginning of the process flow illustrated in Chapter 3.

A converter-like structure (Figure - Perspectives 2) has been simulated and studied in our group [40] in order to predict the design guidelines and challenges for a direct integrations of the fabricated device.

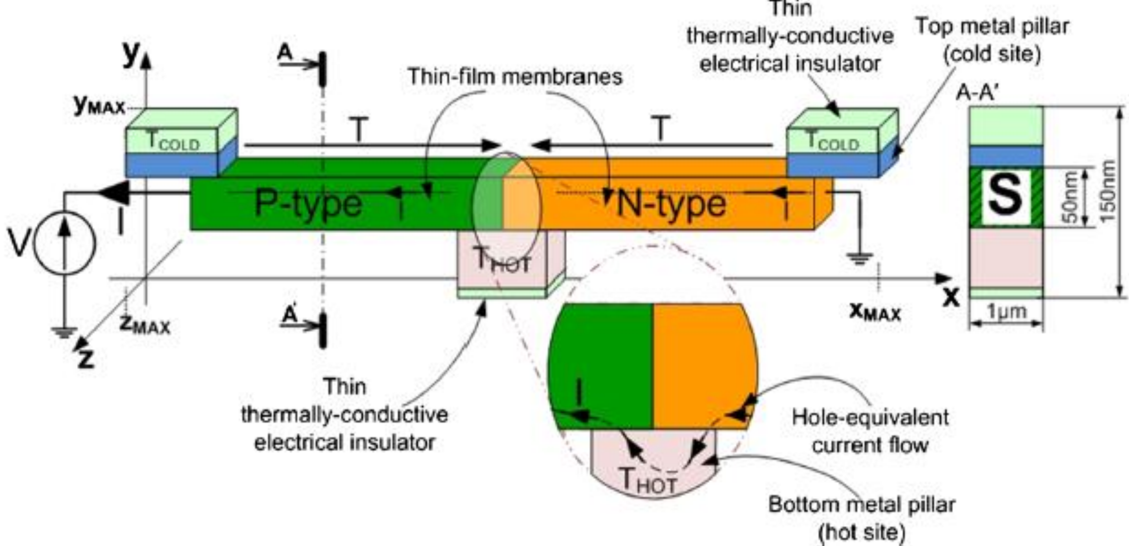

Figure - Perspectives 2 Structure of a membrane Seebeck generator with use of CMOS-compatible thin-film membranes. x_{MAX} = 10 µm (single membrane length 5 µm), y_{MAX}= 150 nm (50 nm membrane thickness), z_{MAX} = 1 µm. [40].

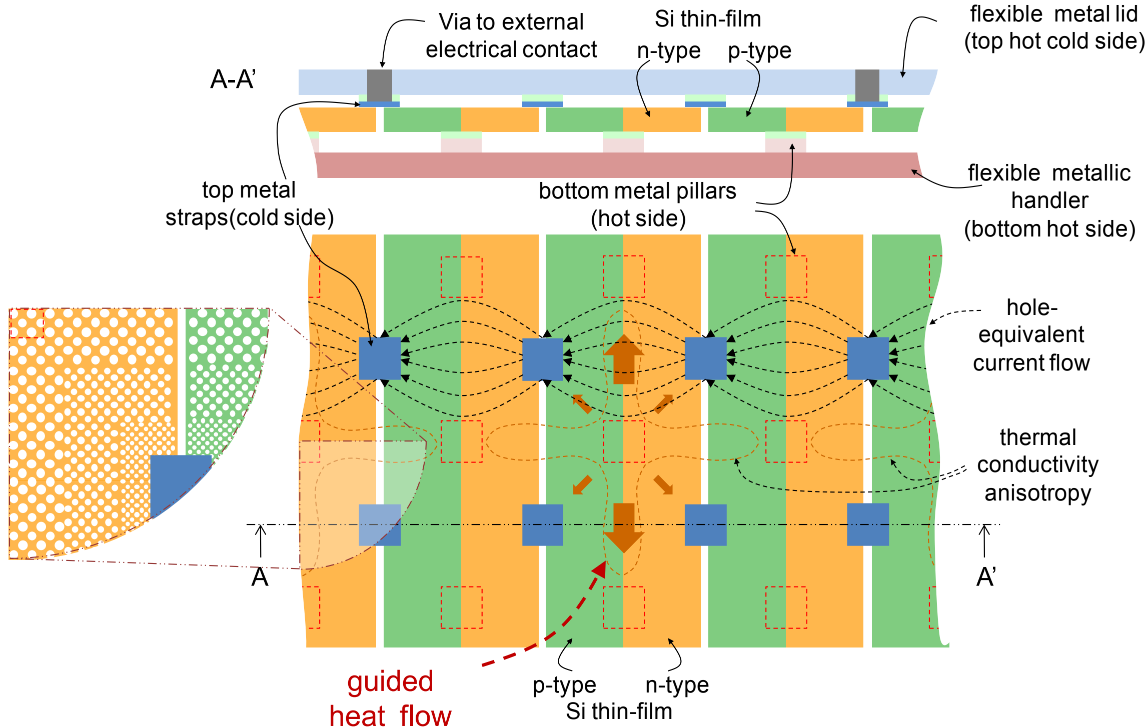

Figure - Perspectives 3 Sketch of a possible device typology converter with phononic crystals patterned to lateral heat flux redirection and vias for the measurements of electrical conductivity and Seebeck parameter.

Furthermore, the established design and measurement procedures open the possibility of characterizing the same parameters cited above for: different membrane thicknesses, SiGe based membranes (exploiting the already lower thermal conductivity of bulk SiGe), measure devices with randomly arranged PnCs (to compare with ordered ones).
Considering the Molecular Dynamics simulations work, the main interest is to focus the attention toward the reproduction of experimental-like dimensions, which would lead to better matching of simulated values with respect to experiments. Another parameter that needs to be investigated is the role played by random periodic enclosures in the reduction of thermal conductivity. Moreover, other effects could be taken into account to improve the simulation agreement with reality, and those should further hinder the phonon transport and reduce the thermal conductivity. Examples are: quantum corrections, silicon's surface native dioxide, defects, impurities, isotopic compositions.

During the last years several groups made efforts to conceive, design and fabricate sonic and thermal devices using different materials ranging from the centimeter to the nanoscale for a wide range of applications. Examples are: acoustic diodes [119], invisibility cloaks by metamaterials [197], thermal metamaterials [198], heat waveguides [199], heat imaging, thermal diodes and thermal cloaking [119], application in radio frequency communications and acoustic imaging for medical ultrasound and nondestructive testing [199]. It is also possible to exploit the feasibility of tuning the band structure of phononic crystals by employing magnetostrictive materials and applying an external magnetic field. Thus, the tuneable phononic crystal behaves like a transmission switch for elastic waves when the magnitude of an applied magnetic field crosses a threshold [200], [201].

This PhD has been conducted entirely exploiting the resources available at the IEMN (Institute of Electronics, Microelectronics and Nanotechnology) in Lille. The research leading to these results has received financial support from the ANRT for CIFRE research grants in the frame of the STMicroelectronics-IEMN common laboratory. Furthermore, funding from the European Research Council under the European Community's Seventh Framework Program (FP7/2007-2013), ERC Grant Agreement No. 338179, has supported the research work presented. The authors acknowledge GENCI for access to high performance computer CURIE.

Résumé en français

Introduction

Les défis sociétaux, environnementaux et technologiques posés par l'approvisionnement énergétique poussent à rechercher des sources fiables, sûres et aisément disponibles d'énergie. Au cours des vingt dernières années, la recherche continue de sources d'énergies alternatives pour alimenter les dispositifs micro- et nanoélectroniques a donné lieu à un regain d'intérêt envers la thermoélectricité. Tous les types de gradients énergétiques peuvent potentiellement servir comme source d'alimentation et, dans de nombreux cas, cette énergie potentielle est perdue sous forme de chaleur évacuée. Les matériaux thermoélectriques peuvent exploiter cette différence de température et la transformer directement, par effet Seebeck, en énergie électrique utile. Dans ce contexte, le silicium apparait comme le meilleur candidat car il est à la fois compatible avec les procédés industriels (C-MOS), bon marché, abondant, et sans risques pour la santé.

Il est connu que, pour améliorer l'efficacité thermoélectrique, un rôle important est joué par les propriétés électroniques du matériau et par sa conductivité thermique. Le silicium présente une très bonne conductivité électrique et un fort coefficient Seebeck, mais sa conductivité thermique représente le plus grand obstacle pour les applications thermoélectriques, empêchant son intégration directe comme matériau massif. Aujourd'hui, les technologies de structuration à l'échelle nanométrique permettent d'envisager une approche radicale et innovante consistant à moduler artificiellement le transport thermique dans un matériau par l'introduction d'une structure périodique dite phononique. Il a été démontré que le silicium nanostructuré en couches minces permet la réduction de la conductivité thermique jusqu'à un ordre de grandeur. Des travaux publiés récemment [122], [127], [129]–[131], [136], [202] montrent qu'un ordre de grandeur de diminution supplémentaire de la conductivité thermique est possible par la nano-fabrication de cristaux phononiques (PnCs), ces motifs périodiques sur la couche mince de silicium. Ces matériaux nanostructurés présentent des propriétés similaires à ceux des cristaux photoniques, tels que: gap phononique, réduction de la vitesse de groupe en raison de l'effet de repliement des bandes dans la courbe de dispersion, résultant de la périodicité du aux PnCs, qui pourrait être à l'origine d'un impressionante réduction de la conductivité thermique. Par ailleurs, les caractéristiques mécaniques d'un tel matériau permettront de l'intégrer dans des dispositifs mécaniquement flexibles.

Même si plusieurs groupes ont déjà établi cet effet phononique, le mécanisme physique à l'origine de la réduction de la conductivité thermique est encore difficile à décrire et a déclenché un fort débat entre les différents chercheurs dans le domaine.

L'objectif de ce travail de thèse est basé sur la conception, la fabrication et la caractérisation d'une plateforme de mesures avec un film mince phononique intégré. Le dispositif doit être capable de mesurer la conductivité thermique du matériau nanostructuré. Le dispositif a été caractérisé par méthode électro-thermique et par spectroscopie Raman. La caractérisation par

microscopie thermique à balayage a aussi été effectuée en collaboration avec le CETHIL-INL à Lyon. L’objectif principal est d'étudier l'effet des phonons et la contribution au transport de la chaleur dans le silicium nanostructuré, en combinant les réalisations expérimentales avec une justification théorique cohérente venant de simulations de dynamique moléculaire par la méthode Green-Kubo (MD-GK).

Chapitre 1 - Théorie et état de l'art

Aujourd'hui, l'approvisionnement en énergie représente l'un des problèmes les plus importants à traiter. La consommation d'énergie est en croissance continue, les réserves naturelles sont en train de s'épuiser, l'effet de serre augmente et la technologie en développement continu. Ces défis poussent l'humanité à trouver des sources d'énergies alternatives.
Le "World Energy Outlook 2014, Executive Summary" [1] souligne que l'accroissement de la demande mondiale d'énergie prévue est de 37%. La consommation d'énergie devrait rester stable dans une grande partie de l'Europe, au Japon, en Corée et en Amérique du Nord, et augmenter de façon spectaculaire dans le reste de l'Asie (60% du total), en Afrique, au Moyen-Orient et en Amérique latine.

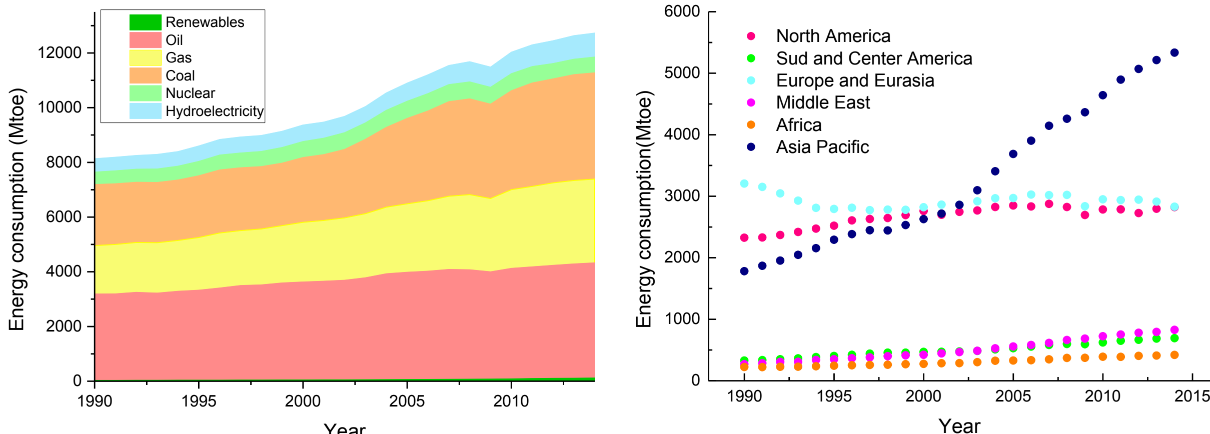

Figure 1 Consommation d'énergie primaire régionale en 2014 (figure de gauche) pour différents combustibles. Croissance de l'énergie primaire mondiale au cours des 15 dernières années (Mtoe : Million tonnes oil equivalent) tel que rapporté par BP Statistical Review of World Energy 2015 [3].

De plus, l'utilisation de matériaux énergétiques non-renouvelables doit être réduite, parce qu'environ 80% de l'électricité produite dans le monde provient de ces ressources. Donc, il faut rendre nos systèmes électriques plus 'verts' avec : l'augmentation de la production d'énergie électrique en provenance de sources renouvelables et la production d'énergie à partir des pertes énergétiques (chaleur, ondes électromagnétiques, vibrations mécaniques,…). La première méthode est surtout adoptée pour des pertes énergétiques à large échelle (macro), en utilisant les ressources naturelles des énergies renouvelables. La deuxième est plus envisageable pour les applications micro-énergétiques.

La chaleur des pertes industrielles se réfère à l'énergie qui est générée dans les procédés industriels, sans être réutilisée. Le montant exact est difficile à quantifier, mais diverses études ont estimé que près de 20 à 50% de la consommation énergétique de l'industrie est finalement évacuée sous forme de chaleur. La récupération de cette chaleur implique sa capture et sa réutilisation dans les procédés industriels d'échauffement ou dans la production de travail mécanique ou électrique. Le Tableau 9 donnes les rendements thermiques typiques de certains systèmes d'énergie et équipements industriels.

Tableau 9 Rendements thermiques typique de certains systèmes d'énergie et d'équipements industriels [203].

Systèmes d'énergie / équipements industriels	Efficacité thermique

Systèmes d'énergie / équipements industriels	Efficacité thermique
Production d'énergie	25-44%
Chaudières à vapeur (gaz naturel)	80%
Chaudières à vapeur (charbon et pétrole)	84-85%
Chaudières de récupération de chaleur	60-70%
Craquage thermique (raffineries)	58-61%
EAF Sidérurgie	56%
Séchage du papier	48%
Mise en pâte Kraft	60-69%
Colonne de distillation	25-40%
Ciment calcinateur	30-70%
Compresseurs	10-20%
Pompes et ventilateurs	55-65%
Motors	90-95%

Les sources les plus courantes d'énergie disponibles pour la récupération et conversion sont les vibrations (ou mouvement), les radiations RF (rayonnement), la lumière et la chaleur. Considérant les alternatives citées précédemment, l'énergie de récupération de chaleur est présentée comme une solution intéressante. Selon E. Cook [6], au moins 50% de l'énergie primaire est libérée sous forme de chaleur (exemple: gaz d'échappement chauds, eau de refroidissement et chaleur perdue par les surfaces des équipements chauds et produits chauffants).

La chaleur perdue est présente partout, libérée par les moteurs, le corps humain, les bâtiments, les procédés industriels. Les principaux avantages offerts par cette méthode sont: la production d'énergie propre, l'absence d'émission de gaz à effet de serre (ex: CO_2) et de gaz polluant pour l'air (NOx, SOx), la réduction de l'effet du réchauffement climatique.

Actuellement, le développement technologique des dispositifs qui sont portables, sans fil, implantables (avec batterie intégrée), pose la nécessité d'une méthodologie d'alimentation efficace. Ces dispositifs nécessitent une source d'énergie bon marché, compact et légère, permettant la portabilité et l'autonomie énergétique. Une réponse à cette demande pourrait être l'intégration d'un module thermoélectrique capable de récupérer la chaleur perdue et de la convertir en énergie électrique. Cette option représenterait une solution à l'éternel problème des batteries, dont la taille et le coût sont un obstacle à l'autonomie de l'appareil. Le Tableau 10 présente quelques appareils fonctionnant sur batterie, avec leur consommation d'énergie et leur autonomie.

Tableau 10 Sélection de systèmes fonctionnant sur batterie avec la leur consommation d'énergie et leur autonomie énergétique

	Typologies de dispositif	
	Puissance utilisée	Autonomie d'energie
Smartphones	1 W	5 h
Lecteur MP3	50 nW	15 h
Aide auditive	1 mW	5 days
Réseau de capteurs sans fil	100 µW	Lifetime
Pacemaker cardiaque	50 µW	7 years
Montre à quartz	5 µW	5 years

En tenant compte des différentes puissances de sortie qui pourraient être obtenues à partir des différentes sources environnementales, détaillées dans le Tableau 11, la conception d'un récupérateur d'énergie approprié doit être choisie, répondant aux contraintes d'être de petite taille et d'avoir une batterie rechargeable (ou autres systèmes de stockage d'énergie).

Tableau 11 Source et puissance récupérée pour différentes sources d'énergie disponibles [204].

	Puissance de la source	Puissance récupérée
Lumière ambiante		
Intérieure	0.1 mW/cm²	10 µW/cm²
Extérieure	100 mW/cm²	10 mW/cm²
Vibration / mouvement:		
Humain	0.5 m @ 1 Hz 1 m/s² @ 50 Hz	4 µW/cm²
Industriel	1 m @ 5 Hz 10 m/s² @ 1 kHz	100 µW/cm²
Energie thermique		
Humain	20 mW/cm²	30 µW/cm²
Industriel	100 mW/cm²	1 – 10 mW/cm²
RF		
Téléphone portable	0.3 µW/cm²	0.1 µW/cm²

Les bases de la production d'énergie thermoélectrique sont relativement simples et facilement réalisables. Si une petite différence de température est appliquée aux extrémités d'une barre en circuit ouvert, reliant un côté à une source de chaleur et l'autre à un dissipateur de chaleur, l'expérience montre que la chaleur ($\vec{q}$) se propage de l'extrémité chaude à la froide. L'équation qui exprime ce phénomène est la loi de Fourier:

$$\vec{q} = -\kappa \vec{\nabla} T \tag{73}$$

où $\vec{\nabla} T$ est le gradient de température et κ la conductivité thermique du matériau. Différents mécanismes contribuent au transport de chaleur dans les solides. Dans les métaux, la chaleur est transportée par les électrons, comme l'indique la loi de Wiedemann-Franz, qui relie la conductivité thermique des électrons, κ_e, à la résistivité ρ de la matière:

$$\kappa_e = \frac{L}{\rho} T \tag{74}$$

où T est la température absolue, L le nombre de Lorenz, égal à $2{,}5 \cdot 10^{-8}$ W Ω^{-1} K^{-2} pour un gaz d'électrons libres. Pour un matériau isolant, le transport de chaleur est réalisée par les vibrations du réseau des atomes. La conductivité thermique des phonons κ_{ph} peut être formulée, en première approximation, en considérant la relation de Debye:

$$k_{ph} = \frac{1}{3} c \Lambda v \tag{75}$$

où c est la chaleur spécifique volumétrique, Λ le libre parcours moyen des phonons et v la vitesse du son. Dans les semi-conducteurs, la chaleur est transportée par les électrons et phonons. Ainsi, la conductivité thermique est constitué par les deux termes:

$$k = k_{ph} + k_e \tag{76}$$

Les deux paramètres dépendent uniquement du matériau choisi.

Donc, le choix d'un matériau pour des applications thermoélectriques dépend uniquement des besoins en termes de transport électrique (la conductivité électrique étant très variable d'un matériau à l'autre) et de transport thermique (la conductivité thermique étant modulable sur une petite plage de valeurs selon le matériau).
La possibilité de générer un champ électrique en appliquant un gradient de température au niveau des extrémités opposées d'une barre a été découvert en 1824 par Thomas Seebeck. La relation est:

$$\vec{E} = S\vec{\nabla}T \tag{77}$$

où S est le coefficient Seebeck, ou pouvoir thermoélectrique, positive ou négative en fonction du dopage du matériau. Le pouvoir thermoélectrique est dépendante de la concentration de porteurs dans le matériau. Pour un métal S est faible à température ambiante. Si la concentration de porteurs diminue, le coefficient Seebeck augmente et il peut atteindre des valeurs de quelques mV/K pour les semiconducteurs de grande pureté. Le coefficient Seebeck n'est pas le seul paramètre qui détermine l'efficacité d'un matériau dans un générateur thermoélectrique ou un refroidisseur thermoélectrique. Avec un gradient de température donné, la capacité d'un matériau à produire de l'énergie électrique efficace est quantifiée par son facteur de puissance:

$$\textit{Power Factor} = \sigma \cdot S^2 \tag{78}$$

Pour améliorer ce facteur, un bon choix de matériau pour le générateur doit être fait. La meilleure solution est de coupler deux matériaux différents, dopées différemment, et de les relier électriquement en série et thermiquement. Si une configuration thermo-générateur est choisie, la tension (force électromotrice) générée par le gradient de température est sommée, conduisant à un coefficient Seebeck plus grand. La Figure 2 montre un module générateur thermoélectrique, composé d'un matériau dopé de type n- et un de type p-, reliés par deux couches métalliques, à des températures différentes (un côté chaud et un froid).

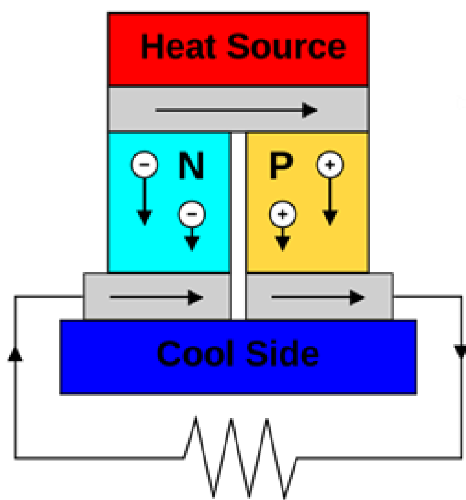

Figure 2 Gauche: Thomas Johann Seebeck; Droite: Un module thermoélectrique composé de matériaux semiconducteurs dopés p- et n- de différents coefficients de Seebeck, configurés comme un générateur thermoélectrique. Si la résistance de charge est remplacée par un voltmètre le circuit peut fonctionner comme un thermocouple de détection de température [10].

Pour augmenter encore le facteur de puissance, les dispositifs thermoélectriques industriels fabriqués sont composés de plusieurs thermocouples, dans la configuration dite de thermopile.

La configuration de la Figure 2 représente un dispositif de générateur d'énergie par effet Seebeck, ayant une résistance de charge et les deux côtés maintenus à des températures froid / chaud constants. En revanche, si une différence de tension est appliquée sur les deux côtés n et p, sans maintenir le gradient de température, la configuration change, et un dispositif de chauffage / refroidissement exploitant l’effet Peltier est créé.

Pour évaluer l’efficacité d'un dispositif thermoélectrique, un paramètre est utilisé dans le but de comparer les performances, il est nommé le rendement de conversion η. Il est caractérisé par le rendement de Carnot et le facteur de mérite zT du matériau. En supposant que les résistances de contact sont négligeables et les résistances de charge optimisées, le rendement de conversion maximum du générateur thermoélectrique, η, est:

$$\eta = \left(\frac{T_{HOT} - T_{COLD}}{T_{HOT}}\right)\left[\frac{\sqrt{1+ZT_m}-1}{\sqrt{1+ZT_m}+\left(\frac{T_{COLD}}{T_{HOT}}\right)}\right] \tag{79}$$

où le rendement de Carnot est le rapport entre la différence de température entre l'extrémité chaude et froide et T_{HOT}, et T_m est la température moyenne. zT est la figure matière de mérite, un paramètre important dans la thermoélectricité:

$$ZT = \frac{\sigma S^2 T}{k} \tag{80}$$

où σ est la conductivité électrique, S le coefficient Seebeck, κ la conductivité thermique.

Le meilleur matériau thermoélectrique est un *phonon glass – electron crystal* ("verre phononique –cristal électronique"), telle que formulée par Slack [15], présentant le κ plus bas et le plus haut σ. Il n'y a pas de limite supérieure pour le facteur de mérite. Figure 3 indique le meilleur dopage par matériau pour obtenir un haut zT, en gardant un bas κ et des hauts S et σ [16]. Les meilleurs matériaux de l'état de l'art ont une valeur de $zT = 1 \sim 2$ au maximum de leur plage de température, étant strictement dépendant de σ, S et κ. $zT = 1$ est la valeur considérée comme une très bonne réalisation pour un matériau concurrentiel industriellement. Les principales approches possibles pour accroître le facteur de mérite zT sont: créer un nouveau matériau avec une structure complexe de cristal (qui peut abaisser la κ_{ph}) [17], ou nanostructurer la matière, en changeant ainsi les propriétés thermoélectriques (S, σ) par rapport à celles du matériau massif [20], [21], [48].

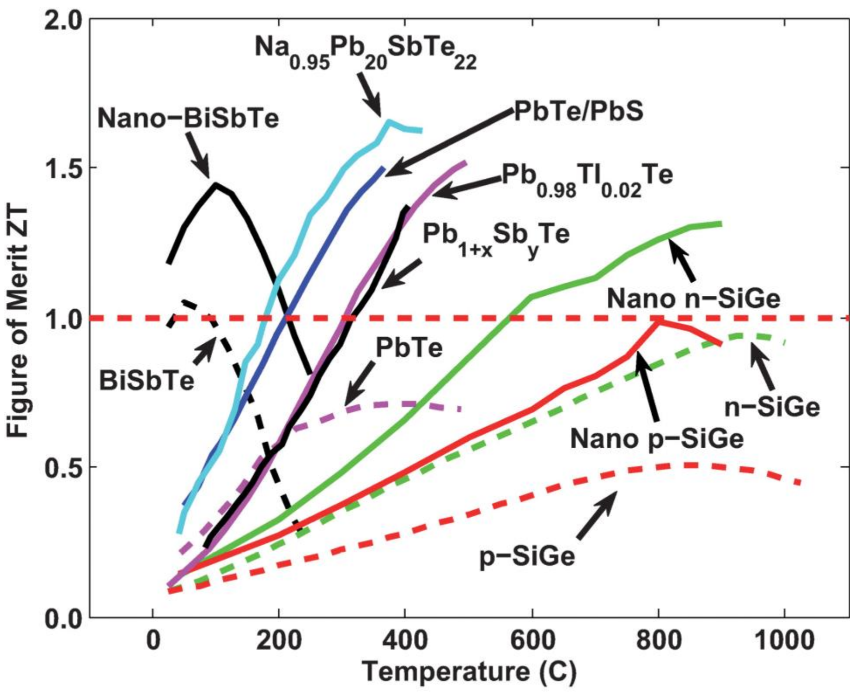

Figure 3 Nombre de mérite *ZT* des matériaux pour applications TE l'état de l’art en fonction de la température. La ligne pointillée rouge indique le *ZT* maximum pour les matériaux massifs, la ligne continue indique des résultats récents de *ZT* pour matériaux nanostructurés ou nanocomposites [16].

L'intérêt pour les matériaux nanostructurés est principalement lié à deux raisons. D'abord, la forte densité d'interfaces conduit à une réduction du flux de chaleur véhiculé par la vibration de réseau (phonons), l'échelle de longueur étant comparable au libre parcours moyen des phonons. Deuxièmement, la dimension réduite du système électronique qui peut être obtenue par ingénierie des bandes et nanostructuration à l'échelle de la longueur d'onde des électrons, peut être exploitée pour améliorer les propriétés des matériaux électroniques.
Les propriétés thermiques des membranes de silicium entièrement suspendues ont largement été étudiées au cours des dernières années. La réduction impressionante de la conductivité thermique jusqu'à un facteur 10 est une étape prometteuse vers l'intégration potentielle du silicium dans les convertisseurs thermoelectriques qui sont rentables et compatible avec la technologie industrielle (CMOS).

Plusieurs travaux présentent les différentes techniques adoptées pour mesurer la conductivité thermique des membranes en silicium cristallin en suspension. Le Tableau 12 résume les rapports les plus intéressants qui étudient les propriétés thermiques de films minces suspendus de silicium avec les différents méthodes de mesure [89].

Tableau 12 Etat de l’art sur la conductivité thermique des films minces de silicium [89].

Reference	Year	Measurement configuration	Doping	Temperature range	Si thickness (nm)
Ju [113]	2005	On-substrate (steady state Joule heating, varying heater width)	p-type	RT	20 to 50
Liu and Asheghi [106]	2004	Suspended heater bridge (steady-state)	Undoped	20 to 300 K	20 to 25

Reference	Year	Measurement configuration	Doping	Temperature range	Si thickness (nm)
Asheghi *et al.* [107]	1997	On-substrate (steady state Joule heating)	n-type	20 to 350 K	420, 830, 1600
Asheghi *et al.*[36]	2002	Suspended film (steady state Joule heating)	B or P (10^{17}-$3\cdot10^{19}$ cm^{-3})	15 to 300 K	3000
Chavez-Angel *et al.*[114]	2014	Raman thermometry	-	RT	9

Les cristaux phononiques sont fabriqués en modelant le matériau de façon périodique et régulière, en lui conférant des propriétés qui dépendent strictement de ses caractéristiques extrinsèques (comme: la hauteur, la taille du cou, la fraction de remplissage, etc.) et celles intrinsèques (comme la vitesse de groupe, le libre parcours moyen, les anisotropies de cristal, etc.).
Récemment, plusieurs groupes, résumés dans le Tableau 13, ont concentré leurs efforts pour démontrer que la structuration du silicium avec des cristaux photoniques sur films minces en suspension représente la méthodologie de nanostructuration la plus efficace pour réduire nettement la conductivité thermique.

Tableau 13 14 Etat de l'art sur la conductivité thermique des films minces de silicium avec PnCs.

Reference	Year	Measurement configuration	Doping	Temperature Range (K)	Si thickness (nm)	Pore diameter/pitch (nm)
Yu *et al.* [108]	2010	Suspended heater thermometer	B ($2\cdot10^{19}$ cm^{-3})	80 to 320	20 to 25	11/34; 16/34; 270/385
Tang *et al.*[123]	2010	Suspended heater thermometer	Intrinsic or B ($5\cdot10^{19}$ cm^{-3})	25 to 300	100	32/55; 81/140; 198/350
Kim *et al.*[124]	2012	Suspended (steady-state Joule heating)	B (10^{16} cm^{-3})	RT	500	200 to 500/ 500 to 900
Song and Chen [121]	2004	Suspended film (steady-state Joule heating)	n- type ($5\cdot10^{14}cm^{-3}$ - $5\cdot10^{15}cm^{-3}$)	50 to 300	4670	2300 to 10900/ 4000 to 20000
Hopkins *et al.*[122]	2010	Thermoreflectance	n-type	RT	500	300/500or600or700; 400/800
Marconnet *et al.* [125]	2012	Suspended heater thermometer	-	RT	196	110/385; 210/385; 280/385
Nomura *et al.* [126]–[128]	2015	Micrometer scale time domain thermoreflectance	B doped (lightly)	4 et RT	145	211/300
Alaie *et al.* [129]	2015	Suspended film (steady-state Joule heating)	-	RT	366	850/1100

Lim *et al.*[130]	2015	Suspended film (steady-state Joule heating)	B doped ($3.1\cdot10^{18}$ cm^{-3} to $6.5\cdot10^{19}$ cm^{-3})	50 to 300	340	26 to 44/60

Considérant les rapports cités, il est clair que la réduction de la conductivité thermique des phonons pour les applications thermoélectriques est un sujet chaud au cours des dernières années. Les facteurs sur lesquels il est important d'attirer l'attention afin de concevoir la meilleure structure de cristal photonique sont: l'épaisseur de la matière active (SOI à couche mince dans ce cas), le facteur de remplissage *ff*, la période et la distance limite entre deux trous. L'influence de ces paramètres sur la réduction de la conductivité thermique est discutée dans les chapitres suivantes.

Chapitre 2 - Simulations de Dynamique Moléculaire

Compte tenu des études récentes dans le domaine du silicium nanostructuré pour les applications thermoélectriques, reproduire les mêmes phénomènes dans un cadre de simulation est d'une grande importance pour la compréhension des résultats expérimentaux ainsi que la prévision des futures applications possibles.

Tout d'abord, un modèle approprié pour le mécanisme de transport de la chaleur et l'analyse de la conductivité thermique doit être choisi.

Plusieurs méthodes existent pour calculer correctement la conductivité des phonons thermiques κ par la distribution d'interaction atomique [101], [205]. Les méthodes les plus connues sont: Green-Kubo (ou d'équilibre) Dynamique Moléculaire (GK-MD)[139], [206], Dynamique Moléculaire Hors Equilibre (NMD, aussi connu sous le nom de méthode directe) [140], Dynamique Moléculaires Approche à l'équilibre (AEMD) [141], l'équation de Transport de Boltzmann (BTE) [94] et Dynamique du réseau cristallin (LD) [101].

Le méthode de Dynamique Moléculaire est base sur l'utilisation d'un potentiel interatomique pour résoudre les équations classiques du mouvement et recueillir des données statistiques thermodynamiques. Cette méthode englobe tous les effets de la partie anharmonique du potentiel. Surtout, aucune hypothèse n'est necessaire pour le temps de vie des phonons et leur vitesse de groupe. Dans ce travail, on a choisi la Dynamique Moléculaire combinée avec la méthode de Green-Kubo pour la prédiction de la conductivité thermique du silicium nanostructuré. Les simulations MD sont effectuées en utilisant le logiciel de LAMMPS [142], [143].

L'approche permet de décrire un ensemble classique de N atomes, chacun d'eux étant décrit comme un point de masse M, avec une position et une vitesse constante, dont le mouvement est décrit par la deuxième loi de Newton. Pour le théorème de fluctuation-dissipation, à chaque étape, les positions et les vitesses de chaque atome peuvent être calculées en tant que fonction du temps et utilisées pour calculer la conductivité thermique du système par la méthode de Green-Kubo:

$$\kappa = \frac{1}{3k_B V T^2} \int_0^\infty \langle \vec{J}(t) \cdot \vec{J}(0) \rangle dt \tag{81}$$

où V est le volume du système, et $\left\langle \vec{J}(t) \cdot \vec{J}(0) \right\rangle$ la fonction d'autocorrélation du courant de chaleur (HCAF). Ce dernier est la moyenne sur un intervalle de temps défini pour une seule simulation, puis le même ensemble est répété pour des simulations avec des conditions initiales différentes randomisées (*seeds*).

La Figure 4 décrit les étapes de simulation.

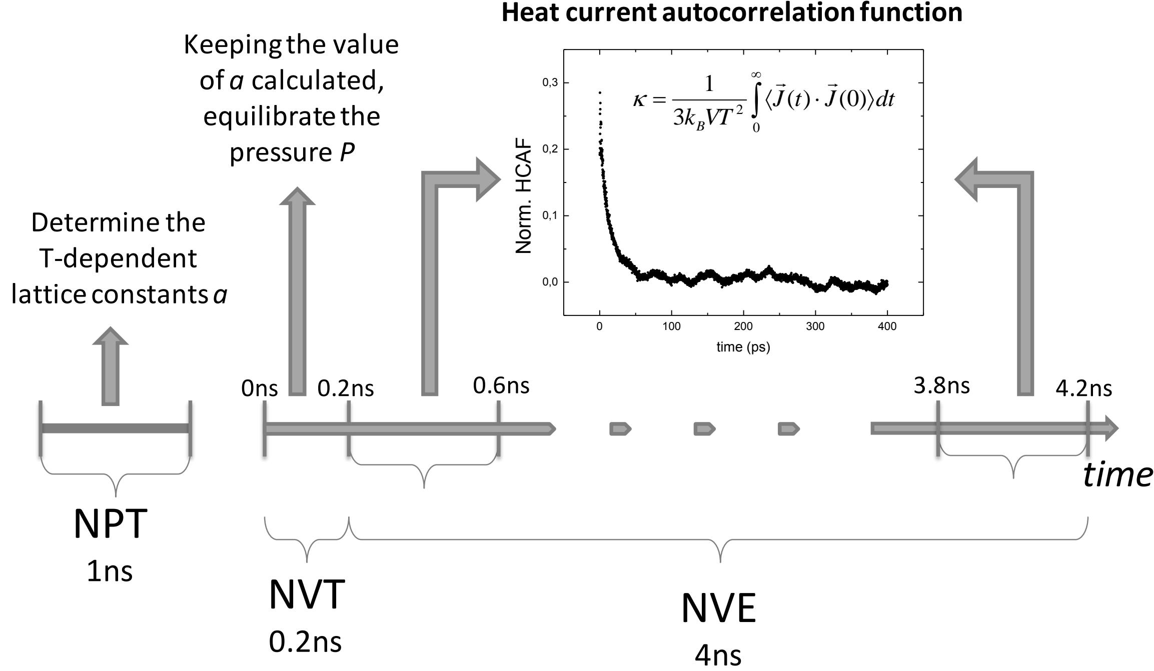

Figure 4 Schéma de la procédure de Dynamique Moléculaire adoptée indiquant les étapes de simulation et les durées caractéristiques.

Les géométries des cellules simulées visent à décrire du silicium massif, en couche mince, avec cristal phononique (PnCs) et une membrane phononique (PM). Elles sont schématisées en Figure 5.

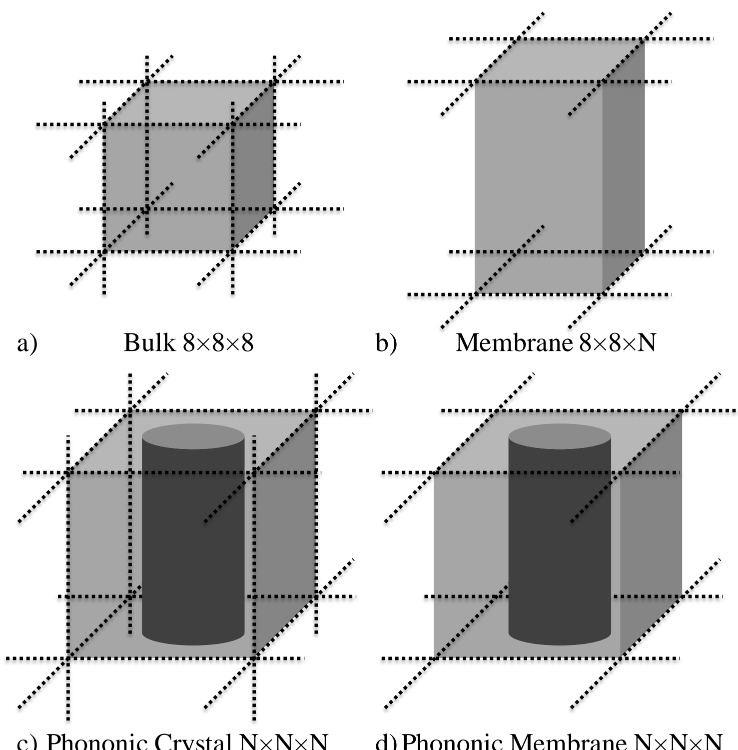

Figure 5 Cellules de simulation MD utilisées dans ce travail afin de décrire: a) du silicium massif, b) une membrane, c) un cristal phononique avec une dimension infinie selon l'axe z et d) une membrane phononique. Les nombres X × Y × Z désignent les dimensions des cellules en terme de constantes de réseau de silicium.

La Figure 6 présente les résultats comparés de nos simulations effectuées avec deux différentes formulations du potentiel (Stillinger-Weber (SW) et Environment Dependent Interatomic Potential (EDIP)) et l'état de l'art.

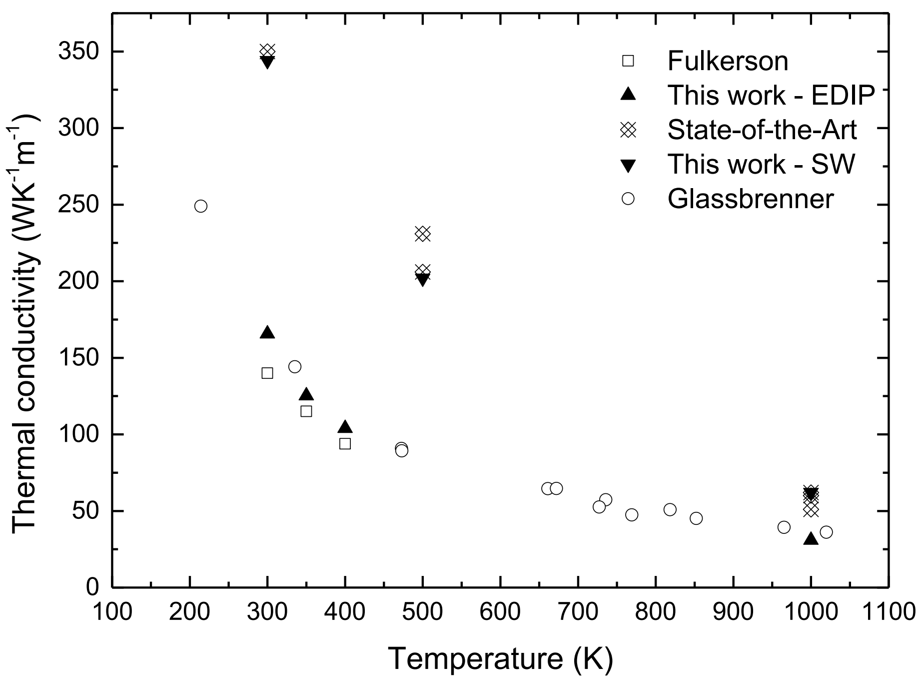

Figure 6 Comparaison des résultats obtenus à partir de MD - GK avec SW et EDIP potentiels dans nos simulations et les state-of-the-art (dans le tableau 2.1 et le tableau 2.2) et points expérimentaux de Fulkerson [31] et Glasbrenner [30].

Les structures simulées sont résumées dans le Tableau 15, la comparaison avec les résultats expérimentaux [99], [150] est aussi indiquée.

Tableau 15 Dimension cellulaire des fractions de remplissage et résultats des simulations MD de conductivité thermique à 300K.

Type / Boundaries	Size N	Radius R	*ff* (%)	(W/m/K) *p p p*	(W/m/K) *p p s*
Bulk 8×8×8	-	-	-	165.7	-
Membrane 8×8×N	15	-	-	-	44.9
	20	-	-	-	54.2
	30	-	-	-	59.3
PC & PM N×N×N	15	3	12.57	19,82	12,03
	15	4	22.34	9.51	7.22
	15	5	34.91	5.76	4.11
	15	6	50.27	2.24	2.36

Un bon accord entre la simulation et le modèle développé est obtenu pour le silicium massif (Figure 7). Pour les membranes et les cristaux phononiques les résultats restent dans les barres d'erreur. Une diminution de la conductivité thermique est illustrée en Figure 7 pour la géométrie film mince (44,9 $Wm^{-1}.K^{-1}$) comparée au silicium massif et aux géométries de cristaux phononiques (5,76 $Wm^{-1}.K^{-1}$). Il est à noter que, malgré le fait que le cristal phononique est infini selon l'axe z (conditions périodiques appliquées aux bords), cette configuration permet d'obtenir une réduction de κ d'un facteur 30 par rapport au silicium

massif. Le même ordre de grandeur est obtenu pour tous les cristaux phononiques quelle que soit la hauteur. Une réduction supplémentaire est obtenue pour les membranes avec des motifs périodiques (4,11 $Wm^{-1}.K^{-1}$), qui souligne que ces deux effets peuvent se cumuler dans de tels systèmes. Cette dernière constatation est d'une grande importance, car elle prend en compte et évalue les contributions respectives de géométrie de la couche mince et de la structure phononique sans nécessité d'autres paramètres *ad-hoc*.

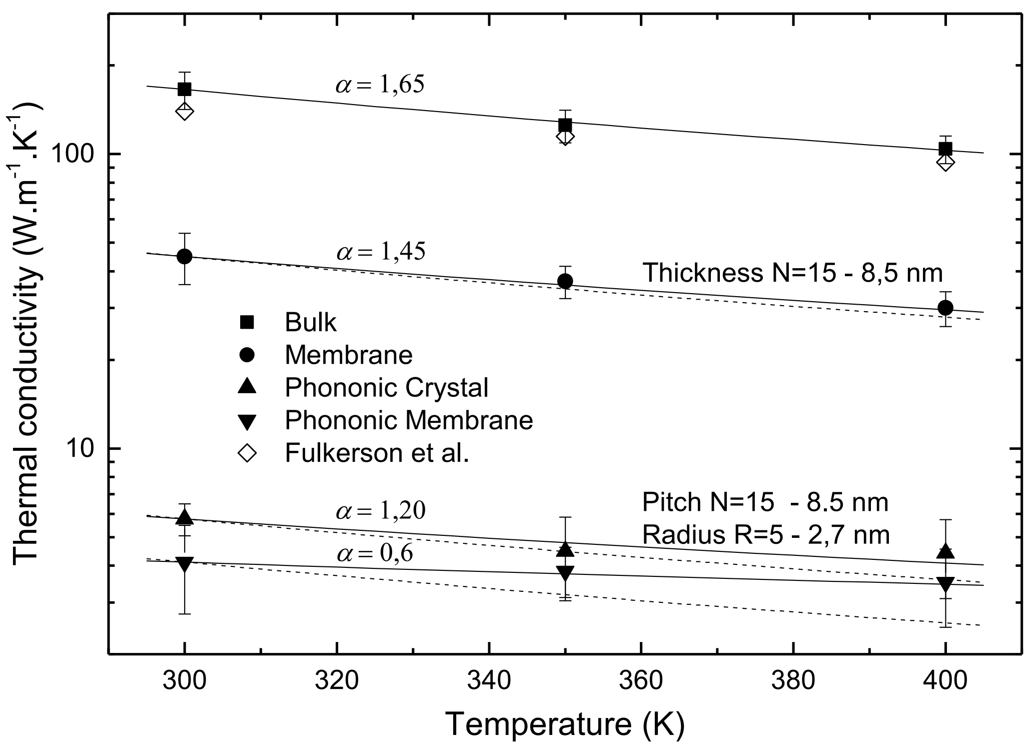

Figure 7 Conductivité thermique simulé par MD Green-Kubo en fonction de la température (symboles plains). Les résultats permettent un ajustement des paramètres avec une loi de puissance. Une comparaison avec les résultats expérimentaux de [150] est aussi faite.

L'effet phononique est considéré comme une entrave au transport de phonons soit par confinement dû à la couche mince, soit par les trous cylindriques gravés ou les deux structures à la fois. Dans cette mesure, la procédure ne fait pas de discrimination entre les effets périodiques "cohérents" et les effets de diffusion, pour lesquels un ensemble de simulations spécifiques est nécessaire.

Considérant l'ordre de grandeur des résultats, un accord raisonnable est trouvé par rapport aux conclusions de Yu *et al.* [131](1,9 $Wm^{-1}K^{-1}$), Tang *et al.* [123] (1,73 à 10,23 $Wm^{-1}K^{-1}$), Lim *et al.* [130](1,8 $Wm^{-1}K^{-1}$) et Alaie *et al.* [129](1,5 $Wm^{-1}K^{-1}$), même si des petits écarts entre les résultats expérimentaux et simulés sont présents.

Enfin, nous pouvons remarquer que la méthodologie MD–GK avec le potentiel EDIP reproduit bien la réduction de la conductivité thermique du silicium nanostructuré. En outre, les résultats mettent en évidence la pertinence des simulations MD pour une comparaison quantitative avec les valeurs expérimentales. Le méthode ne nécessite aucune hypothèse sur la distribution de phonons et le mécanisme de transport. En plus, il est démontré qu'il reproduit bien les différentes tendances expérimentales telles que les effets de la température et de la

dimensionnalité, en permettent de clarifier la physique du transport thermique dans les systèmes à l'échelle nanométrique.

Chapitre 3 - Conception et fabrication du dispositif

Ce chapitre décrit la méthodologie développée pour réaliser une plate-forme de métrologie en couche mince avec des cristaux phononiques pour mesurer la conductivité thermique avec les différentes méthodes décrites dans le chapitre suivant.

La structuration de cristaux phononiques denses et sans défauts représente le principal défi pour le processus de fabrication d'une telle structure périodique. La dimension de la période de répétition, ou pas est établi par deux paramètres: la longueur d'onde des phonons (λ ~ 2 nm) et son libre parcours moyen (Λ_{ph} ~ 100 nm). Pour garantir une réduction efficace de κ sans affecter la conductivité l'électrique un σ_{el}, le pas doit être plus grand que le libre parcours moyen de l'électron (Λ_{el} ~ 2-3 nm) à la température ambiante. De cette manière, il est évitée une dégradation sensible de σ_{el}, comme démontré par Yu et al. [131].
Les principales variables à contrôler durant le processus de fabrication sont la dose incidente du faisceau d'électrons pendant la lithographique électronique, la résolution minimale de la résine et les paramètres de gravure (concentration et de pression du gaz réactif dans la chambre ainsi que la puissance et le temps). Tout d'abord, pour obtenir la meilleure résolution et sensibilité, différentes méthodes de lithographie par faisceau d'électrons ont été étudiées. Deuxièmement, pour assurer un transfert de motif efficace, plusieurs gravures par ions réactifs (RIE) et techniques ont été testées.

La fabrication complète de PnCs sur silicium pour l'intégration dans les dispositifs est effectuée en combinant les avantages de la méthodologie de lithographie *'dots-on-the-fly'* et les capacités de gravure de Cl_2 (RIE). Les résultats obtenus montrent une très haute résolution et des trous denses (SOI) sur SOI (silicium-sur-isolant). Le substrat utilisé pour les dispositifs est un SOI [162] avec 145 nm d'oxyde enterré (BOX) et 72 nm de silicium. Afin d'assurer une ouverture complète des trous et un masquage efficace de la couche de silicium au-dessous, l'épaisseur de la résine choisie est 170 nm (le profilomètre et l'étude par ellipsomètre confirment la valeur).
Une fois que le processus de fabrication a été détaillé et que les différentes méthodologies sont éprouvées, le processus d'intégration de la membrane structurée peut être illustré. Les étapes de fabrications sont résumées dans la Figure 8. Le substrat utilisé SOI (silicium-sur-isolant) est montré dans l'étape 1. Dans l'étape 2 la structuration de cristaux phononiques est illustrée et elle est suivie (étapes 3) du dépôt de nitrure de silicium (SiN) et de la gravure des cavités (pour permettre, après, l'accès à la suspension de la membrane). Ensuit, le SiN est gravé (étape 4) et le silicium exposé latéralement dans les cavités est oxydé (étape 5) afin de les protéger au cours de l'étape de suspension par XeF_2. Les serpentins et les contacts sont créés par dépôt métallique (de Pt et Au, étape 6). La suspension de la membrane peut alors être effectuée par gravure en phase vapeur du substrat de silicium avec XeF_2 (étape 7) et de l'oxyde enterré (BOX, buffered oxyde) par HF vapeur (étape 8). Une image MEB du dispositif est montrée en Figure 8.

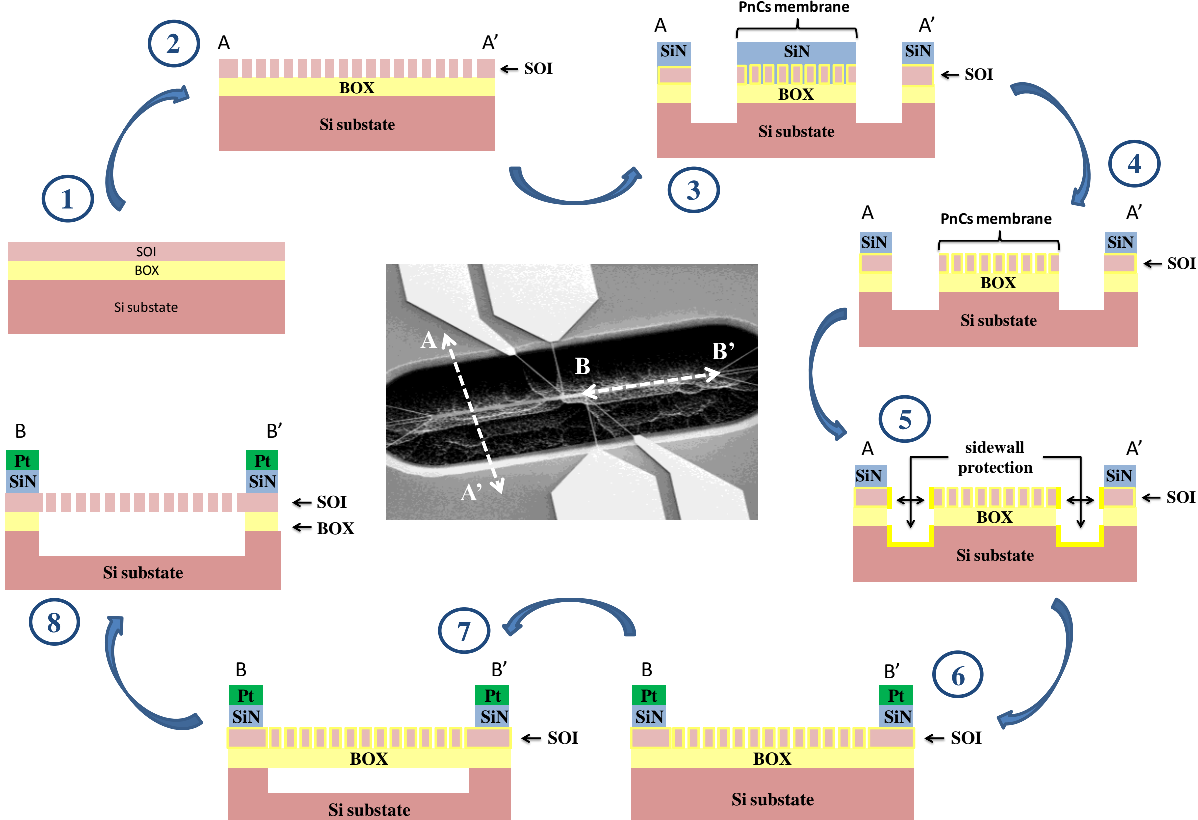

Figure 8 Résumé des principales étapes du processus de fabrication. 1) SOI wafer; 2) PnCs structuration; 3) dépôt de SiN et gravure des cavités; 4) gravure de SiN de membranes; 5) oxydation de silicium pour protéger la paroi latérale; 6) métallisation Pt (et Au); 7) la gravure en phase vapeur XeF_2; 8) gravure en phase vapeur HF. Au centre une image MEB du dispositif, indiquant les différentes coupes des illustrations (AA' et BB').

Dans la Figure 9 six images MEB de la membrane (2eme génération du dispositif) montrent le dispositif entièrement suspendu.

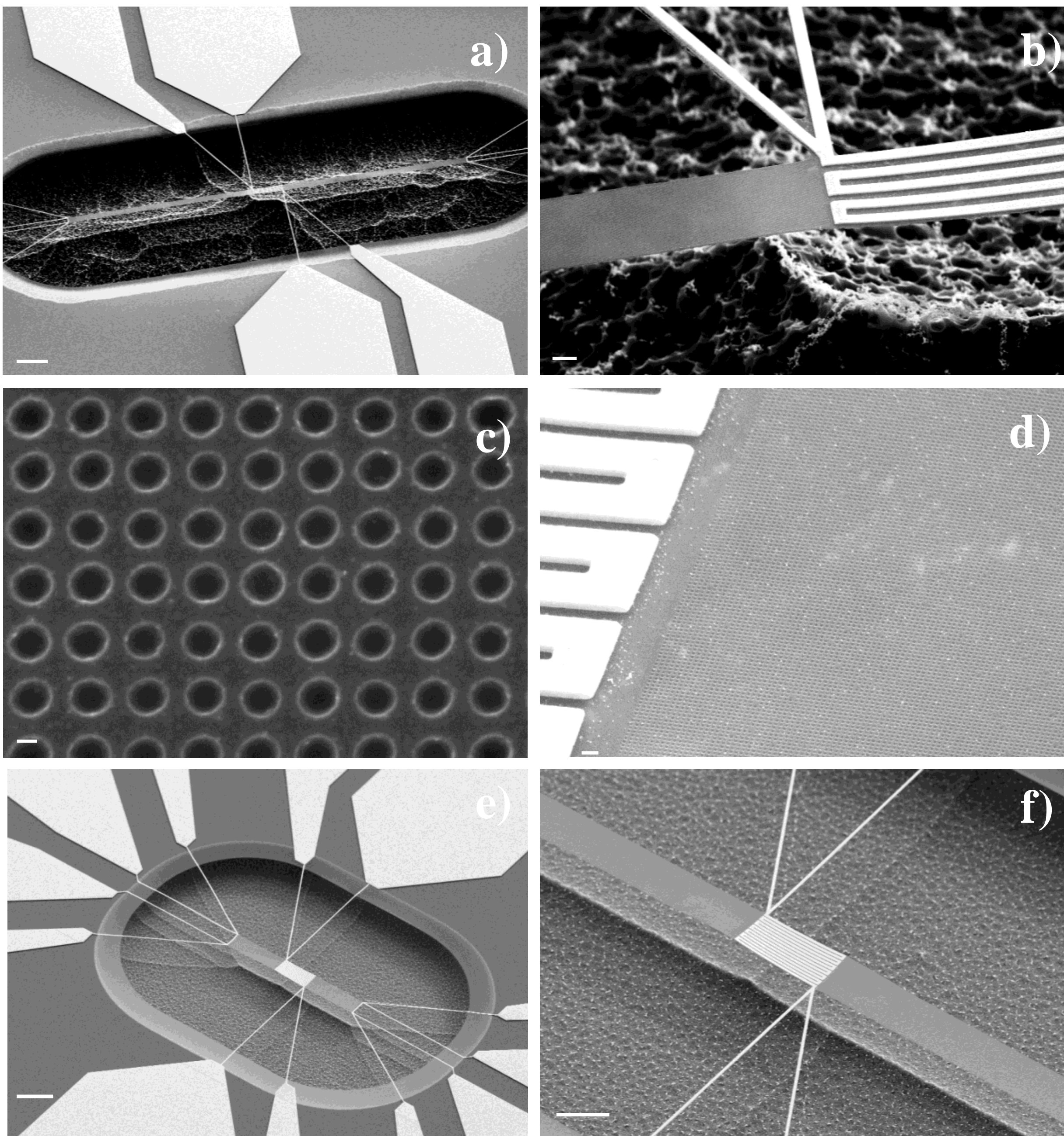

Figure 9 Images MEB des membranes photoniques entièrement suspendues après gravure HF (2e génération). a) La longueur de la membrane est de 120 µm et la largeur 10 µm, la barre d'échelle de 20 microns. b) Détail de la structure en a), barre d'échelle de 1 micron. c) PnCs modèles après gravure HF, pas de 60 nm, barre d'échelle de 20 nm. d) Motifs gravés, le fond de la cavité est visible en transparence. e) 30 µm x 10 µm (barre d'échelle de 20 µm). f) Détails de la membrane de 10 microns et le serpentin de chauffage central. La barre d'échelle est de 10 microns.

La membrane de SOI est entièrement suspendu. L'épaisseur finale est d'environ 62 nm (après le processus d'oxydation qui se produit à la surface entre le silicium et le BOX). Les motifs phononiques ne présentent pas de dégradation (au MEB). Après la gravure HF, le pourcentage de membranes intactes est de 100%. Le procédé développé a pour principal avantage d'être entièrement compatible avec la technologie CMOS, car il ne fait pas usage de masque dur métallique ou de matériaux qui pourraient polluer les surfaces. En outre, il est totalement reproductible et il pourrait être facilement intégré dans un design de type convertisseur (avec une implantation et des petits changements dans la mise en page).

Le travail est focalisé d'abord sur l'intégration de la structure phononique développée sur la plate-forme de mesure pour obtenir le dispositif final.
La première version du dispositif fabriquée et caractérisée est désignée comme $1^{ère}$ génération. Des améliorations structurelles ont été appliquées pour réaliser une 2eme génération avec un serpentin (capteur) totalement suspendu, évitant les pertes, avec quatre bras connectant l'élément chauffant (pour avoir une mesure plus précise de sa résistance). Une autre typologie a été fabriquée pour effectuer des mesures Raman (sans métaux et avec différents dimensions des membranes). Tous les dispositif sont utilisés pour les mesures détaillées dans les prochains chapitres.

Chapitre 4 - Résultats de caractérisations du dispositif

Le chapitre 4 est consacré à la description et l'analyse des résultats obtenus pour les dispositifs dont la fabrication et les caractéristiques sont décrits dans le chapitre 3. Pour étudier la conductivité thermique des motifs phononiques des membranes, différentes méthodologies sont adoptées. La première est la technique électro-thermique pour mesurer la conductivité thermique κ de membranes suspendues en exploitant la variation de résistance en fonction de la température des thermomètres en Pt. Le deuxième technologie présentée est la spectroscopie Raman. Pour cette technique, la position du pic du silicium dépend du décalage du pic Raman en fonction du champ de température établi à travers la membrane. Ainsi, les simulations avec la Méthode des Eléments Finis (FEM) permettent la determination de la conductivité thermique. La dernière technique de mesure est la microscopie à balayage thermique (SThM). Les deux dernières caractérisations sont effectuées dans le cadre de la collaboration établie avec Mouhannad Massoud, Pierre-Olivier Chapuis et Jean-Marie Bluet de l'Institut national des sciences appliquées (INSA, Lyon) à l'Institut des Nanotechnologies de Lyon (INL, Lyon) et au Centre d'Energétique et de thermique (CETHIL, Lyon).

Méthode Electrothermique

Le méthode électrothermique est choisie pour sa simplicité (la méthodologie, les équipements et les explications théoriques), qui permet le maintien de la précision de mesure élevée. Les exigences qui influencent le choix de la structure sont: fuites thermiques faibles (à travers le substrat, les résistances, etc.), distribution de température linéaire dans la longueur de la membrane (pour extraire correctement le comportement caractéristique), sensibilité à la température (liée à la sensibilité de l'équipement électronique, qui permet la sensibilité de la mesure de la conductivité thermique pour les faibles chutes de température). La conductivité thermique de la membrane de silicium en suspension est caractérisée en utilisant 4 ou 6 sondes de mesure électrothermique en régime stable, en s'ispirant des travaux de Liu et Asheghi [106], [107].

Les dispositifs conçus et fabriqués pour les mesures électro-thermique sont de deux types. Ainsi, les procédures d'extraction de la conductivité thermique sont différents, étant donnés les différences de la physique associé. Le principal point à prendre soigneusement en compte est que le serpentin du capteur est fabriqué sur le substrat, où le métal est déposé, pour la première génération, et entièrement suspendu, avec une température différente qui respecte celui du chuck, pour la deuxième génération. La première partie de la mesure consiste à la calibration du serpentin afin d'extraire le coefficient α. La Figure 10 montre l'ajustement linéaire des points expérimentaux de la résistance en fonction de la température du chuck pour estimer α, le coefficient de température de résistance, pour les membranes en suspension.

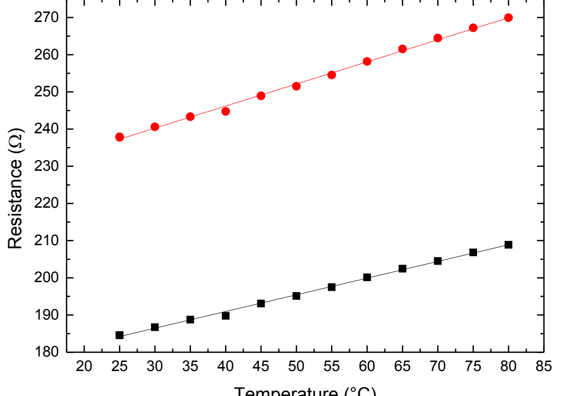

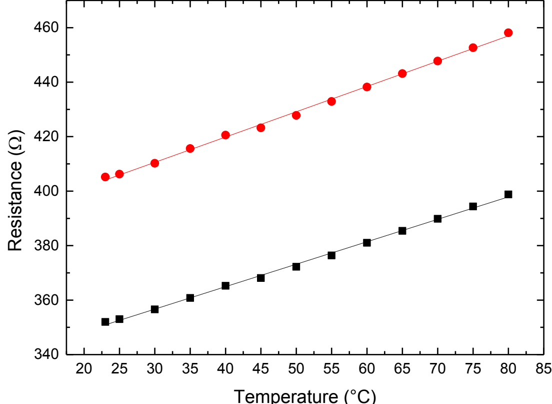

Figure 10 Détermination du coefficient α pour le capteurs en Pt pour les membranes de largeur 5 µm (à gauche) et 10 um (à droite). Les mesures sont effectuées avec quatre sondes sous vide. Les points rouges sont liés à la résistance extérieure mesurée, affectée par des pertes; les points noirs indiquent la résistance interne, pour laquelle les pertes ne sont pas présentes.

Une fois que les deux éléments sont calibrés, la variation de température (et résistance) de l'élément chauffant doit être liée à une variation de température correspondant sur le capteur. Ainsi, un autre étalonnage est réalisé sur le serpentin de chauffage pour relier la variation de la tension appliquée au température du Pt. Le dernier étalonnage permet d'effectuer l'étape suivante (couplage) des mesures. La tension est balayée sur le dispositif de chauffage et induit, par effet Joule, une augmentation de la résistance sur le capteur, qui est directement liée à la variation de température due à la chaleur transférée à travers la membrane. La conductivité thermique est obtenue à partir de la loi de Fourier, étant donné que la chaleur injectée par le serpentin de chauffage, dans les deux membranes identiques et symétriques, est généralement transférée dans les deux sens pour les capteurs par effet Joule.

Pour le deuxième design six sondes ont été utilisées pour améliorer la précision des mesures, comme montré dans Figure 11. Dans le graphique de droite, les températures extraites pour les éléments chauffant et capteurs sont montrées (LA: température de chauffe, TS: température de capteurs et T_0: température du chuck). Il faut préciser que la mesure de couplage est effectué avec deux sondes sur le serpentin de chauffe, et quatre sur les capteurs, à gauche et à droite. Le graphique montre que les membranes conduisent la chaleur de la même façon, en présentant la même température au niveau des serpentins opposés.

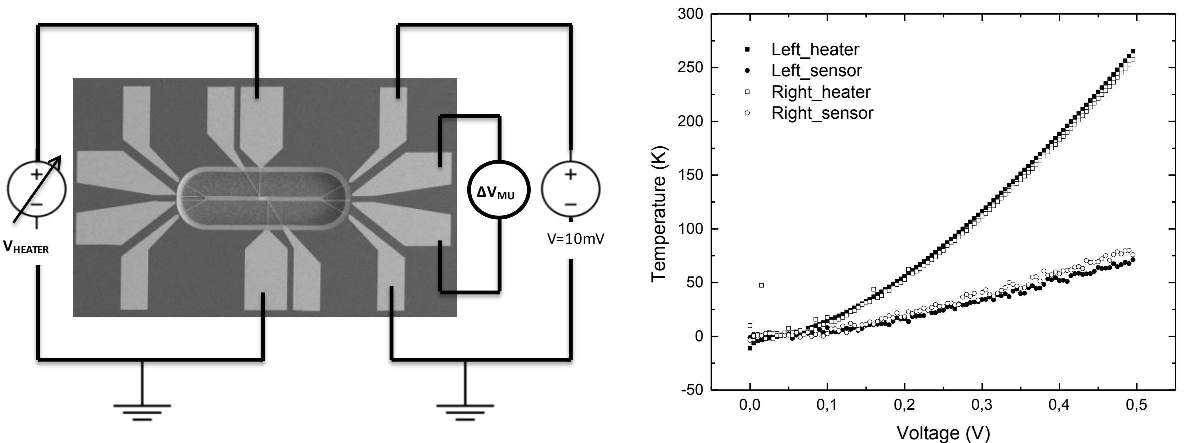

Figure 11 Gauche: connexion avec 6-sondes pour le couplage électrothermique entre l'élément chauffant et le capteur (pour extraire la variation de température). Droite: températures mesurées pour élément chauffant et capteurs (les deux côtés).

Les résultats obtenus par la méthode électrothermique avec le premier et deuxième dispositif sont comparées avec ceux de l'état de l'art dans la Figure 12 (triangles pleins).

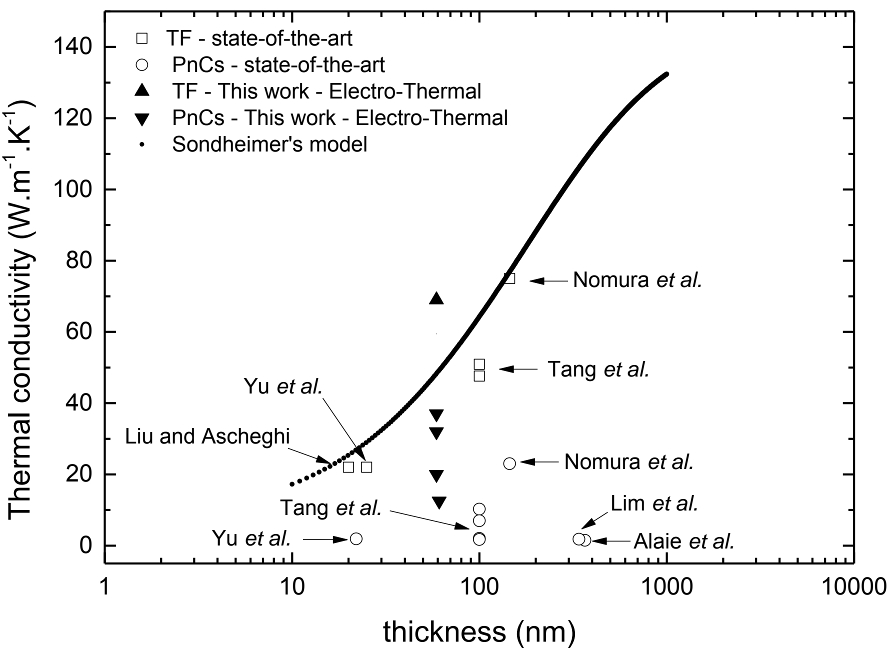

Figure 12 Conductivité thermique des membranes à couches minces (TF) et de celles avec cristal phononique (PNCS) de ce travail et pour l'état de l'art résultats avec la methode électrothermique (pour les deux designs de dispositifs fabriques).

Il est remarquable que la réduction de la conductivité est de 50% relativement à celle enregistrée pour les membranes fines. L'effet phononique observé par de récents travaux [108], [129], [130] n'est pas du même ordre pour les membranes présentées ici. Il doit être pris en compte que la méthode de mesure, l'épaisseur de la membrane et les dimensions des motifs périodiques (emplacements, l'encolure, factor de remplissage) sont différents.

Spectroscopie Raman

La diffusion Raman est la diffusion inélastique de la lumière monochromatique, en général à partir d'un laser dans le domaine visible, infrarouge proche, ou ultraviolet proche. La lumière

du laser interagit avec les vibrations moléculaires, ou d'autres excitations des phonons dans le système, résultant en un décalage de l'énergie des photons du laser vers le haut ou vers le bas. Le changement dans l'énergie donne des informations sur les modes de vibration dans le système. Ainsi, les propriétés du matériau phononique peuvent être étudiés en réalisant une simulation avec la méthode des éléments finis. Celui permet de relier la température constatée avec la dissipation de chaleur dans la membrane et déterminer sa conductivité thermique.
La Figure 13 présente le décalage du pic Raman en fonction du nombre d'onde pour différentes densités de puissance (*D*). Les densités sont liées à la puissance laser (P_0) par l'équation:

$$P = P_0 \cdot 10^{-D} \tag{82}$$

De la Figure 13, on peut remarquer que le pic se déplace dans la bonne direction prévue avec l'augmentation de la puissance et il s'élargit. Une fois que le décalage du pic principal du silicium (522 cm^{-1} pour le silicium à la température ambiante) est déterminé, un ajustement avec une courbe de Lorentz est effectué sur la ligne de base pour obtenir le changement de référence à l'extérieur de la membrane.

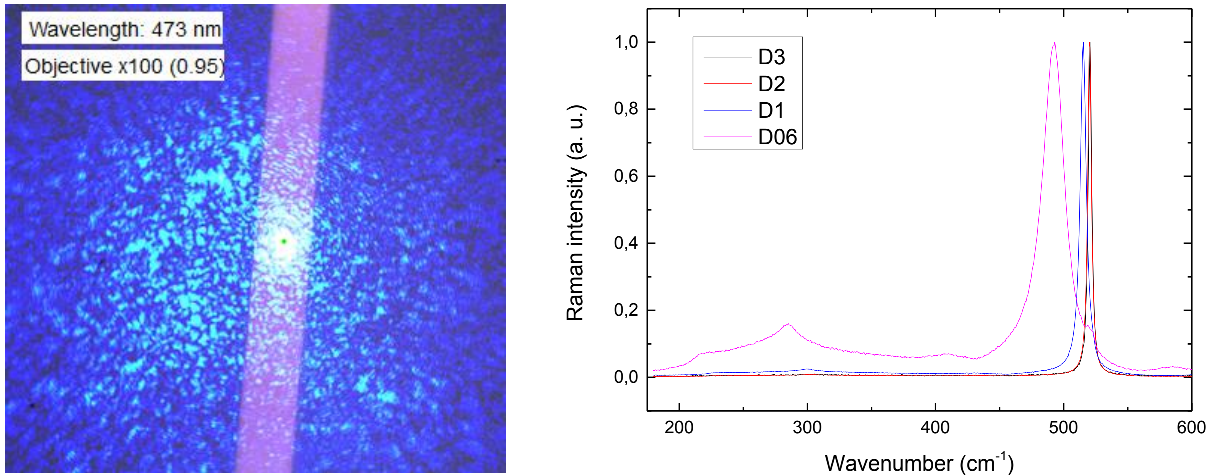

Figure 13 Gauche: La lumière laser (longueur d'onde 473,11 nm) est focalisée sur la membrane. Droite: image du deplacement du pic Raman en fonction du nombre d'onde pour différentes densités de puissance. Les puissances sont: D1 = 0,01 mW, D2=0.1 mW, D3 = 1 mW, D0.6 = 2.51 mW et la puissance nominale P_0 = 10 mW.

La cartographie (Figure 14) montre clairement le décalage du pic Raman dans la longueur de la membrane, ce qui confirme la forme parabolique de la courbe trouvée pour différentes membranes (énumérées ci-dessous) et l'analys dans une gamme de 8 µm de largeur.

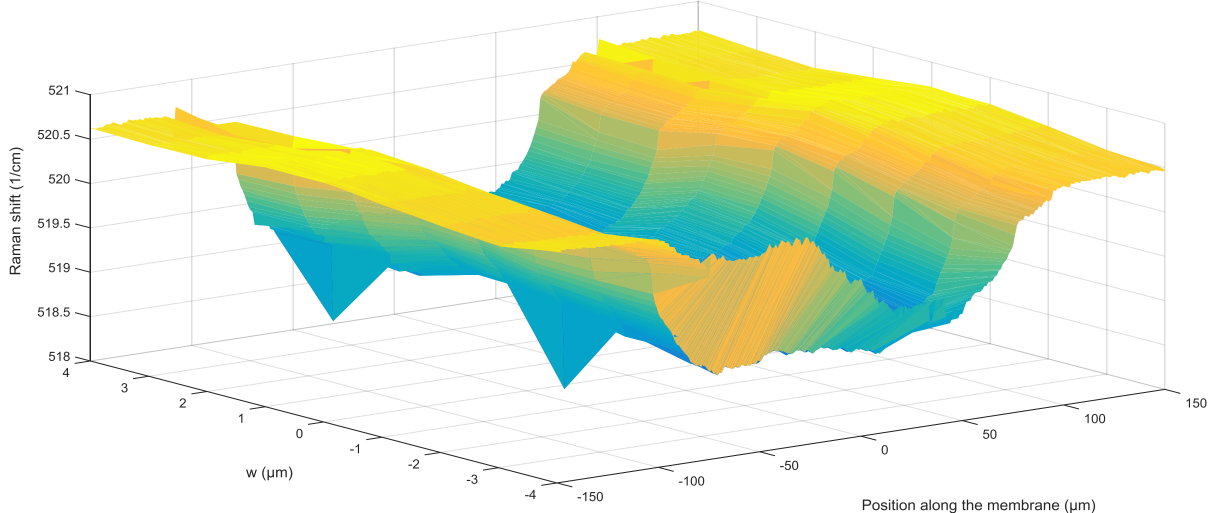

Figure 14 La cartographie 3D montre le décalage du pic en fonction de la longueur de la membrane et la largeur (w).

Les mesures, effectuées sur une membrane d'une longueur de 200 µm et d'une largeur de 10 µm, avec une épaisseur de 59,4 ± 0,3 nm, présentent une valeur moyenne de κ autour de 59,5 W m^{-1} K^{-1} pour les membranes plaines, 30,5 W m^{-1} K^{-1} pour les membranes avec un pas de 60 nm, 32,5 W m^{-1} K^{-1} pour celles de 80 nm et 39,5 W m^{-1} K^{-1} pour celles de 100 nm. Les résultats, qui confirment les attentes et la tendance théorique, sont rapportés dans le Tableau 16.

Tableau 16 Conductivité thermique pour les membranes (longueur 200 µm et la largeur de 10 µm) simple et trouées (de pas différentes) mesurées.

Epaisseur (nm)	κ (W m^{-1} K^{-1}) plaine	κ (W m^{-1} K^{-1}) pas 60 nm	κ (W m^{-1} K^{-1}) pas 80 nm	κ (W m^{-1} K^{-1}) pas 100 nm
59,1	61,5	34,5	33	40
59,4	59,5	30,5	32,5	39,5
59,7	58	30	29	38,5

Microscopie à Balayage Thermique

Le mesures au microscopie à balayage thermique (SThM) sont effectuées au Centre d'Energétique et de Thermique de Lyon (CETHIL), dans le cadre d'un projet de collaboration avec Mouhannad Massoud, Pierre-Olivier Chapuis et Jean-Marie Bluet. La microscopie thermique à balayage (SThM) est une technique basée sur la microscopie à force atomique (AFM). La déflection d'un levier est sondée par un faisceau laser incident sur une partie réfléchissante de la pointe de la sonde (ou un miroir), qui reflète le rayon vers une photodiode. La déviation génère un signal électrique qui est détecté et, à travers une boucle de rétroaction, la force du contact entre la pointe et l'échantillon est ajusté tandis que la pointe balaye latéralement. Le contraste de l'image thermique fournit des informations sur le changement de la quantité de chaleur échangée entre la pointe et l'échantillon.

La sonde fixée à l'extrémité est une thermorésistance métallique. Le levier utilisé est constitué d'un fil de Wollaston [207] constitué d'une coquille d'argent de κ = 429 W·m^{-1}·K^{-1} et un

diamètre de 75 µm. Le noyau du fil est constitué d'un alliage de Pt_{90} / Rd_{10} présentant un κ = 38 $W \cdot m^{-1} \cdot K^{-1}$ et un diamètre de 5 µm. La pointe du levier est pliée en forme de V et une partie de 200 µm est gravée pour exposer le noyau Pt_{90} / Rd_{10} . L'avantage principale de cette méthode repose sur le fait qu'elle ne se limite pas à la résolution latérale par diffraction optique à quelques centaines de nanomètres. En effet, étant une technique basée sur la microscopie de sonde à balayage (SPM), sa résolution spatiale dépend des longueurs caractéristiques associées au transport de la chaleur entre la pointe (sonde thermique) et l'échantillon. Un image de la sonde est présentée (Figure 15).
Les dispositifs de mesure sont ceux décrites dans le chapitre précédent, appelés 1ère génération avec thermomètres à résistance de platine (PRTs) et les échantillons fabriqués pour les mesures Raman (sans Pt et Au métaux).
Un modèle Comsol de la géométrie 3D de pointe a été réalisé au CETHIL par Mouhannad Massoud afin de prendre en compte l'angle de la géométrie et de l'inclinaison pour simuler le balayage de la membrane et les températures liées.

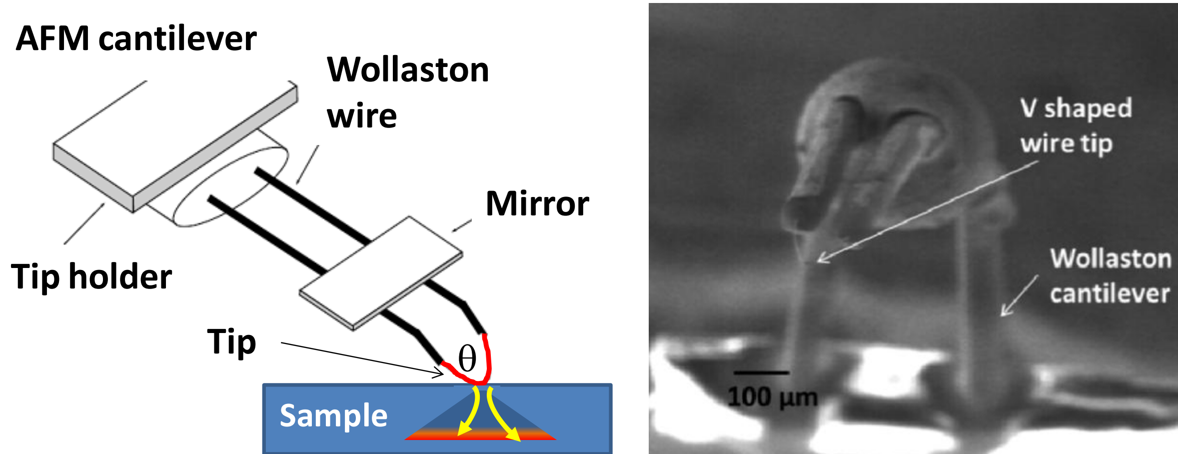

Figure 15 Gauche: image schématique de la sonde à fil Wollaston utilisé pour les mesures SThM. Droite: image pris avec le Microscope Electronique à Balayage de la sonde de fil Wollaston [195].

La résistance dépend de la température, et la relation entre la chute de tension et la variation de température est une proportionnalité directe:

$$\Delta V \propto \Delta T \tag{83}$$

Etant donné que ΔT dépend de la conductivité thermique de l'échantillon, la Figure 16 montre le profil de tension détecté en fonction de la position sur la membrane pour des longueurs différentes (à gauche) et une comparaison entre les membranes pleines et troués (à droite). À première vue, on peut dire que les températures suivent l'ordre théorique attendue. En outre, la partie plate de la courbe peut être justifiée par les pertes de chaleur latérales (aux bords des membranes).

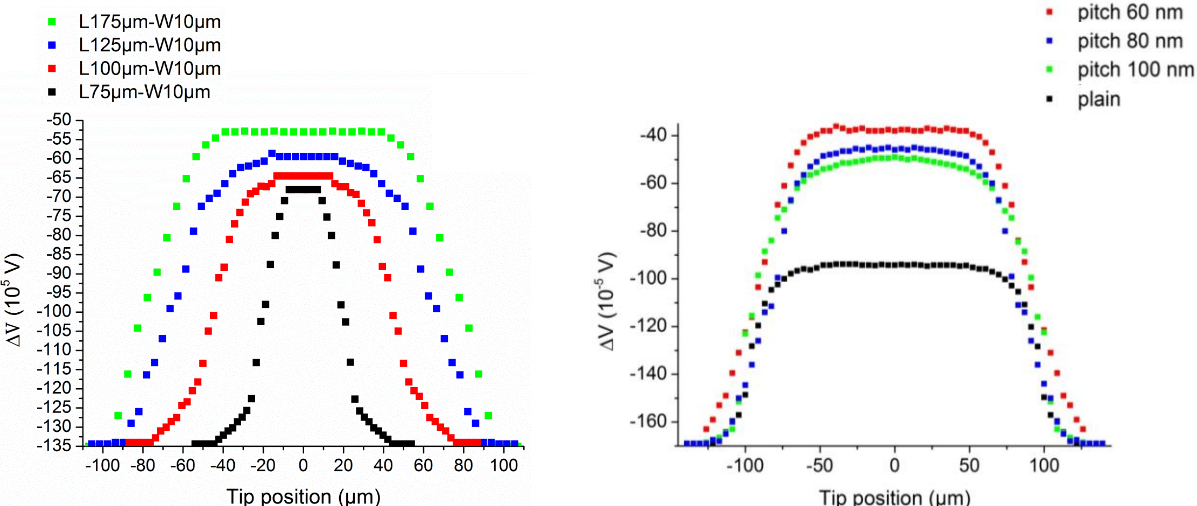

Figure 16 Gauche: profil de tension détecté (proportionnelle à la différence de température) pour différentes longueurs de membranes. Droite: Comparaison entre membranes avec différents nanostructurations de la membrane (différents pas des PnCs et membrane pleine).

La conductivité thermique des membranes est analysée par SThM et comparée à celles d'échantillons d'étalonnage pour extraire leur conductivité thermique. Les échantillons avec PnCs présentent une conductivité thermique dans l'ordre attendu, mais légèrement inférieur à celui obtenu précédemment pour les mesures Raman. La collaboration est encore en cours, des améliorations dans l'extraction des valeurs de κ peuvent être fait et les résultats présentés doivent être vérifié.

Conclusions et Perspectives

Dans la première partie de ce travail de recherche un cadre exhaustif pour les simulations de dynamique moléculaire par le méthode Green-Kubo (MD-GK) a été mis en place afin d'étudier le mécanisme de transport de la chaleur dans les dispositifs nanostructurés et de fournir un outil pour la conception prédictive du design des ceux dispositifs. Les simulations effectuées reproduisent bien la réduction impressionnante de la conductivité thermique du silicium due à la structuration périodique à l'échelle nanométrique. En outre, les résultats mettent en évidence l'aptitude de la methode MD pour une comparaison quantitative des résultats obtenus avec des valeurs expérimentales. La méthode adoptée présente l'avantage de ne pas nécessiter des hypothèses sur la distribution de phonons, ni sur les mécanismes de transport, déjà intégrés dans la formulation du potentiel. Les résultats ont démontré une reproduction des tendances expérimentales, telles que la température et les effets de la dimensionnalité. Enfin, les résultats confirment que le membranes avec une structure phononique présentent une réduction majeure de conductivité thermique par rapport à celles pleines.

La deuxième tâche abordée a été la conception, le design et la fabrication d'une plateforme de métrologie à film mince avec structures phononiques pour mesurer la conductivité thermique. Tout d'abord, un processus robuste de fabrication a été développé utilisant la technique *'dots-on-the-fly'*. De plus, l'utilisation du silicium, avec des matériaux compatibles avec l'industrie (SiN, Pt et Au) pour la fabrication de dispositif complet, garantit la compatibilité avec les technologies CMOS et permet l'intégration des PnCs dans un convertisseur d'énergie thermoélectrique à film mince. En outre, le procédé développé préserve les surfaces de contamination parce qu'il évite le dépôt des masques durs en métal. L'intégration des membranes suspendues donne de la souplesse au dispositif, en prévoyant l'application possible dans le domaine de l'électronique flexible. En effet, l'architecture du dispositif et le choix de fabriquer des thermomètres en Pt pour le chauffage et la détection provient de l'intérêt de réadapter la structure pour les mesures successives de coefficient de Seebeck et conductivité électrique (voir la section Perspectives).

Une fois que le processus de fabrication du dispositif a été établie, la conductivité thermique est mesurée. La première caractérisation est réalisée par la méthode électrothermique, l'exploitation du chauffage du thermomètre à résistance de platine (PRTs), dans le cas de la première et deuxième génération du dispositif, et permet la détection de la variation de température. Une réduction constante de la conductivité thermique a été observé pour le premier dispositif conçu. La conductivité thermique obtenue montre une diminution de sa valeur pour les membranes troués par rapport aux plaines. Les résultats obtenus pour les membranes plaines sont en ligne avec celui présent dans la littérature (et en suivant les modèles théoriques). Les membranes phononiques présentent une conductivité thermique plus faible, ce qui confirme la prédominance d'un phénomène de scattering diffusif dans la réduction de la conductivité thermique à température ambiante.
La deuxième caractérisation menée est la spectroscopie Raman. Les mesures de κ effectuées avec cette méthode confirment celles réalisées avec la méthode électrothermique, dans la

même gamme de valeurs, à la fois pour les membranes pleines et avec PnCs. À notre connaissance, ceci est la première comparaison directe des deux méthodes d'évaluation de la conductivité thermique. Une comparaisons entre les résultats des deux méthodes est montrée dans la Figure 17 pour les membranes pleines et avec trous, montrant l'accord des deux techniques.

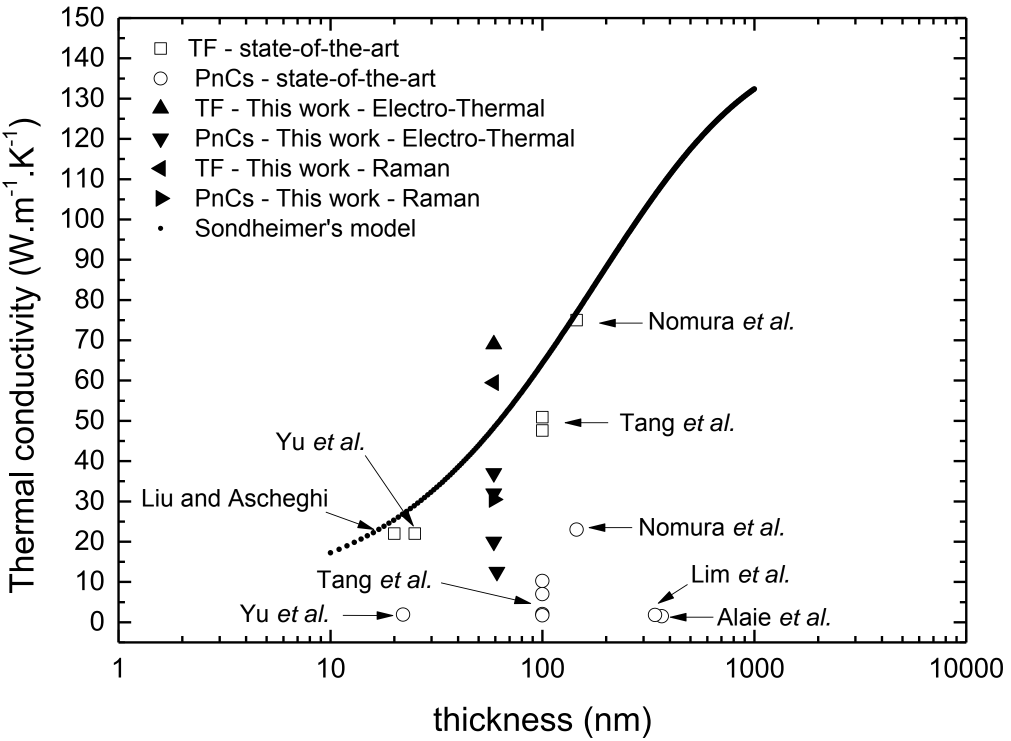

Figure 17 Conductivité thermique des membranes à couches minces (TF) et ceux avec cristaux phononiques (PnCs). Le résultats de ce travail par la méthode électrothermique et spectroscopie Raman et a l'état de l'art sont présentes.

La microscopie thermique (SThM) est la troisième technique adoptée pour etudier le transfert de chaleur à travers les membranes de silicium nanostructuré. Les expériences sont réalisées au CETHIL à Lyon et sont toujours en cours. Une analyse préliminaire des résultats met en évidence une variation de la conductivité dans le même ordre que celui obtenu avec la méthode électrothermique.

Scientific production

Journals:

1. M. Haras, **V. Lacatena**, F. Morini, J.-F. Robillard, S. Monfray, T. Skotnicki and E. Dubois, “Thermoelectric energy conversion: How good can silicon be?”, *Materials Letters*, vol. 157, pp. 193–196, Oct. 2015, doi: 10.1016/j.matlet.2015.05.012.
2. **V. Lacatena**, M. Haras, J.-F. Robillard, S. Monfray, T. Skotnicki and E. Dubois, “Toward quantitative modeling of silicon phononic thermocrystals”, *Applied Physics Letters*, vol. 106, no. 11, p. 114104, Mar. 2015, doi: 10.1063/1.4915619.
3. M. Haras, **V. Lacatena**, F. Morini, J.-F. Robillard, S. Monfray, T. Skotnicki and E. Dubois, “Fabrication of Integrated Micrometer Platform for Thermoelectric Measurements”, *Electron Devices Meeting (IEDM), 2014 IEEE International*, San Francisco, 2014, pp. 8.5.212–8.5.215, doi: 10.1109/IEDM.2014.7047012.
4. M. Haras, **V. Lacatena**, S. Monfray, J.-F. Robillard, T. Skotnicki and E. Dubois, “Unconventional Thin-Film Thermoelectric Converters: Structure, Simulation, and Comparative Study”, *Journal of Electronic Materials*, vol. 43, no. 6, pp. 2109–2114, Jun. 2014, doi: 10.1007/s11664-014-2982-z.
5. **V. Lacatena**, M. Haras, J.-F. Robillard, S. Monfray, T. Skotnicki and E. Dubois “Phononic engineering of silicon using ‘dots on the fly’ e-beam lithography and plasma etching,” *Microelectronic Engineering*, vol. 121, pp. 131–134, Jun. 2014, doi: 10.1016/j.mee.2014.04.034.
6. C. Calò, **V. Lacatena**, S. D. Dhuey, S. Cabrini, S. Babin, C. Peroz, A. Koshelev, I. Ivonin, A. Goltsov and V. Yankov, “Fabrication of digital planar holograms into high refractive index waveguide core for spectroscopy-on-chip applications”, *Journal of vacuum science and technologies B*, vol. 30, pp. 06FE01, Nov. 2012, doi: 10.1116/1.4750038.
7. C. Pina-Hernandez, **V. Lacatena**, G. Calafiore, S. Dhuey, K. Kravtsov, A. Goltsov, D. Olynick, V. Yankov, S. Cabrini, C. Peroz, “A route for fabricating printable photonic devices with sub-10 nm resolution”, *Nanotechnology*, vol. 24, no. 6, pp. 065301, Jan. 2013, doi: 10.1088/0957-4484/24/6/065301.

International conferences:

1. **V. Lacatena**, M. Haras, J.-F. Robillard, S. Monfray, T. Skotnicki, E. Dubois, M. Massoud, P.-O. Chapuis, J.-M. Bluet and A. Scibetta “Thermal conductivity reduction in fully suspended and periodically patterned membranes measured by electro-thermal method,” presented at the 2015 *MRS Fall Meeting*, Boston, Massachusetts, USA, November 29-December 4, 2015.
2. J.-F. Robillard, **V. Lacatena**, M. Haras, F. Morini, V. Giorgis, H. Ftouni and E. Dubois “Unconventional approaches for thermoelectric energy harvesting,” presented at the Hot nanostructures: thermal transport and radiation at the nanoscale workshop (*CECAM2015*), Mainz, Germany, September 30-October 2, 2015.
3. J.-F. Robillard, **V. Lacatena**, M. Haras, A. Scibetta, S. Monfray, T. Skotnicki and E. Dubois “Thermal conductivity of periodic nano-holes structures etched in silicon membranes,” presented at the 2015 *E-MRS Fall Meeting*, Warsaw, Poland, September 15-18, 2015.
4. M. Massoud, **V. Lacatena**, M. Haras, P.-O. Chapuis, J.-M. Bluet, J.-F. Robillard and E. Dubois “Effective thermal conductivity of nanophononic membrane strips investigate by scanning thermal microscopy and Raman thermometry,” presented at the 15th International Conference on Phonon Scattering in Condensed Matter (*Phonons2015*), Nottingham, United Kingdom, July 12-17, 2015.
5. **V. Lacatena**, M. Haras, J.-F. Robillard, S. Monfray, T. Skotnicki and E. Dubois “Reduced Thermal Conductivity of Periodically Nanostructured Silicon: a Quantitative Molecular Dynamics Study,”

presented at the 3rd International Conference on Phononic Crystals/Metamaterials, Phonon Transport and Phonon Coupling (*Phononics2015*), Paris, France, May 31–June 5, 2015.

6. M. Haras, **V. Lacatena**, F. Morini, J.-F. Robillard, S. Monfray, T. Skotnicki and E. Dubois "Fabrication of Integrated Micrometer Platform for Thermoelectric Measurements," presented at the 60th IEEE International Electron Devices Meeting (*IEDM2014*), San Francisco, California, USA, December 15-17, 2014.
7. M. Haras, **V. Lacatena**, F. Morini, J.-F. Robillard, S. Monfray, T. Skotnicki and E. Dubois [*Invited*] "How good silicon for thermoelectric conversion?," presented at the 17th International Symposium on the Physics of Semiconductors and Applications (*ISPSA2014*), Jeju, South Korea, December 7-11, 2014.
8. **V. Lacatena**, M. Haras, J.-F. Robillard, S. Monfray, T. Skotnicki and E. Dubois "Reduction of thermal conductivity in silicon thin film membranes by phononic engineering," presented at the *Eurotherm* seminar, Lyon, France, October 15-17, 2014.
9. J.-F. Robillard, **V. Lacatena**, M. Haras, S. Monfray, T. Skotnicki and E. Dubois "Silicon Thermoelectrics: A Non-conventional Approach Based on Thin-film Phononic Engineering," presented at the International Symposium on the CMOS Emerging Technologies Research (*CMOSETR2014*), Grenoble, France, July 6-8, 2014.
10. **V. Lacatena**, M. Haras, J.-F. Robillard, S. Monfray, T. Skotnicki and E. Dubois [*Invited*]"Efficient reduction of thermal conductivity in silicon using phononic-engineered membranes," presented at the 2014 Spring Conference of the European Materials Research Society (*E-MRS Spring Meeting*), Lille, France, May 27-29, 2014.
11. M. Haras, **V. Lacatena**, S. Monfray, J.-F. Robillard, T. Skotnicki and E. Dubois "Integrated measurement platform for thermal conductivity measurements in thin-film crystalline Silicon and Silicon-Germanium," presented at the 2014 Spring Conference of the European Materials Research Society (*E-MRS Spring Meeting*), Lille, France, May 27-29, 2014.
12. **V. Lacatena**, M. Haras, J.-F. Robillard, S. Monfray, T. Skotnicki and E. Dubois "Phononic Engineering of Silicon using 'Dots on the fly' e-beam lithography and plasma etching," presented at the 39th International Conference on Micro and Nano Engineering (*MNE2013*), London, UK, September 16–19, 2013.
13. M. Haras, **V. Lacatena**, S. Monfray, J.-F. Robillard, T. Skotnicki and E. Dubois "Non-conventional thin-film thermoelectric converters: structure, simulation and comparative study," presented at the 32nd International Conference on Thermoelectrics (*ICT2013*), Kobe, Japan, 30 June – 4 July 2013.

National conference:

1. **V. Lacatena**, M. Haras, J-F. Robillard, S. Monfray, T. Skotnicki and E. Dubois "Phononic crystals patterning by e-beam lithography" dots on the fly" methodology for integration into thermoelectric energy converters" presented at the 17èmes Journées Nationales du Réseau Doctoral en Micro-Nanoélectronique, (*JNRDM2014*), Lille, France, May 26-28, 2014.

Awards:

1. 3rd prize for the best thesis awarded by the Research Council of Lille Catholic University, Edition 2015.
2. Winner of the "Young Scientist Award", Conference e-MRS 2014, Symposium D: *Phonons and Fluctuations in low dimensional structures*, for Invited talk presented.

Activities:

1. Participation at the *"Ecole d'été de thermoélectricité"*, GDR Thermoélectricité, Annecy, June 1-6, 2014.
2. Team member for the organization of the "*17èmes Journées Nationales du Réseau Doctoral en Micro-Nanoélectronique (JNRDM2014)*", Lille, France, May 26-28, 2014.

Bibliography

[1] "World Energy Outlook 2014, Executive Summary - WEO_2014_ES_English_WEB.pdf." [Online]. Available: https://www.iea.org/publications/freepublications/publication/WEO_2014_ES_English_WEB.pdf.

[2] "World Energy Consumption: Map, Figures by Region | Enerdata." [Online]. Available: https://yearbook.enerdata.net/energy-primary-production.html#energy-consumption-data.html. [Accessed: 05-Aug-2015].

[3] "BP Statistical Review of World Energy 2015 - bp-statistical-review-of-world-energy-2015-full-report.pdf." [Online]. Available: http://www.bp.com/content/dam/bp/pdf/Energy-economics/statistical-review-2015/bp-statistical-review-of-world-energy-2015-full-report.pdf. [Accessed: 05-Aug-2015].

[4] R. Perez and M. Perez, "A fundamental look at the energy reserves for the planet," *SHC Sol. UPDATE*, p. 2, 2009.

[5] Peter Allan, Brent Ellison, Roger Hurst, Ajay Khater, Johan A Kritzinger, "Energy and chemical species utility management system," WO2007028158A2, Mar-2007.

[6] E. Cook, "The Flow of Energy in an Industrial Society," *Sci. Am.*, vol. 225, no. 3, pp. 134–144, Sep. 1971.

[7] R. J. M. Vullers, R. van Schaijk, I. Doms, C. Van Hoof, and R. Mertens, "Micropower energy harvesting," *Solid-State Electron.*, vol. 53, no. 7, pp. 684–693, juillet 2009.

[8] J. Shackelford and W. Alexander, Eds., *CRC Materials Science and Engineering Handbook, Third Edition*. CRC Press, 2000.

[9] "Electrical Conduction in Metals and Alloys (Electrical Properties of Materials) Part 1." [Online]. Available: http://what-when-how.com/electronic-properties-of-materials/electrical-conduction-in-metals-and-alloys-electrical-properties-of-materials-part-1/. [Accessed: 12-Aug-2015].

[10] "Metallically Electrically Conductive Si-Ti-C-N Ceramics - Available technology for licensing from the University of California, Davis." [Online]. Available: https://techtransfer.universityofcalifornia.edu/NCD/11340.html. [Accessed: 25-Jan-2016].

[11] "Engineering ToolBox." [Online]. Available: http://www.engineeringtoolbox.com/. [Accessed: 04-Apr-2016].

[12] "WebElements Periodic Table of the Elements." [Online]. Available: https://www.webelements.com/. [Accessed: 04-Apr-2016].

[13] "Thermoelectric Generator Diagram - Thermoelectric effect - Wikipedia, the free encyclopedia." [Online]. Available: https://en.wikipedia.org/wiki/Thermoelectric_effect#/media/File:Thermoelectric_Generator_Diagram.svg. [Accessed: 12-Aug-2015].

[14] H. B. Radousky and H. Liang, "Energy harvesting: an integrated view of materials, devices and applications," *Nanotechnology*, vol. 23, no. 50, p. 502001, Dec. 2012.

[15] D. M. Rowe, *CRC Handbook of Thermoelectrics*. CRC Press, 1995.

[16] A. J. Minnich, M. S. Dresselhaus, Z. F. Ren, and G. Chen, "Bulk nanostructured thermoelectric materials: current research and future prospects," *Energy Env. Sci*, vol. 2, no. 5, pp. 466–479, Feb. 2009.

[17] G. J. Snyder and E. S. Toberer, "Complex thermoelectric materials," *Nat. Mater.*, vol. 7, no. 2, pp. 105–114, 2008.

[18] L. D. Hicks and M. S. Dresselhaus, "Thermoelectric figure of merit of a one-dimensional conductor," *Phys. Rev. B*, vol. 47, no. 24, pp. 16631–16634, 1993.

[19] B. Poudel, Q. Hao, Y. Ma, Y. Lan, A. Minnich, B. Yu, X. Yan, D. Wang, A. Muto, D. Vashaee, X. Chen, J. Liu, M. S. Dresselhaus, G. Chen, and Z. Ren, "High-thermoelectric performance of nanostructured bismuth antimony telluride bulk alloys," *Science*, vol. 320, no. 5876, pp. 634–638, May 2008.

[20] G. Chen and A. Shakouri, "Heat Transfer in Nanostructures for Solid-State Energy Conversion," *J. Heat Transf.*, vol. 124, no. 2, pp. 242–252, Nov. 2001.

[21] M. S. Dresselhaus, G. Chen, M. Y. Tang, R. G. Yang, H. Lee, D. Z. Wang, Z. F. Ren, J.-P. Fleurial, and P. Gogna, "New Directions for Low-Dimensional Thermoelectric Materials," *Adv. Mater.*, vol. 19, no. 8, pp. 1043–1053, Apr. 2007.

[22] А. Ф. Иоффе, *Semiconductor thermoelements, and Thermoelectric cooling*. London: Infosearch, 1957.

[23] H. J. Goldsmid, *Electronic refrigeration*. Pion, 1986.

[24] G. D. Mahan and J. O. Sofo, "The best thermoelectric," *Proc. Natl. Acad. Sci.*, vol. 93, no. 15, pp. 7436–7439, Jul. 1996.

[25] T. M. Tritt, *Recent Trends in Thermoelectric Materials Research III*. Gulf Professional Publishing, 2001.

[26] K. M. F. Shahil, M. Z. Hossain, D. Teweldebrhan, and A. A. Balandin, "Crystal Symmetry Breaking in Few-Quintuple Bismuth Telluride Films: Applications in Nanometrology of Topological Insulators," *Appl. Phys. Lett.*, vol. 96, no. 15, p. 153103, 2010.

[27] T. M. Tritt, "Thermoelectric Phenomena, Materials, and Applications," *Annu. Rev. Mater. Res.*, vol. 41, pp. 433–448, 2011.

[28] P. F. P. Poudeu, J. D'Angelo, A. D. Downey, J. L. Short, T. P. Hogan, and M. G. Kanatzidis, "High Thermoelectric Figure of Merit and Nanostructuring in Bulk p-type $Na_{1-x}Pb_mSb_yTe_{m+2}$," *Angew. Chem.*, vol. 118, no. 23, pp. 3919–3923, 2006.

[29] M. Orihashi, Y. Noda, L.-D. Chen, T. Goto, and T. Hirai, "Effect of tin content on thermoelectric properties of p-type lead tin telluride," *J. Phys. Chem. Solids*, vol. 61, no. 6, pp. 919–923, 2000.

[30] J. Androulakis, C.-H. Lin, H.-J. Kong, C. Uher, C.-I. Wu, T. Hogan, B. A. Cook, T. Caillat, K. M. Paraskevopoulos, and M. G. Kanatzidis, "Spinodal Decomposition and Nucleation and Growth as a Means to Bulk Nanostructured Thermoelectrics: Enhanced Performance in $Pb_{1-x}Sn_xTe$−PbS," *J. Am. Chem. Soc.*, vol. 129, no. 31, pp. 9780–9788, 2007.

[31] J. P. Heremans, V. Jovovic, E. S. Toberer, A. Saramat, K. Kurosaki, A. Charoenphakdee, S. Yamanaka, and G. J. Snyder, "Enhancement of thermoelectric efficiency in PbTe by distortion of the electronic density of states," *Science*, vol. 321, no. 5888, pp. 554–557, Jul. 2008.

[32] J. R. Sootsman, H. Kong, C. Uher, J. J. D'Angelo, C.-I. Wu, T. P. Hogan, T. Caillat, and M. G. Kanatzidis, "Large Enhancements in the Thermoelectric Power Factor of Bulk PbTe at High Temperature by Synergistic Nanostructuring," *Angew. Chem. Int. Ed.*, vol. 47, no. 45, pp. 8618–8622, Oct. 2008.

[33] X. W. Wang, H. Lee, Y. C. Lan, G. H. Zhu, G. Joshi, D. Z. Wang, J. Yang, A. J. Muto, M. Y. Tang, J. Klatsky, S. Song, M. S. Dresselhaus, G. Chen, and Z. F. Ren, "Enhanced thermoelectric figure of merit in nanostructured n-type silicon germanium bulk alloy," *Appl. Phys. Lett.*, vol. 93, no. 19, p. 193121, 2008.

[34] G. Joshi, H. Lee, Y. Lan, X. Wang, G. Zhu, D. Wang, R. W. Gould, D. C. Cuff, M. Y. Tang, M. S. Dresselhaus, G. Chen, and Z. Ren, "Enhanced Thermoelectric Figure-of-Merit in Nanostructured p-type Silicon Germanium Bulk Alloys," *Nano Lett.*, vol. 8, no. 12, pp. 4670–4674, 2008.

[35] M. Haras, V. Lacatena, F. Morini, J.-F. Robillard, S. Monfray, T. Skotnicki, and E. Dubois, "Thermoelectric energy conversion: How good can silicon be?," *Mater. Lett.*, vol. 157, pp. 193–196, Oct. 2015.
[36] M. Asheghi, K. Kurabayashi, R. Kasnavi, and K. E. Goodson, "Thermal conduction in doped single-crystal silicon films," *J. Appl. Phys.*, vol. 91, no. 8, pp. 5079–5088, Apr. 2002.
[37] W. Liu and M. Asheghi, "Thermal Conduction in Ultra-Thin Pure and Doped Single Crystal Silicon Layers at High Temperatures," pp. 821–827, Jan. 2005.
[38] J. He, Y. Liu, and R. Funahashi, "Oxide thermoelectrics: The challenges, progress, and outlook," *J. Mater. Res.*, vol. 26, no. 15, pp. 1762–1772, 2011.
[39] L. Weber and E. Gmelin, "Transport properties of silicon," *Appl. Phys. Mater. Sci. Process.*, vol. 53, no. 2, pp. 136–140, 1991.
[40] M. Haras, V. Lacatena, S. Monfray, J.-F. Robillard, T. Skotnicki, and E. Dubois, "Unconventional Thin-Film Thermoelectric Converters: Structure, Simulation, and Comparative Study," *J. Electron. Mater.*, pp. 1–6, 2014.
[41] R. Venkatasubramanian, E. Siivola, T. Colpitts, and B. O'Quinn, "Thin-film thermoelectric devices with high room-temperature figures of merit," *Nature*, vol. 413, no. 6856, pp. 597–602, Oct. 2001.
[42] L. W. da Silva and M. Kaviany, "Miniaturized thermoelectric cooler," *ASME Int. Mech. Eng. Congr. Expo. New Orleans USA*, pp. 1–15, 2002.
[43] H. J. Goldsmid, A. R. Sheard, and D. A. Wright, "The performance of bismuth telluride thermojunctions," *Br. J. Appl. Phys.*, vol. 9, p. 365, 1958.
[44] S Scherrer and H Scherrer, "Bismuth Telluride, Antimony Telluride, and Their Solid Solutions," in *CRC Handbook of Thermoelectrics*, 0 vols., CRC Press, 1995.
[45] M. Mizoshiri, M. Mikami, K. Ozaki, M. Shikida, and S. Hata, "Lift-off patterning of thermoelectric thick films deposited by a thermally assisted sputtering method," *Appl. Phys. Express*, vol. 7, no. 5, p. 57101, May 2014.
[46] C.-H. Kuo, C.-S. Hwang, M.-S. Jeng, W.-S. Su, Y.-W. Chou, and J.-R. Ku, "Thermoelectric transport properties of bismuth telluride bulk materials fabricated by ball milling and spark plasma sintering," *J. Alloys Compd.*, vol. 496, no. 1–2, pp. 687–690, 2010.
[47] L. M. Gonçalves, "The deposition of Bi_2Te_3 and Sb_2Te_3 thermoelectric thin-films by thermal co-evaporation and applications in energy harvesting," *Thermoelectr. Its Energy Harvest. DM Rowe Ed Boca Raton FL CRC Press*, Jan. 2012.
[48] L. D. Hicks and M. S. Dresselhaus, "Effect of quantum-well structures on the thermoelectric figure of merit," *Phys. Rev. B*, vol. 47, no. 19, pp. 12727–12731, 1993.
[49] R. Kim, S. Datta, and M. S. Lundstrom, "Influence of dimensionality on thermoelectric device performance," *J. Appl. Phys.*, vol. 105, no. 3, p. 34506, Feb. 2009.
[50] R. Landauer, "Spatial Variation of Currents and Fields Due to Localized Scatterers in Metallic Conduction," *IBM J. Res. Dev.*, vol. 1, no. 3, pp. 223–231, Jul. 1957.
[51] K. F. Hsu, S. Loo, F. Guo, W. Chen, J. S. Dyck, C. Uher, T. Hogan, E. K. Polychroniadis, and M. G. Kanatzidis, "Cubic AgPbmSbTe2+m: Bulk Thermoelectric Materials with High Figure of Merit," *Science*, vol. 303, no. 5659, pp. 818–821, Feb. 2004.
[52] D. M. Rowe, *Thermoelectrics Handbook: Macro to Nano*. CRC Press, 2005.
[53] J. P. Heremans, "Low-Dimensional Thermoelectricity," *Acta Phys. Pol. A*, vol. 108, p. 609, Oct. 2006.
[54] J. R. Szczech, J. M. Higgins, and S. Jin, "Enhancement of the thermoelectric properties in nanoscale and nanostructured materials," *J. Mater. Chem.*, vol. 21, no. 12, pp. 4037–4055, Mar. 2011.

[55] W. F. Leonard, *Electronic Structure and Transport Properties of Crystals*, 1st edition. Huntington, N.Y: Krieger Pub Co, 1979.
[56] L. D. Hicks, T. C. Harman, X. Sun, and M. S. Dresselhaus, “Experimental study of the effect of quantum-well structures on the thermoelectric figure of merit,” *Phys. Rev. B*, vol. 53, no. 16, pp. R10493–R10496, 1996.
[57] T. Koga, S. B. Cronin, M. S. Dresselhaus, J. L. Liu, and K. L. Wang, “Experimental proof-of-principle investigation of enhanced Z3DT in (001) oriented Si/Ge superlattices,” *Appl. Phys. Lett.*, vol. 77, no. 10, pp. 1490–1492, Sep. 2000.
[58] R. Venkatasubramanian, “Lattice thermal conductivity reduction and phonon localizationlike behavior in superlattice structures,” *Phys. Rev. B*, vol. 61, no. 4, pp. 3091–3097, Jan. 2000.
[59] R. Venkatasubramanian, T. Colpitts, E. Watko, M. Lamvik, and N. El-Masry, “MOCVD of Bi2Te3, Sb2Te3 and their superlattice structures for thin-film thermoelectric applications,” *J. Cryst. Growth*, vol. 170, no. 1–4, pp. 817–821, Jan. 1997.
[60] S. B. Samavedam, U. Ghoshal, and T. Ngai, “Method for forming a thin-film thermoelectric device including a phonon-blocking thermal conductor,” 20050150535, 14-Jul-2005.
[61] Venkatasubramanian, R, Tritt, and T.M, “Phonon blocking electron transmitting superlattice structures as advanced thin film thermoelectric materials,” *Recent Trends Thermoelectr. Mater. Res. III*, vol. Chapter 4, 2001.
[62] R. Chen, A. I. Hochbaum, P. Murphy, J. Moore, P. Yang, and A. Majumdar, “Thermal Conductance of Thin Silicon Nanowires,” *Phys. Rev. Lett.*, vol. 101, no. 10, p. 105501, Sep. 2008.
[63] A. I. Hochbaum, R. Chen, R. D. Delgado, W. Liang, E. C. Garnett, M. Najarian, A. Majumdar, and P. Yang, “Enhanced thermoelectric performance of rough silicon nanowires,” *Nature*, vol. 451, no. 7175, pp. 163–167, Jan. 2008.
[64] D. Li, Y. Wu, R. Fan, P. Yang, and A. Majumdar, “Thermal conductivity of Si/SiGe superlattice nanowires,” *Appl. Phys. Lett.*, vol. 83, no. 15, pp. 3186–3188, Oct. 2003.
[65] D. Li, Y. Wu, P. Kim, L. Shi, P. Yang, and A. Majumdar, “Thermal conductivity of individual silicon nanowires,” *Appl. Phys. Lett.*, vol. 83, no. 14, pp. 2934–2936, Oct. 2003.
[66] J. Lim, K. Hippalgaonkar, S. C. Andrews, A. Majumdar, and P. Yang, “Quantifying Surface Roughness Effects on Phonon Transport in Silicon Nanowires,” *Nano Lett.*, vol. 12, no. 5, pp. 2475–2482, 2012.
[67] A. I. Boukai, Y. Bunimovich, J. Tahir-Kheli, J.-K. Yu, W. A. Goddard III, and J. R. Heath, “Silicon nanowires as efficient thermoelectric materials,” *Nature*, vol. 451, no. 7175, pp. 168–171, Jan. 2008.
[68] N. W. Ashcroft and N. D. Mermin, *Solid State Physics*. Cengage Learning, 1976.
[69] S. M. Sze, *Physics of Semiconductor Devices*. John Wiley & Sons, 1981.
[70] Y. S. Ju and K. E. Goodson, “Phonon scattering in silicon films with thickness of order 100 nm,” *Appl. Phys. Lett.*, vol. 74, no. 20, pp. 3005–3007, 1999.
[71] P. Martin, Z. Aksamija, E. Pop, and U. Ravaioli, “Impact of Phonon-Surface Roughness Scattering on Thermal Conductivity of Thin Si Nanowires,” *Phys. Rev. Lett.*, vol. 102, no. 12, p. 125503, Mar. 2009.
[72] K. F. Murphy, B. Piccione, M. B. Zanjani, J. R. Lukes, and D. S. Gianola, “Strain- and Defect-Mediated Thermal Conductivity in Silicon Nanowires,” *Nano Lett.*, vol. 14, no. 7, pp. 3785–3792, 2014.
[73] T.-K. Hsiao, B.-W. Huang, H.-K. Chang, S.-C. Liou, M.-W. Chu, S.-C. Lee, and C.-W. Chang, “Micron-scale ballistic thermal conduction and suppressed thermal

conductivity in heterogeneously interfaced nanowires," *Phys. Rev. B*, vol. 91, no. 3, p. 35406, 2015.
[74] T.-K. Hsiao, H.-K. Chang, S.-C. Liou, M.-W. Chu, S.-C. Lee, and C.-W. Chang, "Observation of room-temperature ballistic thermal conduction persisting over 8.3 µm in SiGe nanowires," *Nat. Nanotechnol.*, vol. 8, no. 7, pp. 534–538, 2013.
[75] B.-W. Huang, T.-K. Hsiao, K.-H. Lin, D.-W. Chiou, and C.-W. Chang, "Length-dependent thermal transport and ballistic thermal conduction," *AIP Adv.*, vol. 5, no. 5, p. 53202, May 2015.
[76] B. Sothmann, R. Sanchez, and A. N. Jordan, "Thermoelectric energy harvesting with quantum dots," *Nanotechnology*, vol. 26, no. 3, p. 32001, Jan. 2015.
[77] G. Springholz, M. Pinczolits, P. Mayer, V. V. Holy, G. Bauer, H. H. Kang, and L. Salamanca-Riba, "Tuning of vertical and lateral correlations in self-organized $PbSe/Pb_{1-x}Eu_xTe$ quantum dot superlattices," *Phys. Rev. Lett.*, vol. 84, no. 20, pp. 4669–4672, May 2000.
[78] G. Springholz, V. Holy, M. Pinczolits, and B. Bauer, "Self-organized growth of three-dimensional quantum-Dot crystals with fcc-like stacking and a tunable lattice constant," *Science*, vol. 282, no. 5389, pp. 734–737, Oct. 1998.
[79] T. C. Harman, P. J. Taylor, M. P. Walsh, and B. E. LaForge, "Quantum Dot Superlattice Thermoelectric Materials and Devices," *Science*, vol. 297, no. 5590, pp. 2229–2232, 2002.
[80] T. Harman, P. Taylor, D. Spears, and M. Walsh, "Thermoelectric quantum-dot superlattices with high ZT," *J. Electron. Mater.*, vol. 29, no. 1, pp. L1–L2, Jan. 2000.
[81] D. Bilc, S. D. Mahanti, E. Quarez, K.-F. Hsu, R. Pcionek, and M. G. Kanatzidis, "Resonant States in the Electronic Structure of the High Performance Thermoelectrics $AgPb_mSbTe_{2+m}$: The Role of Ag-Sb Microstructures," *Phys. Rev. Lett.*, vol. 93, no. 14, 2004.
[82] D. I. Bilc, S. D. Mahanti, and M. G. Kanatzidis, "Electronic transport properties of PbTe and $AgPb_m SbTe_{2+m}$ systems," *Phys. Rev. B*, vol. 74, no. 12, p. 125202, Sep. 2006.
[83] X. Shi, L. Chen, J. Yang, and G. P. Meisner, "Enhanced thermoelectric figure of merit of CoSb3 via large-defect scattering," *Appl. Phys. Lett.*, vol. 84, no. 13, pp. 2301–2303, Mar. 2004.
[84] J. P. Heremans, C. M. Thrush, and D. T. Morelli, "Thermopower enhancement in lead telluride nanostructures," *Phys. Rev. B*, vol. 70, no. 11, p. 115334, Sep. 2004.
[85] Y. Ma, Q. Hao, B. Poudel, Y. Lan, B. Yu, D. Wang, G. Chen, and Z. Ren, "Enhanced Thermoelectric Figure-of-Merit in p-Type Nanostructured Bismuth Antimony Tellurium Alloys Made from Elemental Chunks," *Nano Lett.*, vol. 8, no. 8, pp. 2580–2584, août 2008.
[86] D. G. Cahill, W. K. Ford, K. E. Goodson, G. D. Mahan, A. Majumdar, H. J. Maris, R. Merlin, and S. R. Phillpot, "Nanoscale thermal transport," *J. Appl. Phys.*, vol. 93, no. 2, pp. 793–818, Jan. 2003.
[87] Christianne V.D.R. Anderson and Kumar K. Tamma, "An overview of advances in heat conduction models and approaches for prediction of thermal conductivity in thin dielectric filmsnull," *Int. J. Numer. Methods Heat Fluid Flow*, vol. 14, no. 1, pp. 12–65, Jan. 2004.
[88] M. I. Flik, B. I. Choi, and K. E. Goodson, "Heat Transfer Regimes in Microstructures," *J. Heat Transf.*, vol. 114, no. 3, pp. 666–674, 1992.
[89] A. M. Marconnet, M. Asheghi, and K. E. Goodson, "From the Casimir Limit to Phononic Crystals: 20 Years of Phonon Transport Studies Using Silicon-on-Insulator Technology," *J. Heat Transf.*, vol. 135, no. 6, pp. 061601–061601, May 2013.

[90] D. Planck Nernst, Smoluchowski, Sommerfeld, *Vorträge über die Kinetische Theorie der Materie und der Elektrizität*. Teubner, 1914.
[91] C. Cattaneo, "A form of heat conduction equation which eliminates the paradox of instantaneous propagation," *Compte Rendus*, vol. 247, no. 4, pp. 431–433, 1958.
[92] M. P. Vernotte, "Les paradoxes de la theorie continue de l'equation de la chaleur," *Comptes Rendus Acad Sci*, vol. 246, pp. 3154–3155, 1958.
[93] G. Chen, "Ballistic-Diffusive Heat-Conduction Equations," *Phys. Rev. Lett.*, vol. 86, no. 11, pp. 2297–2300, Mar. 2001.
[94] G. P. Srivastava, *The physics of phonons*. A. Hilger, 1990.
[95] J. M. Ziman, *Electrons and Phonons: The Theory of Transport Phenomena in Solids*. OUP Oxford, 1960.
[96] A. Ward, D. A. Broido, D. A. Stewart, and G. Deinzer, "\textit{Ab initio} theory of the lattice thermal conductivity in diamond," *Phys. Rev. B*, vol. 80, no. 12, p. 125203, Sep. 2009.
[97] J. Callaway, "Model for Lattice Thermal Conductivity at Low Temperatures," *Phys. Rev.*, vol. 113, no. 4, pp. 1046–1051, février 1959.
[98] M. G. Holland, "Analysis of Lattice Thermal Conductivity," *Phys. Rev.*, vol. 132, no. 6, pp. 2461–2471, décembre 1963.
[99] C. J. Glassbrenner and G. A. Slack, "Thermal Conductivity of Silicon and Germanium from 3degK to the Melting Point," *Phys. Rev.*, vol. 134, no. 4A, p. A1058, 1964.
[100] F. Yang and C. Dames, "Mean free path spectra as a tool to understand thermal conductivity in bulk and nanostructures," *Phys. Rev. B*, vol. 87, no. 3, p. 35437, Jan. 2013.
[101] J. E. Turney, E. S. Landry, A. J. H. McGaughey, and C. H. Amon, "Predicting phonon properties and thermal conductivity from anharmonic lattice dynamics calculations and molecular dynamics simulations," *Phys. Rev. B*, vol. 79, no. 6, p. 64301, 2009.
[102] A. J. H. McGaughey and M. Kaviany, "Thermal conductivity decomposition and analysis using molecular dynamics simulations: Part II. Complex silica structures," *Int. J. Heat Mass Transf.*, vol. 47, no. 8–9, pp. 1799–1816, 2004.
[103] D. P. Sellan, E. S. Landry, J. E. Turney, A. J. H. McGaughey, and C. H. Amon, "Size effects in molecular dynamics thermal conductivity predictions," *Phys. Rev. B*, vol. 81, no. 21, Jun. 2010.
[104] S. G. Volz and G. Chen, "Molecular dynamics simulation of thermal conductivity of silicon nanowires," *Appl. Phys. Lett.*, vol. 75, no. 14, pp. 2056–2058, Oct. 1999.
[105] V. Lacatena, M. Haras, J.-F. Robillard, S. Monfray, T. Skotnicki, and E. Dubois, "Toward quantitative modeling of silicon phononic thermocrystals," *Appl. Phys. Lett.*, vol. 106, no. 11, p. 114104, Mar. 2015.
[106] W. Liu and M. Asheghi, "Phonon–boundary scattering in ultrathin single-crystal silicon layers," *Appl. Phys. Lett.*, vol. 84, no. 19, pp. 3819–3821, May 2004.
[107] M. Asheghi, Y. K. Leung, S. S. Wong, and K. E. Goodson, "Phonon-boundary scattering in thin silicon layers," *Appl. Phys. Lett.*, vol. 71, no. 13, p. 1798, 1997.
[108] J.-K. Yu, S. Mitrovic, D. Tham, J. Varghese, and J. R. Heath, "Reduction of thermal conductivity in phononic nanomesh structures," *Nat Nano*, vol. 5, no. 10, pp. 718–721, Oct. 2010.
[109] C. Y. Ho, R. W. Powell, and P. E. Liley, "Thermal conductivity of the elements : a comprehensive review," *J. Phys. Chem. Ref. Data*, vol. 3, pp. 756–796, 1974.
[110] K. Fuchs, "The conductivity of thin metallic films according to the electron theory of metals," *Math. Proc. Camb. Philos. Soc.*, vol. 34, no. 1, pp. 100–108, Jan. 1938.
[111] E. H. Sondheimer, "The mean free path of electrons in metals," *Adv. Phys.*, vol. 1, no. 1, pp. 1–42, Jan. 1952.

[112] M. Haras, V. Lacatena, F. Morini, J.-F. Robillard, S. Monfray, T. Skotnicki, and E. Dubois, “Fabrication of integrated micrometer platform for thermoelectric measurements,” in *Electron Devices Meeting (IEDM), 2014 IEEE International*, 2014, p. 8.5.1-8.5.4.

[113] Y. S. Ju, “Phonon heat transport in silicon nanostructures,” *Appl. Phys. Lett.*, vol. 87, p. 153106, Oct. 2005.

[114] E. Chávez-Ángel, J. S. Reparaz, J. Gomis-Bresco, M. R. Wagner, J. Cuffe, B. Graczykowski, A. Shchepetov, H. Jiang, M. Prunnila, J. Ahopelto, F. Alzina, and C. M. S. Torres, “Reduction of the thermal conductivity in free-standing silicon nano-membranes investigated by non-invasive Raman thermometry,” *APL Mater.*, vol. 2, no. 1, p. 12113, Jan. 2014.

[115] S. Wei and M. Y. Chou, “Phonon dispersions of silicon and germanium from first-principles calculations,” *Phys. Rev. B*, vol. 50, no. 4, pp. 2221–2226, juillet 1994.

[116] G. Dolling, *Inelastic Scattering of Neutrons in Solids and Liquids*, IAEA., vol. 2. Vienna: S. Ekland, 1963.

[117] G. Nilsson and G. Nelin, “Study of the Homology between Silicon and Germanium by Thermal-Neutron Spectrometry,” *Phys. Rev. B*, vol. 6, no. 10, pp. 3777–3786, Nov. 1972.

[118] M. Haras, “Non-conventional thermoelectrics based on thin-film silicon technologies,” Ph.D. Thesis, Lille 1 University, Lille, France, 2016.

[119] M. Maldovan, “Sound and heat revolutions in phononics,” *Nature*, vol. 503, no. 7475, pp. 209–217, Nov. 2013.

[120] T. Gorishnyy, C. K. Ullal, M. Maldovan, G. Fytas, and E. L. Thomas, “Hypersonic Phononic Crystals,” *Phys. Rev. Lett.*, vol. 94, no. 11, p. 115501, Mar. 2005.

[121] D. Song and G. Chen, “Thermal conductivity of periodic microporous silicon films,” *Appl. Phys. Lett.*, vol. 84, no. 5, pp. 687–689, Feb. 2004.

[122] P. E. Hopkins, C. M. Reinke, M. F. Su, R. H. Olsson, E. A. Shaner, Z. C. Leseman, J. R. Serrano, L. M. Phinney, and I. El-Kady, “Reduction in the Thermal Conductivity of Single Crystalline Silicon by Phononic Crystal Patterning,” *Nano Lett*, vol. 11, no. 1, pp. 107–112, 2010.

[123] J. Tang, H.-T. Wang, D. H. Lee, M. Fardy, Z. Huo, T. P. Russell, and P. Yang, “Holey Silicon as an Efficient Thermoelectric Material,” *Nano Lett*, vol. 10, no. 10, pp. 4279–4283, 2010.

[124] B. Kim, J. Nguyen, P. J. Clews, C. M. Reinke, D. Goettler, Z. C. Leseman, I. El-Kady, and R. H. Olsson, “Thermal conductivity manipulation in single crystal silicon via lithographycally defined phononic crystals,” in *Micro Electro Mechanical Systems (MEMS), 2012 IEEE 25th International Conference on*, 2012, pp. 176–179.

[125] A. M. Marconnet, T. Kodama, M. Asheghi, and K. E. Goodson, “Phonon Conduction in Periodically Porous Silicon Nanobridges,” *Nanoscale Microscale Thermophys. Eng.*, vol. 16, no. 4, pp. 199–219, 2012.

[126] J. Maire, R. Anufriev, H. Han, S. Volz, and M. Nomura, “Thermal conductivity tuning by thermocrystals,” *ArXiv150804574 Cond-Mat*, Aug. 2015.

[127] M. Nomura, J. Nakagawa, Y. Kage, J. Maire, D. Moser, and O. Paul, “Thermal phonon transport in silicon nanowires and two-dimensional phononic crystal nanostructures,” *Appl. Phys. Lett.*, vol. 106, no. 14, p. 143102, Apr. 2015.

[128] J. Maire and M. Nomura, “Reduced thermal conductivities of Si one-dimensional periodic structure and nanowire,” *Jpn. J. Appl. Phys.*, vol. 53, no. 6S, p. 06JE09, Jun. 2014.

[129] S. Alaie, D. F. Goettler, M. Su, Z. C. Leseman, C. M. Reinke, and I. El-Kady, “Thermal transport in phononic crystals and the observation of coherent phonon scattering at room temperature,” *Nat. Commun.*, vol. 6, p. 7228, 2015.

[130] J. Lim, H.-T. Wang, J. Tang, S. C. Andrews, H. So, J. Lee, D. H. Lee, T. P. Russell, and P. Yang, “Simultaneous Thermoelectric Property Measurement and Incoherent Phonon Transport in Holey Silicon,” *ACS Nano*, 2015.

[131] J.-K. Yu, S. Mitrovic, D. Tham, J. Varghese, and J. R. Heath, “Reduction of thermal conductivity in phononic nanomesh structures,” *Nat. Nanotechnol.*, vol. 5, no. 10, pp. 718–721, Jul. 2010.

[132] E. Dechaumphai and R. Chen, “Thermal transport in phononic crystals: The role of zone folding effect,” *J. Appl. Phys.*, vol. 111, no. 7, pp. 73508-73508–8, Apr. 2012.

[133] B. Abeles, “Lattice thermal conductivity of disordered semiconductor alloys at high temperatures,” *Phys. Rev.*, vol. 131, no. 5, p. 1906, 1963.

[134] M. Maldovan, “Micro to nano scale thermal energy conduction in semiconductor thin films,” *J. Appl. Phys.*, vol. 110, no. 3, p. 34308, Aug. 2011.

[135] J.-K. Yu, S. Mitrovic, D. Tham, J. Varghese, and J. R. Heath, “Reduction of thermal conductivity in phononic nanomesh structures,” *Nat. Nanotechnol.*, vol. 5, no. 10, pp. 718–721, Jul. 2010.

[136] J. Maire and M. Nomura, “Reduced thermal conductivities of Si one-dimensional periodic structure and nanowire,” *Jpn. J. Appl. Phys.*, vol. 53, no. 6S, p. 06JE09, Jun. 2014.

[137] A. J. H. McGaughey and M. Kaviany, “Phonon Transport in Molecular Dynamics Simulations: Formulation and Thermal Conductivity Prediction,” *Adv. Heat Transf.*, vol. 39, p. 169, 2006.

[138] R. Kubo, “Statistical-Mechanical Theory of Irreversible Processes. I. General Theory and Simple Applications to Magnetic and Conduction Problems,” *J. Phys. Soc. Jpn.*, vol. 12, no. 6, pp. 570–586, Jun. 1957.

[139] D. A. McQuarrie, *Statistical Mechanics*. University Science Books, 2000.

[140] P. K. Schelling, S. R. Phillpot, and P. Keblinski, “Comparison of atomic-level simulation methods for computing thermal conductivity,” *Phys. Rev. B*, vol. 65, no. 14, Apr. 2002.

[141] E. Lampin, P. L. Palla, P.-A. Francioso, and F. Cleri, “Thermal conductivity from approach-to-equilibrium molecular dynamics,” *J. Appl. Phys.*, vol. 114, no. 3, p. 33525, 2013.

[142] “LAMMPS Molecular Dynamics Simulator.” [Online]. Available: http://lammps.sandia.gov/. [Accessed: 17-Nov-2015].

[143] S. Plimpton, “Fast Parallel Algorithms for Short-Range Molecular Dynamics,” *J. Comput. Phys.*, vol. 117, no. 1, pp. 1–19, Mar. 1995.

[144] J. Cuffe, E. Chávez, A. Shchepetov, P.-O. Chapuis, E. H. El Boudouti, F. Alzina, T. Kehoe, J. Gomis-Bresco, D. Dudek, Y. Pennec, B. Djafari-Rouhani, M. Prunnila, J. Ahopelto, and C. M. Sotomayor Torres, “Phonons in Slow Motion: Dispersion Relations in Ultrathin Si Membranes,” *Nano Lett.*, vol. 12, no. 7, pp. 3569–3573, Jul. 2012.

[145] P. B. D. Windisch, “Silicon lattice parameters as an absolute scale of length for high precision measurements of fundamental constants,” *Phys. Status Solidi A*, vol. 118, no. 2, pp. 379–388, 1990.

[146] P. C. Howell, “Comparison of molecular dynamics methods and interatomic potentials for calculating the thermal conductivity of silicon,” *J. Chem. Phys.*, vol. 137, no. 22, p. 224111, Dec. 2012.

[147] A. S. Henry and G. Chen, “Spectral Phonon Transport Properties of Silicon Based on Molecular Dynamics Simulations and Lattice Dynamics,” *J. Comput. Theor. Nanosci.*, vol. 5, no. 2, pp. 141–152, Feb. 2008.

[148] J. V. Goicochea, M. Madrid, and C. Amon, “Hierarchical modeling of heat transfer in silicon-based electronic devices,” in *11th Intersociety Conference on Thermal and*

Thermomechanical Phenomena in Electronic Systems, 2008. ITHERM 2008, 2008, pp. 1006–1017.
[149] L. Sun and J. Y. Murthy, “Domain size effects in molecular dynamics simulation of phonon transport in silicon,” *Appl. Phys. Lett.*, vol. 89, no. 17, pp. 171919-171919–3, Oct. 2006.
[150] W. Fulkerson, J. P. Moore, R. K. Williams, R. S. Graves, and D. L. McElroy, “Thermal conductivity, electrical resistivity, and seebeck coefficient of Silicon from 100 to 1300 K,” *Phys. Rev.*, vol. 167, no. 3, p. 765, 1968.
[151] V. Palankovski, R. Schultheis, and S. Selberherr, “Simulation of power heterojunction bipolar transistors on gallium arsenide,” *IEEE Trans. Electron Devices*, vol. 48, no. 6, pp. 1264–1269, 2001.
[152] C. Herring, “Theory of the Thermoelectric Power of Semiconductors,” *Phys. Rev.*, vol. 96, no. 5, pp. 1163–1187, 1954.
[153] V. Lacatena, M. Haras, J.-F. Robillard, S. Monfray, T. Skotnicki, and E. Dubois, “Phononic engineering of silicon using ”dots on the fly” e-beam lithography and plasma etching,” *Microelectron. Eng.*, vol. 121, pp. 131–134, 2014.
[154] J. Trasobares, F. Vaurette, M. François, H. Romijn, J.-L. Codron, D. Vuillaume, D. Théron, and N. Clément, “High speed e-beam lithography for gold nanoarray fabrication and use in nanotechnology,” *Beilstein J. Nanotechnol.*, vol. 5, pp. 1918–1925, Oct. 2014.
[155] K. Koshelev, M. Ali Mohammad, T. Fito, K. L. Westra, S. K. Dew, and M. Stepanova, “Comparison between ZEP and PMMA resists for nanoscale electron beam lithography experimentally and by numerical modeling,” *J. Vac. Sci. Technol. B Microelectron. Nanometer Struct.*, vol. 29, no. 6, p. 06F306, 2011.
[156] “ZEON CHEMICALS - Electronic Materials - Homepage - Electronic Home.” [Online]. Available: http://www.zeonchemicals.com/ElectronicMaterials/.
[157] “ZEON CHEMICALS - Electronic Materials - Product Grade ZED-N50 - ZED-N50.” [Online]. Available: http://www.zeonchemicals.com/ElectronicMaterials/product_grade_ZED-N50.aspx#.
[158] “http://www.microchem.com/pdf/removerpg.pdf.” [Online]. Available: http://www.microchem.com/pdf/removerpg.pdf.
[159] “Home: Vistec - We understand E-Beam.” [Online]. Available: http://www.vistec-semi.com/.
[160] N. Gadegaard, S. Thoms, D. S. Macintyre, K. Mcghee, J. Gallagher, B. Casey, and C. D. W. Wilkinson, “Arrays of nano-dots for cellular engineering,” *Microelectron. Eng.*, vol. 67–68, pp. 162–168, 2003.
[161] “Oxford Instruments.” [Online]. Available: http://www.oxford-instruments.com/.
[162] “Soitec - Matériaux semi-conducteurs d’extrêmes performances pour l’électronique et l’énergie.” [Online]. Available: http://www.soitec.com/fr/.
[163] “MicroChem PMMA WP - PMMA_Data_Sheet.pdf.” [Online]. Available: http://microchem.com/pdf/PMMA_Data_Sheet.pdf. [Accessed: 29-Jul-2015].
[164] “http://www.tannereda.com/l-edit-pro.” [Online]. Available: http://www.tannereda.com/l-edit-pro. [Accessed: 24-Jul-2015].
[165] “Home Page - Oxford Instruments.” [Online]. Available: http://www.oxford-instruments.com/. [Accessed: 22-Jul-2015].
[166] S. M. Sze, *VLSI technology*. McGraw-Hill, 1983.
[167] “www.jobinyvon.com.” [Online]. Available: http://www.jobinyvon.com/usadivisions/TFilms/index.htm. [Accessed: 27-Jul-2015].
[168] “Bulk Micromachining Of Silicon - Proceedings of the IEEE - BulkMicromachining.Kovacs.00704259.pdf.” [Online]. Available: http://www-

inst.eecs.berkeley.edu/~ee245/fa10/lectures/BulkMicromachining.Kovacs.00704259.pdf. [Accessed: 30-Jul-2015].
[169] N. H. Tea, V. Milanovic, C. A. Zincke, J. S. Suehle, M. Gaitan, M. E. Zaghloul, and J. Geist, "Hybrid postprocessing etching for CMOS-compatible MEMS," *J. Microelectromechanical Syst.*, vol. 6, no. 4, pp. 363–372, 1997.
[170] "SPTS etch deposition and thermal equipment for semiconductor industry," *SPTS*. [Online]. Available: http://www.spts.com/products/xef2-release-etch. [Accessed: 03-Aug-2015].
[171] B. D. Bois, G. Vereecke, A. Witvrouw, P. D. Moor, C. V. Hoof, A. D. Caussemaeker, and A. Verbist, "HF Etching of Si-Oxides and Si-Nitrides for Surface Micromachining," in *Sensor Technology 2001*, M. Elwenspoek, Ed. Springer Netherlands, 2001, pp. 131–136.
[172] D. G. Cahill, H. E. Fischer, T. Klitsner, E. T. Swartz, and R. O. Pohl, "Thermal conductivity of thin films: Measurements and understanding," *J. Vac. Sci. Technol. A*, vol. 7, no. 3, pp. 1259–1266, May 1989.
[173] L. Shi, D. Li, C. Yu, W. Jang, D. Kim, Z. Yao, P. Kim, and A. Majumdar, "Measuring Thermal and Thermoelectric Properties of One-Dimensional Nanostructures Using a Microfabricated Device," *J. Heat Transf.*, vol. 125, no. 5, p. 881, 2003.
[174] D. G. Cahill, "Thermal conductivity measurement from 30 to 750 K: the 3ω method," *Rev. Sci. Instrum.*, vol. 61, no. 2, p. 802, 1990.
[175] Jan König, Fraunhofer Institute for Physical Measurement Techniques IPM, "Time Domain Thermoreflectance - Measuring the thermal conductivity of thin films." [Online]. Available: http://www.ipm.fraunhofer.de/content/dam/ipm/en/PDFs/Product%20sheet/FM/TEK/TDTR_thermal_conductivity.pdf. [Accessed: 10-Mar-2016].
[176] W. Liu and M. Asheghi, "Thermal conductivity measurements of ultra-thin single crystal silicon layers," *J. Heat Transf.*, vol. 128, no. 1, pp. 75–83, 2006.
[177] W. Liu and M. Asheghi, "Thermal conduction in ultrathin pure and doped single-crystal silicon layers at high temperatures," *J. Appl. Phys.*, vol. 98, no. 12, p. 123523, Dec. 2005.
[178] M. Asheghi, Y. K. Leung, S. S. Wong, and K. E. Goodson, "Phonon-boundary scattering in thin silicon layers," *Appl. Phys. Lett.*, vol. 71, no. 13, pp. 1798–1800, Sep. 1997.
[179] M. Asheghi, M. N. Touzelbaev, K. E. Goodson, Y. K. Leung, and S. S. Wong, "Temperature-Dependent Thermal Conductivity of Single-Crystal Silicon Layers in SOI Substrates," *J. Heat Transf.*, vol. 120, no. 1, pp. 30–36, 1998.
[180] M. S. Aubain and P. R. Bandaru, "In-plane thermal conductivity determination through thermoreflectance analysis and measurements," *J. Appl. Phys.*, vol. 110, no. 8, p. 84313, Oct. 2011.
[181] M. S. Aubain and P. R. Bandaru, "Determination of diminished thermal conductivity in silicon thin films using scanning thermoreflectance thermometry," *Appl. Phys. Lett.*, vol. 97, no. 25, p. 253102, Dec. 2010.
[182] P. Ferrando-Villalba, A. F. Lopeandia, L. Abad, J. Llobet, M. Molina-Ruiz, G. Garcia, M. Gerbolès, F. X. Alvarez, A. R. Goñi, F. J. Muñoz-Pascual, and J. Rodríguez-Viejo, "In-plane thermal conductivity of sub-20 nm thick suspended mono-crystalline Si layers," *Nanotechnology*, vol. 25, no. 18, p. 185402, 2014.
[183] C. de Tomas, A. Cantarero, A. F. Lopeandia, and F. X. Alvarez, "Enhancing of optic phonon contribution in hydrodynamic phonon transport," *J. Appl. Phys.*, vol. 118, no. 13, p. 134305, Oct. 2015.

[184] *Agilent Technologies 4155C/4156C - Semiconductor Parameter Analyzer - User's Guide: Measurement and Analysis*, 4th ed. Agilent Technologies, 2003.
[185] J. Tang, H.-T. Wang, D. H. Lee, M. Fardy, Z. Huo, T. P. Russell, and P. Yang, "Holey Silicon as an Efficient Thermoelectric Material," *Nano Lett.*, vol. 10, no. 10, pp. 4279–4283, Oct. 2010.
[186] J. S. Reparaz, E. Chavez-Angel, M. R. Wagner, B. Graczykowski, J. Gomis-Bresco, F. Alzina, and C. M. S. Torres, "A novel contactless technique for thermal field mapping and thermal conductivity determination: Two-Laser Raman Thermometry," *Rev. Sci. Instrum.*, vol. 85, no. 3, p. 34901, Mar. 2014.
[187] A. Baladin, "Thermoelectric Applications of Low-Dimensional Structures with Acoustically Mismatched Boundaries," *Phys. Low-Dimens. Struct.*, no. 5–6, p. 2000, 2000.
[188] M. Balkanski, R. F. Wallis, and E. Haro, "Anharmonic effects in light scattering due to optical phonons in silicon," *Phys. Rev. B*, vol. 28, no. 4, pp. 1928–1934, 1983.
[189] P. G. Klemens, "Anharmonic Decay of Optical Phonons," *Phys. Rev.*, vol. 148, no. 2, pp. 845–848, août 1966.
[190] A.S. Nikolenko, "Laser heating effect on Raman spectra of Si nanocrystals embedded into SiOx matrix," *Semicond. Phys. Quantum Electron. Optoelectron.*, vol. 16, pp. 86–90, 2013.
[191] G. S. Doerk, C. Carraro, and R. Maboudian, "Temperature dependence of Raman spectra for individual silicon nanowires," *Phys. Rev. B*, vol. 80, no. 7, p. 73306, 2009.
[192] "Raman Spectrometers - HORIBA." [Online]. Available: http://www.horiba.com/scientific/products/raman-spectroscopy/raman-spectrometers/. [Accessed: 14-Dec-2015].
[193] "Rigorous coupled-wave analysis," *Wikipedia, the free encyclopedia*. 03-Aug-2015.
[194] R. J. Pylkki, P. J. Moyer, and P. E. West, "Scanning Near-Field Optical Microscopy and Scanning Thermal Microscopy," *Jpn. J. Appl. Phys.*, vol. 33, no. Part 1, No. 6B, pp. 3785–3790, Jun. 1994.
[195] S. Gomes, "Contribution Théorique et Expérimentale à la Microscopie Thermique à Sonde Locale: Calibration d'Une Pointe Thermorésistive, Analyse des Divers Couplages Thermiques," Reims University, Reims, 1999.
[196] S. Gomès, A. Assy, and P.-O. Chapuis, "Scanning thermal microscopy: A review," *Phys. Status Solidi A*, vol. 212, no. 3, pp. 477–494, Mar. 2015.
[197] M.-H. Lu, L. Feng, and Y.-F. Chen, "Phononic crystals and acoustic metamaterials," *Mater. Today*, vol. 12, no. 12, pp. 34–42, Dec. 2009.
[198] P. R. Bandaru, K. P. Vemuri, F. M. Canbazoglu, and R. S. Kapadia, "Layered thermal metamaterials for the directing and harvesting of conductive heat," *AIP Adv.*, vol. 5, no. 5, p. 53403, May 2015.
[199] R. H. O. III and I. El-Kady, "Microfabricated phononic crystal devices and applications," *Meas. Sci. Technol.*, vol. 20, no. 1, p. 12002, 2009.
[200] J.-F. Robillard, O. B. Matar, J. O. Vasseur, P. A. Deymier, M. Stippinger, A.-C. Hladky-Hennion, Y. Pennec, and B. Djafari-Rouhani, "Tunable magnetoelastic phononic crystals," *Appl. Phys. Lett.*, vol. 95, no. 12, p. 124104, Sep. 2009.
[201] J. O. Vasseur, O. B. Matar, J. F. Robillard, A.-C. Hladky-Hennion, and P. A. Deymier, "Band structures tunability of bulk 2D phononic crystals made of magneto-elastic materials," *AIP Adv.*, vol. 1, no. 4, pp. 41904-41904–12, Dec. 2011.
[202] J. Tang, H. T. Wang, D. H. Lee, M. Fardy, Z. Huo, T. P. Russell, and P. Yang, "Holey silicon as an efficient thermoelectric material," *Nano Lett.*, 2010.
[203] P. Allan, B. Ellison, R. Hurst, A. Khater, and J. A. Kritzinger, "Energy and chemical species utility management system," 08-Mar-2007.

[204] R. J. M. Vullers, R. van Schaijk, I. Doms, C. Van Hoof, and R. Mertens, “Micropower energy harvesting,” *Solid-State Electron.*, vol. 53, no. 7, pp. 684–693, juillet 2009.
[205] A. J. H. McGaughey and M. Kaviany, “Phonon Transport in Molecular Dynamics Simulations: Formulation and Thermal Conductivity Prediction,” in *Advances in Heat Transfer*, vol. 39, J. P. H. George A. Greene Avram Bar-Cohen and Young I. Cho, Ed. Elsevier, 2006, pp. 169–255.
[206] R. Kubo, M. Yokota, and S. Nakajima, “Statistical-Mechanical Theory of Irreversible Processes. II. Response to Thermal Disturbance,” *J. Phys. Soc. Jpn.*, vol. 12, no. 11, pp. 1203–1211, Nov. 1957.
[207] C. J. Gomes, M. Madrid, J. V. Goicochea, and C. H. Amon, “In-Plane and Out-Of-Plane Thermal Conductivity of Silicon Thin Films Predicted by Molecular Dynamics,” *J. Heat Transf.*, vol. 128, no. 11, pp. 1114–1121, avril 2006.